PICOSECOND DYNAMICS

OF TWIN-EMITTER

COHERENT SEMICONDUCTOR LASER ARRAYS

Geoffrey A. Wilson
B.S., Sonoma State University, Rohnert Park, California, 1984
M.S., Oregon Graduate Institute, Beaverton, Oregon, 1989

A thesis submitted to the faculty
of the Oregon Graduate Institute of Science & Technology
in partial fulfillment of the
requirements for the degree
Doctor of Philosophy
in
Applied Physics

April, 1992

The thesis "Picosecond Dynamics of Twin-Emitter Coherent Semiconductor Laser Arrays" by Geoffrey A. Wilson has been examined and approved by the following Examination Committee:

Richard K. DeFreez, Advisor
Associate Professor

Reinhart Engelmann
Professor

V. S. Rao Gudimetla
Assistant Professor

Herbert G. Winful
Associate Professor, University of Michigan

Andrew M. Fraser
Assistant Professor, Portland State University

Dedication

I dedicate this thesis to my mother, who helped me through college and graduate school, but didn't live to see me finish. God rest her soul. Also to my father, who is responsible for my early education in science and mathematics, without which I wouldn't have been able to come this far. I love them both very much.

Acknowledgements

I thank my advisor, Rick DeFreez, for his guidance during every phase of this project. The motivation for this work originates from his pioneering investigations of array dynamics, which uncovered complicated and interesting behaviors that were not anticipated by the simple theories of that time. His physical intuition has been invaluable in interpreting the theoretical and experimental results discussed in this thesis.

This thesis is to a large extent founded upon the contributions of Herb Winful to the theory of array dynamics. I thank him and the other committee members, Reinhart Engelmann, Rao Gudimetla and Andy Fraser, for their valuable input. I also thank Gary Evans of David Sarnoff Research Center for supplying the coherent arrays for the experimental portion of this work, and Tektronix for the equipment grants that are largely responsible for our diode laser characterization capability.

I am grateful to several fellow graduate students and a member of the staff of the Applied Physics and Electrical Engineering Department of the Oregon Graduate Institute. Nu Yu developed many of the techniques used to characterize arrays in this study. I thank Dave Bossert for many helpful technical discussions. Marc Felisky developed the Tektronix PEP-301 computer-based video frame-grabbing and digitization capabilities used in this work. Pete Carleson performed the focused ion beam micromachining used to modify arrays, and helped code the FORTRAN program twostrip, used to simulate the dynamics of a twin-emitter array.

Table of Contents

List of Figures

List of Tables

List of Symbols

Each symbol has a global definition. The extra definitions of multiple-use symbols hold only in the section(s) enclosed in parentheses.

A_m	real amplitude of the mth optical mode
A_N	stimulated emission rate per carrier
A_S	stimulated emission rate nonlinearity per photon
$\mathbf{A}$	matrix of emitter mode overlap integrals
$\mathbf{B}$	matrix of emitter and array mode overlap integrals magnetic induction vector (2.2)
B	normalized spontaneous emission saturable absorber strength coefficient (3.7)
C_m	complex amplitude of the mth optical mode
C	optical feedback parameter heat capacity per unit volume (A)
$C(\tau)$	autocorrelation
C'_p	complex amplitude of the pth emitter
$\mathbf{C}'$	column vector of C'_p
$\mathbf{D}$	electric displacement vector
$\mathbf{D}_b$	lattice contribution to $\mathbf{D}$
$D_{p(e)}$	hole (effective) diffusion coefficient
D	conduction and valence band joint density of states
$E_m(t)$	electric field of mth optical mode
$\mathbf{E}$	electric field vector
$E_m(\omega)$	Fourier component of $E_m(t)$

F_m	transverse plane profile of mth optical mode
G_m	gain per unit time of mth optical mode
$\mathbf{H}$	magnetic field vector
H	modulation transfer function axial power reflectivity per steradian (D)
I	optical intensity, various normalizations
$\mathbf{I}$	identity matrix
$\mathbf{J}$	free current density vector
J	injection current
J_{th}	threshold injection current
J_e	effective injection current
ΔJ_{th}	change in J_{th} due to saturable absorbers
$\mathbf{J}^{(0)}$	Jacobian matrix evaluated at equilibrium
K	longitudinal-vertical plane effective propagation factor nonlinear gain strength factor (3.4)
L	cavity length
L_T	characteristic length of heat diffusion
$L_{n(p)[e]}$	electron (hole) [effective] mean free path
L_d	carrier diffusion length
L′	diffractive section length
M	number of optical modes
N	cavity carrier number number of nodes in a three-emitter lateral mode (F)
P	number of emitters number of times differentiated (2.2)
$P_{a,m}$	carrier-induced polarization of the mth optical mode
P_{dis}	power dissipated in the cavity

P_{out}	optical power output from one facet
$\mathbf{P}$	induced electromagnetic polarization vector
$\mathbf{P_b}$	lattice contribution to $\mathbf{P}$
$\mathbf{P_a}$	carrier contribution to $\mathbf{P}$
Q	absolute-square fitting error number of active saturable absorbers (3.7)
Q_0	total number of saturable absorbers
$Q_{0,min}$	minimum Q_0 causing instability
R	facet power reflectivity
R_{st}	stimulated recombination rate
R_m	spontaneous emission rate into the mth optical mode
R_{ext}	external cavity effective reflectivity
R_{mo}	microscope objective reflectivity
S_m	photon number of the mth optical mode
S_{shb}	spectral hole-burning characteristic photon number
S_{bnd}	equilibrium S stability boundary
$S_{p,m}$	supermode expansion coefficient
S	emitter spacing
T	ratio of carrier and photon lifetimes temperature (A)
T_{hs}	heat sink temperature
$\mathbf{T}$	time-dependence column vector
ΔT	temperature increase
U	ratio of optical intensities laterally-diffracting gaussian beam (G)
V	optical mode volume

V_{cav}	voltage drop across cavity
V_{SUB}	voltage drop across substrate
V_{tot}	voltage drop across device terminals
V_{th}	terminal voltage drop at lasing threshold
V_0	V-intercept of the J(V) curve tangent at J_{th}
W	stripe width dimensionless waveguiding strength (4.5)
W_S	power spectrum noise spectral density (3.5)
X	normalized field amplitude
X_{shb}	spectral hole-burning characteristic amplitude
X′	$2^{-½}X_2$ of three-emitter array
Y	complex round-trip field propagation factor
Z	normalized gain
a_p	rate of photon decay
a_s	rate of carrier decay
a_β	rate of spontaneous emission per cavity photon
b	gaussian beam confocal parameter
c	speed of light in vacuum
d	active layer thickness surface roughness feature size (D)
f	weighted population inversion derivative of dynamical variables (C)
f_B	Boltzmann factor
f_m	lateral profile of the mth array mode
f_0	lateral profile of emitter mode

$f_{\pm}$	lateral profiles of twin-emitter array modes
$f_{1,2}$	lateral profiles of twin-emitter emitter modes
g_m	position-dependent gain per unit time of the mth optical mode
$\tilde{g}_{1(2)}$	normalized net gain of waveguide layers
h	Planck's constant
$\hbar$	$h/2\pi$
i	$(-1)^{1/2}$
j	mode index, number of wavelengths in a cavity round trip hole injection current density (2.3)
j_e	effective hole injection current density
k	mode index, number of wavelengths in a cavity round trip longitudinal propagation factor (G)
k_m	longitudinal propagation factor of the mth optical mode
k_B	Boltzmann's constant
m	mode index, number of wavelengths in a cavity round trip
$m^*_{n(p)\|\|}$	effective electron (hole) [carrier] mass
n	carrier density
n_{th}	average carrier density at threshold
n_n	electron density
n_p	hole density
p	emitter index normalized injection current (4), (5) and (8)
q	electronic charge
$\vec{r}$	position vector
r_{dk}	position-dependent carrier spontaneous decay rate density
r_{st}	position-dependent carrier stimulated recombination rate density

r_q	heat generation rate density
s	photon density half-spacing of twin emitters (4.5)
s_o	object distance
s_i	image distance
t	time
u	ratio of emitter field amplitudes
v	carrier velocity
$w_{x(y)}$	vertical (lateral) waist of elliptical gaussian beam
w	half-width of emitter
$w_y(z)$	lateral spot size of diffracting gaussian beam
$w_{x(y),i}$	vertical (lateral) waist in image plane
x	vertical coordinate
$\hat{x}$	vertical unit vector
x_{act}	vertical coordinate of active layer
y	lateral coordinate dynamical variables (C)
$\hat{y}$	lateral unit vector
$y_{1(2)}$	left (right) lateral stripe boundaries
y_p	lateral coordinate of pth emitter
z	longitudinal coordinate
$\hat{z}$	longitudinal unit vector
Δ_m	gain roll-off suppression of the mth optical mode
Δ	normalized transition detuning from gain peak normalized frequency spread of supermodes (E)
Γ	vertical mode confinement factor

$\Gamma_{\pm}$	twin-emitter array mode lateral confinement factors
Γ_0	emitter mode lateral confinement factor
Λ	matrix of beat frequencies
Ω	angular modulation frequency angular frequency of carrier density and temperature fluctuations (A)
Ω'	complex quantity related to modulation frequency
Φ	optical field
Φ'	approximate optical field
Ψ	squared ratio of frequencies
$\Theta_{1(2)}$	duty cycles of competing optical modes
$<\lvert\Theta\rvert^2>^{1/2}$	phase disruption factor
α	linewidth-enhancement factor
α_m	linewidth-enhancement factor of the mth optical mode
α'	linewidth-enhancement-factor-like constant
β	spontaneous emission factor
χ_m	susceptibility of mth optical mode
$\chi_{L,m}$	linear part of mth optical mode susceptibility
δ	Dirac function
$\delta_{p,r}$	Kronecker symbol
ϵ_0	vacuum permittivity
$\epsilon(t)$	zero-mean δ-correlated random variable
ϵ	ratio of overlap integrals
η	emitter coupling parameter fraction of beam captured by microscope objective (D)
$\eta_{R(I)}$	real (imaginary) parts of coupling parameter
$\boldsymbol{\eta}$	matrix of coupling parameters

η_{diff}	diffractive coupling parameter
$\eta_{I,res}$	resonance value of η_I
$\eta_{I,bnd}$	out-of-phase stability boundary value of η_I
η'	$2^{1/4}\eta$
γ	polarization relaxation rate cladding layer lateral decay factor (4.5)
$\gamma_{c(v)}$	conduction (valence) intra-band relaxation rate
κ	emitter coupling constant gain compression factor (2.6) guide layer lateral propagation factor (4.5) thermal conductivity (A)
λ	wavelength of light in vacuum Lyapunov exponent (3) and (4)
λ_m	wavelength of the mth optical mode
$\Delta\lambda$	optical mode spacing
$\Delta\lambda_{RO}$	gain curve half-width to transparency
$\mu_{(g,)e}$	effective phase (group) index at gain peak
μ_0	vacuum permeability
$\mu(\vec{r},\omega)$	phase index of refraction
$\mu_{(g,)m}(x,y)$	phase (group) index of refraction at ω_m
$\mu_{(g,)e,m}(y)$	effective vertical phase (group) index
$\mu_{(g,)e,m}$	effective phase (group) index
μ_p	hole mobility
μ	dipole moment carrier mobility (2.4.2)
ν_{max}	temperature fluctuation frequency limit
ν_{res}	out-of-phase modulation resonance frequency

ν_{mod}	modulation frequency
$\Delta\nu$	beat frequency of lateral optical modes noise bandwidth (3.5) emission line half-width (3.6)
$\Delta\nu_{m,k}$	four-wave mixing beat frequency of modes m, k and 2k−m
ω_m	angular frequency of the mth optical mode
ω_r	angular frequency of relaxation oscillations
ω_d	angular decay frequency
ω_{-3dB}	3 dB roll-off angular frequency
ω_0	gain peak angular frequency emitter mode angular frequency (4)
ω_T	band-to-band transition angular frequency
$\omega_{gap(max)}$	bandgap (highest-energy) transition angular frequency
ω_{inst}	instability-onset angular frequency
$\omega_{\pm}$	angular frequencies of twin-emitter lateral modes
$\omega_{+++(+-+)}$	angular frequencies of three-emitter lateral modes
ϕ_m	phase of the mth optical mode
ϕ	random reflection phase of rough surface
ϕ_{mo}	diameter of microscope objective aperture
$\psi(x)$	vertical mode profile
ρ	free charge density
$\rho_{11(22)}$	diagonal elements of density matrix
$\rho_{12(21)}$	off-diagonal elements of density matrix
$\bar{\rho}_{11(22)}$	steady-state values of $\rho_{11(22)}$
σ	conductivity
σ_a	saturable-absorber cross-section

τ	carrier lifetime at lasing threshold density
τ_p	photon lifetime
τ_s	differential carrier lifetime
τ_{nr}	non-radiative carrier lifetime
τ_{rad}	radiative carrier lifetime
τ_L	round-trip time of laser cavity
τ_e	mean time between carrier collisions
τ'	intra-band-lifetime-like constant
$\tau_{m,d}$	sidemode (m) suppressed by dominant mode (d) lifetime
τ_{ext}	round-trip time of external cavity
τ_a	saturable absorber lifetime
θ_p	phase difference between adjacent emitters
θ	round-trip phase shift
ξ	normalized detuning of the mth optical mode
ζ	overlap integral of gaussian modes

ABSTRACT

PICOSECOND DYNAMICS

OF TWIN-EMITTER

COHERENT SEMICONDUCTOR LASER ARRAYS

Geoffrey A. Wilson, Ph.D.

Oregon Graduate Institute of Science and Technology, 1992

Supervising Professor: Richard K. DeFreez

This thesis is a study of the dynamics of coherent semiconductor laser arrays, particularly the dynamical effects stemming from the mutual coupling of the single-lateral-mode light-emitting elements composing the array, as distinct from effects also present in single-emitter (stripe-geometry) semiconductor lasers.

Rate equations describing multiple coupled emitters are derived from the semi-classical interaction of optical waves and carriers near the p-n junction of a diode. Single-emitter dynamical effects are catalogued so that they may be distinguished from those unique to arrays in an experimental setting. The simplest coherent array, consisting of two weakly-coupled, identical emitters, is examined in depth. The two lateral modes of the twin-emitter are each associated with an equilibrium point of the twin-emitter rate equations, and the stability of equilibria is obtained as a function of device parameters, particularly the emitter coupling parameter. The stability

analysis is corroborated by numerical integration of the rate equations. The dependence of the coupling parameter on emitter spacing is derived using a simple model.

Techniques are given for measuring the relevant device parameters. The real part of the coupling parameter is related to the beat frequency of the lateral modes of a twin-emitter array. The imaginary part is related to the relative gain of the lateral modes. Experimental verification of the foregoing theory met with limited success, because the available two-stripe arrays were strongly-coupled, compromising the applicability of the twin-emitter model. Possible solutions to the dearth of devices suited to the experimental verification of the theory are proposed, including variable-coupling and diffraction-coupled twin-emitter arrays.

Finally, high-frequency injection current modulation of coherent arrays is discussed. Using the twin-emitter model, it is shown that modulation beyond the relaxation oscillation frequency, the limiting frequency for single-emitters, is effective only when a 180° phase-shift is introduced between the emitter modulation currents. The response to out-of-phase modulation is greatest near the beat frequency of the lateral modes, typically 10-50 GHz. It is shown that a twin-emitter responsive and yet stable to such modulation can be designed by correctly choosing the coupling parameter.

1. INTRODUCTION

It is hoped that this thesis will contribute both to the theoretical understanding and the experimental techniques used to study the dynamics of coherent semiconductor laser arrays, a subject that has remained virtually unexplored compared to other aspects of semiconductor lasers.

Semiconductor lasers are of paramount technological importance. They are unique among lasers in that they are compact, rugged due to their monolithicity, extremely efficient and easily pumped using a low-voltage current source. Other advantages are that they generally do not require bulky cooling systems, have wide homogeneously-broadened photo-recombination linewidths, and can have long maintenance-free lifetimes. Potential disadvantages include poor spatial coherence, difficulty obtaining single-mode operation, temporal instabilities and linewidths that are large compared to those of other lasers. These are not all independent problems.

The development of coherent arrays was driven by the need for large output power with good spatial coherence. The first semiconductor lasers[1,2] were planar p-n junctions in bulk *GaAs*. It was soon recognized that the large currents and cryogenic temperatures needed to reach threshold were a result of poor carrier and optical confinement in the direction perpendicular to the junction plane, or vertical direction. This prompted the introduction of the double-heterostructure geometry, in which the junction is contained in a thin epitaxial layer sandwiched between layers of

material with a larger bandgap. The larger bandgap helps confine carriers, while the associated lower index of refraction guides the optical wave by total internal reflection. Threshold current densities were drastically reduced using this design, and continuous room-temperature operation was achieved[3].

Early semiconductor lasers had no provision for confining the optical wave or limiting the spread of current in the lateral direction, i.e. in the junction plane and perpendicular to the lasing axis. These broad-area devices were prone to filamentation[4], a self-focusing process causing poor lateral uniformity and coherence of the near field (see Chapter 7 of Reference [5]). This problem was largely eliminated by confining the carriers and photons in a region along the lasing axis sufficiently narrow (<10 μm) to control the lateral modes. Early stripe-geometry semiconductor lasers[6] used a narrow contact to the p-type cladding layer to localize the injection of holes. The gain is sufficient to support lasing directly under the contact only, resulting the so-called "gain-guided" stripe laser. The superior lateral optical confinement of dielectric waveguides was soon appreciated and the rib-waveguide geometry was developed[7]. The buried-heterostructure geometry was then introduced[8] to prevent current spreading as well as to provide index-guiding of the optical wave. Since the middle 1970's, dozens of variations on these basic designs have been used to fabricate stripe-geometry semiconductor lasers with good spatial coherence and stable, single-mode operation.

The output power of stripe-geometry lasers is limited to the hundred-milliwatt range, beyond which the intensity of the circulating optical wave is large enough to initiate a runaway cycle of light absorption and heating at the facets, ending in catastrophic facet damage. The need for higher-power coherent beams lead to the development of coherent semiconductor laser arrays.

Coherent arrays consist of two or more stripes placed side-by-side in the junction plane, close enough so that the optical fields of adjacent stripes couple and hopefully phase-lock, but not so close that carrier diffusion fills in the lossy areas between the stripes, causing the array to act like a broad-area device, i.e., exhibit filamentation and poor spatial coherence. As long as coherence is maintained across the entire array, the output power can be increased indefinitely without risking catastrophic facet damage by simply adding more optical emitters.

The coherent array is not without its problems, however. Although the lateral modes may be spatially stable and coherent, they all have nearly the same wavelengths and threshold gains, making them difficult to discriminate among if single-mode operation is desired. Another problem is that the large ratio between the lateral and vertical apertures is inconvenient for some applications, such as launching the beam into an optical fiber or end-pumping a solid-state laser rod. Because of the large aspect ratio and the fact that the light emerges from a cleaved facet, these devices are referred to in this thesis as linear or edge-emitting arrays.

To have a large aperture in two directions, it is necessary to bring the light out of the surface of the wafer. Some such two-dimensional surface-emitting arrays have 45° turning mirrors[9,10] or diffraction gratings[11] etched into the surface to deflect light propagating parallel to the epitaxial layers. Vertical-cavity surface-emitting lasers[12] (VCSELs) obviate the need to deflect the light by orienting the lasing axis in the direction perpendicular to the surface. Emitters are typically less than 5 μm across and can be packed into two-dimensionally coherent arrays with interesting mode patterns[13]. For simplicity and availability of devices, this thesis is limited to consideration of linear coherent arrays.

Early arrays consisted of equally-spaced identical emitters of some easily-fabricated geometry, such as oxide-stripe or ridge waveguide. Supermode theory[14,15] was developed to describe the lateral modes of the array as linear combinations of the modes of the individual emitters. Supermode theory predicts that arrays will have as many lateral modes as there are emitters: a mode with adjacent emitters in phase, a mode with them 180° out of phase, and possibly other modes with inter-emitter relative phases intermediate to these extremes. In-phase operation is desirable for many applications because of the associated single-lobe far-field. Most arrays were found to lase in the 180° out-of-phase mode and other higher-order modes, because these modes have nodes in the lossy regions between the emitters, reducing absorption[16]. Several strategies have been used to force in-phase operation, most notably Y-coupling[17] and index anti-guiding[18] geometries.

While a great deal of effort was going into designing high-power in-phase arrays, the dynamical properties of arrays received relatively little attention. Part of the reluctance may have been due to the complicated spatial structure of the array near-field, compared to that of a single-emitter, requiring study of the spatio-temporal behavior, rather than merely an intensity time series. A deeper reason may be founded in the conjugate relationship of spatio-spectral and spatio-temporal properties: since single-lateral-mode operation was the goal, it may have been perceived that the target device would be quiescent, and thus dynamically uninteresting.

Neglecting the study of array dynamics may be misguided on two counts. First, models used to justify proposed structures often assumed linear, identical or nearest-neighbor coupling, identical emitters, quiescence, the absence of noise, operation near threshold or a combination of the above; whereas the actual device may violate any or all of these idealizations. Therefore, the mode predicted to have the lowest

threshold may be unstable or not robust to array inhomogeneities, or if stable could have a small basin of attraction (set of initial conditions from which the mode is the asymptotic solution) and thus rarely be observed experimentally, or may dominate as predicted, but only over an impractically small range near lasing threshold. Studying the dynamics of arrays may provide clues to improved designs. Secondly, single-mode quiescent operation is not always desirable. For effective high-frequency modulation of arrays, lateral mode competition may be advantageous, as discussed in Chapter 8.

The spatio-temporal properties of coherent arrays can be studied with picosecond resolution using streak cameras[19]. The dynamics of two- and ten-stripe gain-guided[20,21], Y-coupled[22-24], channeled-substrate planar (CSP)[25], grating surface-emitting (GSE)[26] and GSE ring[27] arrays have been studied. Even with constant injection current, instabilities have been noted in all cases except for some recent work involving GSE arrays[28,29] which exhibited quiescent CW operation under some conditions.

Semiconductor lasers fall into what is known as class B due to the relative magnitude of characteristic time constants (see Chapter 2 of Reference [30]), and class-B ring lasers, whose set of possible instabilities encompasses that of class-B Fabry-Perot lasers, are known to have instabilities with frequencies at or below the relaxation oscillation frequency[31]. In several cases[20,21,26,27], frequency components have been observed in the optical output of arrays that are distinct from and beyond the relaxation oscillation frequency. Since the relaxation oscillation frequency is the upper bound of the frequency range of single-emitter dynamical effects, it is reasonable to conclude that these high-frequency components originate from interactions among the emitters.

To explain these interactions, dynamical models based on weak coupling[32,33] and strong coupling[34,35] among the emitters have been proposed. One of the goals of this thesis is to present a comprehensive theoretical framework from which dynamical models of coherent arrays can be derived. Knowledge of the approximations going into a particular model can help one to understand its limitations.

Because of their large number of degrees of freedom, coherent arrays are capable of complicated spatio-temporal dynamics, reminiscent of turbulent fluid flow and other physical systems used to experimentally demonstrate and study deterministic chaos. This suggests that coherent arrays may be studied to advance the field of nonlinear dynamics, as well as using nonlinear dynamics as a tool to improve array design. Coherent arrays are not ideal subjects for study, however, because of the sub-nanosecond time scale of array dynamics. Moreover, their monolithicity makes it difficult to vary the coupling between emitters, which depends primarily on the fixed inter-emitter spacing. Varying the emitter coupling is necessary to access different dynamical behaviors with a single device.

Chapter 2 derives the single-emitter rate equations from the time-varying fields describing the laser cavity. Although derived assuming a single emitter, these results hold for arbitrary waveguide structures and injection current boundary conditions, and are therefore easily extended to coherent arrays.

Chapter 3 discusses dynamical effects inherent to single-emitter devices in typical experimental conditions, so that they can be recognized and separated from effects unique to the coupling of emitters when observing the dynamics of coherent arrays.

Chapter 4 presents three dynamical models of coherent arrays, in decreasing order of complexity and generality. The simplest model is used to obtain rate equa-

tions for dynamical variables describing the twin-emitter coherent array, and the lateral modes and their stability properties are found.

Chapter 5 discusses the numerical integration of the coupled, nonlinear rate equations of the twin-emitter model, to verify the analytical results of Chapter 4 and explore the dynamics of the twin-emitter model.

Chapter 6 presents the experimental techniques used to measure important parameters and otherwise characterize coherent arrays.

Chapter 7 discusses an attempt to support the twin-emitter model through experiment.

Chapter 8 proposes a novel technique for injection current modulation of coherent arrays beyond the frequency of relaxation oscillations, based on the twin-emitter model.

Chapter 9 contains a summary and suggestions for future work.

2. SINGLE-EMITTER RATE EQUATIONS

2.1 Chapter Overview

Before embarking on the study of coherent array semiconductor laser dynamics, it is necessary to understand the dynamics of the building-blocks of coherent arrays, the single-emitter semiconductor lasers. A vast body of literature has been devoted to this topic, and an exhaustive review is beyond the scope of this dissertation. For our purposes it is sufficient to identify common mechanisms that influence the dynamics of single-emitter semiconductor lasers, particularly the characteristic frequencies associated with each mechanism. This is so that single-emitter and multi-emitter effects, which are both expected to be present in the dynamics of coherent arrays, can be distinguished in intensity time series, be they generated by modeling or experimentally observed. Single emitter lasers are discussed in Chapters 2 and 3. The basic rate equations are derived in this chapter, and dynamical effects are covered in the next.

Two approachs are commonly taken in modeling semiconductor lasers: the continuum model and the rate-equation model. In the continuum model, the state of the device is given by the optical electric field, the carrier density, the temperature, and possibly other variables as a function of position and time. Coupled partial

differential equations are written to describe the evolution of these quantities. While this approach has the virtue of being founded on basic principles, the self-consistent solution of such equations requires numerical solution and often does not offer much physical insight. The continuum model is most useful in the static case, where self-consistent equilibrium solutions are sought.

The rate equation approach is based on the notion of modes. A modal decomposition can be defined as an expansion of a continuum-model field

$$\Phi(\vec{r},t) = \mathrm{Re}\left[\sum_m C_m(t)F_m(\vec{r})e^{-i\omega_m t}\right] \qquad (2.1.1)$$

where C_m is the slowly-varying ($|dC_m/dt| << \omega_m$), possibly complex amplitude, F_m is the spatial "profile" and $e^{-i\omega_m t}$ is the optical-frequency phase factor of the mth mode. If the modal frequency ω_m and profile $F_m(\vec{r})$ are sufficiently independent of operating parameters capable of varying on the time scale of the dynamics of interest, e.g. injection current, the modal decomposition can be very useful.

Optical modes are typically quantified by their time-dependent photon number and slowly-varying phase. A single-emitter device may have many modes with appreciable photon numbers running simultaneously. Because the waveguide under consideration is designed to support a single profile in the transverse plane, the profiles of its optical modes differ only in their longitudinal wave vectors, which are determined by the well-known round-trip self-consistent phase condition. For this reason, the modes of a single-emitter device are referred to as "longitudinal modes". A separate rate equation is accorded each dynamical variable of each longitudinal mode, as well as a rate equation for the carrier density.

This chapter gives a derivation of the rate equations from a self-consistent continuum model. This is important for several reasons: first, it allows us to see how physical processes translate into the terms and factors composing the rate equations, and what approximations are made along the way. Second, it facilitates the estimation of the characteristic time constants associated with the processes, allowing us to identify those which respond too slowly, e.g. junction heating, or too rapidly, e.g. intra-band relaxation, to contribute to dynamics in the 500 MHz-50 GHz range of interest, in which coherent array emitter interactions are expected. Third, phenomena dependent on the lateral profile of modes, such as periodic pulsations due to self-focusing (Section 3.8) and the lateral coupling of emitters in coherent arrays (Chapter 4), are readily understood from the continuum model but are obscure if rate equations are used as the starting point.

In Section 2.2, the index of refraction and net optical gain as functions of position and time are assumed to be known, and the evolution of the optical wave is obtained. Each optical mode is described by two rate equations, one for the photon number and one for the phase. In Section 2.3, the optical wave and injection current boundary conditions are assumed to be given, and the carrier number rate equation is derived. It is shown that the gain medium can be adequately described by the carrier number rate equation in the 500 MHz-50 GHz range.

Section 2.4 establishes the link between the gain term appearing in the optical rate equations and the term accounting for stimulated recombination in the carrier rate equation. This is accomplished by relating the modal photon numbers and gains to the rate of photon generation, which is balanced by the rate of stimulated recombination. The next task is to express the induced material polarization in terms of modal susceptibilities, which are related phenomenologically to measurable

parameters.

Section 2.5 casts the photon number rate equation into its finished form by including spontaneous emission.

The equilibrium values of the dynamical variables are found for the single-mode case in Section 2.6. Both spontaneous emission and gain compression are shown to be negligible for any reasonable operating point.

2.2 Optical Rate Equations

Throughout this thesis, the unit vector $\hat{x}$ represents the direction perpendicular to the plane of the epitaxial layers, also called the vertical direction. $\hat{z}$ points in the direction of the propagation of coherent light in the cavity, also called the longitudinal or axial direction. $\hat{y}$ points in the lateral direction. The plane spanned by $\hat{x}$ and $\hat{y}$ is sometimes referred to as the transverse plane.

Section 2.2.1 proceeds from Maxwell's equations to a scalar lateral-electric wave equation. Section 2.2.2 decomposes the wave equation into modes and derives spatio-temporal partial differential equations for the modal amplitudes. Section 2.2.3 separates the spatial dependence of the modal amplitudes, and Section 2.2.4 derives ordinary differential equations in time (rate equations) for the photon number and phase of each mode.

2.2.1 Scalar Transverse-Electric Wave Equation

The semiclassical derivation of the optical rate equations begins with Maxwell's equations in Rationalized MKS units, given by Table 2 in the appendix of Reference [36]

$$\nabla \cdot \mathbf{D} = \rho \tag{2.2.1.1}$$

$$\nabla \times \mathbf{E} = -\frac{\partial}{\partial t}\mathbf{B} \tag{2.2.1.2}$$

$$\nabla \cdot \mathbf{B} = 0 \tag{2.2.1.3}$$

$$\nabla \times \mathbf{H} = \frac{\partial}{\partial t}\mathbf{D} + \mathbf{J} \tag{2.2.1.4}$$

where $\mathbf{E}$ is the electric field, $\mathbf{D}$ is the electric displacement, $\mathbf{H}$ is the magnetic field, $\mathbf{B}$ is the magnetic induction, and ρ and $\mathbf{J}$ are the free charge and current densities, respectively. Taking the divergence of (2.2.1.4) and using (2.2.1.1) yields the continuity equation

$$\nabla \cdot \nabla \times \mathbf{H} = 0 = \frac{\partial}{\partial t}\rho + \nabla \cdot \mathbf{J} \tag{2.2.1.5}$$

The material is assumed to be non-magnetic so that

$$\mathbf{B} = \mu_0 \mathbf{H} \tag{2.2.1.6}$$

where μ_0 is the vacuum permeability. The relationship between the free current and the electric field is assumed to be

$$\mathbf{J} = \sigma \mathbf{E} \tag{2.2.1.7}$$

where σ is a real, frequency-independent scalar conductivity. This is justified over the anticipated narrow band of lasing modes, and will later be interpreted

phenomenologically as linear damping of the optical field. The electric displacement is conveniently separated as

$$\mathbf{D} \equiv \epsilon_0 \mathbf{E} + \mathbf{P} \equiv \epsilon_0 \mathbf{E} + \mathbf{P}_b + \mathbf{P}_a \equiv \mathbf{D}_b + \mathbf{P}_a \tag{2.2.1.8}$$

where ϵ_0 is the vacuum permittivity, $\mathbf{P}$ is the induced polarization, of which $\mathbf{P}_b$ is the "background" contribution associated with valence-electron resonances of the semiconductor lattice and $\mathbf{P}_a$ is the "active" contribution associated with free carriers, and $\mathbf{D}_b$ is the background electric displacement.

Semiconductor lasers have a marked tendency to operate in lateral-electric modes, i.e. those with the electric field polarized parallel to the epilayers. Thus, the optical wave is described by the scalar wave equation for the $\hat{y}$ component of the electric field. Taking the curl of (2.2.1.2), substituting the vector identity

$$\nabla\times\nabla\times = \nabla\nabla\cdot - \nabla^2 \tag{2.2.1.9}$$

and using (2.2.1.5) and (2.2.1.7) to rewrite $\nabla\nabla\cdot\mathbf{E}$, and using (2.2.1.6), (2.2.1.4), (2.2.1.8) and (2.2.1.7) on the right-hand side and rearranging gives

$$\nabla^2\mathrm{E} - \mu_0\sigma\frac{\partial}{\partial t}\mathrm{E} - \mu_0\frac{\partial^2}{\partial t^2}\mathrm{D}_b - \mu_0\frac{\partial^2}{\partial t^2}\mathrm{P}_a = -\frac{1}{\sigma}\frac{\partial}{\partial t}\nabla\rho \tag{2.2.1.10}$$

Assuming charge neutrality, the last term is dropped. Moreover, $\mathbf{E}$ and the subsidiary fields $\mathbf{D}_b$ and $\mathbf{P}_a$ are assumed to be polarized in the lateral direction

$$\mathbf{E} = \hat{y}\mathrm{E} \tag{2.2.1.11}$$

so that the scalar wave equation

$$\nabla^2\mathrm{E} - \mu_0\sigma\frac{\partial}{\partial t}\mathrm{E} - \mu_0\frac{\partial^2}{\partial t^2}\mathrm{D}_b - \mu_0\frac{\partial^2}{\partial t^2}\mathrm{P}_a = 0 \tag{2.2.1.12}$$

is obtained.

2.2.2 Modal Decomposition

The goal is to separate (2.2.1.12) into modal contributions and factor out the rapid (optical frequency) time dependence. The optical frequency electric field can be expressed as a sum over modes

$$E(\vec{r},t) = \sum_m E_m(\vec{r},t) \tag{2.2.2.1}$$

where

$$E_m(\vec{r},t) = \left[2\frac{\hbar\omega_m}{\epsilon_0\mu_{e,m}^2}\right]^{1/2} Re[C_m(\vec{r},t)e^{-i\omega_m t}] \tag{2.2.2.2}$$

where ω_m are the modal frequencies and C_m are complex amplitudes that vary slowly in time compared to the optical-frequency phase factors. The constant of proportionality, hereafter written as $[...]^{1/2}$, is chosen so that $|C_m|^2$ can be interpreted as the modal photon density. This can be seen by squaring (2.2.2.2) and multiplying by $\epsilon_0\mu_{e,m}^2$, where $\mu_{e,m}$ is the effective phase index of the mth mode, to obtain the instantaneous energy density, and then averaging over an optical cycle and dividing by the photon energy $\hbar\omega_m$. The modal photon number is therefore

$$S_m(t) \equiv \int_0^L dz \int_{-\infty}^{\infty} dy \int_{-\infty}^{\infty} dx\, |C_m|^2 \tag{2.2.2.3}$$

where L is the cavity length.

The modal contribution to the first term of (2.2.1.12) can immediately be written as

$$\nabla^2 E_m = [...]^{1/2} Re[(\nabla^2 C_m)e^{-i\omega_m t}] \tag{2.2.2.4}$$

The other terms of (2.2.1.12) involve time derivatives that can be handled by intro-

ducing the Fourier transform of the modal electric field

$$E_m(\vec{r},t) = \int_{-\infty}^{\infty} d\omega\ e^{-i\omega t} E_m(\vec{r},\omega) \tag{2.2.2.5}$$

Differentiating (2.2.2.5) and (2.2.2.2) P times with respect to time and equating gives

$$\int_{-\infty}^{\infty} d\omega\ e^{-i\omega t}(-i\omega)^P E_m(\omega) =$$

$$[...]^{\frac{1}{2}}\mathrm{Re}\left[\left((-i\omega_m)^P C_m + P(-i\omega_m)^{P-1}\frac{\partial}{\partial t}C_m\right)e^{-i\omega_m t}\right] \tag{2.2.2.6}$$

where the slowly-varying nature of C_m was invoked to justify neglecting its higher-order derivatives. The modal contribution to the second term in (2.2.1.12) can be expressed as

$$-\mu_0\sigma\frac{\partial}{\partial t}E_m = [...]^{\frac{1}{2}}\mathrm{Re}\left[\left(i\mu_0\sigma\omega_m C_m - \mu_0\sigma\frac{\partial}{\partial t}C_m\right)e^{-i\omega_m t}\right] \tag{2.2.2.7}$$

To obtain the modal contribution to the third term of (2.2.1.12), we expand the background electric displacement D_b similarly to (2.2.2.1), and assume that

$$D_{b,m}(\vec{r},t) = \epsilon_0 \int_{-\infty}^{\infty} d\omega\ e^{-i\omega t}\mu^2(\vec{r},\omega)E_m(\vec{r},\omega) \tag{2.2.2.8}$$

where μ is the (real) phase index of refraction. This is based on the notion that the valence-electron resonances responsible for the background polarization are distant from the lasing frequency ω_0, such that the real part of the associated susceptibility is substantial and frequency-dependent, while the imaginary part is small and frequency-independent. The latter represents loss which can be included in the term containing the phenomenological parameter σ. A consequence of the slowly-varying

nature of C_m is that $E_m(\vec{r},\omega)$ is sharply-peaked about ω_m, justifying the use of

$$\mu^2 \approx \mu_m^2 + 2\mu_m \left[\frac{\partial \mu}{\partial \omega}\right]_m (\omega - \omega_m) \tag{2.2.2.9}$$

where the subscript "m" denotes evaluation at ω_m. Differentiating (2.2.2.8) twice with respect to time, using (2.2.2.9) and (2.2.2.6) and multiplying by $-\mu_0$ allows the third term of (2.2.1.12) to be written as

$$-\mu_0 \frac{\partial^2}{\partial t^2} D_{b,m} =$$

$$[...]^{1/2} \mathrm{Re}\left[\left(\frac{\omega_m^2 \mu_m^2}{c^2} C_m + 2i \frac{\omega_m \mu_m \mu_{g,m}}{c^2} \frac{\partial}{\partial t} C_m\right) e^{-i\omega_m t}\right] \tag{2.2.2.10}$$

where the group index of refraction at ω_m

$$\mu_{g,m} \equiv \mu_m + \omega_m \left[\frac{\partial \mu}{\partial \omega}\right]_m \tag{2.2.2.11}$$

and the speed of light in vacuum

$$c = \frac{1}{[\mu_0 \epsilon_0]^{1/2}} \tag{2.2.2.12}$$

were introduced.

The free-carrier polarization term of (2.2.1.12) can be formally separated by introducing an expansion similar to (2.2.2.1) for P_a and defining a modal susceptibility χ_m such that

$$P_{a,m}(\vec{r},t) \equiv [...]^{1/2} \mathrm{Re}[\epsilon_0 \chi_m(\vec{r},t) C_m e^{-i\omega_m t}] \tag{2.2.2.13}$$

This modal susceptibility contains all the coupling between modes, and will be further discussed in Section 2.4. Differentiating (2.2.2.13) twice with respect to time

and multiplying by $-\mu_0$ gives the modal contribution to the fourth term of (2.2.1.12)

$$-\mu_0 \frac{\partial^2}{\partial t^2} P_{a,m} =$$

$$[...]^{1/2} \mathrm{Re}\left[\left(2i\frac{\omega_m}{c^2} C_m \frac{\partial}{\partial t}\chi_m + 2i\frac{\omega_m}{c^2}\chi_m \frac{\partial}{\partial t} C_m + \frac{\omega_m^2}{c^2}\chi_m C_m\right) e^{-i\omega_m t}\right] \quad (2.2.2.14)$$

where the second-derivatives and product-of-derivatives of the slowly-varying quantities χ_m and C_m have been neglected.

Substituting (2.2.2.4), (2.2.2.7), (2.2.2.10) and (2.2.2.14) into (2.2.1.12), separating modal contributions, cancelling the common $[...]^{1/2}$ factor, suppressing the "Re" operation and cancelling the common phase factor gives the desired result. Before doing this, we make some simplifying approximations. In Section 2.2.4, it will be shown that

$$\frac{\sigma}{2\omega_m \epsilon_0} << 1 < \mu_m \mu_{g,m} \quad (2.2.2.15)$$

Also, the carrier-induced susceptibility is small ($|\chi_m| << 1$), so that the second terms in Re[...] of (2.2.2.7) and (2.2.2.14) can be neglected in favor of the second term in Re[...] of (2.2.2.10). Furthermore, in Section 2.4.2, the first term in Re[...] in (2.2.2.14) is shown to be negligible compared to the third, and so is dropped. (2.2.1.12) becomes

$$-2i\frac{\omega_m \mu_m(x,y)\mu_{g,m}(x,y)}{c^2}\frac{\partial}{\partial t} C_m =$$

$$\left[\nabla^2 + \frac{\omega_m^2}{c^2}\left(\mu_m^2(x,y) + i\frac{\sigma}{\omega_m \epsilon_0} + \chi_m(x,y,t)\right)\right] C_m \quad (2.2.2.16)$$

2.2.3 Modal Spatial Profiles

We turn now to removing the spatial dependence. (2.2.2.16) has been written with the assumption that all quantities characterizing the waveguide are independent of the longitudinal coordinate. We also make the distributed mirror-loss approximation, in which the abrupt loss of light due to transmission at the facets of Fabry-Perot or the edge of the grating in distributed-Bragg-reflecting semiconductor lasers is considered to be distributed along the length of the gain medium such that the round-trip loss is equivalent to that of the real device. The treatment remains exact for distributed-feedback devices. Thus the only z-dependence in (2.2.2.16) lies in ∇^2 and C_m, and is easily separated.

It is consistent with the distributed-loss approximation to consider the facets as perfect reflectors. Therefore, the cavity modes are standing waves with nodes at the facets (z=0 and z=L). The modal amplitudes can be factored as

$$C_m(x,y,z,t) \rightarrow C_m(x,y,t)\left(\frac{2}{L}\right)^{1/2}\sin(k_m z) \qquad (2.2.3.1)$$

where the longitudinal propagation factor of the mth mode is

$$k_m \equiv \frac{\omega_m \mu_{e,m}}{c} \qquad (2.2.3.2)$$

where $\mu_{e,m}$, the effective phase index of the mth mode, is defined by (2.2.3.2).

Constraining the optical intensity to be independent of z limits the validity of the model to frequencies somewhat less than the frequency associated with the cavity round-trip time. Since the latter is typically greater than 100 GHz, this is not a problem in studying dynamics in the 500 MHz-50 GHz range of interest, but is obviously incorrect for treating longitudinal mode-locking.

To remove the remaining spatial dependence, we make the separation

$$C_m(x,y,t) \rightarrow C_m(t)F_m(x,y) \tag{2.2.3.3}$$

where F_m, a complex function normalized so that

$$\int_{-\infty}^{\infty} dy \int_{-\infty}^{\infty} dx \, |F_m|^2 = 1 \tag{2.2.3.4}$$

is the "profile" of the mode. This is tantamount to assuming that the modal profile is independent of amplitude and phase changes, which is a good assumption for index-guided devices since the guiding mechanism is passive. This assumption may not always be valid for gain-guides, and is obviously violated in the cases of lateral position instability and self-focusing, which are treated in Section 3.8.

If we assume that there exists some equilibrium modal susceptibility $\chi_m^{(0)}$ for which $C_m(t)$ is constant, then inserting (2.2.3.1) and (2.2.3.3) into (2.2.2.16) gives

$$\left[\nabla_t^2 + \frac{\omega_m^2}{c^2}\left(\mu_m^2(x,y) - \mu_{e,m}^2 + i\frac{\sigma}{\omega_m \epsilon_0} + \chi_m^{(0)}(x,y)\right)\right] F_m = 0 \tag{2.2.3.5}$$

where ∇_t^2 is the Laplacian operator in the transverse plane. Given the longitudinal propagation factor k_m, which is subject to the round-trip phase condition

$$k_m L = 2\pi m \tag{2.2.3.6}$$

where m is the integer number of wavelengths in a cavity round trip (on the order of 1000 for a typical device), (2.2.3.5) can be regarded as a characteristic equation for the unknowns ω_m and F_m, subject to the boundary condition that F_m vanishes sufficiently rapidly as $x^2+y^2 \rightarrow \infty$ so that (2.2.3.4) can be fulfilled. The effective-index method (see section 2.5.1 of Reference [37]) is commonly used to solve (2.2.3.5). Dur-

ing the solution of the vertical portion of the transverse problem, it is permissible to neglect $\mathrm{Re}[\chi_m]$ and the imaginary terms, because the graded and abrupt index variations of the epitaxial layers dominate the waveguiding. For an index-guided device, this approximation can be made during the solution of the lateral portion of the problem as well, while for a gain-guided device these terms must be included to account for gain guiding and index anti-guiding.

Multiplying (2.2.3.5) from the left by F_m^*, subtracting the complex conjugate of the equation just obtained, and integrating over the transverse plane gives

$$\int_{-\infty}^{\infty} dy \int_{-\infty}^{\infty} dx \, (F_m^* \nabla_t^2 F_m - F_m \nabla_t^2 F_m^*)$$

$$+2i\frac{\omega_m^2}{c^2}\left[\frac{\sigma}{\omega_m \epsilon_0}+\mathrm{Im}[\chi_m^{(0)}]\right] |F_m|^2 = 0 \qquad (2.2.3.7)$$

The term in parentheses can be eliminated by using the divergence theorem to write it as a surface integral, and invoking the rapid decay of F_m as $x^2+y^2 \to \infty$. This results in

$$-\langle \mathrm{Im}[\chi_m^{(0)}] \rangle = \frac{\sigma}{\omega_m \epsilon_0} \qquad (2.2.3.8)$$

as a condition for modal equilibrium, where $\langle ... \rangle$ represents averaging over the transverse plane weighted with $|F_m|^2$. This merely states that the modal gain balances the losses in equilibrium.

2.2.4 Modal Rate Equations

We now restore the dynamics by allowing

$$\chi_m(t) = \chi_m^{(0)} + \chi_m^{(1)}(t) \tag{2.2.4.1}$$

so that substituting (2.2.3.1), (2.2.3.3), (2.2.3.5) and (2.2.4.1) into (2.2.2.16) gives

$$-2i\mu_m\mu_{g,m}F_m\frac{d}{dt}C_m = \omega_m\chi_m^{(1)}F_mC_m \tag{2.2.4.2}$$

Multiplying by F_m^* and integrating over the transverse plane gives

$$\frac{d}{dt}C_m = i\frac{\omega_m<\chi_m^{(1)}>}{2<\mu_m\mu_{g,m}>}C_m \tag{2.2.4.3}$$

Next we simplify the multiplicative factor in (2.2.4.3) by approximating

$$<\mu_m\mu_{g,m}> \approx <\mu_m><\mu_{g,m}> \approx \mu_{e,m}\mu_{g,e,m} \approx \mu_e\mu_{g,e} \tag{2.2.4.4}$$

In the first step, the weighted average of the product of the position-dependent phase and group indices of the mth mode is replaced by the product of the weighted averages, in the second step, the weighted averages are replaced by the effective indices of the mth mode, which are in turn replaced by the effective indices of the "main mode" in the third step. Also, the mth mode frequency is replaced by the frequency of the main mode

$$\omega_m \approx \omega_0 \tag{2.2.4.5}$$

and the complex amplitude C_m is separated into the product of a real amplitude and a phase factor

$$C_m \rightarrow A_m(t)e^{i\phi_m(t)} \tag{2.2.4.6}$$

Substituting (2.2.4.4), (2.2.4.5), and (2.2.4.6) into (2.2.4.3) and separating real and

imaginary parts gives

$$\frac{d}{dt}A_m = -\frac{\omega_0}{2\mu_e\mu_{g,e}}<\mathrm{Im}[\chi_m^{(1)}]>A_m \qquad (2.2.4.7)$$

and

$$\frac{d}{dt}\phi_m = \frac{\omega_0}{2\mu_e\mu_{g,e}}<\mathrm{Re}[\chi_m^{(1)}]> \qquad (2.2.4.8)$$

Note that by (2.2.2.3), (2.2.3.1), (2.2.3.3), (2.2.3.4) and (2.2.4.6), that

$$A_m^2 = S_m \qquad (2.2.4.9)$$

can be interpreted as the modal photon number. Differentiating (2.2.4.9) with respect to time and using (2.2.4.7) and (2.2.4.1) gives

$$\frac{d}{dt}S_m = \left[G_m - \frac{1}{\tau_p}\right]S_m \qquad (2.2.4.10)$$

where

$$G_m \equiv -\frac{\omega_0}{\mu_e\mu_{g,e}}<\mathrm{Im}[\chi_m]> \qquad (2.2.4.11)$$

is the modal gain and

$$\frac{1}{\tau_p} \equiv \frac{\sigma}{\mu_e\mu_{g,e}\epsilon_0} = -\frac{\omega_0}{\mu_e\mu_{g,e}}<\mathrm{Im}[\chi_0^{(0)}]> \qquad (2.2.4.12)$$

where (2.2.3.8) was used, is the photon loss rate, assumed to be the same for all the modes. The photon loss rate is typically $\approx 10^{12}\ s^{-1}$, which is small compared to optical frequencies of $\approx 2\times 10^{15}\ s^{-1}$, justifying (2.2.2.15). To proceed, it is necessary to have an expression for $<\chi_m>$, the derivation of which is postponed until Section 2.4.3.

2.3 Gain Medium Dynamics

In Section 2.2 the state of the gain medium was assumed known to obtain the time evolution of the optical wave. In this section we assume the opposite. We continue to assume that the waveguide has no longitudinal structure, and that mirror losses are distributed. Thus the static and dynamic spatial functions used to describe the gain medium are independent of the longitudinal coordinate z.

Static spatial functions include the composition and crystalline orientation of the host material, the identity and concentration of dopants, the temperature and possibly the stress at every point in the transverse plane. The temperature is considered a static effect because its characteristic response time is slow compared to the 500 MHz-50 GHz regime of interest, as shown in Appendix A.

Dynamic spatial functions include the optical electric field and the density of carriers. Ideally, the occupancy of carrier states as a function of energy should be known, but since intra-band and polarization relaxations are quite rapid compared to the dynamics of interest, their effects can be simply included in the carrier-induced susceptibility, as discussed in Section 2.4.2 and Appendix B. Thus the gain medium can be adequately described by the carrier density summed over the band states. This overall carrier density can then be averaged over the cavity to give the cavity carrier number.

2.3.1 Carrier-Number Rate Equation

The active region is the only part of the structure at which both electrons and holes exist in quantities sufficient for optical gain through stimulated recombination.

It is usually intrinsic or lightly-doped and very thin, typically less than 0.2 μm. Since this is small compared to both the carrier diffusion length and the vertical spot size of the optical mode, the vertical dependence of the carrier concentrations can be neglected, reducing the problem to one dimension. During operation, the carrier density is typically much larger than the concentration of dopants. Neglecting the latter and invoking detailed charge neutrality

$$n_n(y,t) = n_p(y,t) \equiv n(y,t) \tag{2.3.1.1}$$

where n_n and n_p are the concentrations of electrons and holes, respectively, makes it sufficient to keep track of the concentration of only one of the carrier species. A "stationary-electron, diffusing-hole" model has been proposed[38] for the dominant n-type substrate stripe-geometry semiconductor laser technology, in which it is appropriate to solve for the hole concentration, using the time-dependent diffusion equation

$$\frac{\partial}{\partial t}n = \frac{j(y,t)}{qd} - r_{dk}(n) - r_{st}(n,s) + D_e\frac{\partial^2}{\partial y^2}n \tag{2.3.1.2}$$

where j(y,t) is the injected hole current density, q is the electronic charge, d is the thickness of the active layer, r_{dk} is the rate of carrier loss due to spontaneous (radiative and non-radiative) decay, r_{st} is the rate of carrier loss due to stimulated recombination and thus depends on the local photon density

$$s(x_{act},y,t) = \frac{1}{L}\sum_m S_m(t)\,|F_m(x_{act},y)|^2 \tag{2.3.1.3}$$

where x_{act} is the vertical coordinate of the active layer, and D_e is an effective diffusion coefficient[38], given by

$$D_e \equiv 2D_p = 2\frac{kT}{q}\mu_p \tag{2.3.1.4}$$

where D_p and μ_p are the hole diffusion coefficient and mobility, respectively. Note the implicit assumption that the active layer is flat and of uniform thickness.

We assume that longitudinal carrier diffusion is effective in washing out holes burned in the carrier density by the standing optical wave, so that the carrier density can be considered to be independent of z. It has been estimated[39] that the amplitude of the longitudinal variation in the carrier density due to hole burning is more than three orders of magnitude smaller than the average carrier density.

Given s(y,t), the hole-current boundary condition at the p-contact and the ground-plane boundary condition at the n-contact, (2.3.1.2) and Laplace's equation for the voltage in the cladding layers are solved self-consistently[40] for p and j. The procedure is arduous and beyond the scope of this thesis, which is concerned with dynamical effects. For this reason, we henceforth consider the profile of the carrier density to be known, preferably through experimental measurement.

The form of r_{dk} has been discussed in the literature[41]. To avoid the complications of a power-series representation or more exotic analytical forms, r_{dk} can be expanded to first order about $n=n_{th}$, the spatially-averaged lasing threshold carrier density

$$r_{dk}(n) \approx \frac{n_{th}}{\tau} + \frac{n-n_{th}}{\tau_s} \qquad (2.3.1.5)$$

where τ is the threshold carrier lifetime and τ_s is the differential carrier lifetime at threshold[41]

$$\frac{1}{\tau_s} \equiv \left[\frac{dr_{dk}}{dn}\right]_{th} \qquad (2.3.1.6)$$

The constant terms of (2.3.1.5) can be included in the pumping term of (2.3.1.2) by

defining an effective current density

$$\frac{j_e}{qd} \equiv \frac{j}{qd} - \left[\frac{1}{\tau} - \frac{1}{\tau_s}\right] n_{th} \tag{2.3.1.7}$$

Let the active region be bounded in the lateral dimension such that $y_1 \leq y \leq y_2$. These bounds can be at infinity, as in a carrier-diffusion-limited gain-guide, or finite, as in the case of a buried heterostructure. In the former case, because of finite diffusion, the following boundary conditions hold

$$\frac{\partial n}{\partial y}(y_1) = \frac{\partial n}{\partial y}(y_2) = 0 \tag{2.3.1.8}$$

In the latter case, y_1 and y_2 represent the lateral positions of current-blocking junctions. At these junctions, the net lateral current is zero, that is, the diffusion and drift contributions cancel. Since it is actually the total current that is expressed as an effective diffusion current in the stationary-electron, diffusing-hole model[38], (2.3.1.8) holds for finite boundaries as well.

We can integrate (2.3.1.2) over the lateral coordinate and multiplied by the cavity length L and the active layer thickness d to obtain the rate equation for the cavity carrier number

$$\frac{d}{dt}N = \frac{J_e}{q} - \frac{N}{\tau_s} - R_{st} \tag{2.3.1.9}$$

where J_e is the effective injection current and R_{st} is the stimulated recombination rate, to be discussed in Section 2.4.1. The diffusion term vanishes according to (2.3.1.8). We assume that J_e can be replaced by the actual injection current J, since these differ by an additive constant, and only changes in current enter into the dynamics. Henceforth, we will ignore the distinction and drop the subscript "e".

2.4 Optical Mode and Carrier Interactions

The purpose of this section is to express the coupling of the optical mode rate equations (2.2.4.8) and (2.2.4.10) and the carrier-number rate equation (2.3.1.9) in a simple manner, keeping in mind our interest in dynamics in the 500 MHz-50 GHz frequency range.

Section 2.4.1 uses the balance between the rate of stimulated recombination and the rate of stimulated emission into all the optical modes to link the carrier and photon number rate equations. Section 2.4.2 models the gain medium as an ensemble of two-level systems. Each system consists of a conduction- and valence-band state pair with the same k-vector, so that they can interact radiatively. States in the same band are coupled to model intra-band relaxation. A transition frequency dependent two-level density matrix is used to write the driving term of the lateral-electric scalar wave equation (2.2.1.12), $\partial^2 P_a/\partial t^2$, in terms of the carrier-induced susceptibility χ_m, and χ_m in terms of fundamental properties of the gain medium. In Section 2.4.3, the modal susceptibility $<\chi_m>$ is expressed in terms of measurable parameters.

2.4.1 Stimulated Recombination and Emission Balance

The first step is to relate R_{st}, the loss rate of the cavity carrier number due to stimulated emission, to the gain rate of the cavity photon number. The latter is given by the first term in (2.2.4.10), summed over the modes, and thus

$$R_{st} = \sum_m G_m S_m \qquad (2.4.1.1)$$

The rate equation for the carrier number is found by substituting (2.4.1.1) into

(2.3.1.9)

$$\frac{d}{dt}N = \frac{J}{q} - \frac{N}{\tau_s} - \sum_m G_m S_m \qquad (2.4.1.2)$$

Note that the stimulated recombination rate density is given by

$$r_{st} = -\frac{\omega_0}{\mu_e \mu_{g,e} L} \sum_m \mathrm{Im}[\chi_m] S_m |F(x,y)|^2 \qquad (2.4.1.3)$$

which can be verified by integrating over the cavity and using (2.2.4.11) and (2.4.1.1).

2.4.2 Carrier-Induced Susceptibility

The carrier-induced susceptibility χ_m, introduced in (2.2.2.13), drives the time evolution of the photon number S_m and the phase ϕ_m of each mode. This section discusses the dependence of χ_m on the carrier and photon densities. The mechanisms contributing to χ_m can be separated into those involving stimulated transitions between a conduction band state and a valence band state, and those involving transitions between states in the same band. Inter-band effects will be discussed in this section, while intra-band effects will be touched upon at the end of Section 2.4.3.

Two major approaches have been taken to model the induced polarization associated with inter-band transitions in bulk semiconductor material, one based on band tails[42] and the other based on relaxation broadening[43]. The band-tail model is appropriate to heavily-doped semiconductors, in which "tails" extending from the conduction and valence bands into the gap between the bands can explain the absorption of photons with less than the bandgap energy. The band-tail states are partially localized and are thus not exact momentum eigenstates, in contrast with the

conduction and valence states of a flawless intrinsic semiconductor. This causes the momentum-selection rule, which governs the allowed radiative transitions in the pure material, to be relaxed. This model is not applicable to semiconductor lasers with lightly-doped active regions, or those lasing with photon energy sufficiently greater than the bandgap such that band-tail states are not significantly involved.

The relaxation-broadening approach assumes that the momentum-selection rule limits radiative transitions from a given conduction band state to the state with the same vector momentum in the valence band. This model is almost equivalent to the two-level atom paradigm that has been a cornerstone in the theory of gas and solid-state lasers, with injection and intra-band scattering of carriers serving as pump mechanisms for the band states. Thus the semiconductor medium can be considered to be a large number of pairs of states, such that each state interacts radiatively with its partner in the other band and non-radiatively with the other states in its band. The non-radiative interactions are described simply by the decay of non-equilibrium state populations at rates proportional to the deviations of the state populations from their equilibrium values.

A complication is that while a two-level atom is localized (at least on the time scale associated with absorption and stimulated emission), the band states exist throughout the bulk material and interact with spatially extended optical modes. Fortunately, it has been pointed out[43] that band states can be considered localized on a length scale large compared to the carrier mean free path in the active region, and if this scale is small compared to the wavelength of light in the material, a meaningful localized macroscopic polarization can be defined. The carrier mean free path is given in Section 5.1 of Reference [44]

$$L_e = v\tau_e = \left[3k_B\frac{T}{m^*}\right]^{\frac{1}{2}}\frac{m^*\mu}{q} \qquad (2.4.2.1)$$

where v is the thermal velocity, τ_e is the mean free time between collisions, k_BT is the thermal energy, m^* is the effective mass of the carrier, μ is the carrier mobility and q is the electronic charge. Table 13.1 of Reference [44] gives $m_n^*/m=0.065$, $m_p^*/m=0.5$, $\mu_n=0.89\ m^2V^{-1}s^{-1}$ and $\mu_p=0.04\ m^2V^{-1}s^{-1}$ for GaAs at 300 kelvin, where m is the mass of an electron. Using these along with $m=9.11\times10^{-31}$ kg, $q=1.6\times10^{-19}$ C and $k_BT=4.14\times10^{-21}$ J at 300 kelvin gives the geometrical mean of the carrier mean free paths $[L_nL_p]^{\frac{1}{2}}=$ 53 nm, which is somewhat smaller than the wavelength of light in the material, given by $\lambda/\mu_e=$ 248 nm using $\lambda=818$ nm and $\mu_e=3.3$, typical of GaAs/AlGaAs lasers. Thus there is some sense in considering pairs of carrier states as localized dipoles in a spatially-uniform electric field.

The induced polarization due to the carriers is given by[45]

$$P_a(t) = \int_{-\infty}^{\infty} d\omega_T\ \mu(\omega_T)D(\omega_T)[\rho_{12}(\omega_T,t)+\rho_{21}(\omega_T,t)] \qquad (2.4.2.2)$$

where ω_T is the inter-band transition frequency, μ is the transition dipole moment and D is the joint density-of-states of the conduction and valence bands between all momentum-conserving transitions of energy $\hbar\omega_T$. The off-diagonal matrix elements of the two-level density matrix for the transitions with frequency ω_T are denoted by ρ_{12} and ρ_{21}, which are a complex conjugate pair. The integration over all frequencies is permitted by requiring that $D(\omega_T<\omega_{gap})=0$ and $D(\omega_T>\omega_{max})=0$, where $\hbar\omega_{gap}$ is the band-gap energy and $\hbar\omega_{max}$ is the energy of the maximum-energy k-conserving transition between the conduction and valence bands.

It is necessary to obtain an expression for ρ_{12}. The following equations describe the time evolution of the two-level matrix elements[46]

$$\frac{d}{dt}\rho_{11} + \gamma_c(\rho_{11}-\bar{\rho}_{11}) = \frac{\mu}{i\hbar}(\rho_{12}-\rho_{21})E(t) \qquad (2.4.2.3)$$

$$\frac{d}{dt}\rho_{22} + \gamma_v(\rho_{22}-\bar{\rho}_{22}) = -\frac{\mu}{i\hbar}(\rho_{12}-\rho_{21})E(t) \qquad (2.4.2.4)$$

$$\frac{d}{dt}\rho_{12} + (\gamma+i\omega_T)\rho_{12} = \frac{\mu}{i\hbar}(\rho_{11}-\rho_{22})E(t) \qquad (2.4.2.5)$$

where $\gamma_{c(v)}$ is the intra-band energy relaxation rate for the conduction (valence) band, γ is the polarization relaxation rate and $\bar{\rho}_{11(22)}$ is the occupation probability for electrons in state $|1>$ (holes in state $|2>$) in thermal equilibrium and is determined by the quasi-Fermi level of the conduction (valence) band.

Substituting multi-mode expansions for the electric field and the density matrix elements yields a coupled set of modal equations that are in practice difficult to solve. A perturbative solution to third order in the electric field has been described[46,47], in which three contributions to the third-order non-linear susceptibility were identified and associated with spectral hole burning, population pulsations and four-wave mixing. The effects of these mechanisms on the stability of the main mode is discussed in Section 3.4, and the neglect of population pulsations and four-wave mixing in the dynamics is discussed in Appendix B.

Each lasing mode burns a hole in the gain curve, centered at the modal frequency and wide compared to the emission spectrum of a reasonably good semiconductor laser. In view of this, all the modes suffer about the same reduction of gain due to the unresolved hole burnt by all of them. Therefore, it is plausible to assume a monochromatic or single-mode approximation of the optical field to obtain the gain

reduction, or "compression", due to the optical field. This approach has appeared in the literature[45] and is outlined below.

We assume that the slowly-varying amplitude of all the modes except the lasing mode (m=0) are small in (2.2.2.1), so that the following solutions to (2.4.2.3)-(2.4.2.5) are found

$$\rho_{11} = \bar{\rho}_{11} - \frac{\gamma_v}{\gamma_c+\gamma_v}[\bar{\rho}_{11}-\bar{\rho}_{22}]\frac{I(t)}{1+\Delta^2+I(t)} \tag{2.4.2.6}$$

$$\rho_{22} = \bar{\rho}_{22} + \frac{\gamma_c}{\gamma_c+\gamma_v}[\bar{\rho}_{11}-\bar{\rho}_{22}]\frac{I(t)}{1+\Delta^2+I(t)} \tag{2.4.2.7}$$

$$\rho_{12} = -\frac{\mu}{2\hbar\gamma}[\bar{\rho}_{11}-\bar{\rho}_{22}]\frac{1+\Delta^2}{1+\Delta^2+I(t)}\sum_m \frac{E_m e^{-i\omega t}}{\Delta-\xi-i} \tag{2.4.2.8}$$

where

$$I(t) \equiv \frac{\mu^2}{2\hbar^2\gamma}\left[\frac{1}{\gamma_c}+\frac{1}{\gamma_v}\right]|E_0(t)|^2 \tag{2.4.2.9}$$

is the normalized optical intensity,

$$\Delta = \frac{\omega_T-\omega_0}{\gamma} \tag{2.4.2.10}$$

is the normalized detuning of the transition from the lasing mode frequency and

$$\xi = \frac{\omega_m-\omega_0}{\gamma} \tag{2.4.2.11}$$

is the normalized detuning of the mth modal frequency from the lasing mode frequency. $E_0(t)$ is assumed to be slowly-varying on the γ_c^{-1}, $\gamma_v^{-1}\approx 100$ fs time scale[46], and so $I(t)$ can be considered constant with respect to the time derivatives of

(2.4.2.3)-(2.4.2.5). Note that (2.4.2.6) and (2.4.2.7) are slowly-varying and that (2.4.2.8) contains no inter-modal amplitude cross-products, so that neither population pulsations nor four-wave mixing are accounted for.

The second time derivative of the carrier-induced polarization, given by (2.4.2.2), is

$$\frac{\partial^2}{\partial t^2}P_a = 2\int_{-\infty}^{\infty} d\omega_T\ \mu D\ \mathrm{Re}\left[\frac{\partial^2}{\partial t^2}\rho_{12}\right] \tag{2.4.2.12}$$

Differentiating (2.4.2.5) with respect to time and taking the real part gives

$$\mathrm{Re}\left[\frac{\partial^2}{\partial t^2}\rho_{12}\right] = \mathrm{Re}[(\gamma+i\omega_T)^2\rho_{12}] - \frac{\mu\omega_T}{\hbar}[\rho_{11}-\rho_{22}]E(t) \tag{2.4.2.13}$$

Substituting (2.4.2.6)-(2.4.2.8) into (2.4.2.13) gives

$$\mathrm{Re}\left[\frac{\partial^2}{\partial t^2}\rho_{12}\right] = -\frac{\mu\gamma}{2\hbar}[\bar{\rho}_{11}-\bar{\rho}_{22}]\frac{1+\Delta^2}{1+\Delta^2+I(t)}\times$$

$$\mathrm{Re}\left[\sum_m \frac{1+(\Delta-\xi)^2-\frac{\omega_m^2}{\gamma^2}}{\Delta-\xi-i}E_m(t)e^{-i\omega_m t}\right] \tag{2.4.2.14}$$

If $1+(\Delta-\xi)^2$ is neglected in favor of ω_m^2/γ^2 in (2.4.2.14) (as will be justified below), and (2.4.2.14) is substituted into (2.4.2.12), reversing the order of integration and summation results in

$$\frac{\partial^2}{\partial t^2}P_a = -\epsilon_0 \mathrm{Re}\sum_m \omega_m^2 \chi_m(t)E_m(t)e^{-i\omega_m t} \tag{2.4.2.15}$$

where

$$\chi_m(t) \equiv -\int_{-\infty}^{\infty} \frac{1+\Delta^2}{1+\Delta^2+I(t)}\frac{f(\Delta,t)d\Delta}{\Delta-\xi-i} \tag{2.4.2.16}$$

is the susceptibility for the mth mode associated with stimulated generation and recombination of carrier pairs, and

$$f(\Delta,t) \equiv \frac{\mu^2(\Delta)D(\Delta)[\bar{\rho}_{11}(\Delta,t)-\bar{\rho}_{22}(\Delta,t)]}{\hbar\epsilon_0} \qquad (2.4.2.17)$$

is the population inversion weighted by the square of the dipole moment. For Δ corresponding to $\omega<\omega_{gap}$, f=0 because no states exist. For $\Delta<0$, but above the band gap, f increases with Δ because of an increasing density of states. For $0<\Delta$, f decreases with Δ because of diminishing occupancy. From (2.4.2.10) it can be seen that f is maximum at $\Delta=0$ for Fabry-Perot devices, since they lase near the gain peak. As Δ increases further, the population inversion becomes negative, $f<0$ and light is absorbed. Finally, for Δ corresponding to $\omega>\omega_{max}$, there are no states and f=0.

The dependence of χ_m on the modal index m enters through the detuning parameter ξ. The time dependence of χ_m has two sources: the normalized optical intensity I and the gain spectrum f, whose time dependence enters through the population inversion, which is in turn dependent on the local carrier density n(t). It has been assumed that n(t) is also slowly-varying on the time-scale associated with intra-band and polarization relaxations. Since χ_m is slowly-varying on the optical-frequency time scale, the neglect of the first term in favor of the third term in Re[...] in (2.2.2.14) is justified, an approximation used to obtain (2.2.2.16).

The approximation made to obtain (2.4.2.15) can now be justified: since the gain spectrum width is of the same order as the intra-band and polarization relaxation rates, $f(\Delta)$ is substantial only for $|\Delta|$ of the order of 1, so that by the time $1+(\Delta-\xi)^2$ is comparable to $\omega_m^2/\gamma^2\approx 4\times 10^4$, f is so small that the integrand is negligi-

ble. Thus the $1+(\Delta-\xi)^2$ contribution to (2.4.2.14) is negligible along the entire range of integration.

Note that the right-hand side of (2.4.2.15) contains no time derivatives of χ_m or E_m, a direct consequence of requiring only the real part of $\partial^2\rho_{12}/\partial t^2$. This is a significant simplification compared to other formulations[48] which are complicated by such time derivatives.

2.4.3 Phenomenological Modal Susceptibility

The next step is to express $<\chi_m>$ in measurable quantities. This quantity is the susceptibility at ω_m, weighted by the absolute square of the modal profile and averaged over the transverse plane (hence the angle brackets).

First, by continuing the analysis of Section 2.4.2, it can be shown[45] that $<\mathrm{Im}[\chi_m]>$ is subject to gain compression of the form

$$<\mathrm{Im}[\chi_m]> = \frac{<\mathrm{Im}[\chi_{L,m}]>}{\left[1+\frac{\sum_k S_k}{S_{shb}}\right]^{1/2}} \qquad (2.4.3.1)$$

due to spectral hole burning, where $<\mathrm{Im}[\chi_{L,m}]>$ is the imaginary part of the modal susceptibility in the absence of light (the linear contribution) and S_{shb} is a parameter that can be fit to experiment[49]. A comparison of the effects of $[1+S/S_{shb}]^{-1/2}$-type and $[1+S/S_{shb}]^{-1}$-type gain compression on the relaxation oscillation frequency and damping rate of single-mode semiconductor lasers[50] implies that the former type more accurately predicts observed dynamical behavior, and so $[1+S/S_{shb}]^{-1/2}$-type gain compression is assumed in this thesis.

Next, the position-dependent gain is defined as

$$g_m \equiv -\frac{\omega_0}{\mu_e \mu_{g,e}} \mathrm{Im}[\chi_m] \tag{2.4.3.2}$$

of which the linear contribution can be phenomenologically expressed as

$$g_{L,m} = \frac{1}{\tau_p} + \Delta_m + \left[\frac{\partial g_0}{\partial n}\right]_{th} (n - n_{th}) \tag{2.4.3.3}$$

where $1/\tau_p$ is the threshold gain of the main mode, Δ_m is the gain roll-off at ω_m and $[\partial g_0/\partial n]_{th}$ is the differential gain evaluated at ω_0 at threshold. Performing a weighted average over the transverse plane gives the linear contribution to the modal gain

$$G_{L,m} = \frac{1}{\tau_p} + \Delta_m + \left[\frac{\partial G_0}{\partial N}\right]_{th} (N - N_{th}) \tag{2.4.3.4}$$

This can be combined with (2.4.3.1) to give the modal gain

$$G_m = \frac{\frac{1}{\tau_p} + \Delta_m + \left[\frac{\partial G_0}{\partial N}\right]_{th} (N - N_{th})}{\left[1 + \frac{\sum_k S_k}{S_{shb}}\right]^{1/2}} \tag{2.4.3.5}$$

which is related to $<\mathrm{Im}[\chi_m]>$ by (2.2.4.11).

Finally, we relate $<\mathrm{Re}[\chi_m^{(1)}]>$, the deviation of the real part of the modal susceptibility from its equilibrium value, to $<\mathrm{Im}[\chi_m^{(1)}]>$ to further develop the phase rate equation (2.2.4.8). It has been argued in Section 6.5.1 of Reference [37] that the nonlinear contribution to $<\mathrm{Re}[\chi_m]>$ can be neglected compared to the linear contribution, so we allow

$$<\mathrm{Re}[\chi_m^{(1)}]> \rightarrow <\mathrm{Re}[\chi_{L,m}(1)]> \tag{2.4.3.6}$$

The linewidth-enhancement factor can be defined for each mode as

$$\alpha_m \equiv \left[\frac{\frac{\partial <\mathrm{Re}[\chi_{L,m}]>}{\partial N}}{\frac{\partial <\mathrm{Im}[\chi_{L,m}]>}{\partial N}} \right]_{th} \tag{2.4.3.7}$$

Note that evaluation at threshold implies measurement of the linear contribution. By separating $\chi_{L,m}$ into an equilibrium component $\chi_{L,m}^{(0)}$ and a carrier-number dependent contribution $\chi_{L,m}^{(1)}$, as in (2.2.4.1), we can make the linear approximation

$$<\mathrm{Re}[\chi_{L,m}^{(1)}]> = \alpha_m <\mathrm{Im}[\chi_{L,m}^{(1)}]> \tag{2.4.3.8}$$

Combining (2.2.4.8), (2.4.3.6), (2.4.3.8), (2.2.4.11) and the last term of (2.4.3.4) ($G_{L,m}^{(1)}$ contribution) gives the rate equation for the modal phase

$$\frac{d}{dt}\phi_m = -\frac{\alpha_m}{2}\left[\frac{\partial G_0}{\partial N}\right]_{th}(N-N_{th}) \tag{2.4.3.9}$$

This section concludes with a discussion of intra-band optical transition contributions to the susceptibility. The detuning between the optical wave and the much lower-frequency intra-band transitions is large enough so that the associated susceptibility is almost completely reactive, and has been modeled[51] by considering the carriers as a free gas with a plasma frequency $\omega_p << \omega_0$. This effect is linear and is automatically included when α is measured. The reduction of gain by carrier heating due to intra-band absorption of photons has been recently discussed[52], and may contribute to gain compression.

neglected in favor of the spontaneous photon contribution, given by (2.5.2), to the total noise.

The ensemble-average of the right-hand side of (2.5.2) can be written as

$$R_m = \frac{N}{\tau_{rad}} \cdot \beta_m \tag{2.5.4}$$

where the first factor is the total rate of spontaneous radiative decay of carriers and the second factor is the fraction entering the mth mode. Precise evaluation of R_m is not as critical as with G_m, because in the latter case the net gain $G_m - 1/\tau_p$ is a small difference that is highly sensitive to changes in N. Therefore we can make the approximation

$$N \approx N_{th} \tag{2.5.5}$$

We can also make the approximation

$$\frac{1}{\tau_{rad}} \approx \frac{1}{\tau_{rad}} + \frac{1}{\tau_{nr}} \equiv \frac{1}{\tau} \approx \frac{1}{\tau_s} \tag{2.5.6}$$

where $\tau_{rad(nr)}$ is the radiative (non-radiative) spontaneous decay lifetime of carriers at lasing threshold, not differential lifetimes at threshold. The first approximation is justified since $\tau_{rad} \ll \tau_{nr}$ for high-quality GaAs/AlGaAs lasers (see Section 2.3.3. of Reference [53]). The second approximation can be absorbed into the phenomenological parameter β, as discussed below.

Of all spontaneous photons, only a fraction are emitted in a direction and polarization consistent with the guided modes. Of these, few will be in the correct frequency range to enter the mth mode. Both the geometrical and spectral effects are included in β_m. Because the longitudinal modes have very similar spatial properties, only spectral effects enter into the m dependence. For equally-spaced Fabry-Perot

modes, β_m should be linear in G_m, which is nearly constant over the lasing modes near the center of the gain peak. Therefore we replace

$$\beta_m \rightarrow \beta \tag{2.5.7}$$

which is independent of m. Combining (2.5.4)-(2.5.7) gives

$$R_m = \beta \frac{N_{th}}{\tau_s} \tag{2.5.8}$$

Assuming that N_{th} and τ_s are known, β can be determined from experiment and absorbs all the approximations made in deriving (2.5.8).

2.6 Single-Mode Equilibrium

Before discussing dynamical effects (Chapter 3), it is interesting to solve the single-mode steady-state problem, particularly to estimate the effect of spontaneous emission and gain compression on the continuous-wave light/current characteristic. The equilibrium photon number is related to the power output from one facet P_{out} according to

$$S^{(0)} = \frac{2\mu_{g,e}L}{c} \cdot \frac{1}{1-R} \cdot \frac{P_{out}}{\hbar\omega_0} \tag{2.6.1}$$

where R is the facet power reflectivity. The first factor is the cavity round-trip time, the second is the reciprocal of the probability of transmission of a given photon at the output facet and the third is the rate at which photons are transmitted. Substituting

$$\hbar\omega = \frac{hc}{\lambda} \tag{2.6.2}$$

and

$$\mu_{g,e} = \frac{\lambda^2}{2L\Delta\lambda} \tag{2.6.3}$$

where $\Delta\lambda$ is the longitudinal mode spacing, into (2.6.1) gives

$$S^{(0)} = \frac{1}{hc^2}\frac{1}{1-R}\frac{\lambda^3}{\Delta\lambda}P_{out} \tag{2.6.4}$$

Setting the left-hand side of (2.5.1) equal to zero gives

$$G^{(0)} = \frac{1}{\tau_p} - \frac{\beta N_{th}}{\tau_s S^{(0)}} \tag{2.6.5}$$

where (2.5.2) and (2.5.8) were used, neglecting the stochastic term. (2.4.3.5) gives

$$N^{(0)} = N_{th} - \frac{\frac{1}{\tau_p} - G^{(0)}\left[1+\frac{S^{(0)}}{S_{shb}}\right]^{\frac{1}{2}}}{\left[\frac{\partial G_0}{\partial N}\right]_{th}} \tag{2.6.6}$$

and setting the right-hand side of (2.4.1.2) equal to zero gives

$$J = q\left[\frac{N^{(0)}}{\tau_s} + G^{(0)}S^{(0)}\right] \tag{2.6.7}$$

so that (2.6.4)-(2.6.7) give the injection current necessary to support a prescribed optical output.

Using typical parameter values for semiconductor lasers (collected in Tables 2.6.1 and 2.6.2), the effect of gain compression and spontaneous emission on the single-mode equilibrium point can be estimated. The saturation photon number was

Parameter	Symbol	Table 4.2 of Reference [20] Value	Table 4.2 of Reference [20] Symbol
Cavity length	L	240 μm	L
Stripe width	W	4 μm	w
Mode volume	V	4.5×10^{-10} cm^3	V
Vertical Confinement Factor	Γ	0.15	Γ
Active Layer Thickness	d	0.14 μm	d
Linewidth-Enhancement Factor	α	7.5	α
Wavelength	λ	818 nm	λ
Effective Group Index	$\mu_{g,e}$	4.1	n_g
Photon Lifetime	τ_p	1.5 ps	τ_p
Carrier Lifetime	τ_s	2.4 ns	τ_s
Threshold Carrier Density	$\frac{N_{th}}{V}$	3.0×10^{18} cm^{-3}	N_{th}
Differential Material Gain	$\frac{V\mu_{g,e}}{\Gamma c}\frac{\partial G_{L,0}}{\partial N}$	3.8×10^{-16} cm^2	dg/dN

Table 2.6.1 Semiconductor Laser Parameters I

Parameter	Symbol	Value	Origin
Effective Phase Index	μ_e	3.3	typical value
Facet Reflectivity	R	0.32	"
Spontaneous Emission Factor	β	1.6×10^{-4}	see text
Threshold Carrier Number	N_{th}	1.4×10^{9}	derived from Table 2.6.1
Differential Modal Gain	$\frac{\partial G_{L,0}}{\partial N}$	$9\times10^{2}\ s^{-1}$	"
Gain Compression Factor	κ	$1.2\ W^{-1}$	Reference [49]
Spectral Hole-Burning Photon Number	S_{shb}	1.7×10^{7}	derived from κ
Typical Photon Number	$S^{(0)}$	4×10^{5}	P_{out}=10 mW

Table 2.6.2 Semiconductor Laser Parameters II

calculated by equating the threshold limits of $[1+S^{(0)}/S_{shb}]^{-\frac{1}{2}}$ and $1-\kappa P_{out}$, a gain-compression factor popular in the literature[49], to obtain

$$S_{shb} = \frac{1}{2hc^2}\frac{1}{1-R}\frac{\lambda^3}{\Delta\lambda}\frac{1}{\kappa} \tag{2.6.8}$$

where (2.6.4) was used.

The value of β cited in Table 2.6.2 was obtained by the author and Nu Yu for a single longitudinal mode of one emitter of a gain-guided twin-emitter device, by using $P_{out}(J)$ data taken below lasing threshold to fit β to (2.6.4)-(2.6.7) (neglecting gain compression). The single-mode output of a single emitter was isolated by dispersing the light in a spectrometer and using the exit slit to mask all but the desired mode. The near field was masked in the vertical direction using the entrance slit of the spectrometer, and in the lateral direction using a slit placed after the spectrometer exit slit. The absolute output power of the remaining light was then measured using a detector that had been calibrated by measuring its response to the unmasked output and comaring to the known light-versus-current characteristic of the twin-emitter. We can get a rough idea of the steady-state light levels at which the ensemble-average of spontaneous emission contributes significantly to the equilibrium photon number by finding the photon number that corresponds to $G^{(0)}=0$ (transparency) from (2.6.5), and finding the corresponding output power from (2.6.4). Using Tables 2.6.1 and 2.6.2 gives $P_{out}\approx 4\ \mu W$, which is much smaller than typical output powers. Spontaneous emission is important only at low light levels, and can be neglected in calculating the equilibrium point under normal operating conditions. It is responsible for rounding of the "knee" of the light/current characteristic near threshold in the static case and for "seeding" the recovery of the photon population after a large optical pulse has depleted the gain in dynamical operation.

To estimate the effect of gain compression on the linearity of $J(P_{out})$, we use (2.6.4) and Tables 2.6.1 and 2.6.2 to calculate the output power corresponding to $S^{(0)}=S_{shb}$, which gives $P_{out}\approx 400$ mW, several times the catastrophic facet damage limit of typical single-emitter devices. Therefore, gain compression can also be neglected in calculating the equilibrium point under normal operating conditions. It acts primarily to limit large optical pulses and reduce the peak responsivity of the device to injection current modulation (Section 3.3).

Neglecting spontaneous emission and gain compression, (2.6.5)-(2.6.7) simplify to give

$$G^{(0)} = \frac{1}{\tau_p} \tag{2.6.9}$$

$$N^{(0)} = N_{th} \tag{2.6.10}$$

$$S^{(0)} = \frac{\tau_p}{q}(J-J_{th}) \tag{2.6.11}$$

where

$$J_{th} \equiv \frac{q}{\tau_s}N_{th} \tag{2.6.12}$$

3. THEORY OF SINGLE-EMITTER DYNAMICS

3.1 Chapter Overview

Some of the dynamical mechanisms at work in single-emitter semiconductor lasers are discussed in this chapter. The list is not meant to be exhaustive, only those mechanisms likely to influence the dynamics of coherent arrays under normal experimental conditions are included. Many interesting phenomena, e.g. passive mode-locking in a multi-section device, are beyond the scope of this chapter.

The most important aspect of a dynamical effect is its characteristic frequency. Several effects will be found to occur at frequencies far below the 500 MHz-50 GHz regime of interest, while others will be near the relaxation oscillation frequency, typically a few gigahertz. These can often be distinguished by their effects on various other characteristics, such as the light-versus-current curve, the emission spectrum, the near-field and the far-field.

Section 3.2 examines the simplest case, that of a noiseless and undriven single-mode device. The phase of the optical field is found to be subsidiary, and the dynamics are contained in the photon-number, carrier-number phase plane, precluding optical chaos. The stability of the equilibria found in Section 2.6 is discussed, and the relaxation oscillation and characteristic damping frequencies are introduced.

Section 3.3 discusses small-signal sinusoidal injection current modulation of a single-mode device. The responsivity transfer function is found, and some aspects of bandwidth optimization are touched upon.

Section 3.4 looks into the self-stabilization of the lasing mode in the quiescent single-mode case, and the suppression of side modes during transient multi-mode operation.

Section 3.5 discusses dynamical noise in single- and multi-mode devices, and uncovers a possible complication in measuring the imaginary part of the coupling coefficient of coherent arrays (Section 6.6), related to mode-hopping.

Section 3.6 assesses the effects of optical feedback, present in any experiment, on the stability of a single-mode device. It is estimated that optical feedback will not be troublesome during ordinary experimental conditions.

Section 3.7 examines the effect of homogeneously-distributed saturable absorbers, presumably defects due to aging. Instabilities leading to self-sustained pulsations at the relaxation oscillation frequency are shown to arise if certain conditions on absorber saturability and density are met.

Section 3.8 discusses mode profile dynamics, in which the shape of the optical mode and carrier distribution change with time, rendering the number rate equations invalid.

3.2 Autonomous, Deterministic Single-Mode Dynamics

This section deals with the simplest case, in which optical field and carrier profiles are constant so that modal rate equations can be used, and only one mode is lasing and is not subject to noise, feedback, saturable absorbers or modulation. Each of these issues will be touched upon in subsequent sections of this chapter.

The single-mode versions of (2.5.1) and (2.4.1.2) are

$$\frac{d}{dt}S = \left[G(S,N) - \frac{1}{\tau_p}\right]S + \beta\frac{N_{th}}{\tau_s} \tag{3.2.1}$$

and

$$\frac{d}{dt}N = \frac{J}{q} - \frac{N}{\tau_s} - G(S,N)S \tag{3.2.2}$$

where the functional form of G has been left unspecified for the moment.

Note that the phase equation (2.4.3.9) has not been included. This is because the phase does not appear in the right-hand side of either the photon number or the carrier number equation, and so is a subsidiary dynamical variable. Because there are only two coupled dynamical variables, the Poincare-Bendixson Theorem informs us that an asymptotic solution of (3.2.1) and (3.2.2) must be a fixed point or a limit cycle[54], and that chaos is impossible[55]. This has been discussed in a different context by Arecchi (see Chapter 2 of Reference [30]), by whose classification scheme semiconductor lasers fall into class B, for which chaos is ruled out. The semiconductor laser is designated class B because its material depolarization rate is rapid compared to its photon and carrier decay rates, allowing the material polarization to be adiabatically eliminated, leaving only two degrees of freedom.

The procedure for finding the equilibrium points of (3.2.1) and (3.2.2) was given in Section 2.6. The linear stability of an equilibrium point is assessed by investigating the evolution of small perturbations about the equilibrium point (see Chapter 5 of Reference [56]). To this end we set

$$S \to S^{(0)} + \mathrm{Re}[S^{(1)}e^{\lambda t}] \tag{3.2.3}$$

with a similar expression for N, and

$$G \to \frac{1}{\tau_p} + \left[\frac{\partial G}{\partial S}\right]_{th} S^{(1)}e^{\lambda t} + \left[\frac{\partial G}{\partial N}\right]_{th} N^{(1)}e^{\lambda t} \tag{3.2.4}$$

We then linearize (3.2.1) and (3.2.2) using the procedure described in Appendix C, obtaining the matrix equation

$$\begin{bmatrix} \lambda - A_S + a_\beta & -A_N \\ a_p + A_S - a_\beta & \lambda + a_s + A_N \end{bmatrix} \cdot \begin{bmatrix} S^{(1)} \\ N^{(1)} \end{bmatrix} = 0 \tag{3.2.5}$$

where

$$a_p \equiv \frac{1}{\tau_p} \tag{3.2.6}$$

$$A_S \equiv \left[\frac{\partial G}{\partial S}\right]_{th} S^{(0)} \approx -\frac{S^{(0)}}{2\tau_p S_{shb}} \tag{3.2.7}$$

where (2.4.3.5) and $S^{(0)} << S_{shb}$ was used, and

$$A_N \equiv \left[\frac{\partial G}{\partial N}\right]_{th} S^{(0)} \tag{3.2.8}$$

$$a_s \equiv \frac{1}{\tau_s} \tag{3.2.9}$$

$$a_\beta \equiv \frac{\beta N_{th}}{\tau_s S^{(0)}} \tag{3.2.10}$$

are various rates that have been evaluated using Tables 2.6.1 and 2.6.2 and collected in Table 3.2.1 for convenient reference. A_S is negative because gain compression has been assumed, but if a photon/gain positive feedback mechanism were present, A_S could be positive. A_N is positive, since gain must increase with carrier number, and a_p, a_s and a_β are positive by definition. Note that a_s, A_N and a_β are of similar magnitude.

Setting the determinant of (3.2.5) to zero gives the characteristic equation

$$\lambda^2 + [-A_S+A_N+a_s+a_\beta]\lambda + [a_pA_N-A_Sa_s+a_sa_\beta] = 0 \tag{3.2.11}$$

The roots of (3.2.11) will both have negative real parts, i.e. the equilibrium point will be stable, if and only if both bracketed coefficients are positive. The only way to violate either condition is if $A_S > A_N+a_s+a_\beta = 1.0\times10^9\ s^{-1}$ or $A_S > a_pA_N/a_s+a_\beta = 570\times10^9\ s^{-1}$. Because of this disparity, only the stability boundary corresponding to the linear term will be considered. Two of the cases in which the stability condition

$$A_S < A_N + a_s + a_\beta \tag{3.2.12}$$

can be violated are when saturable absorption (Section 3.7) or self-focusing (Section 3.8) mechanisms are present.

The roots of (3.2.11) are approximately

$$\lambda \approx -\frac{\omega_r^2}{2\omega_d} \pm i\omega_r \tag{3.2.13}$$

where

parameter	value
a_p	$670\times10^9\ s^{-1}$
A_S	$-7.8\times10^9\ s^{-1}$
a_s	$0.42\times10^9\ s^{-1}$
A_N	$0.36\times10^9\ s^{-1}$
a_β	$0.23\times10^9\ s^{-1}$
$\nu_r \equiv \frac{\omega_r}{2\pi}$	2.5 GHz
$\nu_d \equiv \frac{\omega_d}{2\pi}$	4.3 GHz for $A_S=-7.8\times10^9\ s^{-1}$
$\nu_d \equiv \frac{\omega_d}{2\pi}$	38 GHz for $A_S=0\ s^{-1}$

Table 3.2.1 Typical Dynamical Process Rates

$$\omega_r \equiv [a_p A_N]^{1/2} = \left[\frac{1}{\tau_p}\left(\frac{\partial G}{\partial N}\right)_{th} S^{(0)}\right]^{1/2} \tag{3.2.14}$$

is the relaxation oscillation frequency (where (3.2.6) and (3.2.8) were used), and

$$\omega_d \equiv \frac{\omega_r^2}{-A_S+A_N+a_s+a_\beta} \tag{3.2.15}$$

is the "damping frequency", a parameter related to the rate of damping of relaxation oscillations. These have previously been introduced in Chapter 4 of Reference [53]. Because of the dependence of the damping rate (real part of (3.2.13)) on $\partial G/\partial S$, it has been proposed that the measured damping rate could be used to evaluate rival models of gain compression[57].

Note that a_p is much larger than $|A_S|$, a_s, A_N and a_β. This causes $Im[\lambda]$, which gives the angular frequency of small oscillations about the equilibrium point, to be nearly independent of A_S, so that the instability frequency is fixed at the relaxation oscillation frequency, irrespective of the destabilizing mechanism.

3.3 Injection Current Modulation

Although the primary focus of this thesis is on autonomous dynamics, injection current modulation of semiconductor lasers is an important burgeoning technology. This section reviews modulation of single-emitter lasers as a prelude to Chapter 8, which discusses the modulation of coherent arrays. Here, consideration is limited to the case of small-signal, sinusoidal modulation of a single-mode semiconductor laser.

To obtain the response of the optical output to injection current modulation, we write the injection current as

$$J(t) = J^{(0)} + \mathrm{Re}[J^{(1)}e^{i\Omega t}] \tag{3.3.1}$$

where Ω is the modulation frequency, with similar expressions for S and N. G is written in a form analogous to (3.2.4), and the rate equations are linearized to give a matrix equation analogous to (3.2.5), with

$$\lambda \to i\Omega \tag{3.3.2}$$

and an inhomogeneous right-hand side given by

$$0 \to \begin{bmatrix} 0 \\ \dfrac{J^{(1)}}{q} \end{bmatrix} \tag{3.3.3}$$

By inverting the matrix equation we obtain the ratio of the amplitudes of the small-signal optical and injection current modulation

$$\frac{S^{(1)}}{J^{(1)}} = \frac{\tau_p}{q} H(\Omega) \tag{3.3.4}$$

where

$$H(\Omega) \equiv \frac{1}{1+i\dfrac{\Omega}{\omega_d}-\dfrac{\Omega^2}{\omega_r^2}} \tag{3.3.5}$$

is the transfer function[53,58], and ω_r and ω_d were defined by (3.2.14) and (3.2.15), respectively. It is interesting to note in passing the similarities between the stability analysis of Section 3.2 and the small-signal analysis of this section: if we find the roots $i\Omega$ of the denominator of H, which represents a finite optical modulation for no injection current modulation (incipient instability), we recover both the stability

boundary (3.2.12) and the angular frequency of incipient instability.

Figure 3.3.1 plots $|H(\Omega)|$ for the values of ν_r and ν_d given in Table 3.2.1. Both curves have flat low-frequency responses, rising to a peak at the relaxation oscillation frequency and rolling off at -40 dB/decade for $\Omega >> \omega_r$. Figure 3.3.1 shows the importance of including gain compression (ν_d=4.3 GHz) in a realistic calculation.

The modulation bandwidth can be defined by the -3 dB point of the transfer function,

$$|H(\omega_{-3dB})| \equiv \frac{1}{2^{1/2}} |H(0)| = \frac{1}{2^{1/2}} \tag{3.3.6}$$

where the common convention[58,59]

$$X \text{ (in dB)} = 20 \cdot \log_{10} X \tag{3.3.7}$$

is used. Substituting (3.3.6) into (3.3.5) gives

$$\left[\frac{\omega_{-3dB}}{\omega_d}\right]^2 = \Psi - \frac{\Psi^2}{2} + \left[2\Psi^2 - \Psi^3 + \frac{\Psi^4}{4}\right]^{1/2} \tag{3.3.8}$$

where

$$\Psi \equiv \left(\frac{\omega_r}{\omega_d}\right)^2 \tag{3.3.9}$$

We shall now find the maximum bandwidth $\omega_{-3dB}(\max)$. If the laser is driven hard, $S^{(0)}$ is large and $-A_S + A_N >> a_s + a_\beta$, so that (3.2.15) gives

$$\lim_{S^{(0)} \to \infty} \omega_d^{-1} = \tau_p \left[1 + \frac{1}{2\tau_p \left[\frac{\partial G}{\partial N}\right]^{(0)} S_{shb}}\right] \tag{3.3.10}$$

This limit is not at all difficult to approach under typical semiconductor laser

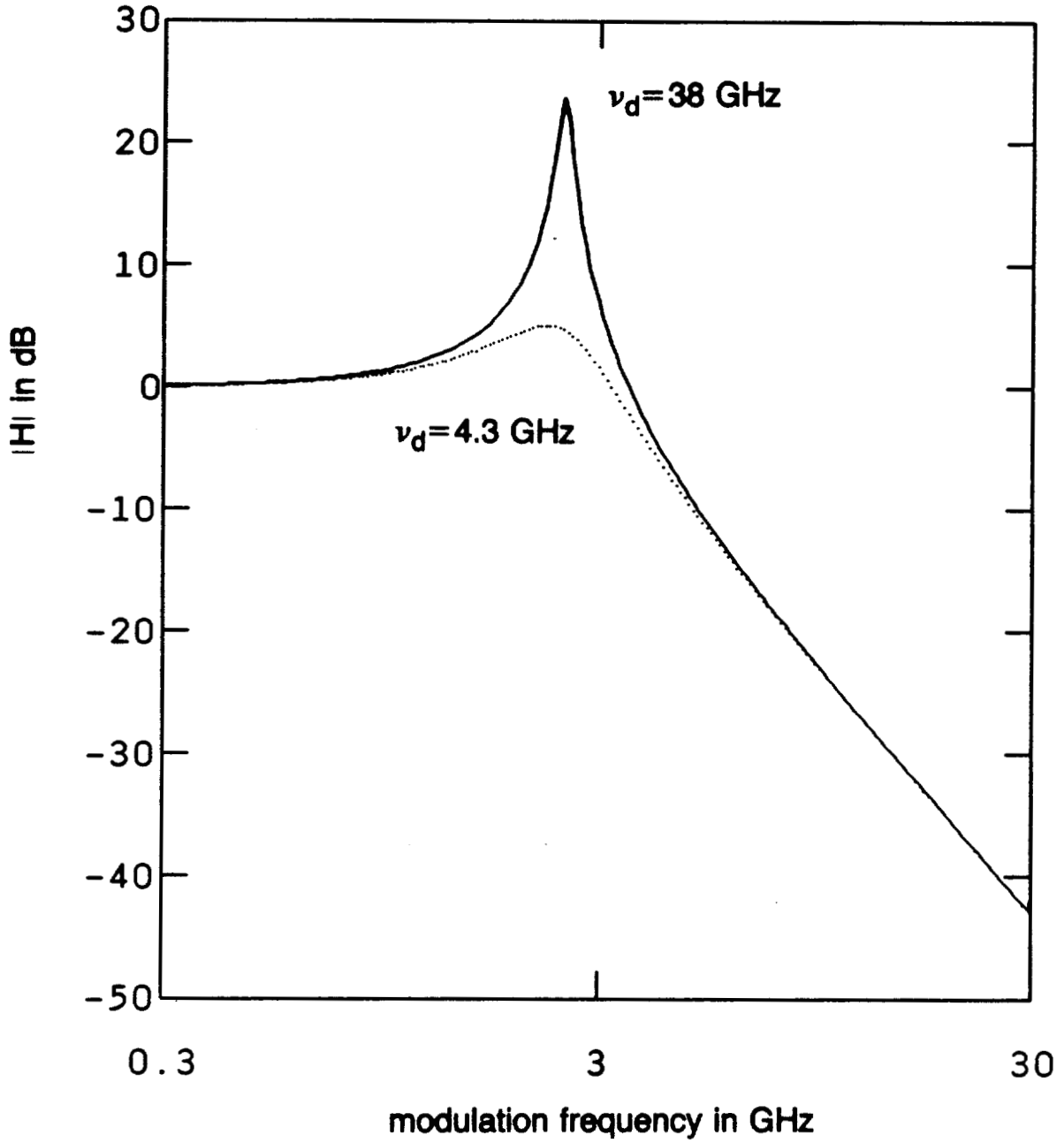

Figure 3.3.1 Single-Emitter Modulation Transfer Functions

Note that the relaxation oscillation resonance at 2.5 GHz is drastically dampened by including gain compression (ν_d=4.3 GHz).

operating conditions. Since ω_d is constant under hard-driving conditions, we can maximize ω_{-3dB} with respect to ω_r by differentiating (3.3.8) with respect to Ψ and setting the derivative to zero. This gives

$$\omega_r(\max) = 2^{\frac{1}{2}}\omega_d = \omega_{-3dB}(\max) \tag{3.3.11}$$

This condition also yields the flattest response over the bandwidth (see Fig. 4.5 of Reference [53]), an important consideration in communications applications. Using the values given in Tables 2.6.1 and 2.6.2, (3.3.10) and (3.3.11) give ν_d=4.6 GHz and $\nu_{-3dB}(\max)$=6.6 GHz. It is apparent that the bandwidth is limited by gain compression.

If we could eliminate gain compression by setting $S_{shb}=\infty$, (3.3.10) would give ν_d=106 GHz. Unfortunately, it then becomes impossible to fulfill (3.3.11), and in fact $\omega_r << \omega_d$. It is then appropriate to expand (3.3.8) to first order in $\Psi << 1$, to get

$$\omega_{-3dB} = [1+2^{\frac{1}{2}}]^{\frac{1}{2}}\omega_r \tag{3.3.12}$$

This justifies the simple and widely-used strategy of seeking to increase the relaxation oscillation frequency, by reducing the photon lifetime, increasing the photon number or increasing the modal differential gain (see (3.2.14)). Standard tactics include shortening the cavity and operating far above threshold[60]. Catastrophic facet damage is often avoided by using a window structure[61]. The differential gain can be increased by operating at low temperatures, which shortens the tail of the Fermi-Dirac distribution of the carriers, putting a greater fraction of added carriers near the gain peak where they can contribute to lasing. This approach is not practical for remote transmitters in communications systems. It has been suggested[62] that quantum well

lasers might have larger modulation bandwidths than double-heterostructure devices because of their larger differential gain dg/dn. The present room-temperature ω_{-3dB} record is 24 GHz, held by a double-heterostructure InGaAsP device[63].

Another factor limiting the injection-current modulation bandwidth of semiconductor lasers is electrical parasitics. The total device response is the product of the intrinsic and electrical transfer functions, so it does no good to increase ω_{-3dB} if the bandwidth is parasitic-limited. AC equivalent-circuit models of semiconductor lasers have been formulated[60,64], which typically treat the active region as a series resistance and a shunt capacitance, insulating layers as capacitances and buried-heterostructure blocking layers as distributed RC-networks. Much progress has been achieved in optimizing these parameters, notably the elimination of distributed capacitance by using a constricted-mesa geometry[65].

Measurement of the intrinsic transfer function by injection current modulation is complicated by the presence of electrical-parasitic roll-off. The intrinsic transfer function can be obtained directly from the spectrum of the intensity noise (Section 3.5) of the device, biased at the intended operating point but not modulated. An alternate technique is active-layer photo-mixing[66].

Finally, several techniques have been proposed for modulation above the limit imposed by the relaxation oscillation frequency. Since, physically, ω_r is related to the rate at which the gain medium can recover after being depleted by an optical pulse, all such techniques are founded on minimizing reliance on gain modulation. Active and passive longitudinal mode-locking[67,68] have been used to obtain a narrow-band response at the inter-modal frequency of the longitudinal modes of a Fabry-Perot semiconductor laser, which is typically above 100 GHz. Active mode-locking of the

lateral modes of a coherent twin-emitter array has been proposed[69-71], and is discussed in detail in Chapter 8. Active mode locking requires modulation of the gain medium with a depth on the order of the difference of the gains of the main and side modes, which can be quite small. Polarization self-modulation[72] is a technique that is completely independent of gain modulation.

3.4 Longitudinal Mode Self-Stabilization

For quasi-single-mode devices, it is commonly observed that side modes are suppressed to a greater degree than is expected from the roll-off of the gain curve at threshold. This self-stabilization of the dominant mode is the subject of this section.

In Chapter 4, the coherent array lateral modes belonging to a longitudinal mode are treated as a closed system, in that interactions with the lateral modes of other longitudinal modes are not considered. This is partially justified because the frequency spread of a group of lateral modes is typically small compared to the longitudinal mode spacing, so that intra-group and inter-group beat frequencies are easily isolated. Further justification arises from longitudinal mode self-stabilization.

The multi-mode rate equations are given by (2.5.1) and (2.4.1.2). As in the single-mode dynamics case discussed in Section 3.2, the phases ϕ_m are subsidiary. Equilibrium points are given by

$$S_m^{(0)} = \frac{\beta \frac{N^{(0)}}{\tau_s}}{\frac{1}{\tau_p} - G_m(S^{(0)}, N^{(0)})} \tag{3.4.1}$$

$$\frac{J}{q} = \frac{N^{(0)}}{\tau_s} + \sum_m G_m(S^{(0)},N^{(0)})S_m^{(0)} \tag{3.4.2}$$

where $S^{(0)}$ refers to all the equilibrium modal photon numbers collectively. Under some conditions more than one equilibrium point may exist. A means of measuring the equilibrium modal gains $G_m^{(0)}(J)$ is afforded by fitting (3.4.1) to $S_m^{(0)}(J)$, provided there is an equilibrium point sufficiently impervious to noise-driven mode hops (Section 3.5) to allow time-averaged measurement of $S_m^{(0)}$.

When the injection current is below threshold, gain compression is negligible and $G_m^{(0)}$ is a function of $N^{(0)}$ alone. Since $\partial G_m^{(0)}/\partial N^{(0)}>0$, $S_m^{(0)}$, $G_m^{(0)}$ and $N^{(0)}$ monotonically increase with J such that (3.4.1) and (3.4.2) are fulfilled. If we momentarily assume that the gain medium is homogeneously broadened, i.e. that $G_m^{(0)}$ continues to be independent of the modal photon numbers even above threshold, then the photon numbers $S_m^{(0)}$ will continue to monotonically increase as $J\to\infty$. It is commonly observed, however, that the power of side modes decreases with increasing injection current over some range above threshold[73]. The lasing mode often persists after a shift in temperature or some other parameter has reduced its linear gain below that of another mode. Such self-stabilization makes possible a set of equilibrium points, each of which is associated with a different lasing mode. A lasing mode lasts until noise of sufficient strength disrupts it, at which time another mode begins lasing. To the extent that only one longitudinal mode lases at a time, only one group of lateral modes need be considered in studying coherent array dynamics.

Modal gain can be approximated by[46,74]

$$G_m(S,N) \approx G_0(N) + \Delta_m - K\sum_k \frac{1+\alpha'\omega_{m,k}\tau'}{1+\omega_{m,k}^2\tau'^2} S_k \tag{3.4.3}$$

where

$$\omega_{m,k} \equiv \omega_m - \omega_k \tag{3.4.4}$$

and S represents modal photon numbers collectively. $G_0(N)$ is the linear (homogeneously-broadened) gain of the central mode and Δ_m is the suppression of the mth mode due to gain roll-off. The final term takes gain suppression of the mth mode due to all the other modes into account. Here, K is a strength factor that can in principle be obtained by expanding the material polarization to third-order in the electric field, or by fitting (3.4.1) to experimental data. α' and τ' have been tentatively identified as the linewidth-enhancement factor and the intra-band relaxation time[74], an identification that has been contested[46]. These quantities have been primed to reflect the uncertainty of this identification.

If we assume that only the dominant mode contributes significantly to the gain compression, the sum in (3.4.3) collapses to k=d, where the dominant mode is not necessarily at the gain peak. The nonlinear gain then has components symmetric and anti-symmetric in $\omega_{m,d}$, with the anti-symmetric component enhancing longer-wavelength and suppressing shorter-wavelength side modes[74].

Several mechanisms contributing to gain compression can be identified. Spectral hole burning, shown to be Lorentzian in shape[45], has a hole-width that is large compared to a typical longitudinal mode spacing, and so contributes weakly to side-mode enhancement. Population pulsations and four-wave mixing help suppress side modes[46,47], the latter mechanism contributing to the anti-symmetric term. Longitudinal hole burning of the gain is expected to enhance the side modes[39,75], while longitudinal hole burning of saturable absorbers in the n-cladding layer has been proposed as a side-mode suppression mechanism[39].

It is interesting to note which of these mechanisms come into play for lateral modes. Since lateral mode spacing is typically smaller than longitudinal mode spacing, spectral hole burning is expected to be even less important in discriminating among lateral modes than among longitudinal modes (Section 2.4.2), although it contributes an overall gain compression which is important to take into account (Section 3.3). Population pulsations and four-wave mixing can still contribute, but longitudinal spatial hole burning of either gain or absorbers is irrelevant because all the lateral modes of a group have the same longitudinal structure. Lateral spatial hole burning may be important, and is most naturally accounted for in the coupled-array-mode model of Section 4.2.

For a device with sufficiently stable modes, the asymptotic dynamics are described by the single-mode model given in Section 3.2. The transient dynamics of the side modes can be obtained in terms of the lasing mode photon number, assuming that (3.4.3) is accurate over the period of interest and spontaneous emission can be ignored. (2.5.1) can be rewritten as

$$\frac{1}{S_m}\frac{dS_m}{dt} = \frac{1}{S_d}\frac{dS_d}{dt} + (\Delta_m - \Delta_d) - K\frac{\alpha'\omega_{m,d}\tau' - \omega_{m,d}^2\tau'^2}{1+\omega_{m,d}^2\tau'^2}S_d \qquad (3.4.5)$$

which can be integrated to give

$$\frac{S_m}{S_d}(t) = \frac{S_m}{S_d}(0)\exp\left[-\frac{t}{\tau_{m,d}(t)}\right] \qquad (3.4.6)$$

where

$$\frac{1}{\tau_{m,d}} \equiv \Delta_d - \Delta_m + K\frac{\alpha'\omega_{m,d}\tau' - \omega_{m,d}^2\tau'^2}{1+\omega_{m,d}^2\tau'^2}\frac{1}{t}\int_0^t dt' S_d(t') \qquad (3.4.7)$$

A similar expression for the linear gain case has appeared in Section 4.5.1 of

Reference [53]. This can be used to estimate dynamic side-mode suppression, which is more difficult to achieve than quiescent side-mode suppression.

3.5 Dynamical Noise

So far we have dealt with noiseless semiconductor lasers, which can be described by deterministic rate equations. In this section we discuss the effects of spontaneous emission, the dominant noise source in semiconductor lasers, on single-emitter dynamics. The discussions of single-mode intensity noise and mode-partition noise have been drawn from Chapter 7 of Reference [53], in which they are covered in greater depth.

The relative intensity noise (RIN) over a bandwidth $\Delta\nu$ is given by Equation (7.12) of Reference [53]

$$\mathrm{RIN}(\Omega)\,\Delta\nu = \frac{2W_S(\Omega)}{<S>^2}\Delta\nu \tag{3.5.1}$$

where W_S is the spectral density of the intensity noise. Here, S may represent either the total photon number or the photon number of a particular mode. For single-mode operation, the expression analogous to Equation (7.41) of Reference [53] in our notation is

$$\mathrm{RIN}(\Omega)\,\Delta\nu = 4\frac{\beta N_{th}}{\tau_s}\frac{1}{<S>}\left[\frac{1}{\omega_d^2}+\left(\frac{\Omega}{\omega_r^2}\right)^2\right]|H(\Omega)|^2\Delta\nu \tag{3.5.2}$$

where H is the small-signal modulation transfer function defined by (3.3.5) and ω_r and ω_d are the relaxation oscillation and damping frequencies defined by (3.2.14) and

(3.2.15). Because $|H|^2$ appears in (3.5.2), RIN(ω_r) can be much larger than RIN(0). Using Tables 2.6.1, 2.6.2 and 3.2.1, the low-frequency limit of (3.5.2) gives RIN(0)=1.3×10^{-12} Hz^{-1}. With the 200 MHz resolution bandwidth associated with a streak camera window of 5 ns, the relative intensity noise is 2.5×10^{-4}.

The observed noise is typically much greater than this, due to three factors. The first is measurement noise. The second "noise" contribution is actually deterministic chaos, which may be caused by optical feedback, saturable absorbers or self-focusing, treated in Sections 3.6, 3.7 and 3.8, respectively. The third source is mode-partition and mode-hopping noise, found in multi-mode lasers.

Mode-partition noise is the intensity noise of a particular mode of a multi-mode laser, and can be orders of magnitude larger than the noise observed for the spectrally-unresolved output. This reduction in the intensity noise of the total output compared to that of a particular mode can be traced to the near-homogeneous interaction between the modes and the gain medium, which fixes the total output at the level supported by the injection current without constraining the fluctuations of any particular mode. The quasi-single-mode case, in which a lasing mode and a weak side mode are present, has been analyzed.

The equilibrium number of the side mode is given by (2.5.1), with the net modal gain $-1/\tau_{1,0}$, where $\tau_{1,0}$ is the time constant associated with the transient suppression of the side mode, given by (3.4.7) with m=1 and d=0. One obtains

$$<S_1> = \frac{\beta N_{th}\tau_{1,0}}{\tau_s} \tag{3.5.3}$$

where (2.5.2) and (2.5.8) were used, neglecting the stochastic term. Neglecting the nonlinear gain and inserting some reasonable values gives

$$\frac{1}{\tau_{1,0}} = -\Delta_1 = \frac{1}{\tau_p}\left[\frac{\Delta\lambda}{\Delta\lambda_{RO}}\right]^2$$

$$= \frac{1}{1.5\times10^{-12}\ \mathrm{s}}\left[\frac{3\ \text{Å}}{50\ \text{Å}}\right]^2 = 2.4\times10^{9}\ \mathrm{s}^{-1} \qquad (3.5.4)$$

where $\Delta\lambda$ is the spacing of the longitudinal modes and $\Delta\lambda_{RO}$ is half the distance between the G=0 (transparency) points on the modal gain curve at threshold. The mean photon number of the side mode is then $<S_1>=3.8\times10^4$, which when compared to a typical (see Table 2.6.2) mean photon number of the main mode $<S_0>=4\times10^5$ implies that 9 % of the output power is in the side mode.

The mode-partition noise of the main mode can be found by using (3.5.3) to rewrite Equation (7.58) of Reference [53]

$$\mathrm{RIN}(\Omega)\,\Delta\nu = 4\left[\frac{\beta N_{th}}{\tau_s}\right]^2 \frac{1}{<S_0>^2}\,\frac{\tau_{1,0}^3}{1+(\tau_{1,0}\Omega)^2}\Delta\nu \qquad (3.5.5)$$

The low-frequency limit of (3.5.5) gives $\mathrm{RIN}(0)=1.6\times10^{-11}\ \mathrm{Hz}^{-1}$, over an order of magnitude larger than the low-frequency limit of the single-mode RIN, giving a 200 MHz streak camera resolution bandwidth relative intensity noise of 0.3 %.

Mode hopping involves the extinction of the lasing mode in a quasi-single-mode device, simultaneous with the commencement of lasing in another mode, which then becomes the metastable lasing mode. This contrasts with mode-partition fluctuations, in which the dip in main mode power is transient. The hops are instigated by spontaneous emission noise. Assuming that no long-term drift or the deliberate change of a parameter shifts the linear net gain curve, the existence of more than one metastable mode implies that some self-stabilization mechanism is at work, as discussed in Section 3.4.

Hopping between two metastable modes has been studied experimentally and theoretically for both InGaAsP[76] and AlGaAs[77] semiconductor lasers. In both cases, each mode had a rectangle-wave power output, with transitions between the "on" and "off" states occurring after random dwell times, and rapidly compared to the mean dwell time. It is intuitively clear that hopping will occur more frequently with increasing spontaneous emission noise, and that the mean "on" dwell time of a mode will increase with increasing suppression of the other mode. The outputs of the modes are roughly complementary, and the deviation of the total output from its mean value is called mode-hopping noise[78].

The InGaAsP device of Reference [76] was run such that each mode had approximately a 50 % duty cycle and the same average power output, and their intensity time series were found to be statistically similar. The power spectra of these time series were found to be Lorentzian with a corner frequency (frequency at which the lines asymptotic to the low- and high-frequency limits of a log-log plot of the power spectrum intersect) of ν_c=1.4 MHz, corresponding to a mean dwell time of $1/\pi\nu_c$=230 ns. The dwell times reported for the AlGaAs device of Reference [77] are in the 10 μs regime.

These cutoff frequencies are far lower than the 500 MHz-50 GHz range of interest, alternately, since the dwell times are much longer than the 5 ns window accessible to the streak camera, it is unlikely a mode hop will occur during a given frame. Nevertheless, unequal dwell times cause the ratio of the average power of the modes, which is easy to measure, to differ from the ratio of the "on" power of the modes, which will be of importance in determining the imaginary part of the coupling coefficient of the twin-emitter device, as described in Section 6.6. The relationship between these quantities is

$$\frac{P_1(on)}{P_2(on)} = \frac{\Theta_2}{\Theta_1}\frac{P_1(ave)}{P_2(ave)} \tag{3.5.6}$$

where Θ_1 and $\Theta_2=1-\Theta_1$ are the duty cycles of the modes. If these are unknown, it is necessary to measure $P_1(on)$ and $P_2(on)$ directly, using a spectrally-resolved streak camera setup.

3.6 Optical Feedback

So far we have examined dynamical effects present in isolated semiconductor lasers. In real life there is always some optical feedback. Feedback is often intentionally introduced by coupling the semiconductor laser to an external cavity, for the purpose of side-mode suppression, linewidth reduction, or tuning. Here we are concerned with unwanted feedback caused by reflections from the surfaces of optical components in a characterization setup.

Regardless of its source, optical feedback can be modeled as an external cavity with a round-trip time delay τ_{ext}, an effective power reflectivity R_{ext} and a frequency-dependent phase shift. Since this phase shift is unknown and may be time-dependent due to mechanical vibrations, it will be ignored in the following discussion, which is intended only to estimate the magnitude of unwanted feedback.

The feedback strength is commonly expressed (e.g. Chapter 9, Reference [53]) as

$$C \equiv \left[\frac{R_{ext}}{R}\right]^{1/2}(1-R)\cdot\frac{\tau_{ext}}{\tau_L}\cdot[1+\alpha^2]^{1/2} \tag{3.6.1}$$

This expression has been grouped into three factors. The first is the ratio of the

fields of the external cavity reflection to the facet reflection. Multiple external cavity reflections are negligible for the low feedback levels expected. The second factor is the ratio of the external cavity to the laser cavity round-trip times, which can be quite large. The third factor includes the destabilizing effect of the amplitude-phase coupling described by the linewidth-enhancement factor.

Five feedback regimes have been identified[79] and are discussed below in order of increasing feedback strength. Regime I is defined by $C<1$, which allows only one external cavity mode per laser longitudinal mode to satisfy the overall round-trip phase condition. Thus the feedback is too weak to destabilize the laser. Regime II occurs for C somewhat greater than 1, where two or more external cavity modes exist and have comparable gains, causing mode hopping. As feedback increases, the external cavity mode with the smallest linewidth becomes favored and relatively stable emission is obtained. This has been designated Regime III. At still higher feedback, the coherence collapse[80] Regime IV is encountered, in which the output is wildly erratic. Finally, at very high feedback levels the laser and external reflector must be considered a single composite cavity and stable operation is obtained once more. This is Regime V.

In Appendix D it is shown that the power reflectivity of the optical components in a typical setup for the characterization of coherent semiconductor laser arrays is in the $R_{ext}=5\times10^{-7}$ to $R_{ext}=2\times10^{-5}$ range. Assuming a round-trip time ratio of

$$\frac{\tau_{ext}}{\tau_L}=\frac{L_{ext}}{\mu_{g,e}L}=\frac{50\text{ cm}}{4.1\cdot240\ \mu\text{m}}\approx 500 \qquad (3.6.2)$$

and using $\alpha=7.5$ from Table 2.6.1 gives $C=3.2$ to $C=20$, and we expect Regime II behavior.

The power spectrum of the intensity of a nominally single-mode laser operating in an unstable feedback regime is greatly enhanced compared to the intensity noise spectrum of the isolated device. The following features have been noted[81]: peaks at multiples of τ_{ext}^{-1}, under an envelop with peaks at multiples of the relaxation oscillation frequency, with a bandwidth approximately equal to the spectral linewidth, which is given by

$$\Delta\nu = \frac{1}{2\pi}\frac{1}{\tau_L}\left[\frac{R_{ext}}{R}\right]^{1/2}(1-R)(1+\alpha^2)[1-C(\tau_{ext})] \qquad (3.6.3)$$

where $C(\tau_{ext})$ is the autocorrelation of the electric field with a delay of one external-cavity round trip. Assuming the worst case of $C(\tau_{ext})=0$ and $R_{ext}=2\times10^{-5}$, the linewidth is $\Delta\nu$=7.5 GHz, which is a frequency range somewhat lower than that associated with the dynamics of the lateral modes of coherent arrays, the main topic of this thesis. Moreover, any feedback effects should be recognizable by their characteristic frequency τ_{ext}^{-1}, which can be detected using a spectrum analyzer. For these reasons, as well as the expected feedback levels being too small to cause coherence collapse (Regime IV), optical feedback is not expected to be troublesome in the experimental work to follow.

3.7 Dynamics Associated with Saturable Absorbers

Photon loss mechanisms can be divided into two classes: unsaturable and saturable. The former include facet transmission and absorption, and waveguide scattering, all of which can be combined into a linear loss term S/τ_p.

Saturable absorbers have a finite recovery time after disposing of a photon, during which they cannot absorb another photon. A sufficiently large photon density can "bleach" the absorbers, reducing the cavity loss. As discussed in Section 3.2, positive feedback between the photon number and the net gain can destabilize the dynamics. Saturable absorbers can cause two fundamentally different types of instability.

The first type is passive longitudinal mode-locking caused by an inhomogeneous spatial distribution of saturable absorbers. This is typically accomplished using a two-section device, where one section is reverse-biased to form the saturable absorber[68]. Although of considerable interest in its own right, this topic is beyond the scope of this chapter.

In the second case, microscale defects are invoked to explain the self-sustained pulsations that are often observed as semiconductor lasers age or are otherwise damaged[82]. These defects are envisioned as local traps which can absorb a photon and make a transition to an excited state, which persists for a characteristic time τ_a before decaying. The excited state is unavailable for further absorption, making the absorber saturable.

It is assumed that the defects are uniformly distributed throughout the mode volume. This prevents saturable-absorber coupling of the longitudinal modes (see Section 27.6 of Reference [83]), and allows the use of the single-mode rate equations. The rate equation for the absorber number is

$$\frac{d}{dt}Q = \frac{Q_0 - Q}{\tau_a} - \frac{B}{\tau_a}QS \tag{3.7.1}$$

where Q_0 is the cold-cavity absorber number and

$$B \equiv \frac{c}{\mu_{g,e}} \frac{\sigma_a}{V} \tau_a \tag{3.7.2}$$

where σ_a is the absorber cross-section and V is the mode volume, is the rate at which a single photon is absorbed by a single absorber, normalized to the absorber recovery time. The other rate equations are

$$\frac{d}{dt}S = \left[\left(\frac{\partial G}{\partial N} \right)_{th} (N - N_{th}) - \frac{B}{\tau_a} Q \right] S \tag{3.7.3}$$

and

$$\frac{d}{dt}N = \frac{J}{q} - \frac{N}{\tau_s} - \left[\frac{1}{\tau_p} + \left(\frac{\partial G}{\partial N} \right)_{th} (N - N_{th}) \right] S \tag{3.7.4}$$

where N_{th} is the threshold carrier number in the absence of saturable absorbers, and the gain has been assumed to be independent of S for simplicity. Note that since there are now three dynamical variables, optical chaos is possible.

The steady-state absorber number is

$$Q^{(0)} = \frac{Q_0}{1 + BS^{(0)}} \tag{3.7.5}$$

which can be substituted into the steady-state version of (3.7.3) to eliminate $N^{(0)}$ in favor of $S^{(0)}$, which in turn can be substituted into the steady-state version of (3.7.4) to obtain the injection current as a function of the photon number

$$\frac{J^{(0)} - J_{th}}{q} = \frac{S^{(0)}}{\tau_p} + \left[\frac{1}{\tau_s (\partial G / \partial N)_{th}} + S^{(0)} \right] \frac{B}{\tau_a} \frac{Q_0}{1 + BS^{(0)}} \tag{3.7.6}$$

where J_{th}, the threshold current in the absence of saturable absorbers, was defined in (2.6.12). The increase in threshold current due to saturable absorbers is found by setting $S^{(0)} = 0$ in (3.7.6)

$$\frac{\Delta J_{th}}{q} = \frac{B}{\tau_s(\partial G/\partial N)_{th}} \frac{Q_0}{\tau_a} \tag{3.7.7}$$

The stability of the equilibrium given by (3.7.6) can be evaluated by noting whether the injection current increases or decreases with increasing photon number to maintain equilibrium. Normally, an increase is required to support the increased rate of stimulated emission. If a *decrease* is required, positive feedback exists between the photon number and the modal gain, and the equilibrium is unstable. In the $S^{(0)} \to \infty$ limit, $J^{(0)}$ clearly increases with $S^{(0)}$, so that the equilibrium is always stable for large enough photon numbers. To find the stability boundary, we differentiate (3.7.6) with respect to $S^{(0)}$ and set the result equal to zero to get an expression for the photon number S_{bnd}, above which the equilibrium point is stable

$$B^2 S_{bnd}^2 + 2BS_{bnd} + 1 + \frac{\tau_p}{\tau_a} BQ_0 \left[1 - \frac{B}{\tau_s(\partial G/\partial N)_{th}} \right] = 0 \tag{3.7.8}$$

For a real, positive root to exist, the term independent of S_{bnd} must be negative. This can happen only if

$$B > \tau_s \left[\frac{\partial G}{\partial N} \right]_{th} \tag{3.7.9}$$

The left-hand side of (3.7.9) can be interpreted as the ratio of the excitation to the relaxation rates of an absorber due to each photon, while the right-hand side is the ratio of the stimulated to the spontaneous recombination rates of a carrier pair due to each photon. Thus, a necessary requirement for saturable-absorption instability is that the absorbers must be bleached more easily than the gain is saturated, a well-known result[84]. Table 3.7.1 shows that this condition is fulfilled, using some published parameter values. Given (3.7.9), minimum absorber number is

parameter	value	reference
τ_a	100 ps	[82]
σ_a	10^{-14} cm^2	"
B	1.6×10^{-5}	(3.7.2)
$\dfrac{B}{\tau_s\left[\dfrac{\partial G}{\partial N}\right]_{th}}$	7.5	Tables 2.6.1 and 2.6.2
$Q_{0,min}$	6.3×10^{5}	(3.7.10)
ΔJ_{th}	7.6 mA	(3.7.7)

Table 3.7.1 Saturable Absorption Parameters

$$Q_{0,min} \equiv \frac{\tau_a}{\tau_p}\frac{1}{B}\frac{1}{\frac{B}{\tau_s(\partial G/\partial N)_{th}}-1} \tag{3.7.10}$$

Assuming that Q_0 is only slightly larger than $Q_{0,min}$ gives

$$S_{bnd} = \frac{1}{2B}\left[\frac{Q_0}{Q_{0,min}}-1\right] \tag{3.7.11}$$

The increase in lasing threshold corresponding to $Q_{0,min}$ is found to be 7.6 mA, which is easily noticeable. Thus, if a device with a threshold that has increased over its lifetime begins to exhibit sustained self-pulsations, saturable absorber defect formation might be suspected. As discussed in Section 3.2, the frequency of pulsations is expected to be the relaxation oscillation frequency, in the small-signal limit.

3.8 Mode Profile Dynamics

This section considers cases in which the lateral profile of the optical mode is time-dependent. This renders invalid the separation of lateral and time dependencies of the fields, used in Section 2.2.3 to derive the rate equations. The coupled problem is very difficult. Small-signal[85] and fully-numerical[86] spatio-temporal models have been published.

The most conspicuous sign of mode-profile instability is a "kink", or discontinuity of the slope of the light-versus-current curve. Kinks are typically accompanied by the lateral shift or narrowing of the fundamental mode, or the onset of lasing of a higher-order mode[86]. Dynamic instabilities at a fixed injection current have

been theoretically predicted[86], which involve periodic variations of the lateral position and width of the fundamental mode. All of these problems can be avoided by using an index-guided or even a narrow-stripe gain-guided design, as do nearly all modern single-emitter devices. Gain-guided arrays continue to be popular due to their relative fabrication simplicity, however, providing a motivation to study mode profile dynamics. We assume that no lateral index-guiding structures have been built into the devices discussed in the remainder of this section.

Even in a device with no intentional lateral index-guiding, inhomogeneities, inevitable during growth, can cause variations in the effective index along the lateral direction. Small flaws can have surprisingly large consequences, particularly for lateral position stability. It has been estimated that an active layer thickness taper of one lattice constant over the stripe width can induce noticeable lateral mode shifts[86].

Thermal lensing is an important waveguiding mechanism. The dominant heat source in semiconductor laser appears to be the non-radiative decay of carriers[40,87], which induces a temperature difference of a few kelvin between the center and edges of the stripe. Since the index of refraction for an GaAs/AlGaAs increases with temperature, positive thermal lensing is weakly guiding. Index differences between stripe center and edge of 1×10^{-3} to 3×10^{-3} are typically assumed[88,89]. It has been proposed that thermal lensing may be responsible for giving the Hermite-Gaussian-like higher-order modes observed for wide-stripe devices, which cannot be explained by purely carrier-induced guiding[87]. Both index-inhomogeneities and thermal lensing can be considered static in the 500 MHz-50 GHz dynamical regime. Inhomogeneities are of course strictly static, while thermal effects react too slowly to enter into sub-nanosecond dynamics, as discussed in Appendix A.

The carriers, however, can respond rapidly enough. Carriers have two effects: a higher-density region will contribute both gain guiding and index anti-guiding relative to an adjacent lower-density region. These effects always oppose each other, and either can dominate depending on the situation. Since thermal lensing and carrier anti-guiding are both proportional to the carrier density, they partially cancel. It has been noted that carrier anti-guiding is the stronger effect[87,89]. The net guiding due to carriers and thermal lensing must be strong enough to overcome diffraction for effective lateral waveguiding.

Two types of lateral modes, "well-behaved" and "filamentary", have been identified[87]. Well-behaved modes rely on gain-guiding, while filaments are essentially index-guided, due either to inhomogeneities[87] or carrier density dips caused by spatial-hole burning[90]. Well-behaved modes typically occupy the entire stripe width, while filaments are narrow and occur at random lateral positions. The most important prognosticator of mode behavior is $W/2L_d$, where W is the stripe width and L_d is the carrier diffusion length, typically about 3 μm in GaAs/AlGaAs devices[86,90]. For $W/2L_d<1$, spatial hole burning is difficult to achieve and the modes are well-behaved. For $W/2L_d>2$, dips in the carrier density at the filament have been observed by viewing the lateral spontaneous emission profile during filamentary lasing[90]. These modes were probably self-focused, but it can be argued that the carrier dip was an effect rather than a stable self-consistent solution to the interaction of photons and carriers, and the filament was stabilized by an inhomogeneity[87].

Inhomogeneities are obviously necessary to explain lateral shifts in otherwise symmetric devices. Models that include an asymmetric index perturbation are able to predict the sharper, lower-threshold kinks caused by lateral shifts, while symmetric

models can predict only the softer, higher-threshold kinks caused by self-focusing and higher-order lateral modes[86]. An increase in the linewidth-enhancement factor has been associated with a greater tendency toward lateral shifting[88].

Self-focusing self-sustained pulsations have been studied for wide-stripe gain-guided GaAs/AlGaAs lasers[89]. The optical mode was observed to narrow from a full-width of 9 μm at the beginning to 7.2 μm at the end of the ≈1 ns pulses, with no lateral shifting. The pulse repetition frequency (150-300 MHz) was substantially less than the relaxation oscillation frequency and had a different dependence on the injection current, contrary to predictions of small-signal theory[85]. To account for the unexpectedly long period between pulses, it was proposed that the gain had to build to considerably beyond the quiescent threshold before emission of a pulse. Differential efficiencies >100 % were noted at the threshold of self-sustained pulsations, which indicated that the self-sustained pulsation state used gain more efficiently than the quiescent state, probably because the time-averaged carrier number was lower, allowing less loss due to spontaneous carrier decay.

The process of pulse emission can be considered as an interaction of carrier gain guiding and index anti-guiding, and static thermal lensing. As the pulse builds in intensity, carriers are depleted and gain guiding is reduced, but anti-guiding, in which the effect of the carriers is partially offset by thermal lensing, is reduced more rapidly so that there is a net focusing effect. This causes the modal gain to increase despite the partial depletion of carriers, and the pulse grows until the carriers are fully depleted. The thermal lensing effect is crucial to this process[89].

Existing models seem to indicate that self-focusing alone is insufficient to account for self-sustained pulsations. In one case[85], failure of the model to predict

self-focusing instabilities may have been due to the use of a small value (α=1.5) of the linewidth-enhancement factor. Saturable absorbers are often invoked as a further destabilizing mechanism. That self-pulsations in index-guides are less common but by no means unheard-of argues that self-focusing is only partially responsible for instabilities. On the other hand, chirps of $\approx$0.5Å toward longer wavelengths during pulsing have been observed[89], indicating an increase in the effective index consistent with self-focusing. Finally, index perturbations along with large values of α have predicted self-sustained pulsations in both the lateral position and width of the lasing mode[86].

4. DYNAMICAL MODELS OF COHERENT ARRAYS

4.1 Chapter Overview

This chapter extends the analyses of Chapter 2 to coherent arrays. Three models of array dynamics are presented. In order of decreasing complexity and generality, they are the continuum, the coupled-lateral-mode and the coupled-emitter models. In all cases, a distributed-loss, standing-wave approach is used to separate the longitudinal modes, and it is assumed that longitudinal mode interactions can be neglected, for the reasons discussed in Section 3.4. A single vertical mode is assumed and accounted for by the use of the effective index and a vertical confinement factor, reducing the problem to one spatial dimension.

Section 4.2 describes the continuum and coupled-lateral-mode models. The continuum model is generally applicable and requires the self-consistent solution of the optical and carrier diffusion equations, along with Laplace's equation in the p-type cladding layer. The coupled-lateral-mode model assumes that the optical wave can be separated into modes with distinct and constant frequencies of oscillation and normalized lateral profiles, and characterized by time-dependent complex amplitudes. By replacing the optical eigenvalue equation of the continuum model with a set of modal rate equations, the volume of computations is radically reduced. It remains

necessary to solve the carrier diffusion equation and Laplace's equation at every time increment, however.

Section 4.3 describes the coupled-emitter model, in which all spatial dependence is eliminated and coupling between emitters is described by complex constants. This model forms the basis for all subsequent work in this thesis. The connection with the coupled-lateral-mode model is discussed.

Section 4.4 discusses twin-emitters, the simplest of coherent arrays. The coupled-emitter model is applied to weakly-coupled twin-emitters, to obtain the twin-emitter rate equations. The equilibrium points of the rate equations are shown to correspond to the lateral modes of the array. This allows the coupling coefficient, a key parameter in the rate equations, to be related to the frequency and gain differences between the lateral modes, which can be measured spectroscopically. Lastly, the dependence of the stability of the lateral modes on the coupling coefficient is found.

Section 4.5 uses a simple model of a twin-emitter to obtain the coupling coefficient as a function of emitter spacing. The utility of the coupled-emitter approach becomes apparent when the coupling coefficient has been related to spectroscopic properties (Section 4.4) and the design (Section 4.5) of the twin-emitter array.

4.2 Continuum and Coupled-Lateral-Mode Models

The continuum model is obtained by substituting

$$C_m(x,y,z,t) \rightarrow C_m(y,t)\psi(x)\left(\frac{2}{L}\right)^{1/2}\sin(k_m z) \tag{4.2.1}$$

into (2.2.2.16) and cancelling the common x and z dependence, where the vertical profile $\psi(x)$ is normalized analogously with (2.2.3.4). The longitudinal mode index "m" is then dropped in accordance with the neglect of longitudinal mode interactions to get

$$-2i\frac{\omega_0\mu_e\mu_{g,e}}{c^2}\frac{\partial}{\partial t}C(y,t) =$$

$$\left[\frac{\partial^2}{\partial y^2}+\frac{\omega_0^2}{c^2}[\mu_e^2(y)+\Gamma\chi(y,t)]-K^2+i\frac{\omega_0\mu_e\mu_{g,e}}{c^2}\frac{1}{\tau_p}\right]C(y,t) \tag{4.2.2}$$

where K encompasses the longitudinal and vertical propagation constants and Γ is the vertical confinement factor. The carrier diffusion equation (2.3.1.2) is used, with the spontaneous decay r_{dk} given by (2.3.1.5) and the stimulated recombination given by

$$r_{st} = -\frac{\omega_0}{\mu_e\mu_{g,e}}\frac{\Gamma}{Ld}\mathrm{Im}[\chi]\,|C|^2 \tag{4.2.3}$$

The presence of j(y,t) in (2.3.1.2) requires the solution of Laplace's equation in the p-type cladding layer, as discussed in Section 2.3.1, subject to the boundary conditions given by current injection from each of the emitter contacts. While being founded the most directly on basic principles, the continuum approach is unwieldy for numerical implementation and offers little physical insight. The partial differential equation for the optical field typically requires several orders of magnitude more computations than the diffusion equation[86], therefore the volume of computations can be drastically reduced by a modal decomposition of the optical wave equation to yield rate equa-

tions. This gives the coupled-lateral-mode model, to be discussed for the remainder of this section.

The coupled-lateral-mode model is obtained from the continuum model by substituting

$$C(y,t) \rightarrow \sum_m C_m(t) f_m(y) \tag{4.2.4}$$

where the index "m" now refers to lateral modes. It is assumed that the modes are close enough in frequency to all see the same local carrier-induced susceptibility $\chi(y)$. Discrimination between the lateral modes will be dominated by their relative overlap with the gain regions, rather than the roll-off due to their position on the gain curve.

We now assume, as in Chapter 2, that some $\chi^{(0)}$ exists such that all the lateral modes and the carrier density co-exist in equilibrium. Substituting (4.2.4) into (4.2.2) gives

$$\left[\frac{\partial^2}{\partial y^2}+\frac{\omega_m^2}{c^2}[\mu_e^2(y)+\Gamma\chi^{(0)}(y)]-K^2+i\frac{\omega_0\mu_e\mu_{g,e}}{c^2}\frac{1}{\tau_p}\right]f_m(y) = 0 \tag{4.2.5}$$

In practice, rather than solve (4.2.5) for each mode, ω_m can be measured spectroscopically, $|f_m|$ can be obtained from the spectrally-resolved near-field intensity, and the phase of f_m can be determined using interference techniques[91]. Once the lateral profiles are known, the dynamics of the complex modal amplitudes are given by

$$\frac{d}{dt}C_m = i\frac{\omega_0}{2\mu_e\mu_{g,e}}\Gamma<\chi^{(1)}>_m C_m \tag{4.2.6}$$

where $\chi^{(1)}$ is defined similarly to (2.2.4.1), and $<...>_m$ represents integration over the lateral coordinate, weighted with $|f_m|^2$.

The carrier diffusion equation (2.3.1.2) is used, with the spontaneous decay r_{dk} given by (2.3.1.5), but the stimulated recombination term

$$r_{st} = -\frac{\omega_0}{\mu_e \mu_{g,e}} \frac{\Gamma}{Ld} \mathrm{Im}[\chi] \left| \sum_m C_m f_m e^{-i\omega_m t} \right|^2 \tag{4.2.7}$$

must be used, because the beat frequencies between lateral modes can be on the order of the relaxation oscillation frequency, typically a few gigahertz, allowing the carriers to respond to modal interference. This contrasts with the situation for longitudinal modes, whose beat frequencies are far larger than the carriers can respond to.

Despite the vast simplification of eliminating the optical eigenvalue equation of the continuum model, the coupled-lateral-mode model remains cumbersome to implement because of the carrier diffusion equation and Laplace's equation. Furthermore, the complexity of the model obscures the qualitative dynamical behavior. For these reasons, a simpler, more intuitive model is sought.

4.3 Coupled-Emitter Model

To achieve the desired simplicity, we must eliminate all spatial dependence from the model, leaving only ordinary differential equations in time (rate equations) for the dynamical variables. We can extend the single-emitter rate equation approach to arrays by allowing linear coupling between the emitters. This approach has its origin in coupled-mode theory[92]. The first task is to show how the coupled-emitter model develops from the coupled-lateral-mode model. Next, the real part of the coupling matrix is experssed in terms of the frequencies and overlap integrals of the profiles of

the lateral array and emitter modes. Finally, the coupled-emitter rate equations are derived, assuming nearest-neighbor-only coupling described by a complex constant.

The coupled-emitter model is derived from the coupled-lateral-mode model by expanding the optical field in the lateral eigenmodes of the array

$$\Phi(t) = \sum_{m=1}^{M} C_m(t) f_m(y) e^{-i\omega_m t} \tag{4.3.1}$$

and also in the set of single-emitter TE_{00} modes for an array of P emitters

$$\Phi'(t) = \sum_{p=1}^{P} C'_p(t) f_0(y-y_p) e^{-i\omega_0 t} \tag{4.3.2}$$

where f_0 is the unperturbed single-emitter profile and y_p is the lateral displacement of the center of the pth emitter. Since the single-emitter modes are not eigenfunctions of (4.2.5), the set of profiles $f_0(y-y_p)$ are neither complete nor orthogonal, so that Φ' is only an approximation to the optical field Φ.

The goal is to express the emitter coupling dynamics in a set of linear, homogeneous, first-order differential equations with constant coefficients, i.e.

$$\left[\tau_p \frac{d}{dt} \mathbf{C}'\right]_{\text{coupling}} = i\boldsymbol{\eta}\cdot\mathbf{C}' \tag{4.3.3}$$

where $\mathbf{C}'$ is a P×1 column vector of the emitter amplitudes and $\boldsymbol{\eta}$ is a P×P constant matrix of complex coupling coefficients. To proceed, we require that $\mathbf{C}'$ be such that the best fit of Φ' to Φ be maintained at all times. Defining

$$Q(t) \equiv \int_{-\infty}^{\infty} dy \; |\Phi-\Phi'|^2 \tag{4.3.4}$$

a best-fit criterion can be expressed as

$$\frac{\partial Q}{\partial C'_p} = 0 \tag{4.3.5}$$

which insures a minimum for each p and all t. Substituting (4.3.1), (4.3.2) and (4.3.4) into (4.3.5) gives

$$\mathbf{A}\cdot\mathbf{C}' = \mathbf{B}\cdot\mathbf{T} \tag{4.3.6}$$

where **A** is the P×P matrix

$$A_{p,q} = \int_{-\infty}^{\infty} dy\ f_0^*(y-y_p) f_0(y-y_q) \tag{4.3.7}$$

B is the P×M matrix

$$B_{p,m} = \int_{-\infty}^{\infty} dy\ f_0^*(y-y_p) f_m(y) \tag{4.3.8}$$

and **T** is the M×1 column vector

$$T_m = C_m(t) e^{-i(\omega_m-\omega_0)t} \tag{4.3.9}$$

Solving (4.3.6) for **C′** and differentiating with respect to time normalized to the photon lifetime gives

$$\tau_p \frac{d}{dt}\mathbf{C}' = \mathbf{A}^{-1}\cdot\mathbf{B}\cdot\tau_p \frac{d}{dt}\mathbf{T} \tag{4.3.10}$$

Since the coupling matrix η must be independent of $C_m(t)$, we are free to make the simplest choice, that the modal amplitudes are given by their time-independent equilibrium values

$$C_m(t) = C_m^{(0)} \tag{4.3.11}$$

The coupling matrix obtained by this procedure is constrained to be real. This is because the imaginary part of the coupling matrix is related to the differences in the

gains of the lateral modes. When spontaneous emission is neglected, as it has been in this section, different modal gains prevent any two modes from simultaneously being in equilibrium, since the stronger mode will clamp its gain at threshold, causing the weaker mode to die off exponentially. Spontaneous emission acts as a source of photons to sustain the weaker mode at some finite equilibrium photon number.

The twin-emitter coupling matrix is calculated using (4.3.16) in Section 4.4, and is explicitly shown to be real. The imaginary part of the twin-emitter coupling matrix is introduced *ad hoc* in Section 4.5. An experimental method for measuring the imaginary part of the twin-emitter coupling matrix is given in Section 6.6.

Using (4.3.11), the time derivative of $\mathbf{T}$ can then be expressed as

$$\tau_p \frac{d}{dt}\mathbf{T} = i\mathbf{\Lambda}\cdot\mathbf{T} \tag{4.3.12}$$

where $\mathbf{\Lambda}$ is the M×M diagonal matrix

$$\Lambda_{m,m} \equiv \tau_p(\omega_0 - \omega_m) \tag{4.3.13}$$

Inserting (4.3.12) into (4.3.10) and using (4.3.6) to eliminate $\mathbf{T}$ gives

$$\tau_p \frac{d}{dt}\mathbf{C}' = i\mathbf{A}^{-1}\cdot\mathbf{B}\cdot\mathbf{\Lambda}\cdot\mathbf{B}^{-1}\cdot\mathbf{A}\cdot\mathbf{C}' \tag{4.3.14}$$

where $\mathbf{B}^{-1}$ is the M×P left inverse of $\mathbf{B}$

$$\mathbf{B}^{-1}\cdot\mathbf{B} = \mathbf{I} \tag{4.3.15}$$

where $\mathbf{I}$ is the M×M identity matrix. Comparing (4.3.14) with (4.3.3) gives

$$\boldsymbol{\eta}_R = \mathbf{A}^{-1}\cdot\mathbf{B}\cdot\mathbf{\Lambda}\cdot\mathbf{B}^{-1}\cdot\mathbf{A} \tag{4.3.16}$$

This is an important general result. It says that the real part of the coupling matrix is completely determined by the frequencies and profiles of the single-emitter mode

and array modes. Appendix E demonstrates the application of (4.3.16) to the case of the array lateral modes being given by sinusoidal supermodes[14], which results in a bi-diagonal coupling matrix (nearest-neighbor-only coupling) with equal elements.

We turn now to deriving the coupled-emitter rate equations. From this point on we assume uniform nearest-neighbor-only coupling

$$\eta_{p,p\pm1} \equiv \eta_R + i\eta_I \tag{4.3.17}$$

Separating the dynamical variables into products of real amplitudes and unit-modulus phase factors as in (2.2.4.6), defining

$$\theta_p \equiv \phi_{p+1} - \phi_p \tag{4.3.18}$$

as the difference in phase of successive emitters and separating the real and imaginary parts of (4.3.3) gives

$$\left[\tau_p \frac{d}{dt} A_p\right]_{coupling} = \eta_R A_{p-1}\sin\theta_{p-1} - \eta_I A_{p-1}\cos\theta_{p-1}$$

$$- \eta_R A_{p+1}\sin\theta_p - \eta_I A_{p+1}\cos\theta_p \tag{4.3.19}$$

and

$$\left[\tau_p \frac{d}{dt} \theta_p\right]_{coupling} = -\eta_R \frac{A_{p-1}}{A_p}\cos\theta_{p-1} - \eta_I \frac{A_{p-1}}{A_p}\sin\theta_{p-1}$$

$$+ \eta_R \left[\frac{A_p}{A_{p+1}} - \frac{A_{p+1}}{A_p}\right]\cos\theta_p + \eta_I \left[\frac{A_p}{A_{p+1}} + \frac{A_{p+1}}{A_p}\right]\sin\theta_p$$

$$+ \eta_R \frac{A_{p+2}}{A_{p+1}}\cos\theta_{p+1} - \eta_I \frac{A_{p+2}}{A_{p+1}}\sin\theta_{p+1} \tag{4.3.20}$$

In addition to coupling, the dynamical equations contain terms corresponding to gain and spontaneous emission. These are assumed to be given by the single-emitter expressions. Substituting (2.5.2) and (2.5.8) into (2.5.1) and using (2.2.4.9) and (2.4.3.5) gives

$$\left[\tau_p \frac{d}{dt} A_p\right]_{\text{uncoupled}} = \frac{1}{2}\left[\frac{1+\tau_p\left(\frac{\partial G_0}{\partial N}\right)_{th}(N_p-N_{th})}{\left[1+\frac{A_p^2}{S_{shb}}\right]^{\frac{1}{2}}}-1\right]A_p$$

$$+ \frac{\beta N_{th}}{2}\frac{\tau_p}{\tau_s}\frac{1}{A_p} + \left[\frac{\beta N_{th}}{2}\frac{\tau_p}{\tau_s}\right]^{\frac{1}{2}}\tau_p^{\frac{1}{2}}\epsilon(t) \qquad (4.3.21)$$

where $\omega_m \approx \omega_0$ has been used to neglect gain roll-off and it has been assumed that only the pth emitter amplitude contributes to the gain compression of the pth emitter. Differentiating (4.3.18) with respect to time and using (2.4.3.9) gives

$$\left[\tau_p \frac{d}{dt}\theta_p\right]_{\text{uncoupled}} = -\frac{\alpha}{2}\tau_p\left[\frac{\partial G_0}{\partial N}\right]_{th}(N_{p+1}-N_p) \qquad (4.3.22)$$

The dynamics of A_p are given by adding (4.3.19) and (4.3.21), and the dynamics of θ_p are given by adding (4.3.20) and (4.3.22).

The carrier number dynamics are given by

$$\tau_s \frac{d}{dt} N_p = \frac{\tau_s J_p}{q} - N_p - \frac{\tau_s}{\tau_p}\frac{1+\tau_p\left[\frac{\partial G_0}{\partial N}\right]_{th}(N_p-N_{th})}{\left[1+\frac{A_p^2}{S_{shb}}\right]^{\frac{1}{2}}}A_p^2 \qquad (4.3.23)$$

which is a generalization of (2.4.1.2) such that each emitter has an independently-adjustable current J_p and it has been assumed that diffusion of carriers between

emitters is negligible. The special case of real coupling and no spontaneous emission or gain compression has previously been reported[32]. This completes the coupled-emitter formalism.

4.4 Twin-Emitter Arrays

The twin-emitter is the simplest coherent semiconductor laser array, consisting of two identical emitters placed side-by-side in the junction plane. The epilayers provide index-guiding in the vertical direction, and lateral waveguiding is provided by the same mechanisms as in single-emitter devices. The emitter widths are 2-4 μm, which typically yields single TE_{00}-mode operation for an isolated emitter. The emitter center-to-center spacing is typically 6-12 μm, which is small enough to allow mutual coupling, but not so small that the array succumbs to the instabilities associated with broad-area devices.

The approach taken in this thesis is to assume that the dynamics of the twin-emitter array are representative of array dynamics, so that the direct modeling of larger arrays can be avoided.

The emitters are often electrically isolated from each other by etching the epilayer metallization and cap layer between the emitters. If the resistance between the emitter contacts is large compared to the effective resistance of the diodes, then the diode currents can be independently controlled. This makes possible a number of interesting applications, including beam-scanning[93], optically-[94] and electronically-[95] triggered bistable optical logic elements, picosecond optical pulsing[95] and high-

frequency modulation[69-71], which is discussed in Chapter 8.

Depending on the lateral guiding mechanism and the emitter spacing, several coupling regimes can be identified. For our purposes, a strongly-coupled device is one which must be modeled using a continuum approach, and is really just a wide single-emitter, although some control of the lateral carrier profile may be afforded by separate contacts. Lateral modes may be structurally unstable (sensitive to the variation of parameters, i.e. injection currents), or even spatio-temporally unstable at a fixed operating point, limiting their usefulness as a concept. The gain-guided twin-emitter described in Reference [95] had 3 μm stripes with a 6 μm center-to-center spacing, and was clearly a strongly-coupled device. Self-consistent continuum models for twin-emitters have been published[96, 97].

A moderately-coupled device is characterized by the existence of well-defined lateral modes, but the deviation of these modes and the carrier profile from linear combinations of the isolated-emitter modes and carrier profiles are sufficiently severe as to require retention of the carrier diffusion equation and Laplace's equation in the p-type cladding layer. Thus the coupled-lateral-mode model is the simplest applicable formalism.

A weakly-coupled device is one in which the lateral modes and the carrier profile sufficiently resemble linear combinations of the isolated-emitter profiles, so that the coupled-emitter model may be used. In a gain-guided device, this requires that the width of the region between emitters be greater than about two carrier diffusion lengths ($L_d \approx 3$ μm in GaAs)[86, 90]. The weakly-coupled case is the focus of the remainder of this thesis.

The TE_{00} modes of the emitters combine to give a pair of lateral array modes,

one symmetric and the other anti-symmetric about the lateral symmetry plane, as shown in Figure 4.4.1. Such a pair exists for each longitudinal mode of the array. They are also called the "in-phase" and "out-of-phase" modes, respectively, because of the relative phase of their lobes. In general, the array modes have different oscillation frequencies and threshold gains than each other or the single-emitter mode. The longitudinal propagation constant and the vertical profile being the same for both modes, the oscillation frequency increases with the lateral curvature (the absolute ratio of the second derivative of the profile to the profile itself) of the lateral profile. The out-of-phase mode must change sign in the symmetry plane, forcing greater curvature and a higher oscillation frequency than the in-phase mode. This is both experimentally observed and predicted by coupled-mode theory[98]. The gain of each lateral mode is given by the overlap integral of its intensity profile with the position-dependent gain. Depending on the geometry of the array, either array mode may have a lower threshold gain than the other, and thus dominate the emission spectrum.

The frequency splitting of the array modes gives rise to mode beating, which can also be viewed as "energy sloshing" between the emitters. This is shown in Figure 4.4.2, where it has been assumed that both modes are present with equal amplitudes. At $t=0$, the modes add constructively at emitter #1 and destructively at emitter #2. At $t=\pi/(\omega_- - \omega_+)$, the out-of-phase mode has advanced by a half-cycle relative to the in-phase mode, and the situation has reversed.

The next task is to obtain the coupling matrix. In the twin-emitter case, it turns out that η, given by (4.3.16), is independent of the modal profiles, being completely determined by the frequencies of the lateral array and emitter modes. This result will now be proven.

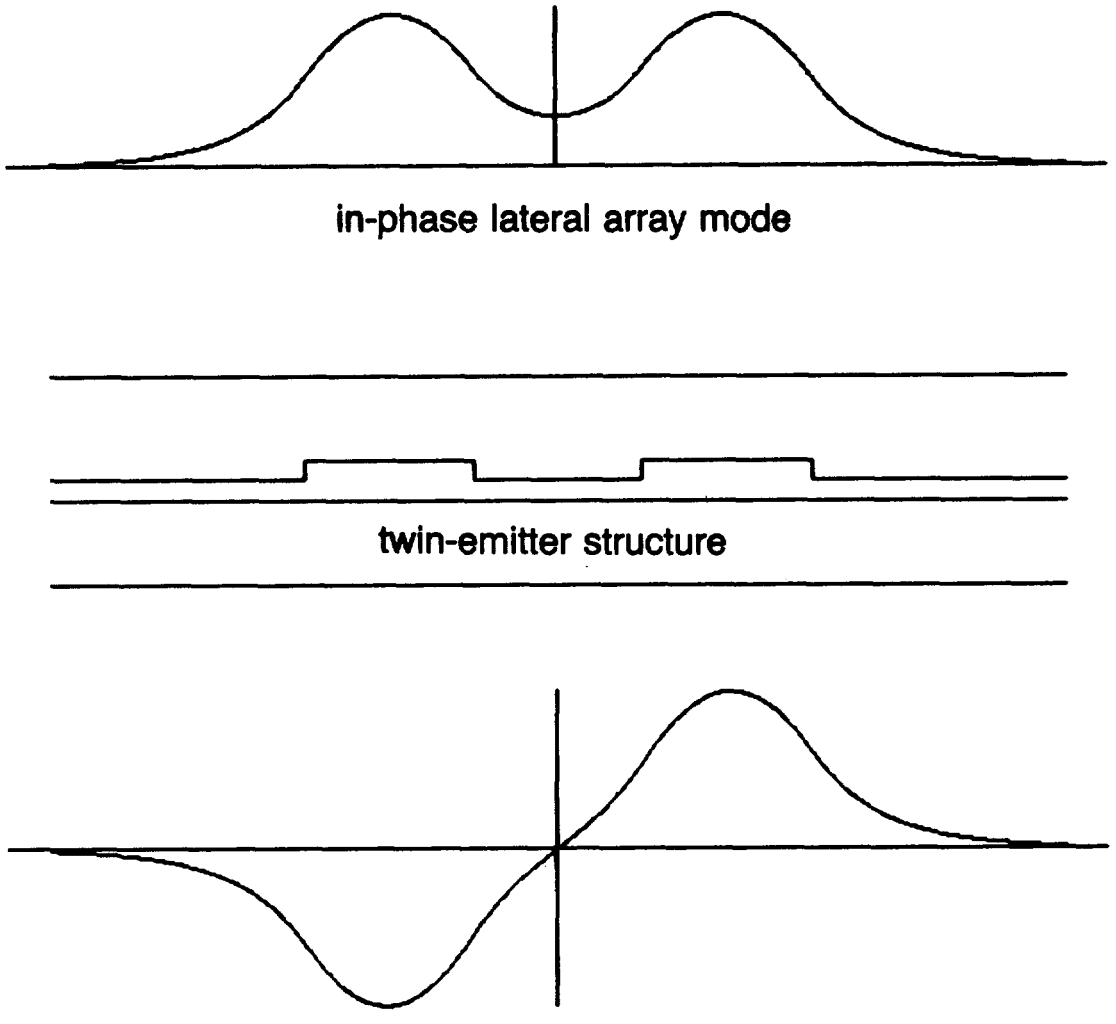

Figure 4.4.1 Twin-Emitter Geometry and Lateral Modes

Linear combinations of the single-emitter modes yield non-degenerate, orthogonal array modes in the limit of weak coupling.

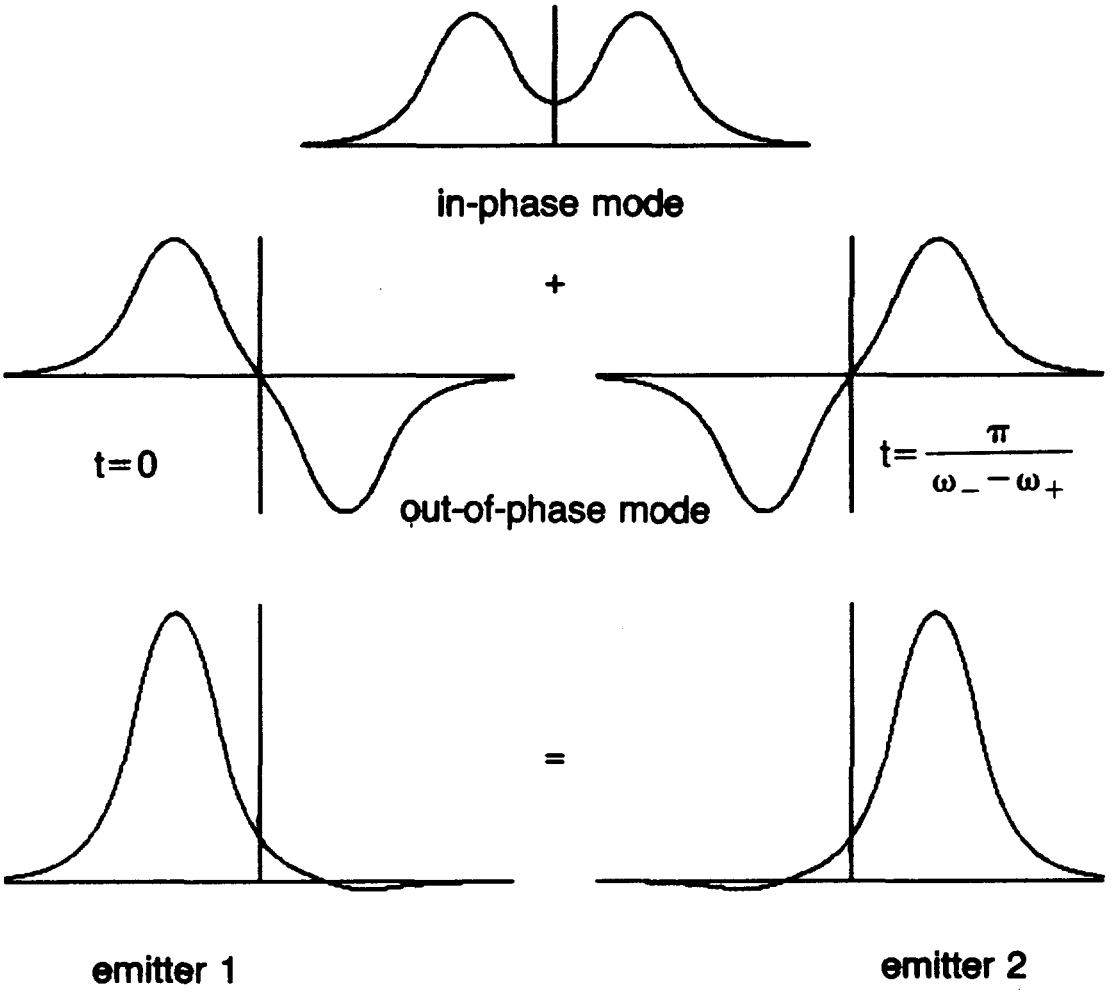

Figure 4.4.2 Mode Beating and Energy "Sloshing"

The slight detuning of the in-phase and out-of-phase array modes causes their constructive interference to shift back and forth between the emitters.

Referring to (4.3.7), the diagonal elements of **A** are real and equal, since they are the overlap integrals of identical emitter modes with themselves. Therefore

$$A_{2,2} = A_{1,1} \tag{4.4.1}$$

It is also clear that the off-diagonal elements are complex conjugates of each other,

$$A^*_{2,1} = A_{1,2} = \int_{-\infty}^{\infty} dy\ f_0^*(y+y_0)f_0(y-y_0) \tag{4.4.2}$$

where emitter #1 (#2) is centered at $-y_0$ (y_0). If we make the reasonable assumption that the emitter modes are laterally symmetric

$$f_0(-y) = f_0(y) \tag{4.4.3}$$

for an emitter centered at y=0, then the off-diagonal elements are real, and therefore equal. This is because (4.4.2) is invariant under the combined operations of complex conjugation and reflection in the array lateral symmetry plane ($y \to -y$), upon use of (4.4.3). Therefore

$$A_{2,1} = A_{1,2} \tag{4.4.4}$$

By the symmetry properties of the array modes, it is apparent that

$$B_{2,1} = B_{1,1} \tag{4.4.5}$$

and

$$B_{2,2} = -B_{1,2} \tag{4.4.6}$$

Using (4.4.1) and (4.4.4)-(4.4.6) and the general property

$$\begin{bmatrix} p & q \\ r & s \end{bmatrix}^{-1} = \frac{1}{ps-qr} \begin{bmatrix} s & -q \\ -r & p \end{bmatrix} \tag{4.4.7}$$

gives

$$\eta_R = \frac{\tau_p}{2}\begin{bmatrix} -\omega_- + 2\omega_0 - \omega_+ & \omega_- - \omega_+ \\ \omega_- - \omega_+ & -\omega_- + 2\omega_0 - \omega_+ \end{bmatrix} \tag{4.4.8}$$

Note that η_R is real. This results from the equilibrium assumption (4.3.11), as discussed in Section 4.3. Because $\omega_0 - \omega_+ \approx \omega_- - \omega_0$, the diagonal elements can be neglected, and we henceforth drop the row and column indices and understand η to refer specifically to cross-coupling, and no longer to self-coupling.

The next step is to write the twin-emitter rate equations. It is convenient to renormalize the optical field amplitude, gain and injection current as in Reference [33]

$$X \equiv \left[\frac{\tau_s}{2}\left(\frac{\partial G}{\partial N}\right)_{th} S\right]^{1/2} \tag{4.4.9}$$

$$Z \equiv \frac{\tau_p}{2}\left(\frac{\partial G}{\partial N}\right)_{th} (N - N_{th}) \tag{4.4.10}$$

$$p \equiv \frac{\tau_p}{2}\left(\frac{\partial G}{\partial N}\right)_{th} N_{th}\left(\frac{J}{J_{th}} - 1\right) \tag{4.4.11}$$

and renormalize the spontaneous emission

$$B \equiv \frac{\beta N_{th}\tau_p}{4}\left(\frac{\partial G}{\partial N}\right)_{th} \tag{4.4.12}$$

and gain compression

$$X_{shb} \equiv \left[\frac{\tau_s}{2}\left(\frac{\partial G}{\partial N}\right)_{th} S_{shb}\right]^{1/2} \tag{4.4.13}$$

Substituting (4.4.9)-(4.4.13) into (4.3.19)-(4.3.23) gives

$$\tau_p \frac{d}{dt} X_1 = \frac{1}{2}\left[\frac{1+2Z_1}{[1+X_1^2/X_{shb}^2]^{1/2}} - 1\right] X_1 + \frac{B}{X_1} + B^{1/2}\tau_p^{1/2}\epsilon(t)$$

$$- \eta_R X_2 \sin\theta - \eta_I X_2 \cos\theta \qquad (4.4.14)$$

$$\tau_p \frac{d}{dt} X_2 = \frac{1}{2}\left[\frac{1+2Z_2}{[1+X_2^2/X_{shb}^2]^{1/2}} - 1\right] X_2 + \frac{B}{X_2} + B^{1/2}\tau_p^{1/2}\epsilon(t)$$

$$+ \eta_R X_1 \sin\theta - \eta_I X_1 \cos\theta \qquad (4.4.15)$$

$$\tau_p \frac{d}{dt}\theta = -\alpha[Z_2 - Z_1]$$

$$+ \eta_R\left[\frac{X_1}{X_2} - \frac{X_2}{X_1}\right]\cos\theta + \eta_I\left[\frac{X_1}{X_2} + \frac{X_2}{X_1}\right]\sin\theta \qquad (4.4.16)$$

$$\tau_s \frac{d}{dt} Z_1 = p_1(t) - Z_1 - \frac{1+2Z_1}{[1+X_1^2/X_{shb}^2]^{1/2}} X_1^2 \qquad (4.4.17)$$

$$\tau_s \frac{d}{dt} Z_2 = p_2(t) - Z_2 - \frac{1+2Z_2}{[1+X_2^2/X_{shb}^2]^{1/2}} X_2^2 \qquad (4.4.18)$$

Note that θ is an integral part of the dynamics, as opposed to its single-emitter counterpart ϕ. The role of the linewidth-enhancement factor α is now apparent, large values magnify fluctuations in θ and destabilize the array. Chaos is possible in the five-dimensional phase space that contains the dynamics.

The remaining analyses in this thesis are small-signal linearizations about equilibria, so for simplicity and to emphasize emitter coupling effects, spontaneous emission and gain compression are neglected by setting $B=0$ and $X_{shb}=\infty$. The general equations (4.4.14)-(4.4.18) are retained for numerical integration in Chapter 5. Except

during the discussion of injection current modulation (Chapter 8), the injection currents will be assumed to be constant and equal

$$p_1(t) = p_2(t) \equiv p \tag{4.4.19}$$

We next solve for the steady-state solutions of (4.4.14)-(4.4.18) by setting the time derivatives equal to zero.

$$\theta^{(0)} = 0 \text{ or } \pi \tag{4.4.20}$$

$$Z_1^{(0)} = Z_2^{(0)} = \eta_I \cos\theta^{(0)} \equiv Z^{(0)} \tag{4.4.21}$$

$$X_1^{(0)} = X_2^{(0)} = \left[\frac{p-\eta_I\cos\theta^{(0)}}{1+2\eta_I\cos\theta^{(0)}}\right]^{1/2} \equiv X^{(0)} \tag{4.4.22}$$

The $\theta^{(0)}=0$ and $\theta^{(0)}=\pi$ equilibrium points correspond to the in-phase and out-of-phase array modes, respectively. We can interpret (4.4.21) and (4.4.22) by noting that if $\eta_I>0$, $Z^{(0)}(\pi)<Z^{(0)}(0)$ and $S^{(0)}(\pi)>S^{(0)}(0)$, so that the out-of-phase mode has a lower threshold and a larger photon number than the in-phase mode, and thus dominates the emission spectrum. The opposite argument holds for $\eta_I<0$.

We will now determine the stability of the equilibrium points to small perturbations. Linear stability theory is summarized in Appendix C. For the system given by (4.4.14)-(4.4.18) and (4.4.20)-(4.4.22), (C.7) becomes

$$\begin{bmatrix} \lambda-Z^{(0)} & Z^{(0)} & \eta_R X^{(0)}\cos\theta^{(0)} & -X^{(0)} & 0 \\ Z^{(0)} & \lambda-Z^{(0)} & -\eta_R X^{(0)}\cos\theta^{(0)} & 0 & -X^{(0)} \\ -\dfrac{2\eta_R\cos\theta^{(0)}}{X^{(0)}} & \dfrac{2\eta_R\cos\theta^{(0)}}{X^{(0)}} & \lambda-2Z^{(0)} & -\alpha & \alpha \\ \dfrac{2X^{(0)}(1+2Z^{(0)})}{T} & 0 & 0 & \lambda+\dfrac{1+2X^{(0)2}}{T} & 0 \\ 0 & \dfrac{2X^{(0)}(1+2Z^{(0)})}{T} & 0 & 0 & \lambda+\dfrac{1+2X^{(0)2}}{T} \end{bmatrix} \cdot \begin{bmatrix} X_1^{(1)} \\ X_2^{(1)} \\ \theta^{(1)} \\ Z_1^{(1)} \\ Z_2^{(1)} \end{bmatrix} = 0 \qquad (4.4.23)$$

where

$$T \equiv \frac{\tau_s}{\tau_p} \qquad (4.4.24)$$

By alternately adding and subtracting the first and second rows and the fourth and fifth rows, (4.4.23) can be separated into a 2×2 subsystem

$$\begin{bmatrix} \lambda & -X^{(0)} \\ \dfrac{2X^{(0)}(1+2Z^{(0)})}{T} & \lambda+\dfrac{1+2X^{(0)2}}{T} \end{bmatrix} \begin{bmatrix} X_1^{(1)}+X_2^{(1)} \\ Z_1^{(1)}+Z_2^{(1)} \end{bmatrix} = 0 \qquad (4.4.25)$$

and a 3×3 subsystem

$$\begin{bmatrix} \lambda-2Z^{(0)} & 2\eta_R X^{(0)}\cos\theta^{(0)} & -X^{(0)} \\ -\dfrac{2\eta_R\cos\theta^{(0)}}{X^{(0)}} & \lambda-2Z^{(0)} & -\alpha \\ \dfrac{2X^{(0)}(1+2Z^{(0)})}{T} & 0 & \lambda+\dfrac{1+2X^{(0)2}}{T} \end{bmatrix} \begin{bmatrix} X_1^{(1)}-X_2^{(1)} \\ \theta^{(1)} \\ Z_1^{(1)}-Z_2^{(1)} \end{bmatrix} = 0 \quad (4.4.26)$$

Note that a linear transformation to new variables cannot affect the stability of the equilibrium point.

Taking the determinant of (4.4.25) gives

$$\lambda^2 + A_1\lambda + A_2 = 0 \quad (4.4.27)$$

where

$$A_1 = \frac{1+2X^{(0)2}}{T} \quad (4.4.28)$$

and

$$A_2 = \frac{2X^{(0)2}(1+2Z^{(0)})}{T} \quad (4.4.29)$$

Note that since the renormalized equilibrium photon number $X^{(0)2}$ is always positive and $Z^{(0)}>-1/2$ by (4.4.21) and (4.4.22), condition (C.11) is fulfilled and the 2×2 subsystem is always stable.

Taking the determinant of (4.4.26) gives

$$\lambda^3 + A_1\lambda^2 + A_2\lambda + A_3 = 0 \quad (4.4.30)$$

where

$$A_1 = \frac{2X^{(0)2}-4T\eta_I\cos\theta^{(0)}+1}{T} \quad (4.4.31)$$

$$A_2 = 4\eta_R^2 - \frac{(4\eta_I\cos\theta^{(0)}-2)X^{(0)2}-4T\eta_I^2+4\eta_I\cos\theta^{(0)}}{T} \tag{4.4.32}$$

and

$$A_3 = \frac{8X^{(0)2}+4}{T}\eta_R^2 - \frac{(8\alpha\eta_I+4\alpha\cos\theta^{(0)})X^{(0)2}}{T}\eta_R$$

$$- \frac{4\eta_I\cos\theta^{(0)}X^{(0)2}-4\eta_I^2}{T} \tag{4.4.33}$$

Setting $A_3=0$ gives a quadratic equation in η_R as a function of η_I for the stability boundary corresponding to the third condition of (C.13). This boundary is easily plotted in the complex-η plane.

The stability boundary corresponding to the second condition of (C.13) is found by setting $A_1A_2-A_3=0$, where

$$A_1A_2-A_3 = -16\eta_I\cos\theta^{(0)}\eta_R^2 + \frac{(8\alpha\eta_I+4\alpha\cos\theta^{(0)})X^{(0)2}}{T}\eta_R$$

$$- \frac{(8\eta_I\cos\theta^{(0)}-4)X^{(0)4}+(4T\eta_I\cos\theta^{(0)}-24T\eta_I^2+12\eta_I\cos\theta^{(0)}-2)X^{(0)2}}{T^2}$$

$$- \frac{16T^2\eta_I^3\cos\theta^{(0)}-16T\eta_I^2+4\eta_I\cos\theta^{(0)}}{T^2} \tag{4.4.34}$$

which can be plotted similarly to (4.4.33).

We are now able to partition the complex-η plane into stability regions. Since $\eta_R>0$ is always observed, it is not necessary to plot the other half plane. It is convenient to use a logarithmic scale, so the horizontal axis of the standard stability plot is assigned the range $-5\leq\log_{10}(\eta_R)\leq 0$. Since both signs of η_I are observed, the upper vertical axis is assigned the range $-5\leq\log_{10}(\eta_R)$ and the lower vertical axis is

assigned the range $-5 \leq \log_{10}(-\eta_R)$, and are joined at $|\eta_I| = 10^{-5}$, which is small enough to be considered zero for all practical purposes. Thus the horizontal axis can be considered the real-η axis. Figures 4.4.3-4.4.5 were generated using the FORTRAN program "stability.f", listed in Appendix H, with $\alpha = 7.5$, $T = 1600$ and $p = 0.66$.

Figure 4.4.3 shows the regions of stability and instability for the in-phase mode. The boundary is formed entirely by the $A_3 = 0$ condition of (C.13). As discussed in Appendix C, the frequency of incipient instability as this boundary is crossed is zero, so that dynamical variables diverge without oscillation from their unstable equilibrium values, as will be seen in Figure 5.3.4.

Figure 4.4.4 shows the regions of stability and instability for the out-of-phase mode. The boundary is formed partially by the $A_3 = 0$ condition and partially by the $A_1 A_2 - A_3$ condition, which intersect at the cusp whose position is given by $A_1 = 0$. The $A_3 = 0$ portion of the boundary of Figure 4.4.4 coincides with that of Figure 4.4.3, so that the figures can be combined to give three disjoint regions in the portion of interest in the complex-η plane: two regions where one mode is stable and the other is unstable in turn, and the third region in which both modes are unstable. These stability boundaries have been verified by numerically integrating the rate equations for η on either side of a boundary, and checking for the loss of stability of the appropriate equilibrium point. They also conform to published results[33] for $\eta_I = 0$.

Note the correlation between the stability of the equilibrium points and the threshold gains, given by (4.4.21), of the corresponding lateral modes. This can be interpreted as follows: when $\eta_I > 0$, the out-of-phase mode has a greater overlap with

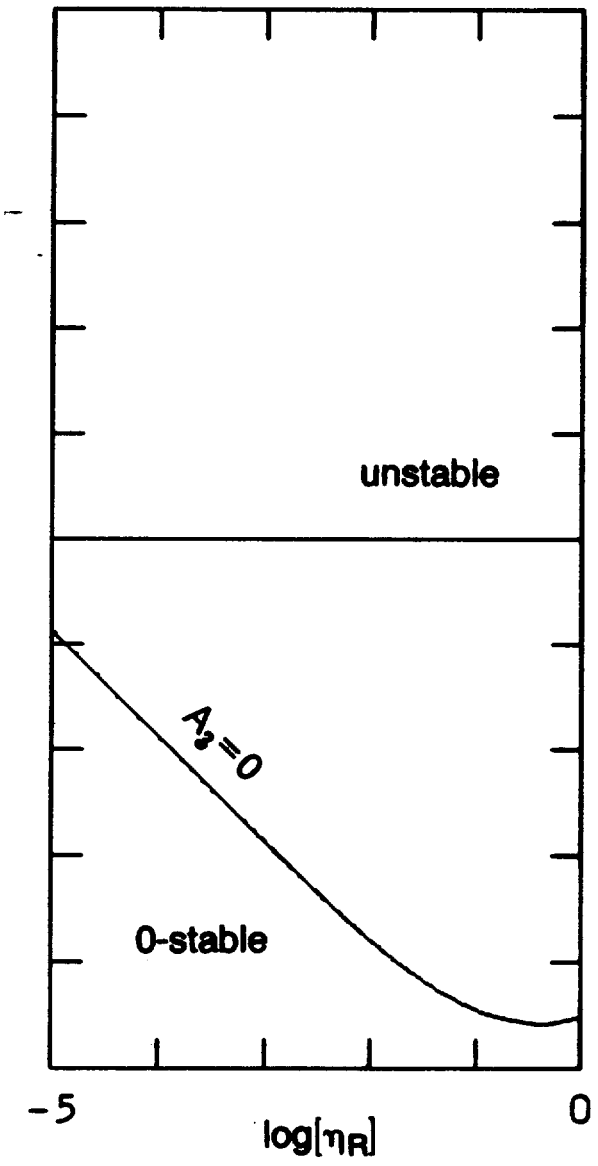

Figure 4.4.3
In-Phase Mode
Stability Boundary

The Hurwitz condition $A_3=0$ partitions the complex-η plane into regions of in-phase mode stability and instability.

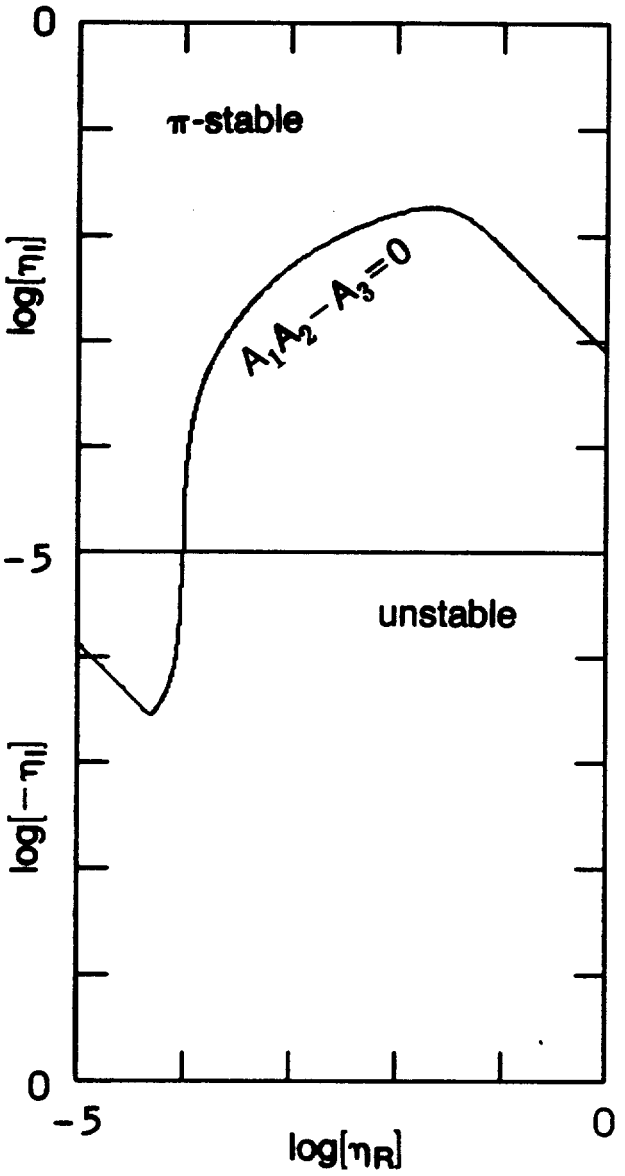

Figure 4.4.4
Out-of-Phase Mode
Stability Boundary

The Hurwitz conditions $A_3=0$ and $A_1A_2-A_3=0$ form boundaries that meet at $A_1=0$ and define the region of out-of-phase mode stability.

the lateral gain distribution than does the in-phase mode. Thus, if the device is lasing in the purely in-phase mode, the out-of-phase mode has a higher-than-threshold gain available to it, and any perturbation will be quickly amplified so that the out-of-phase mode takes over lasing, clamps the gain at its threshold, and suppresses the in-phase mode. We therefore conclude that the in-phase mode is unstable. For $\eta_I<0$, the opposite argument holds.

The frequency of incipient instability ω_{inst} along the $A_1A_2-A_3$ portion of the out-of-phase mode stability boundary is plotted in Figure 4.4.5. Different behavior is encountered depending on the magnitude of the beat frequency

$$\omega_- - \omega_+ = \frac{2\eta_R}{\tau_p} \tag{4.4.35}$$

compared to the relaxation oscillation frequency, given by (3.2.14). For $\omega_--\omega_+ \ll \omega_r$,

$$\omega_{inst} \approx \frac{1}{\tau_p}\left[\frac{2p}{T}\right]^{1/2} = \omega_r \tag{4.4.36}$$

where (4.4.11) and (4.4.24) were used. For $\omega_--\omega_+ \gg \omega_r$,

$$\omega_{inst} \approx \frac{2\eta_R}{\tau_p} \tag{4.4.37}$$

In other words, in the limits of large disparity, the instability frequency is the larger of the mode beating and relaxation oscillation frequencies. Therefore, although the mechanism of instability is mode competition, on the small-η_R end of the boundary the dynamics will resemble relaxation oscillations. This is supported by numerical simulations. This concludes the analysis of the dynamics of the unmodulated twin-emitter array.

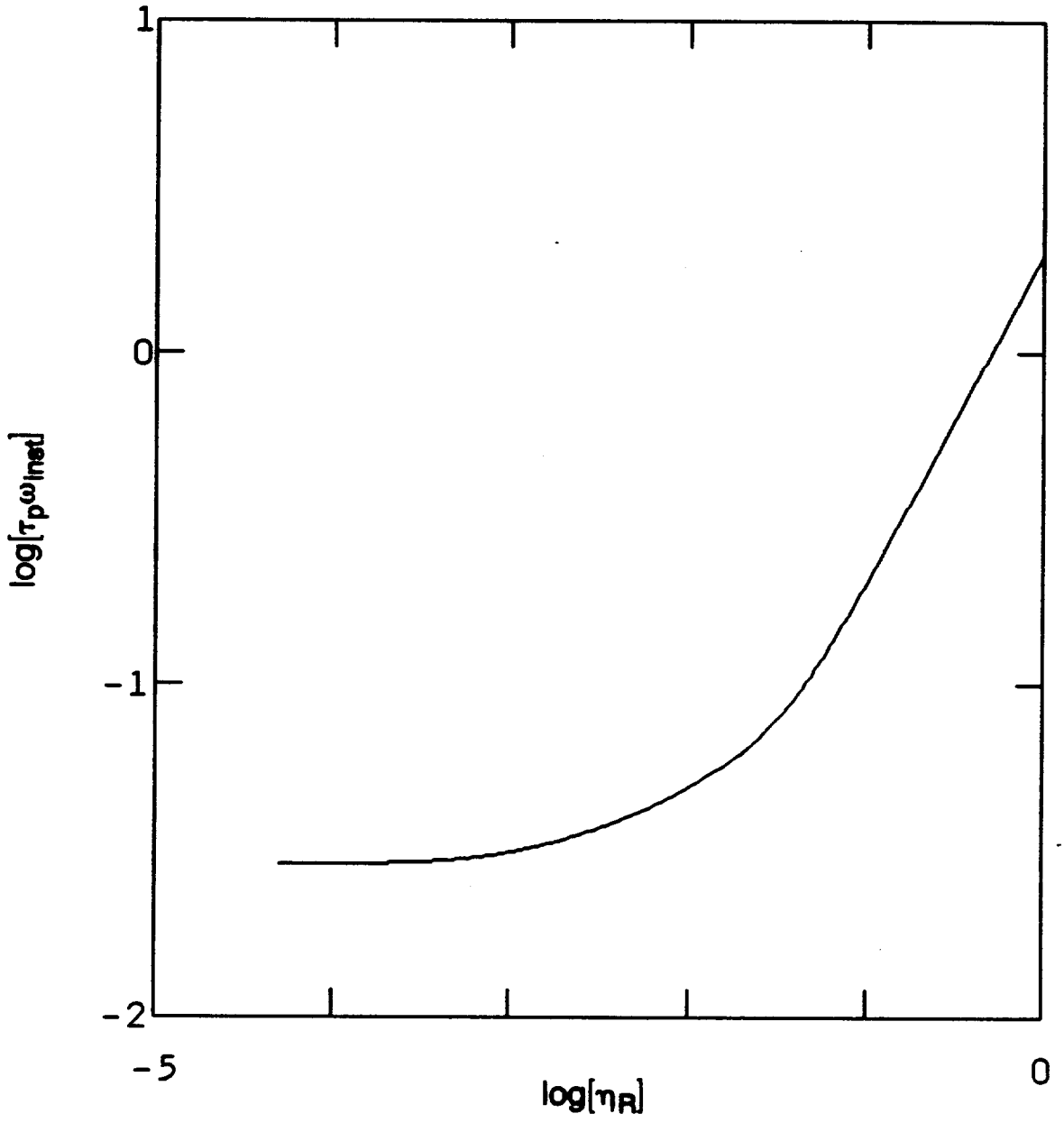

Figure 4.4.5 Frequency of the Onset of Instability

The angular frequency, normalized to the photon lifetime, of small oscillations about the out-of-phase equilibrium point is plotted along the out-of-phase stability boundary.

4.5 Dependence of η on Twin-Emitter Spacing

In the previous section, it was shown that η_R is proportional to the beat frequency and η_I is related to discrimination between the twin-emitter array modes. Since dynamical behavior depends sensitively on η, it is highly desirable to understand the dependence of η on design. In this section η will be related to the spacing of the emitters using a simple model of a twin-emitter array. The goodness-of-fit of the single-emitter mode expansion of the array modes, upon which the validity of the coupled-emitter model depends, will also be examined.

The twin-emitter is modeled as the five-layer slab waveguide shown in Figure 4.5.1. The layers are fictitious in that they represent abruptly-changing effective indices of the vertical waveguide, rather than real epitaxial features. Layers 2 and 4 have indices of refraction μ_1 and act as guides, while layers 1, 3 and 5 have indices of refraction $\mu_2 < \mu_1$ and act as clads. The indices of refraction are taken as real, and for the moment the waveguide is assumed to be lossless.

The lateral profile is obtained by solving (4.2.5), which in this case reduces to

$$\left[\frac{d^2}{dy^2}+\frac{\omega_\pm^2}{c^2}\mu^2(y)-K^2\right]f_\pm(y) = 0 \qquad (4.5.1)$$

This is easily solved for constant $\mu(y)$ within each layer, and solutions are matched at layer boundaries according to

$$f_\pm(\text{left}) = f_\pm(\text{right}) \qquad (4.5.2)$$

and

$$\frac{df_\pm}{dy}(\text{left}) = \frac{df_\pm}{dy}(\text{right}) \qquad (4.5.3)$$

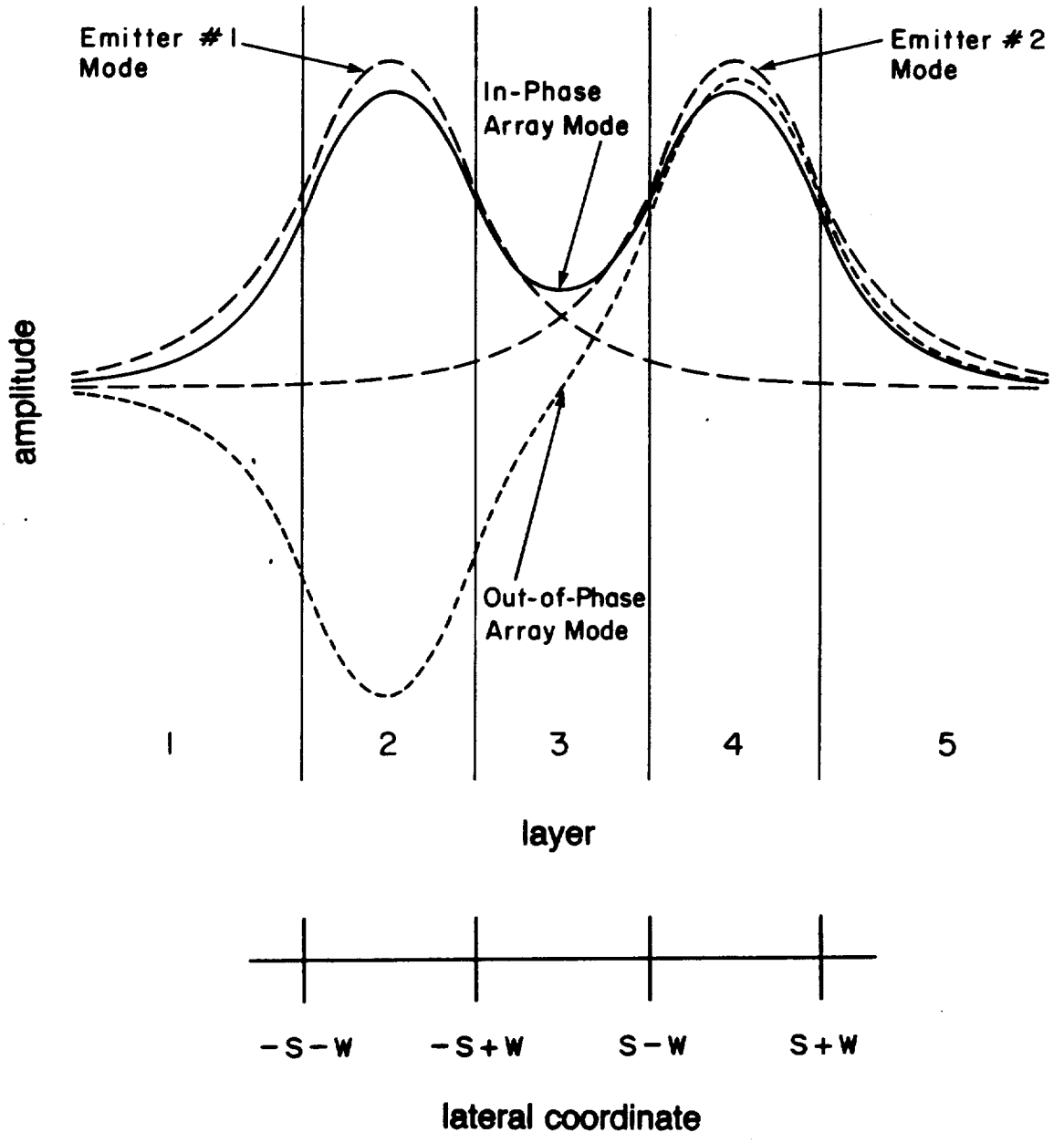

Figure 4.5.1 Five-Layer Dielectric Slab Waveguide

Layers 2 and 4 act as waveguides, and 1, 3 and 5 act as cladding layers. The exact (array) and approximate (emitter) lateral modes of the structure are shown.

which are obtained by integrating (4.5.1) over an infinitesimal interval straddling the boundary. To obtain the guided modes of the array we require that

$$K > \frac{\omega}{c}\mu_2 \tag{4.5.4}$$

Assuming that each guiding layer by itself can support only the fundamental mode limits the number of guided array modes to two. Making use of the symmetry of the structure about the y=0 plane, the guided array modes can be required to have the symmetry properties

$$\pm f_{\pm}(-y) = f_{\pm}(y) \tag{4.5.5}$$

Unnormalized solutions of (4.5.1)-(4.5.5) are

$$f_{+}(0<y<s-w) = H_{+}\cosh[\gamma_{+}y] \tag{4.5.6}$$

$$f_{-}(0<y<s-w) = H_{-}\sinh[\gamma_{-}y] \tag{4.5.7}$$

$$f_{\pm}(s-w<y<s+w) = C_{\pm}\cos[\kappa_{\pm}(y-s)] + S_{\pm}\sin[\kappa_{\pm}(y-s)] \tag{4.5.8}$$

$$f_{\pm}(s+w<y) = D_{\pm}\exp[\gamma_{\pm}(s+w-y)] \tag{4.5.9}$$

where

$$H_{\pm} \equiv \frac{\kappa_{\pm}w}{\cosh[\gamma_{\pm}(s-w)]} \tag{4.5.10}$$

$$C_{+} \equiv \gamma_{+}w\,\tanh[\gamma_{+}(s-w)]\sin[\kappa_{+}w] + \kappa_{+}w\,\cos[\kappa_{+}w] \tag{4.5.11}$$

$$C_{-} \equiv \gamma_{-}w\,\sin[\kappa_{-}w] + \kappa_{-}w\,\tanh[\gamma_{-}(s-w)]\cos[\kappa_{-}w] \tag{4.5.12}$$

$$S_{+} \equiv \gamma_{+}w\,\tanh[\gamma_{+}(s-w)]\cos[\kappa_{+}w] - \kappa_{+}w\,\sin[\kappa_{+}w] \tag{4.5.13}$$

$$S_- \equiv \gamma_- w \cos[\kappa_- w] - \kappa_- w \tanh[\gamma_-(s-w)]\sin[\kappa_- w] \tag{4.5.14}$$

$$D_\pm \equiv C_\pm \cos[\kappa_\pm w] + S_\pm \sin[\kappa_\pm w] \tag{4.5.15}$$

where $\kappa_\pm$ is the lateral propagation factor in the guiding layers and $\gamma_\pm$ is the lateral decay factor in the cladding layers of the lateral modes. They are related by

$$(\kappa_\pm w)^2 + (\gamma_\pm w)^2 = \left[\frac{\omega_0}{c} w\right]^2 (\mu_1^2 - \mu_2^2) \equiv W^2 \tag{4.5.16}$$

and are solutions to

$$\tan[2\kappa_+ w] = \kappa_+ \gamma_+ \frac{1+\tanh[\gamma_+(s-w)]}{\kappa_+^2 - \gamma_+^2 \tanh[\gamma_+(s-w)]} \tag{4.5.17}$$

$$\tan[2\kappa_- w] = \kappa_- \gamma_- \frac{1+\tanh[\gamma_-(s-w)]}{\kappa_-^2 \tanh[\gamma_-(s-w)] - \gamma_-^2} \tag{4.5.18}$$

The modal eigenfrequencies are related to the propagation factor components by

$$\omega = \frac{c}{\mu_1}[K^2 + \kappa^2]^{1/2} \tag{4.5.19}$$

The eigenfrequencies and lateral profiles of the single-emitter (three layer) waveguide are also needed. These are conveniently obtained by letting $s \to \infty$ in the foregoing. Both (4.5.17) and (4.5.18) reduce to

$$\tan[\kappa_0 w] = \frac{\gamma_0 w}{\kappa_0 w} \tag{4.5.20}$$

which can be rewritten as

$$\kappa_0 w = W \cos[\kappa_0 w] \tag{4.5.21}$$

where W was defined in (4.5.16). Single lateral mode behavior of a single emitter can be assured by requiring that $W \leq \pi/2$. The unnormalized profile for emitter 1 (2)

centered at y=s (y=−s) is

$$f_{1(2)}(y<+(-)s-w) = \kappa_0 w \exp[\gamma_0(-(+)s+w+y)] \tag{4.5.22}$$

$$f_{1(2)}(+(-)s-w<y<+(-)s+w) = \frac{\kappa_0 w}{\cos[\kappa_0 w]}\cos[\kappa_0(y-(+)s)] \tag{4.5.23}$$

$$f_{1(2)}(+(-)s+w<y) = \kappa_0 w \exp[\gamma_0(+(-)s+w-y)] \tag{4.5.24}$$

which are the well-known symmetric three-layer waveguide solutions (see Section 2.3 of Reference [99]).

Finally, we require various overlap integrals of these modes.

$$\int_{-\infty}^{+\infty} \frac{dy}{w} f_{\pm}^2 = D_{\pm}^2 \frac{1}{\gamma_{\pm} w} + C_{\pm}^2 \left[2+\frac{\sin[2\kappa_{\pm} w]}{\kappa_{\pm} w}\right]$$

$$+ S_{\pm}^2 \left[2-\frac{\sin[2\kappa_{\pm} w]}{\kappa_{\pm} w}\right] + H_{\pm}^2 \left[\frac{\sinh[2\gamma_{\pm}(s-w)]}{2\gamma_{\pm} w} \pm (s/w-1)\right] \tag{4.5.25}$$

$$\int_{-\infty}^{+\infty} \frac{dy}{w} f_+ f_- = 0 \tag{4.5.26}$$

$$A_{1,1} = \int_{-\infty}^{+\infty} \frac{dy}{w} f_1^2 = \frac{(\kappa_0 w)^2}{\gamma_0 w} + W\cdot\sin[\kappa_0 w] + W^2 \tag{4.5.27}$$

$$A_{1,2} = \int_{-\infty}^{+\infty} \frac{dy}{w} f_1 f_2 = (\kappa_0 w)^2 \exp[-2\gamma_0 s]\times$$

$$\left[\frac{1}{\gamma_0 w}+2\exp[2\gamma_0 w]\left(\frac{2\gamma_0 w}{W^2}+s/w-1\right)\right] \tag{4.5.28}$$

$$B_{1,1} = \int_{-\infty}^{+\infty} \frac{dy}{w} f_1 f_+ = D_+ \kappa_0 w \frac{1+\exp[-\gamma_0(2s)]}{(\gamma_0+\gamma_+)w} + \frac{2\kappa_0 w \exp[-\gamma_0(2s-w)]}{(\gamma_0 w)^2+(\kappa_+ w)^2} \times$$

$$[(\gamma_0 wC_+ - \kappa_+ wS_+)\sinh[\gamma_0 w]\cos[\kappa_+ w] + (\kappa_+ wC_+ + \gamma_0 wS_+)\cosh[\gamma_0 w]\sin[\kappa_+ w]]$$

$$+ H_+\kappa_0 w \exp[-\gamma_0(s-w)]\left[\frac{\sinh[(\gamma_0+\gamma_+)(s-w)]}{(\gamma_0+\gamma_+)w} + \frac{\sinh[(\gamma_0-\gamma_+)(s-w)]}{(\gamma_0-\gamma_+)w}\right]$$

$$+ C_+ W\left[\frac{\sin[(\kappa_0+\kappa_+)w]}{(\kappa_0+\kappa_+)w} + \frac{\sin[(\kappa_0-\kappa_+)w]}{(\kappa_0-\kappa_+)w}\right] \qquad (4.5.29)$$

$$B_{1,2} = \int_{-\infty}^{+\infty} \frac{dy}{w} f_1 f_- = D_-\kappa_0 w \frac{1-\exp[-\gamma_0(2s)]}{(\gamma_0+\gamma_-)w} - \frac{2\kappa_0 w \exp[-\gamma_0(2s-w)]}{(\gamma_0 w)^2+(\kappa_- w)^2} \times$$

$$[(\gamma_0 wC_- - \kappa_- wS_-)\sinh[\gamma_0 w]\cos[\kappa_- w] + (\kappa_- wC_- + \gamma_0 wS_-)\cosh[\gamma_0 w]\sin[\kappa_- w]]$$

$$+ H_-\kappa_0 w \exp[-\gamma_0(s-w)]\left[\frac{\sinh[(\gamma_0+\gamma_-)(s-w)]}{(\gamma_0+\gamma_-)w} - \frac{\sinh[(\gamma_0-\gamma_-)(s-w)]}{(\gamma_0-\gamma_-)w}\right]$$

$$+ C_- W\left[\frac{\sin[(\kappa_0+\kappa_-)w]}{(\kappa_0+\kappa_-)w} + \frac{\sin[(\kappa_0-\kappa_-)w]}{(\kappa_0-\kappa_-)w}\right] \qquad (4.5.30)$$

where A and B are the matrix elements described by (4.4.1)-(4.4.6). The orthogonality of the array modes is expressed by (4.5.26).

We are now in a position to determine the the real part of the coupling matrix η as a function of emitter spacing. Making the approximation

$$\omega_0 - \omega_\pm \approx \frac{\omega_0^2 - \omega_\pm^2}{2\omega_0} \qquad (4.5.31)$$

and using (4.5.19) in (4.4.8) gives

$$\eta_R = \frac{\tau_p}{4\omega_0}\left(\frac{c}{\mu_1}\right)^2 \begin{bmatrix} -\kappa_-^2 + 2\kappa_0^2 - \kappa_+^2 & \kappa_-^2 - \kappa_+^2 \\ \kappa_-^2 - \kappa_+^2 & -\kappa_-^2 + 2\kappa_0^2 - \kappa_+ \end{bmatrix} \qquad (4.5.32)$$

Figures 4.5.2-4.5.4 were generated using the FORTRAN program "five.guide.f", listed in Appendix H. Figure 4.5.2 plots the self-coupling (diagonal elements) and cross-coupling (off-diagonal elements) of the emitters as a function of s/w for W=π/2, w=3.5 μm and the parameters given in Table 2.6.1. The emitters touch to form a single emitter of width 4w when s/w=1. It is apparent that the self-coupling effect is indeed negligible. Since the real part of the cross-coupling coefficient η_R is always positive, the model predicts that the out-of-phase mode oscillates at a higher frequency than the in-phase mode regardless of emitter spacing, matching experiments.

The next task is to calculate the error made in fitting the single-emitter modes to the array modes. In the s$\rightarrow\infty$ limit, coupling is weak, and we expect the approximation of the array modes as linear combinations of single-emitter modes to be good. As s decreases, coupling increases and the best fit to the array modes becomes increasingly poor. The fit error may be defined as

$$Q_{\pm} \equiv \frac{\int_{-\infty}^{\infty} dy \; |f_{\pm} - C'_{\pm,1} f_1 - C'_{\pm,2} f_2|^2}{\int_{-\infty}^{\infty} dy \; |f_{\pm}|^2} \tag{4.5.33}$$

where $C'_{\pm,1(2)}$ are the best-fit coefficients defined by (4.3.5). We now assume that the in-phase array mode has unit amplitude and the out-of-phase array mode has zero amplitude, and use (4.3.6)-(4.3.9) to find the best fit at t=0, which is

$$C'_{+,1} = C'_{+,2} = \frac{B_{1,1}}{A_{1,1}+A_{1,2}} \tag{4.5.34}$$

Making the opposite assumption gives

$$C'_{-,1} = -C'_{-,2} = \frac{B_{1,2}}{A_{1,1}-A_{1,2}} \tag{4.5.35}$$

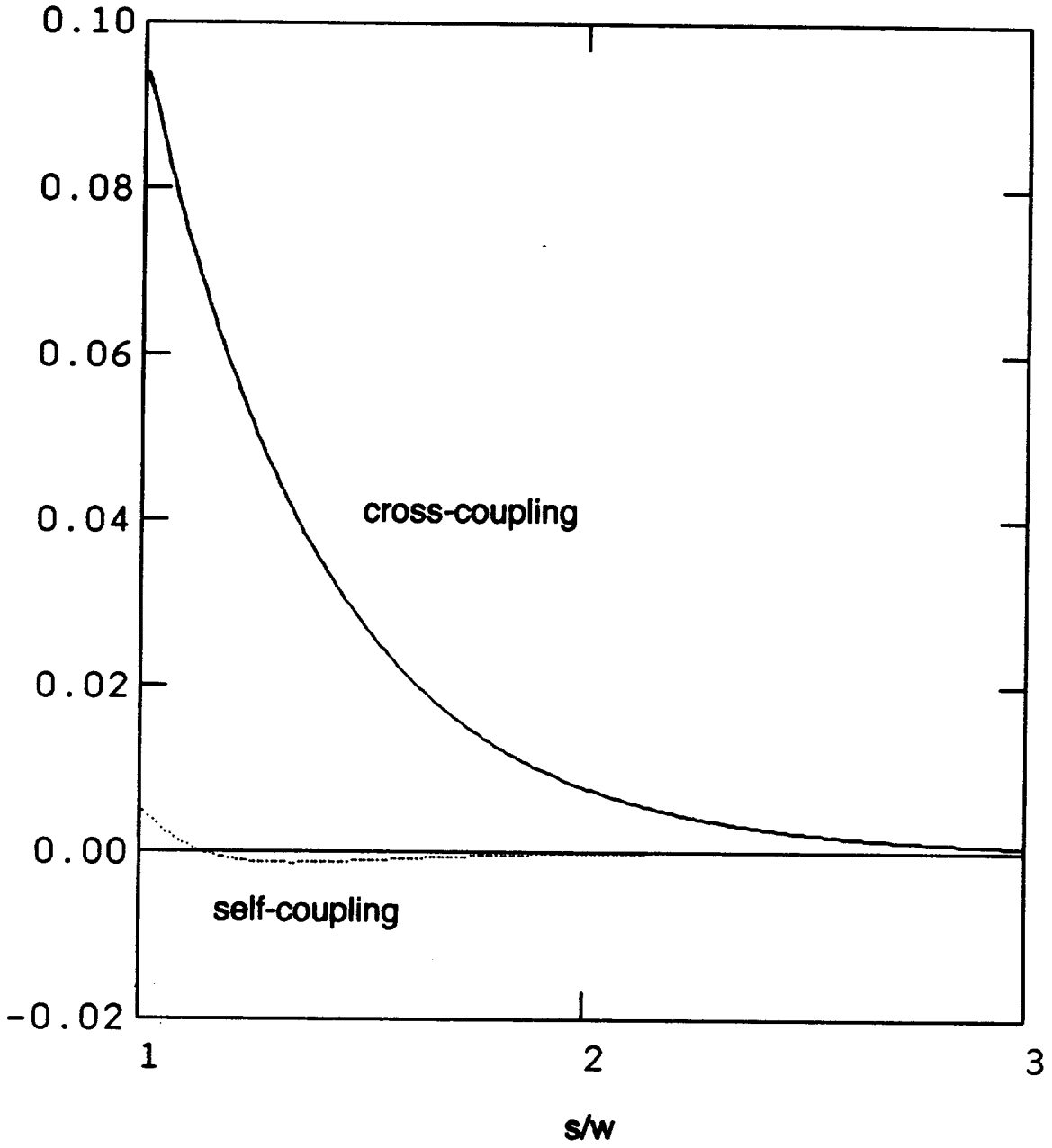

Figure 4.5.2 Emitter Self- and Cross-Coupling

The diagonal (self-coupling) and off-diagonal (cross-coupling) elements of the five-layer dielectric-slab coupling matrix are plotted against emitter spacing normalized to the emitter width. Self-coupling is found to be negligible.

Substituting these into (4.5.33) and integrating gives

$$Q_+ = 1 - \frac{2B_{1,1}^2}{(A_{1,1}+A_{1,2})\int_{-\infty}^{\infty} dy \ |f_+|^2} \tag{4.5.36}$$

and

$$Q_- = 1 - \frac{2B_{1,2}^2}{(A_{1,1}-A_{1,2})\int_{-\infty}^{\infty} dy \ |f_-|^2} \tag{4.5.37}$$

These are plotted against η_R in Figure 4.5.3, using s/w as an adjustable parameter. It can be seen that the fit grows worse $\propto\eta_R^2$, such that $Q>10$ % for $\eta_R=0.1$, giving a qualitative indication of the validity range of the model.

To obtain η_I, we violate the passive waveguide assumption by allowing gain $\tilde{g}_1>0$ in the guiding layers and loss $\tilde{g}_2<0$ in the cladding layers, but assume that the mode profiles and frequencies are unaffected by these perturbations. $\tilde{g}_1$ and $\tilde{g}_2$ are normalized to the photon lifetime τ_p. The net gain of a mode is given by

$$\tau_p \frac{d}{dt} C = \frac{1}{2}[\Gamma\tilde{g}_1+(1-\Gamma)\tilde{g}_2]C \tag{4.5.38}$$

where Γ is the lateral mode confinement factor

$$\Gamma \equiv \frac{\int_{s-w}^{s+w} dy \ |f|^2}{\int_0^{\infty} dy \ |f|^2} \tag{4.5.39}$$

We assume that the clads have uniform loss equal to the inverse of the photon lifetime, independent of the injection current to the guides. Therefore

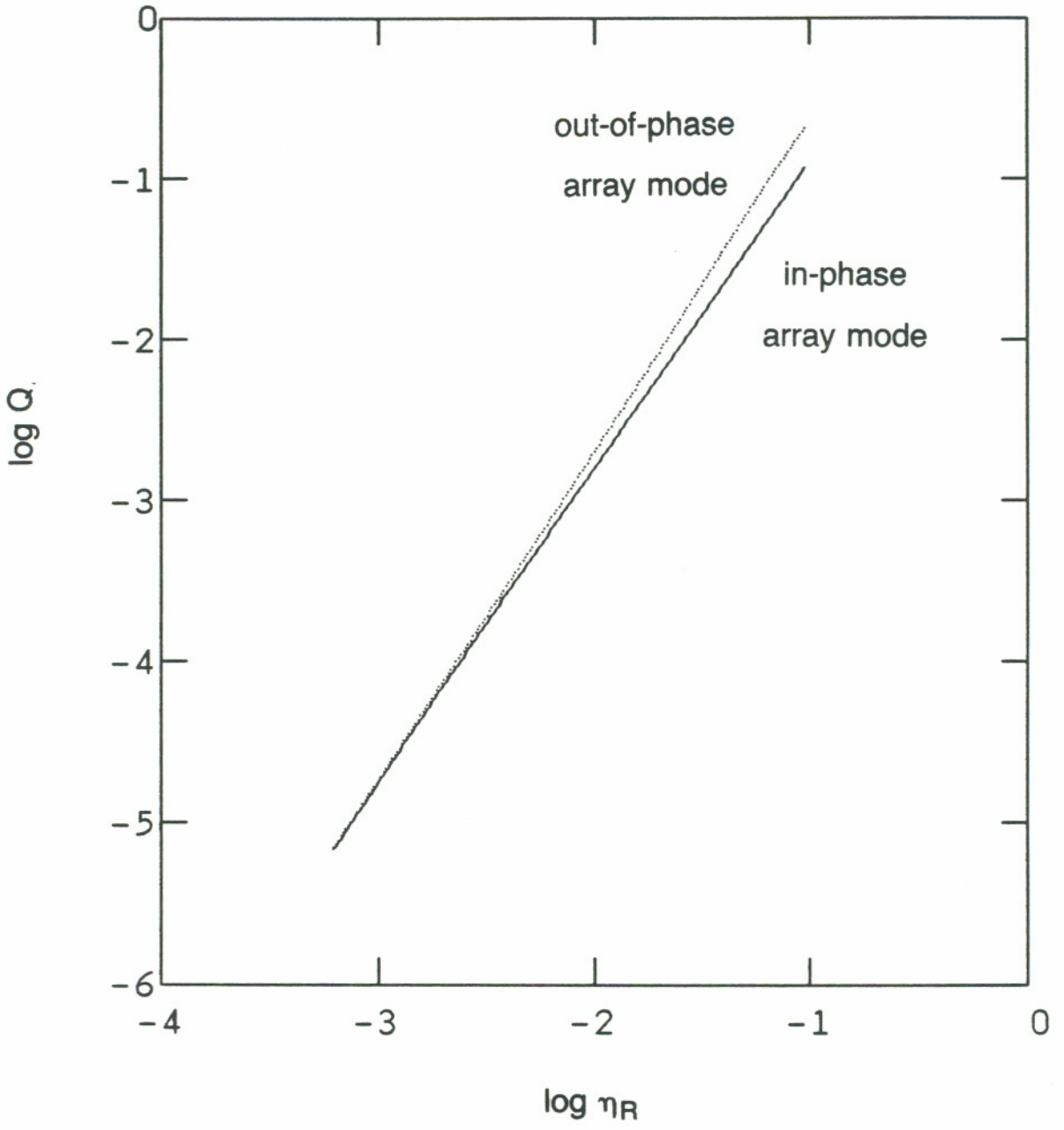

Figure 4.5.3 Fitting Error as a Function of Coupling

The error in fitting the emitter modes to the array modes grows as the square of the coupling, showing that the twin-emitter model begins to break down as η_R exceeds 0.1.

$$\tilde{g}_2 = -1 \tag{4.5.40}$$

Next we assume that

$$\Gamma_+ > \Gamma_- \tag{4.5.41}$$

and that the in-phase mode is in equilibrium with a net gain of zero. Then

$$\tilde{g}_1 = \frac{1-\Gamma_+}{\Gamma_+} \tag{4.5.42}$$

The net gain of the out-of-phase mode is negative, thus it will die out as $t\to\infty$, leaving the pure in-phase mode. In that case, we can identify the modal amplitude with the amplitude of each emitter. The opposite argument can be made by reversing the sense of (4.5.41). In either case we can identify $Z^{(0)}$ with the net gain experienced by the single-emitter mode as

$$\frac{1}{2}\frac{\Gamma_0-\Gamma_\pm}{\Gamma_\pm} = Z^{(0)} = \eta_I \cos\theta^{(0)} \tag{4.5.43}$$

where (4.4.21) was invoked and the confinement factor of the dominant mode is intended to be chosen. $\Gamma_\pm$ can be found from (4.5.25) by dividing the sum of the "C" and "S" terms by the entire right-hand side. Similarly, Γ_0 can be found from (4.5.27) by dividing the sum of the "W" terms by the entire right-hand side.

Figure 4.5.4 plots both η_R and η_I as functions of s/w. At large spacing η_I is positive, which means that the out-of-phase mode is favored. This is physically reasonable since the out-of-phase mode has a node at y=0, and consequently less overlap with the wide, lossy region between the guides than does the in-phase mode. For closely-spaced emitters η_I is negative, favoring the in-phase mode. Apparently the severe curvature imposed on the out-of-phase mode by requiring it to change sign in

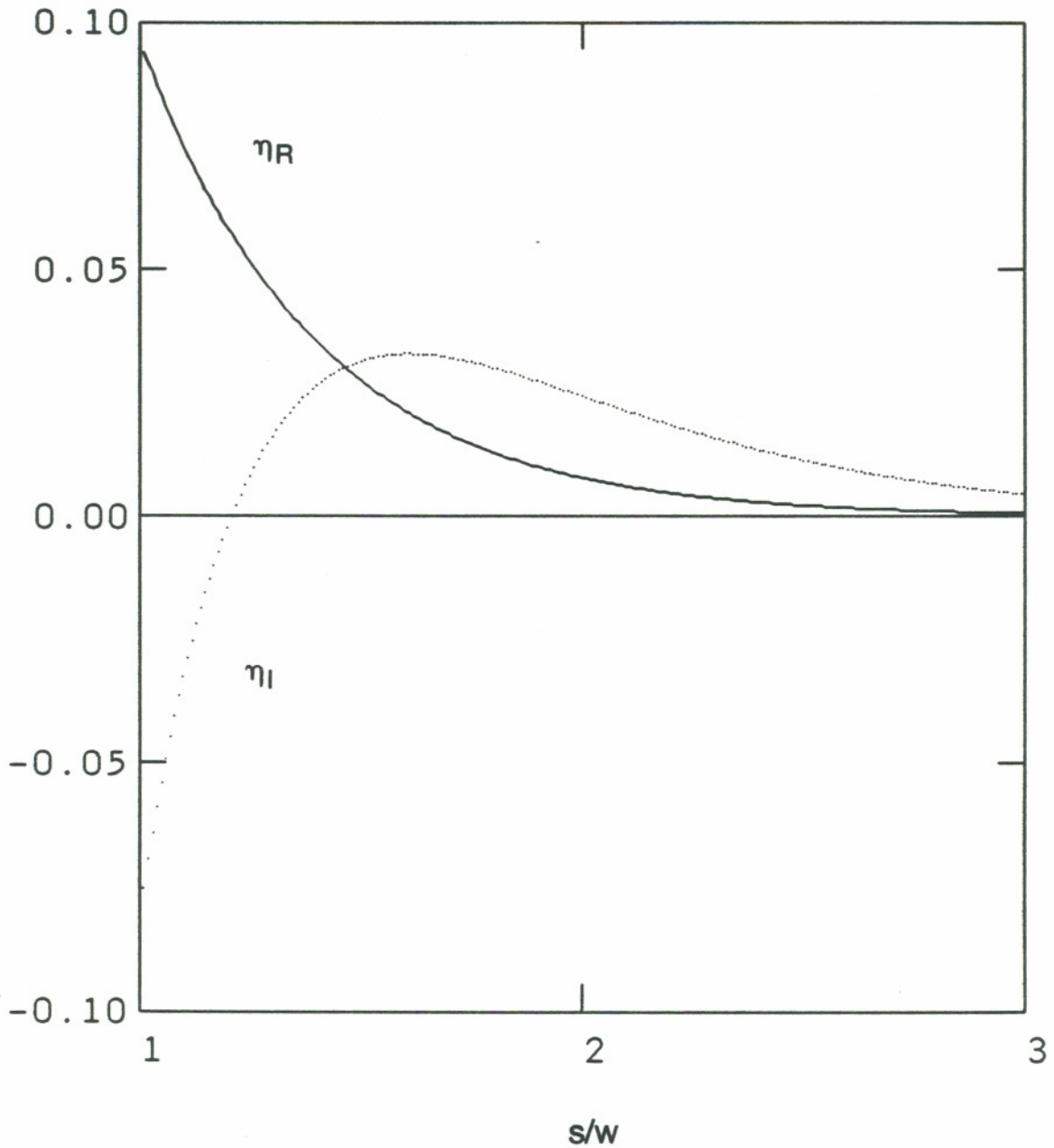

Figure 4.5.4 Real and Imaginary Parts of the Coupling Parameter

$\eta_R>0$ corresponds to the observation that the out-of-phase mode has a shorter wavelength than the in-phase mode. η_I changing sign implies that the in-phase (out-of-phase) mode is favored by strong (weak) coupling.

the narrow central region causes it to have large tails in the outer lossy regions which reduce the net gain.

The values for η_R and η_I obtained using this model are significantly smaller than the value measured for the device[21] whose parameters were used to generate the numerical results of this section. The author believes that this discrepancy can be attributed to the comparison of a gain-guided device, whose curved wavefronts presumably cause more rapid "communication" between the emitters, to an index-guided model with flat wavefronts. Nevertheless, the $\eta(s/w)$ features discussed above are probably general, and indicate that considerable control of the coupling coefficient is available to the designer. In the actual design process, a numerical calculation appropriate to the device geometry can be used[15] to determine η as a function of the design parameters.

At least two other coupling constants, κ and c, appear in the literature[14,15]. These are proportional to each other and to η. It may be noted that there is a difference in sign between the relations of η and c to the relative frequency and gain of the array modes. A more serious conflict becomes apparent when comparing Figure 4.5.4 to Figure 4 of Reference [15], where it is the real part c_r that changes sign as the emitter separation is varied. This cannot be explained as a relative factor of i between the definitions of η and c, because in both cases the real (imaginary) parts are proportional to the frequency (gain) splitting of the array modes.

5. NUMERICAL INTEGRATION OF THE TWIN-EMITTER MODEL

5.1 Chapter Overview

The twin-emitter rate equations (4.4.14)-(4.4.18) cannot be integrated analytically without simplification, which is a perilous undertaking with non-linear equations because seemingly minor modifications can yield results that are not even approximately similar to the true solution. Numerical integration offers the only hope of exploring the dynamics of the model in any depth. The fundamental analytical result of Section 4.4, the stability boundaries, barely scratch the surface of the subject. In fact, since their basin of attraction is not known, the probability of convergence to a stable equilibrium point starting from arbitrary initial conditions may be so small as to make that equilibrium point negligible.

On the other hand, numerical integrations require a considerable amount of computer time, and must be done separately for each set of device parameters, operating point and initial conditions, whereas analytical results establish continuous regions of dynamical behavior in the parameter space with few computations. Thus, the techniques are complementary.

Section 5.2 describes the FORTRAN program "twostrip.for" used to numerically integrate the twin-emitter rate equations. Section 5.3 discusses the results in a

qualitative manner. The predictions of Section 4.4, summarized in Figures 4.4.3-4.4.5, are verified, and several interesting dynamical regimes within the unstable region are identified.

5.2 Numerical Integration

The twin-emitter rate equations (4.4.14)-(4.4.18) were numerically integrated using the FORTRAN program "twostrip.for", whose source code is listed in Appendix H. A variable-order, variable step Gear method (NAG library routine "d02ebf") is used to integrate the equations, which are quite stiff because (4.4.14)-(4.4.16) vary on a time scale characterized by the photon lifetime τ_p, while the dynamics of (4.4.17) and (4.4.18) are characterized by the carrier lifetime τ_s, and $\tau_p \ll \tau_s$. The integration routine refers to the user-defined subroutines "fcn" and "pederv", which specify the differential equations and their Jacobian matrix, respectively, and writes the integrated dynamical variables to output files using the subroutine "out".

Twostrip reads the file "twostrip.prm", which contains device parameters (except η), quantities specifying the injection current, the initial conditions and program control parameters. The program is designed to scan over multiple η values, which are read sequentially from the file "etatable.prm". Each η point is specified by a quadruplet of integers (sigfigr,tenpwrr,sigfigi,tenpwri), from which η is determined using

$$\eta_R = \frac{\pi[\tau_p \text{ in ps}]}{40} \cdot \text{lookup(sigfigr)} \cdot 10^{-\text{tenpwrr}} \tag{5.2.1}$$

where lookup(sigfigr) is given in the "twostrip.for" source code. An analogous expres-

sion is used to determine η_I. This rather arcane scheme insures that the modulation frequency, given by

$$\nu_{mod} = \frac{\eta_R}{\pi\tau_p} \tag{5.2.2}$$

for out-of-phase resonant modulation, is a multiple of 250 MHz and a divisor of 1 THz. This simplifies interpretation of the power spectra used in injection current modulation studies, which are calculated at increments of 250 MHz from 4000 consecutive data points spaced at 1 ps intervals.

The final preliminary task is to synthesize the output file names. These are of the form xx.yyyy, where xx specifies the dynamical variable (xx = x1, x2, th, z1 or z2) and yyyy is the η-specifying quadruplet discussed above. Actually, it is the intensities (X^2) and the phase shift normalized to π (θ/π) that are recorded in the appropriate output files.

If the injection current is modulated, the program searches for convergence of the dynamical variables to a limit cycle with a period equal to or a multiple of the modulation period. The multiple-modulation-period provision allows investigation of sub-harmonic response cycles. The search is accomplished by successive integration over the anticipated period of the response, and comparing the dynamical variables at the beginning and end of the period, according to a criterion with a preset tolerance. If the system converges to a limit cycle or a preset number of iterations is exceeded, the program proceeds to the output stage. The convergence search can be bypassed in the case of unmodulated injection current by setting the iteration limit to zero. In the output stage, 80 ns of the dynamical variable time series are recorded, at every 1 ps.

5.3 Qualitative Behavior

In this section, the behavior of the numerically-integrated twin-emitter rate equations is studied as a function of device parameters. The asymptotic behavior is of particular interest, since the details of the transient dynamics are specific to the somewhat arbitrary choice of initial conditions.

The device parameters α, τ_p and τ_s and the normalized injection current $p^{(0)}$ are fixed, and the coupling parameter is allowed to vary as in Section 4.4. Spontaneous emission was included by using $\beta=1.6\times10^{-4}$ from Table 2.6.2, but both gain compression and the stochastic contribution of spontaneous emission were neglected in the early version of "twostrip.for" used to generate the time series shown in this section. The initial values of the dynamical variables were set vanishingly close to the in-phase equilibrium point, presumably making convergence to the out-of-phase equilibrium point as unlikely as possible. This was done to find the basin of attraction of the out-of-phase equilibrium point, which is of interest for high-frequency injection current modulation (Chapter 8).

Although the following discussion is essentially qualitative, several quantitative tools were used to gain insight into the often complicated behavior of the modeled time series. The most useful is the power spectrum $W_S(\omega)$, defined as the absolute square of the Fourier transform of the time series. Because of the finite length of the time series, a discrete Fourier transform (DFT) is used.

A second characteristic of a time series is its autocorrelation function, defined as

$$C(\tau) \equiv \frac{\int_{-\infty}^{\infty} dt\, I(t+\tau)I(t)}{\int_{-\infty}^{\infty} dt\, I^2(t)} \tag{5.3.1}$$

for the (real) intensity I, and related to the power spectrum by

$$W_S(\omega) \propto \int_{-\infty}^{\infty} d\tau \, e^{-i\omega\tau} C(\tau) \tag{5.3.2}$$

A third characteristic, not directly related to the others, is the set of all local maxima of the intensity time series, here referred to as the "bifurcation set". FORTRAN programs for calculating the power spectrum, autocorrelation and bifurcation set of time series are listed in Appendix H.

Four types of asymptotic behavior are encountered in the modeled time series: quiescent, periodic, quasi-periodic and erratic. Quiescence is the approach to a stable equilibrium point. Periodicity implies limiting behavior that repeats after some characteristic time, i.e. a limit cycle, while quasi-periodicity is characterized by two or more incommensurate frequencies. "Erratic" covers all the more complicated and disorderly dynamics not classified above. Erratic behavior may or may not be chaotic, depending on whether sensitivity to initial conditions exists. Since this thesis makes no attempt to rigorously demonstrate the presence of deterministic chaos, the neutral term "erratic" is used. It should be stressed, however, that the twin-emitter model used in this chapter is entirely deterministic, and it is quite probable that some of behavior called erratic is in fact chaotic.

In principle, one can distinguish the four types of dynamics from their power spectra. Quiescence has only a zero-frequency component, periodicity has a fundamental and possibly its harmonics, quasi-periodicity has two or more fundamental and their harmonics and erraticity is characterized by a broad spectrum. In practice, if the time series is short, the frequency resolution of the DFT, which is the inverse of the time series length, may be so coarse as to prevent interpretation of a complicated

quasi-periodic or erratic spectrum. For the modeled time series discussed here, the frequency resolution of 12.5 MHz is more than adequate, so that the autocorrelation and bifurcation set yield no additional information and will not be discussed further.

The primary goal is to verify the stability boundaries found in Section 4.4. Other goals include comparing observed frequency components with those predicted in Figure 4.4.5, mapping behavioral regimes in the unstable region and investigating transient dynamics. For the remainder of this section, the coupling parameter is written (η_R,η_I).

Figure 5.3.1 shows the quadrant of the complex-η plane containing the in-phase mode stability boundary. This analytically-predicted boundary was verified by integrating the twin-emitter rate equations for the coupling parameters (.01,−.1), (.02,−.1) and (.03,−.1), shown as crosses in Figure 5.3.1. The intensity of emitter 1 for (.01,−.1), (.02,−.1) and (.03,−.1) are shown in Figures 5.3.2 and 5.3.3, 5.3.4 and 5.3.5, and 5.3.6 and 5.3.7, respectively. Each pair of figures show the entire 0−80 ns time window and the final 4 ns, presumably the asymptotic dynamics. (.01,−.1) is in the in-phase stability region. This is supported by the rapid damping of the intensity, as seen in Figure 5.3.2, and the relative phase to $\theta=0$.

Figure 5.3.4 describes the behavior of (.02,−.1), just inside the unstable region. Intermittent bursts of erratic behavior continue throughout the 80 ns window. The non-oscillatory exponential divergence of the intensity from its nearly-stable equilibrium value, occurring from 44 ns to 47 ns, supports the Section 4.4 prediction that the frequency of incipient instability is zero upon crossing the in-phase stability boundary. Figure 5.3.5 shows a jagged spike stimulated by mode competition, followed by ordinary relaxation oscillations and another jagged spike. The emitter

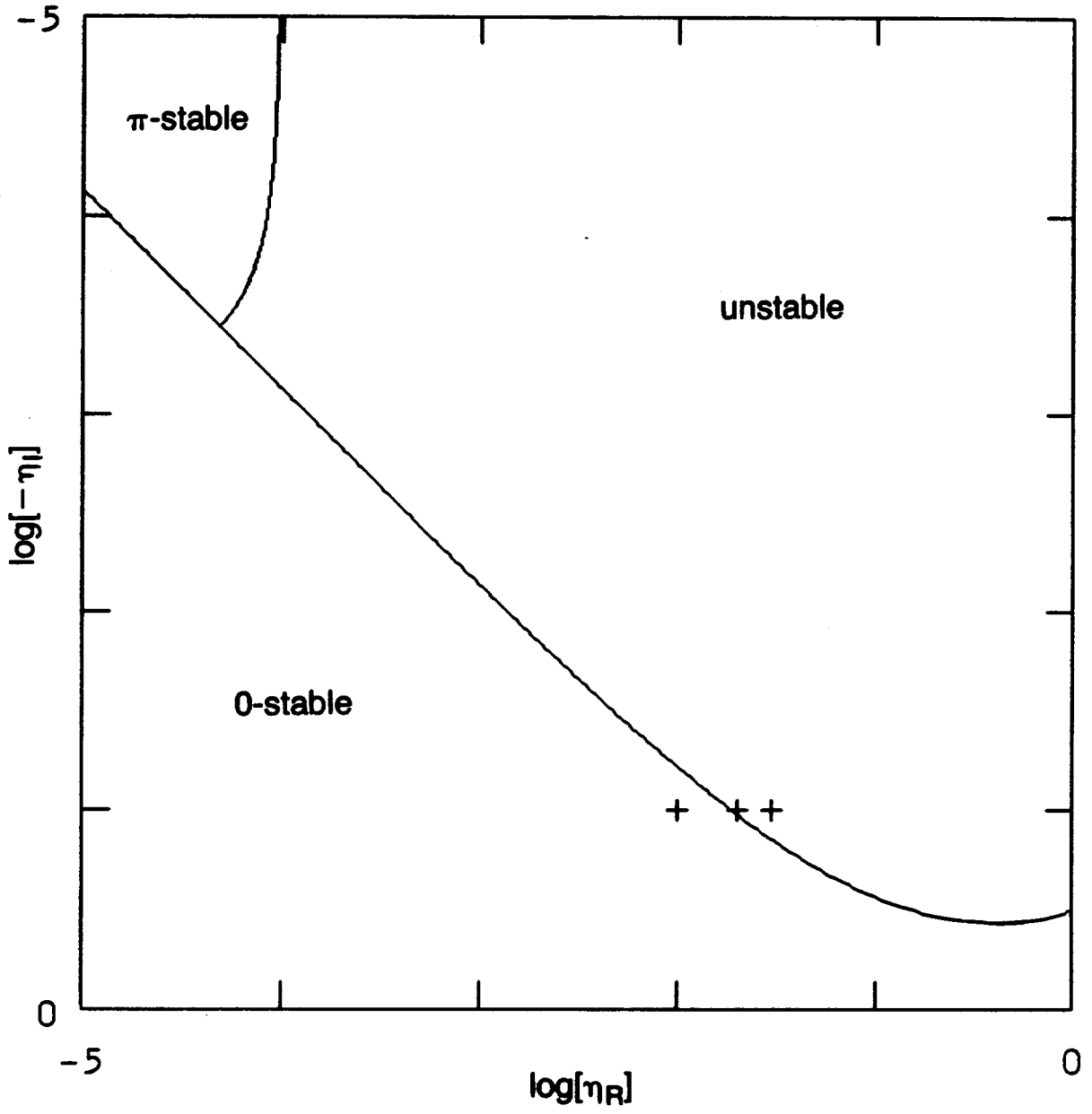

Figure 5.3.1 Stability Boundary Verification

The in-phase mode stability boundary is verified by numerical integration of the twin-emitter rate equations for the complex-η points denoted by crosses in the figure. The intensity time series are shown in Figures 5.3.2-7.

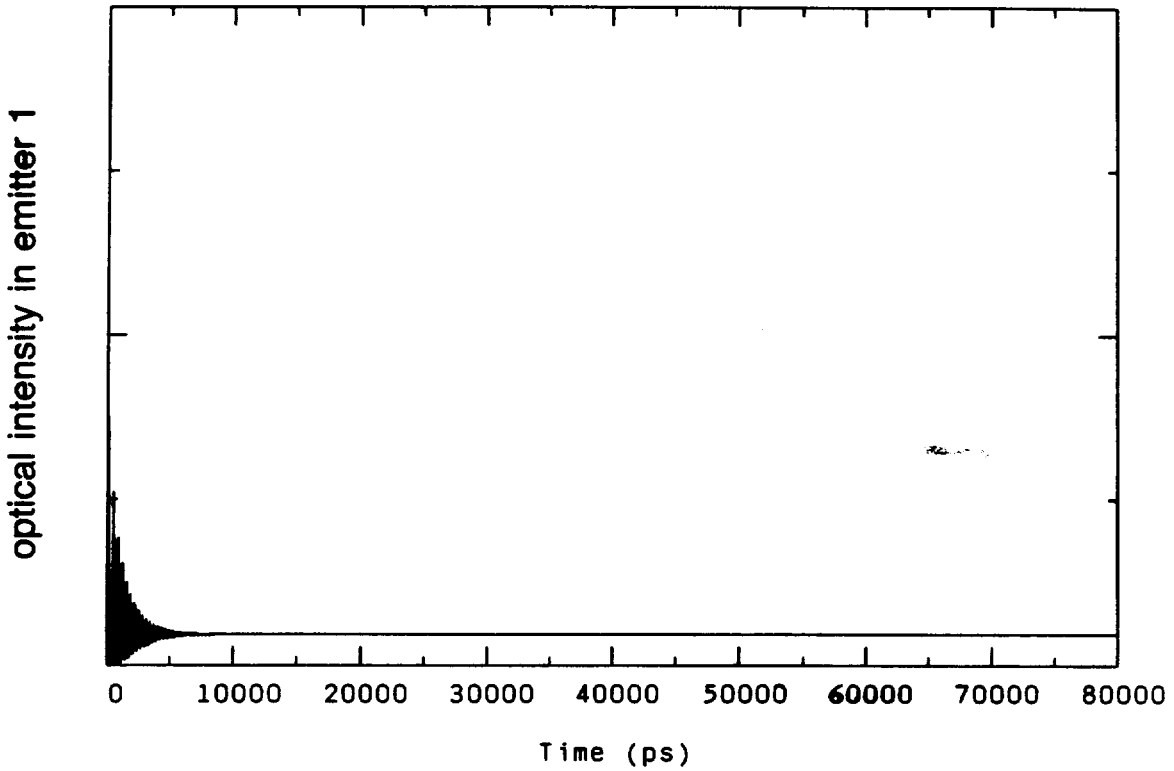

Figure 5.3.2 Intensity Time Series, $\eta=(.01,-.1)$, 0−80 ns

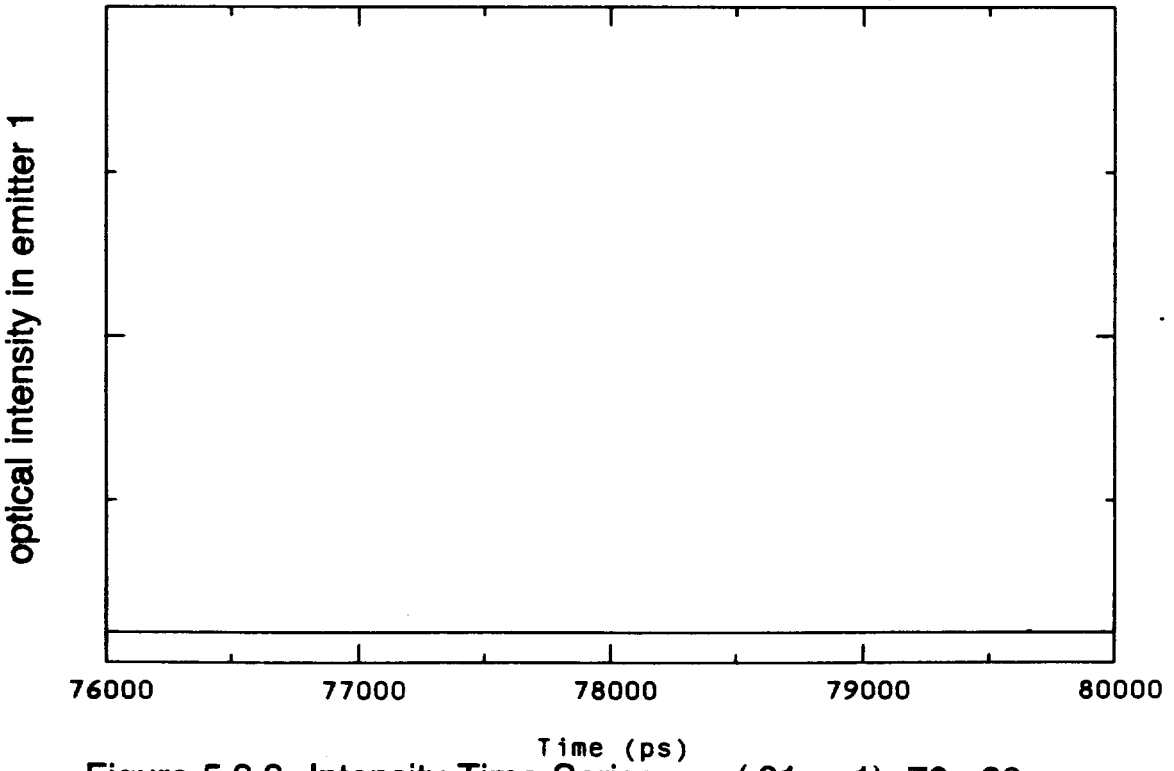

Figure 5.3.3 Intensity Time Series, $\eta=(.01,-.1)$, 76−80 ns

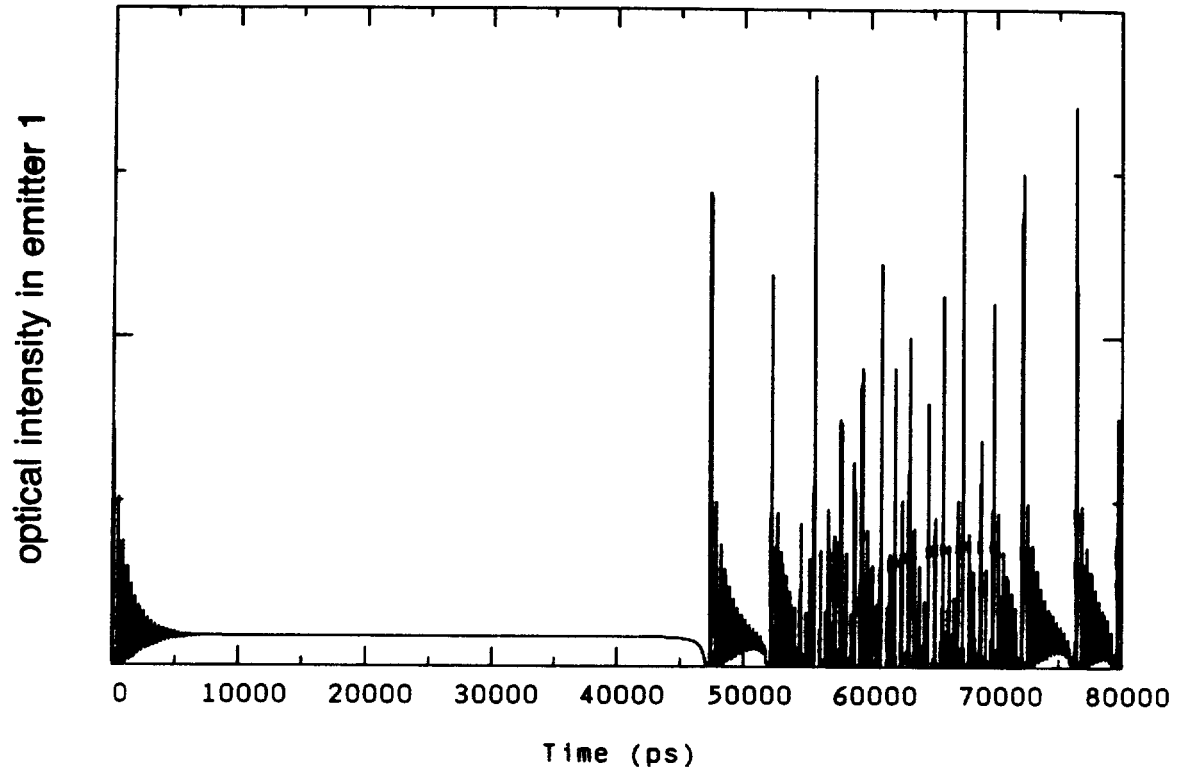

Figure 5.3.4 Intensity Time Series, $\eta=(.02,-.1)$, 0−80 ns

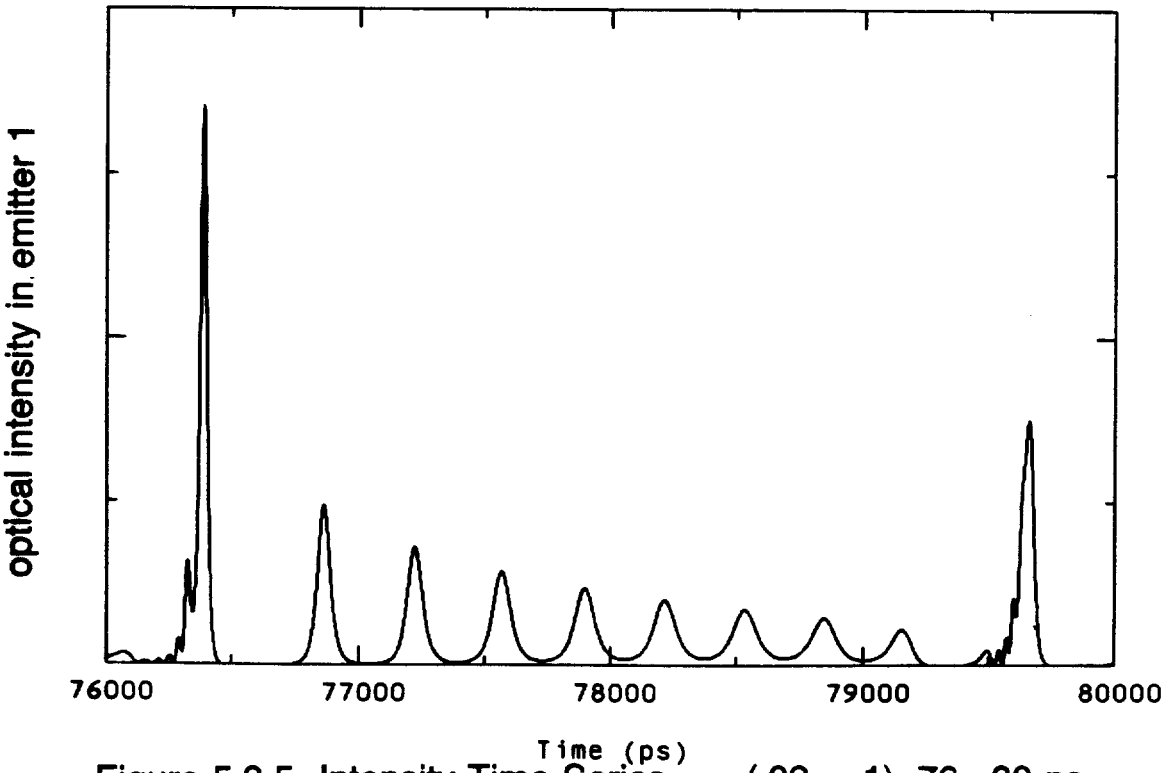

Figure 5.3.5 Intensity Time Series, $\eta=(.02,-.1)$, 76−80 ns

intensities were synchronized.

(.03,−.1) is farther inside the unstable region, so it is surprising that periodicity emerges at about 15 ns in Figure 5.3.6. Actually, although the emitter intensities and gains are periodic, θ changes by 2π per period. This asymptotic behavior is referred to here as an "unbound" limit cycle and is analogous to orbits outside the separatrix of a simple pendulum. These are true limit cycles because θ mod 2π, the quantity of physical significance, is periodic. The constant slippage of θ can be interpreted as indicating that one emitter is lasing at a higher average frequency than the other. The observed frequency of 24.2 GHz, shown in Figure 5.3.7, is not predicted in Section 4.4. The emitter intensities are synchronized.

Figure 5.3.8 shows some interesting dynamical regimes in the unstable region of the complex-η plane. Solid line segments contain at least two test points for which the twin-emitter rate equations were integrated numerically, but only the end points are shown for clarity. All the points tested along solid line segments, including the end points, were found to have the same qualitative behavior. Dotted segments indicate that the end points have the same behavior, which is presumed to exist along the dotted segment, although no intermediate points were investigated.

(.0003,.001)-(.001,.001) lie within a "bound" limit cycle regime (B), in which θ oscillates about π but never escapes, analogous to orbits inside the separatrix of a simple pendulum. Plots of the dynamical variables show many interesting patterns, but coupling is so small as to be of no practical importance, since phase-locking of the "twin" emitters is easily disrupted by slight emitter dissimilarities and spontaneous emission noise in a real device. Thus, an extended discussion is omitted for brevity. This regime is assumed to extend along the stability boundary as shown in Fig-

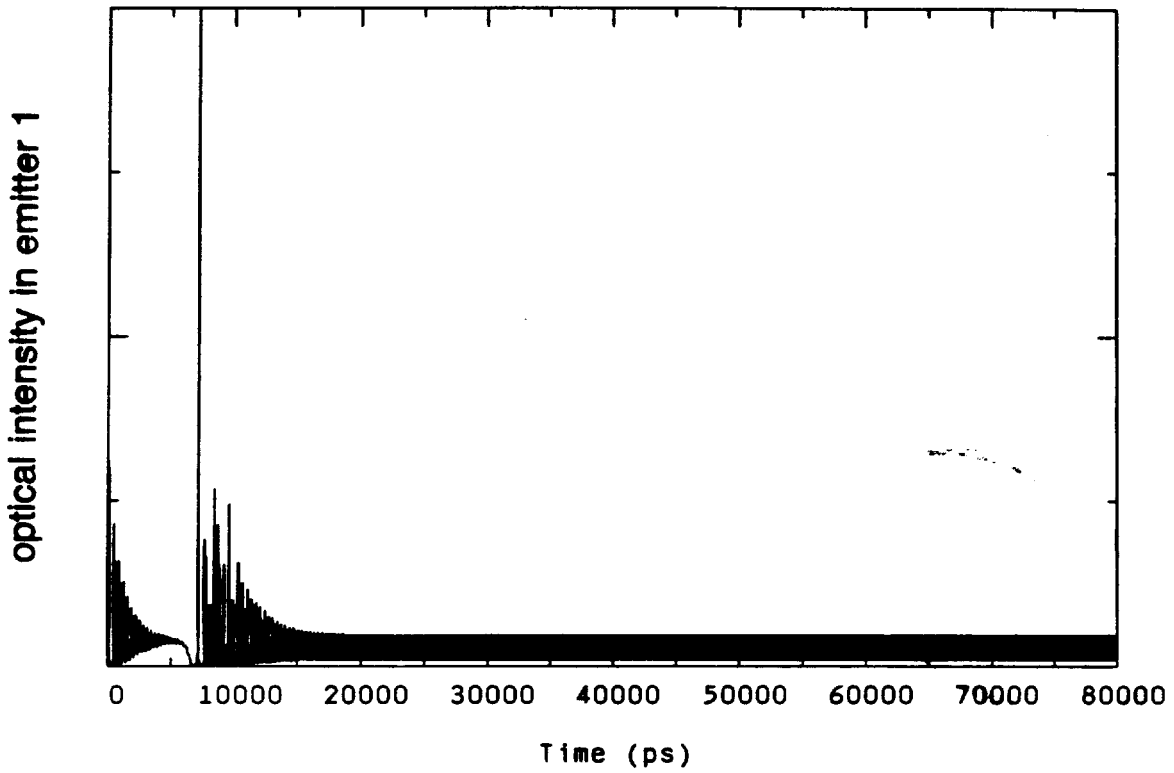

Figure 5.3.6 Intensity Time Series, $\eta=(.03,-.1)$, 0−80 ns

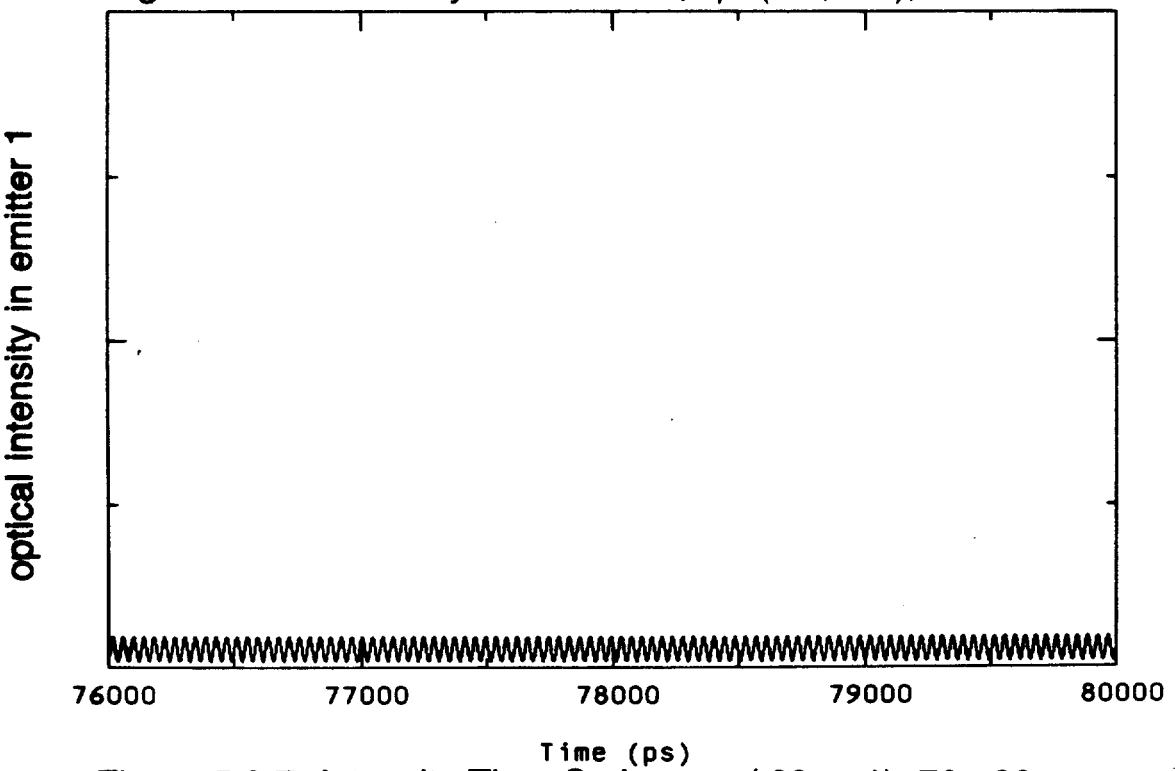

Figure 5.3.7 Intensity Time Series, $\eta=(.03,-.1)$, 76−80 ns

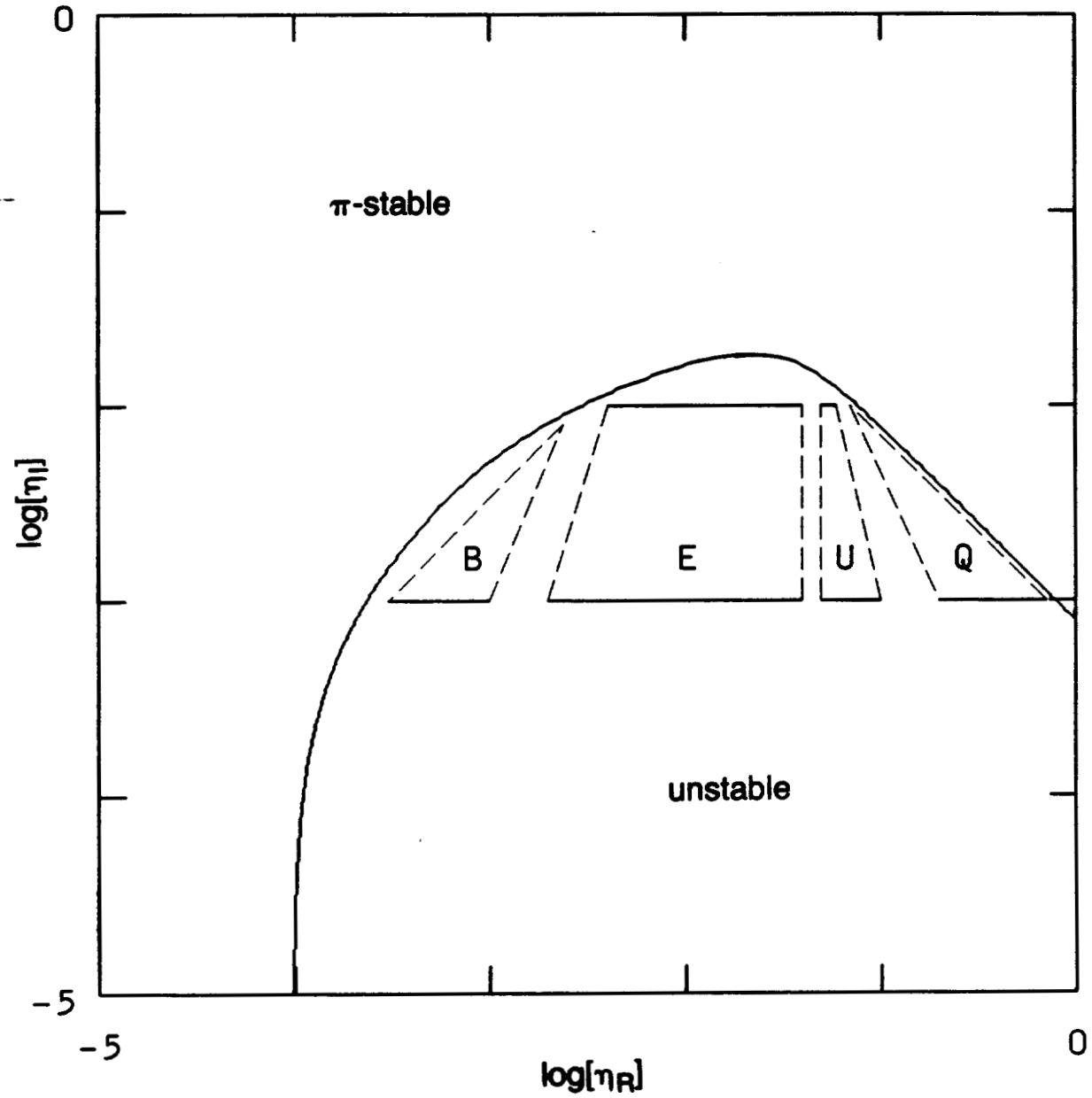

Figure 5.3.8 Dynamical Regimes of the Twin-Emitter Model

Bound limit cycle (B), erratic (E), unbound limit cycle (U) and quasi-periodic (Q) dynamical regimes were found in the unstable region by numerical integration of the twin-emitter rate equations.

ure 5.3.8, although no η_I=.01 points with this behavior were observed.

(.004,.01)-(.04,.01) and (.002,.001)-(.04,.001) lie within an erratic regime (E), characterized by broad (20 GHz) power spectra not foreseen in the analyses of Section 4.4. Their intensity time series are even more erratic than the latter half of Figure 5.3.4.

(.05-.01)-(.06,.01) and (.05,.001)-(.1,.001) lie within an unbound limit cycle regime (U). The frequencies of oscillation match those predicted in Figure 4.4.5. The emitter intensities are anti-synchronized.

(.07,.01) and (.2,.001)-(.7,.001) lie within a quasi-periodic regime (Q). The power spectra show five or more frequencies clustered in a narrow band about the modal beat frequency. The behavior of θ is quite interesting and is shown for (.6,.001) in Figure 5.3.9. The large jumps occur from states in which θ oscillates about 0 to states in which θ oscillates about π. The π state is unstable, and the initially small oscillations grow until θ slips into one of the two neighboring 0 states. Here the oscillations dampen, giving the appearance of approach to equilibrium. Suddenly, θ jumps to a distant π state, and the process continues indefinitely.

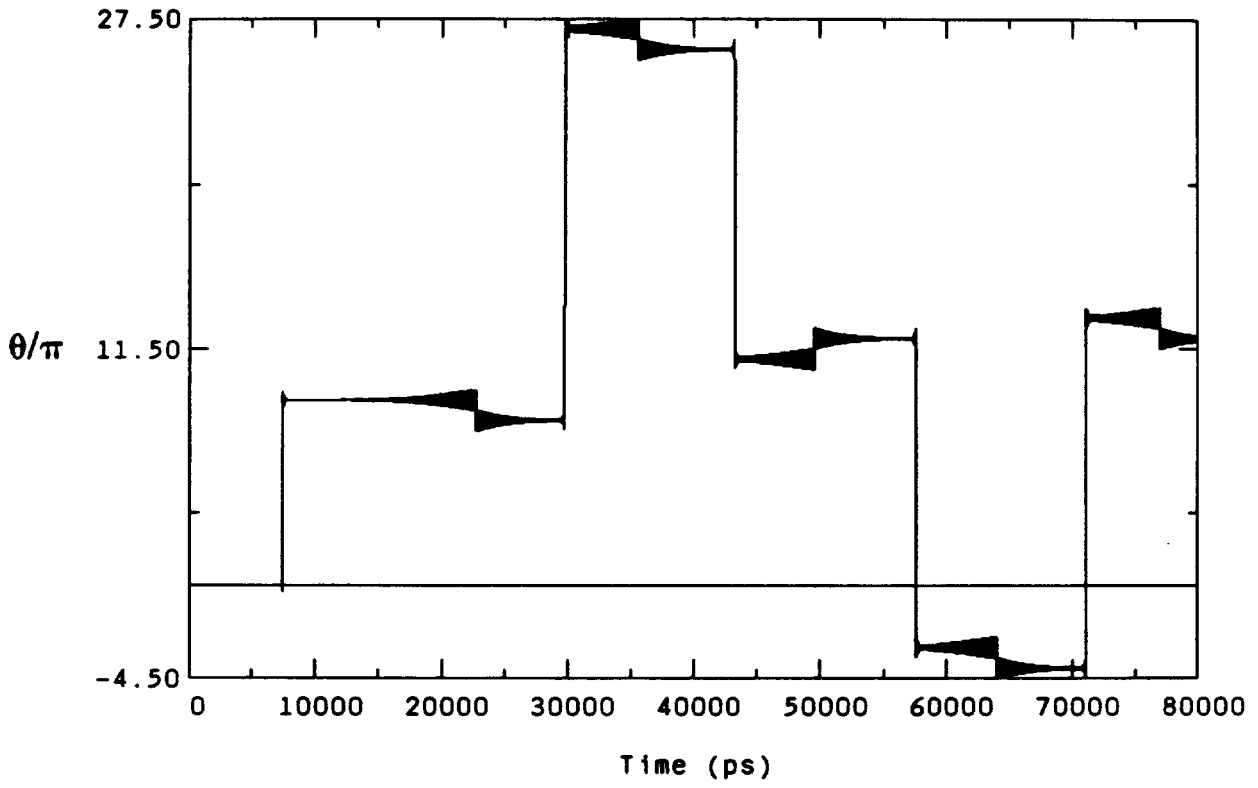

Figure 5.3.9 Relative Phase Time Series, $\eta=(.6,.001)$

The peculiar behavior of the emitter relative phase for a point in the quasi-periodic (Q) dynamical regime.

6. CHARACTERIZATION OF COHERENT ARRAYS

6.1 Chapter Overview

This chapter introduces the techniques used in this work to characterize coherent semiconductor laser arrays. Characterization encompasses both qualitative behavior, observable in the spectrally- and temporally-resolved near-fields, and the measurement of the parameters appearing in the theory. The four-stripe device PGE4600B#1D4, hereafter referred to as "1D4", is used as an example throughout the chapter. 1D4 was studied because its lateral modes resembled those expected from weakly-coupled twin-emitter theory more than did the modes of any of the two-stripe devices tested, which proved to be strongly-coupled. Justification for using 1D4 to test twin-emitter theory is provided in Section 7.2 and Appendix F. The origin and preparation of 1D4 and other devices is discussed in Section 7.1

The parameters fall into three classes, depending on their importance in the model. The photon lifetime τ_p, the differential gain $[\partial G/\partial N]_{th}$, the linewidth-enhancement factor α and the coupling parameter η are crucial, and are each accorded a separate section in the chapter. The carrier lifetime τ_s is needed to establish some points of the theory, but is not necessary in obtaining the in-phase lateral mode stability boundary, given by (4.4.33). Since the stability of the in-phase mode

is the only feature of the theory compared to experiment in this thesis, τ_s was not measured. Finally, the spontaneous emission factor β and the gain compression factor S_{shb} have been neglected in the analyses of Section 4.4, so their measurement was not attempted.

The parameters listed above are derived quantities, and an effort was made to write them in terms of easily- and accurately-measurable "primary" quantities, rather than other derived quantities, to avoid compounding errors. Examples of primary quantities include the injection current J, the emission wavelength λ, the longitudinal mode spacing $\Delta\lambda$ and the device length L. Examples of quantities that were avoided include the effective group index $\mu_{g,e}$, which can be written in terms of λ, $\Delta\lambda$ and L, and the vertical mode confinement factor Γ, which is unnecessary when modal gains and indices both appear in the model and are measured. The use of carrier and photon numbers rather than densities obviates the need to estimate the mode volume. Wherever possible, absolute optical power measurements are avoided, since they are notoriously difficult to perform accurately. Two parameters, the effective index μ_e and the facet power reflectivity R, are difficult to measure but fairly typical for GaAs/AlGaAs devices, so values of μ_e=3.3 and R=0.32 are assumed.

Section 6.2 discusses the measurement of the photon lifetime τ_p. Section 6.3 describes spectrally-resolved near-fields, which are important for qualitative characterization, as well as measuring the differential gain, the linewidth-enhancement factor and the coupling parameter, discussed in Sections 6.4, 6.5 and 6.6, respectively. Section 6.7 describes temporally-resolved near-fields, which allow comparison of the actual dynamics with those obtained from theory.

6.2 Photon Lifetime Measurement

The photon lifetime τ_p is a ubiquitous and easily-measured parameter. It is the mean time that a photon exists in a cavity pumped to transparency (G=0) before being absorbed or scattered by waveguide inhomogeneities, or absorbed or transmitted at one of the facets. The photon lifetime is assumed to be independent of wavelength and injection current.

In a multi-mode device operating above threshold, any modes with appreciable intensity will have gains

$$G_m \approx \frac{1}{\tau_p} \tag{6.2.1}$$

and the carrier number is clamped near the threshold value

$$N \approx N_{th} \tag{6.2.2}$$

Therefore, the steady-state version of (2.4.1.2) gives

$$\frac{J}{q} = \frac{N_{th}}{\tau_s} + \frac{S}{\tau_p} \tag{6.2.3}$$

where

$$S \equiv \sum_m S_m = \frac{1}{hc^2} \frac{1}{1-R} \frac{\lambda^3}{\Delta\lambda} P_{out} \tag{6.2.4}$$

by (2.6.4), where P_{out} is the output power from one facet of all the modes, assuming the other facet to be identical. Differentiating (6.2.3) with respect to J and using (6.2.4) gives

$$\tau_p = \frac{q}{hc^2} \frac{1}{1-R} \frac{\lambda^3}{\Delta\lambda} \frac{dP_{out}}{dJ} \tag{6.2.5}$$

The single-facet external differential efficiency dP_{out}/dJ can be found from the slope of a linear fit of P_{out} to J for $J>J_{th}$.

While it is the instantaneous power P_{out} that is desired, it is the average power $<P_{out}>$ which is actually measured. In the CW case these are identical, but continuous operation causes the temperature of the cavity to be greater than that of short-pulse, low-duty-cycle operation, which may affect the measured photon lifetime. Since short-pulse, low-duty-cycle operation is used for the rest of the characterization, the device should be pulsed to measure τ_p as well. However, the current pulse must be long enough to be sufficiently rectangular, that is, its rise and ring time should be short compared to the pulse width. For a rectangular pulse

$$P_{out} = \frac{\text{pulse repetition time}}{\text{pulse width}} <P_{out}> \qquad (6.2.6)$$

The experimental setup is shown in Figure 6.2.1. The current pulse was chosen to compromise between rectangularity and heating. The average power was linear in pulse width over the range available to the Avtech AVO-5-B pulser, indicating that the device lased uniformly for the duration of the pulse. The detector aperture was large enough to subtend virtually the entire far-field of the device at the working distance. Uncaptured light was probably the dominant source of error in this measurement, and would tend to underestimate the photon lifetime. A linear fit to the data appears in Figure 6.2.2, giving J_{th}=86 mA and dP_{out}/dJ=.326 W/A. Using λ=8150 Å and $\Delta\lambda$=4.27 Å (Section 6.3), (6.2.5) gives τ_p=1.65 ps.

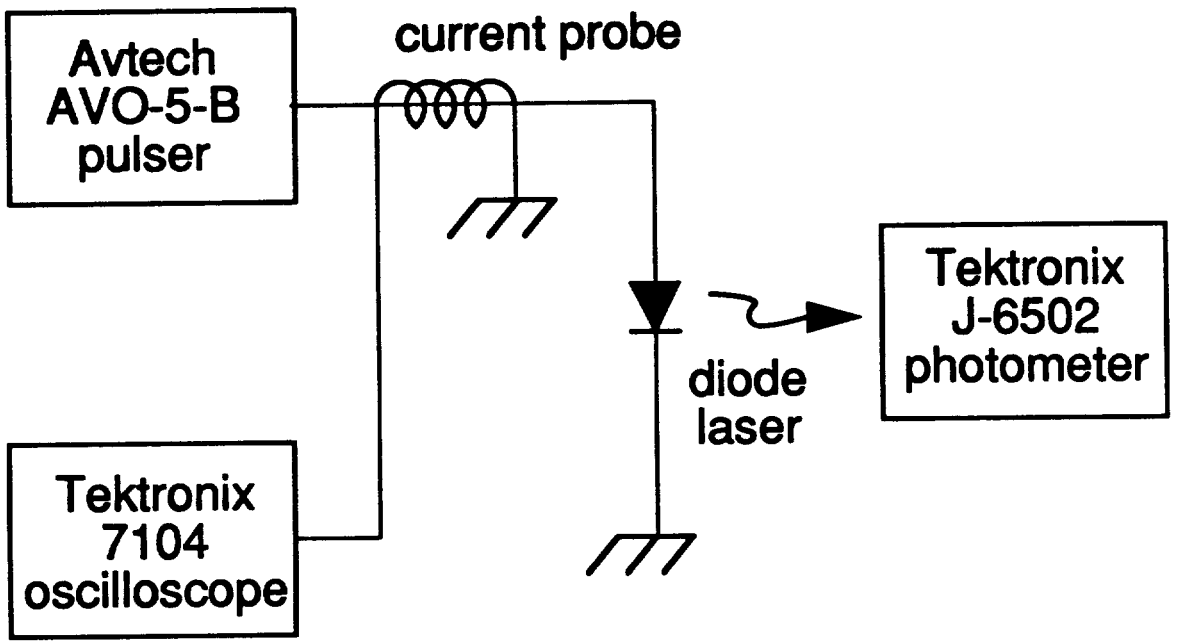

Figure 6.2.1 Photon Lifetime Measurement Setup

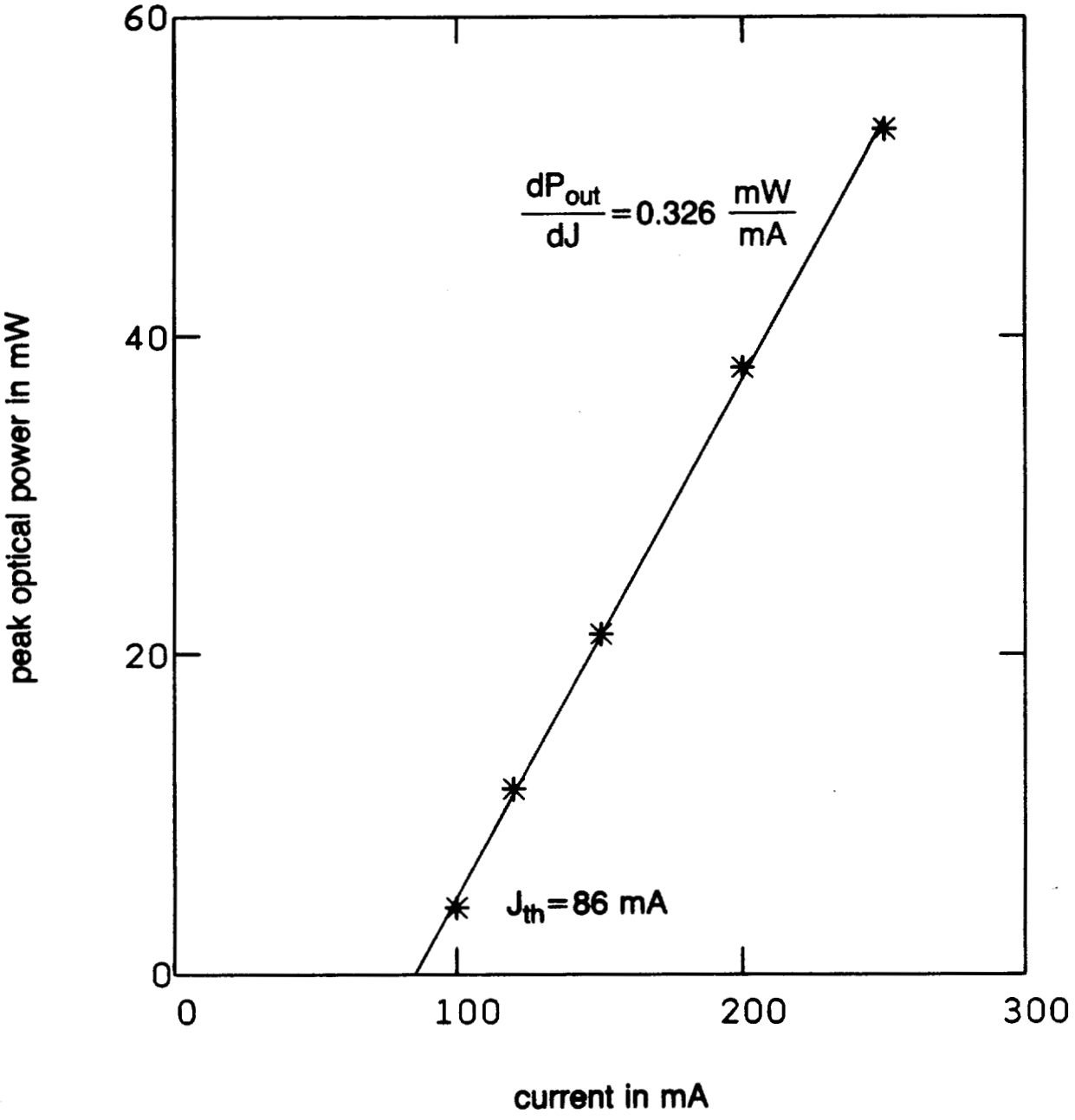

Figure 6.2.2 Light vs. Current Characteristic of 1D4

Measured points are denoted by asterisks, the best linear fit by a solid line.

6.3 Spectrally-Resolved Near-Fields

Knowledge of the spectrally-resolved near-field is indispensable in characterizing coherent semiconductor laser arrays. The shape of the observed lateral modes tells much about the quality of the array and the strength of coupling between the emitters. The wavelength spacing and relative intensities of the lateral modes determines the coupling parameter, and the peak position and depth-of-modulation of the sub-threshold spectrum allows the differential gain and the linewidth-enhancement factor to be calculated.

The setup used to obtain spectrally-resolved near-fields is shown in Figure 6.3.1. Short current pulses are necessary to minimize chirping due to heating during the pulse, while pulse rectangularity is not particularly important. Thus a Tektronix PG-502 pulser, with a minimum pulse width of 8 ns at the base, was used to drive the array. The PG-502 pulser had the advantage of a longer duty cycle than the AVO-5-B pulser, giving six times the average power for the same operating point, but had the disadvantage of being able to supply only 180 mA of peak current. The array was mounted with its epilayers parallel to the entrance slit of the spectrometer so that the lateral near-field could be observed while dispersing the spectrum in the orthogonal direction. A CCD camera was used to obtain a video image of the spectrally-resolved near-field, with wavelength and lateral coordinate displayed in the horizontal and vertical directions, respectively. The image was horizontally calibrated by changing the wavelength setting of the spectrometer grating and dividing by the shift in pixel number of a prominent spectral feature, and vertically calibrated by raising the microscope objective a known amount using a translation stage, and dividing by the pixel number shift. The video image was frame-grabbed using a

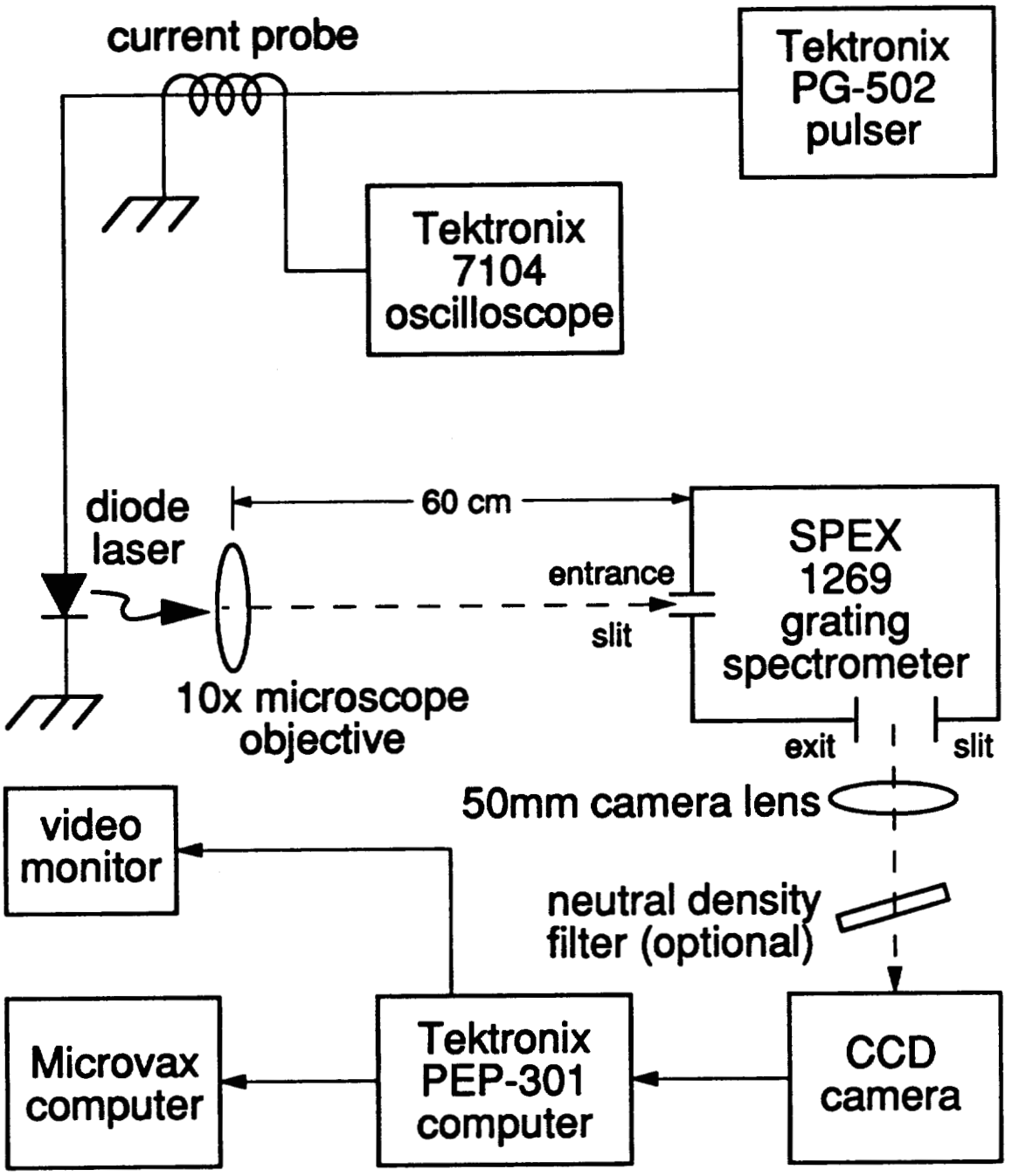

Figure 6.3.1 Spectrally-Resolved Near-Field Measurement Setup

Tektronix PEP-301 computer. Horizontal windowing allowed spatially-resolved spectra, while vertical windowing allowed spectrally-resolved near-fields. Raw data files were transferred to a MicroVax computer for analysis. For each set of data files sharing a common window, a background file was taken using the same window with the laser off, to obtain the net signal by subtraction.

Figure 6.3.2 shows the spectra of the four emitters of 1D4 at $J=1.65 \cdot J_{th}$. The longitudinal mode spacing is 4.27 Å. Emitters 2-4 appear to be phase-locked, while emitter 1 seems to operate independently. Thus emitters 2-4 form a three-stripe "sub-array". The sub-array modes begin to lase at J_{th}, while emitter 1 begins to lase at about $1.3 \cdot J_{th}$. The two dominant longitudinal modes have been designated "C" and "S", for central and next-shortest, and the next-longest mode has been named "L". The +++ lateral mode (see Appendix F) is responsible for the output at C and S, while both the +++ and +−+ modes can be seen at L.

Figures 6.3.3 and 6.3.4 show the spectrally-resolved near-fields of the lateral modes of longitudinal mode "C", somewhat below threshold where the modes have comparable intensities. Other longitudinal modes had a similar lateral mode pattern. The mode spacings have been given in frequency, which is related to the spacing in wavelength by

$$\Delta\nu = -\frac{c}{\lambda^2}\Delta\lambda \tag{6.3.1}$$

in anticipation of the search for mode beating in the time series presented in Section 6.7.

The modes designated "+++" and "+−+", shown in Figure 6.3.3, are apparently the in-phase and out-of-phase modes of the three-stripe sub-array. A

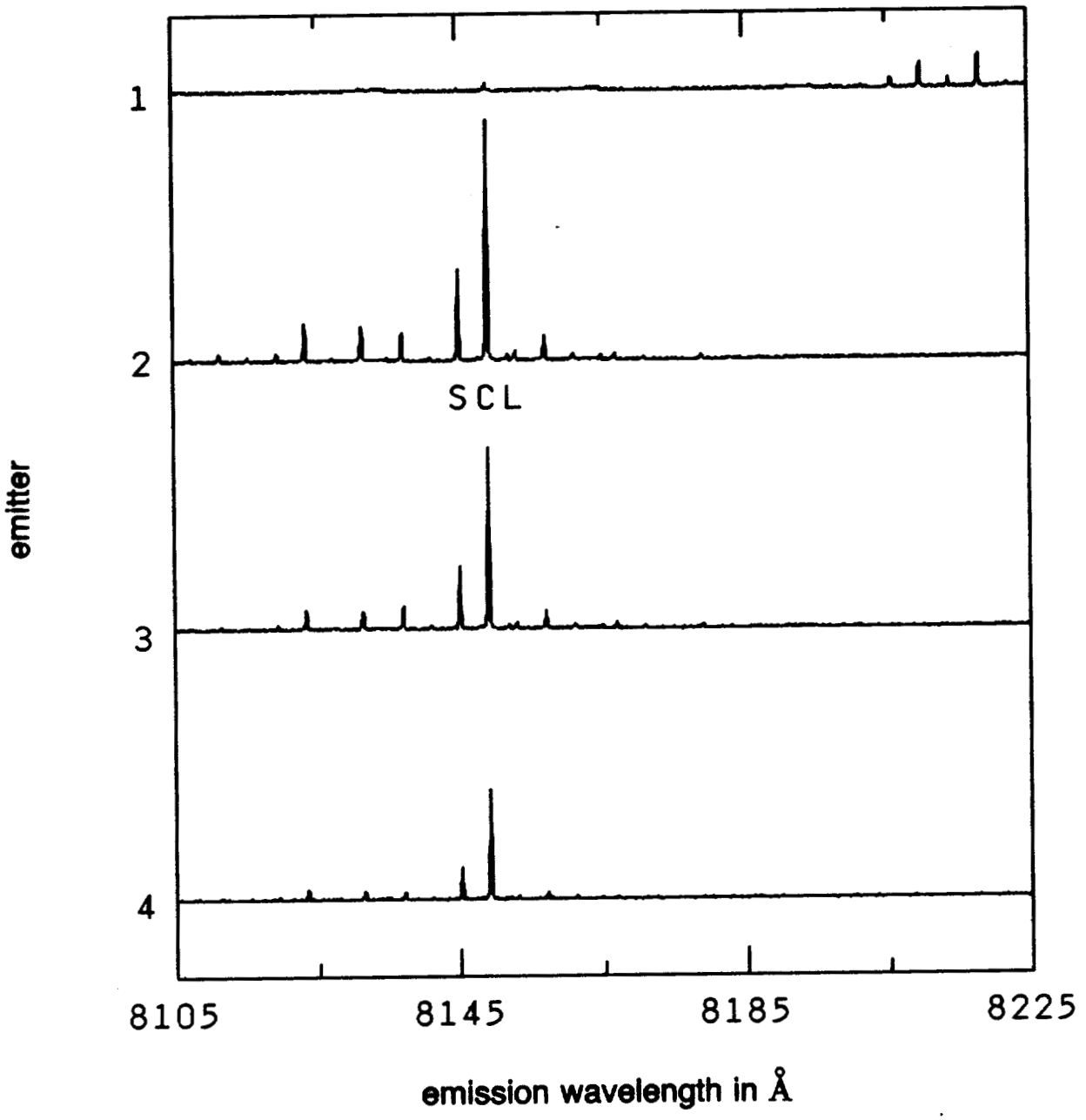

Figure 6.3.2 Spatially-Resolved Spectra

Device 1D4 consists of a phased-locked sub-array (emitters 2-4) and a free-running emitter (1). The in-phase or +++ three-emitter lateral mode dominates above threshold, although the +−+ lateral mode can also be discerned at "L".

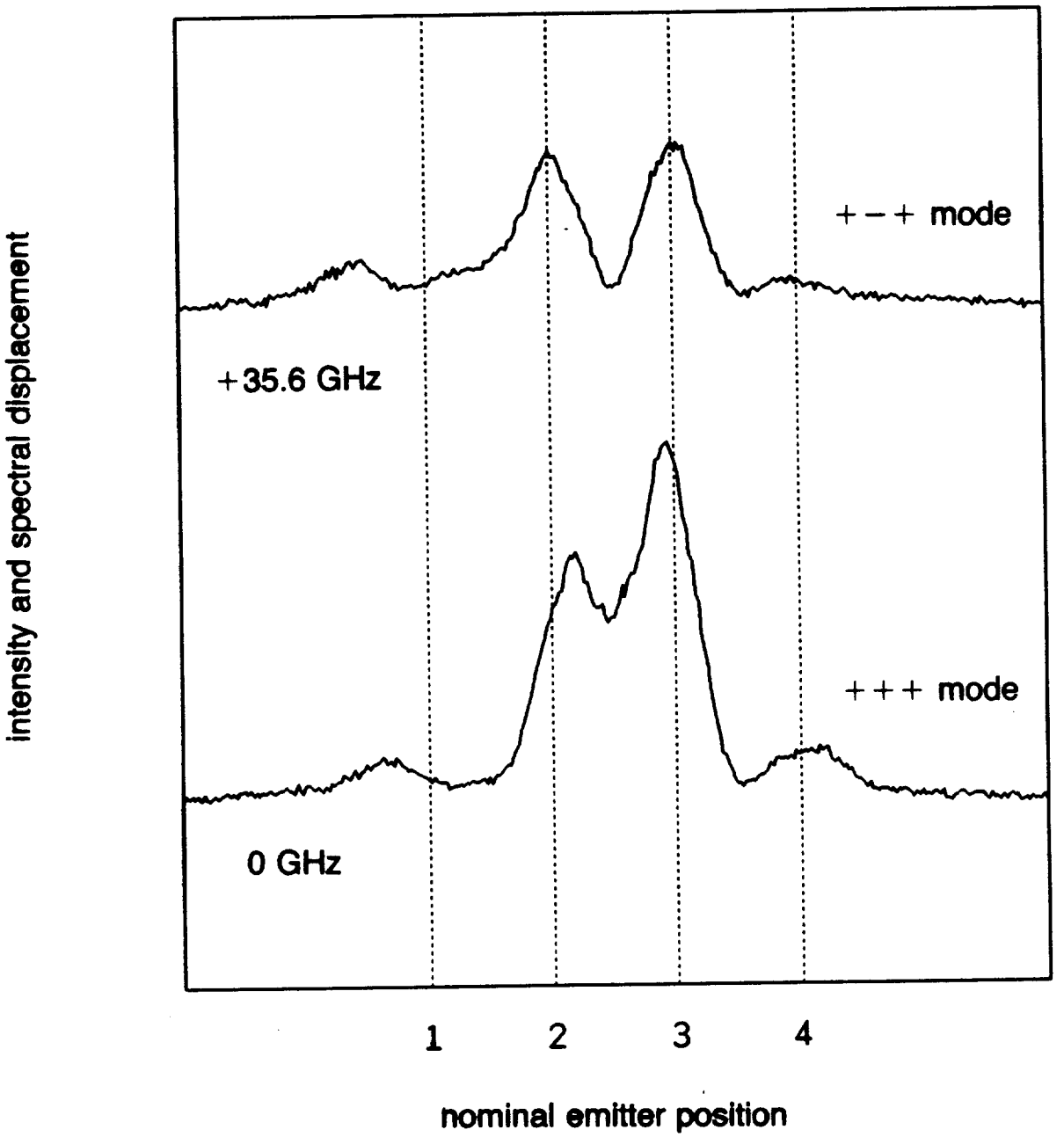

Figure 6.3.3 Three-Emitter Sub-Array Lateral Modes of 1D4

These spectrally-resolved near-fields were observed slightly below threshold, where the modal intensities are comparable. Above threshold, + + + dominates and both modes have greater relative emitter 4 intensities. The + 0 − mode is not observed, as predicted in Appendix F.

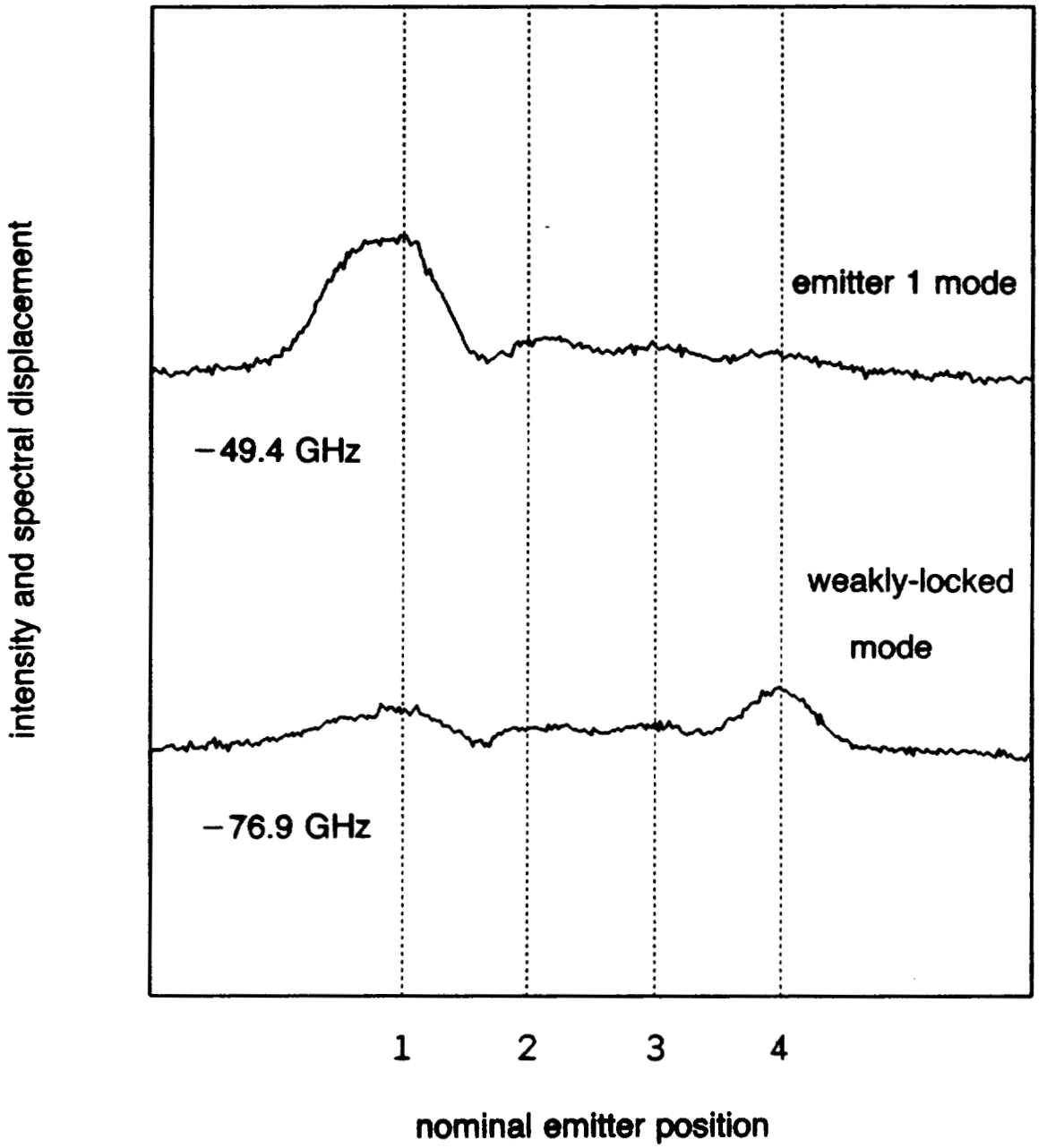

Figure 6.3.4 Other Lateral Modes of 1D4

Two other 1D4 lateral modes are observed, with spectral displacements given relative to the +++ mode. Emitter 1 modes lase for $J > 1.3 \cdot J_{th}$, but in longitudinal modes approximately 60 Å longer wavelength than "C" (see Figure 6.3.2). The weakly-locked modes were not observed to lase.

spectrally-resolved far-field of +−+ would be necessary to show conclusively that the near-field lobes are out-of-phase, but the node between the lobes strongly suggests that this is the case. Supermode theory predicts a third mode, +0−, but this mode is not expected to exist because it does not use the gain in the central emitter, an energetically unfavorable situation, as discussed in Appendix F. As the current is increased beyond threshold, +++ dominates and is responsible for the peaks at S and C in Figure 6.3.2. Both +++ and +−+ have comparable intensity at L. Note that the shape of +++ is different below (Figure 6.3.3) and above (Figure 6.3.2) threshold, with emitter 4 responsible for a much greater share of the output above threshold. This is not predicted by coupled-emitter theory, in which the lateral profiles must be independent of injection current, and probably indicates deviation from the assumption of equal emitter gains of Appendix F.

As mentioned above, the "emitter 1" lateral mode, shown in Figure 6.3.4, begins to lase at about $1.3 \cdot J_{th}$, but at about 60 Å to the long wavelength side of the sub-array modes. The lateral mode designated "weakly-locked" in Figure 6.3.4 never lases, apparently locking of the entire array is energetically unfavorable.

6.4 Differential Gain Measurement

In this section, the depth-of-modulation of the sub-threshold emission spectrum is used to calculate the differential gain, a method similar to that given in Reference [100]. Because the sub-threshold spectra tended to be noisy due to the low light levels, and the characterization of may devices was anticipated, the FORTRAN program "fabry.perot.f" was written to automate this procedure. The source code

appears in Appendix H. A derivation of the algorithm appears below.

The cavity is considered a Fabry-Perot resonator with a slight round-trip loss, where the field is maintained by a small spontaneous emission contribution. For simplicity, consider the spontaneous emission to be supplied from a monochromatic, unidirectional point source within the cavity. The total field at that point is found by summing the infinite series of contributions from previous round trips, and is given by

$$E = \frac{E_{sp}}{1-|Y|e^{i\theta}} \tag{6.4.1}$$

where E_{sp} is the source strength, θ is the round-trip phase shift,

$$|Y| \equiv \exp\left[\frac{\tau_L}{2}\left(G-\frac{1}{\tau_p}\right)\right] \tag{6.4.2}$$

is the round-trip field gain and τ_L is the round-trip cavity transit time. Taking the absolute square of (6.4.1), the observed intensity can be written

$$I(\theta) = \frac{I_0}{1-2|Y|\cos\theta+|Y|^2} \tag{6.4.3}$$

where I_0 is an undetermined constant. Fabry-Perot resonances and anti-resonances occur at $\theta=2m\pi$ and $\theta=(2m+1)\pi$, respectively, where m is an integer.

Note that the ratio of the reciprocal intensity at the peak to the reciprocal intensity averaged from $\theta=-\pi$ to $\theta=\pi$ allows I_0 to be cancelled

$$U \equiv \frac{1}{I(\theta=0)<I^{-1}(\theta)>} \tag{6.4.4}$$

Substituting (6.4.3) into (6.4.4) and solving for |Y| gives

$$|Y| = \frac{1-[2U-U^2]^{\frac{1}{2}}}{1-U} \tag{6.4.5}$$

where the root given was chosen because both U and |Y| exist in the domain (0,1). The round-trip transit time is given by

$$\tau_L = \frac{2\mu_{g,e}L}{c} = \frac{\lambda^2}{c\Delta\lambda} \tag{6.4.6}$$

by (2.6.3). Substituting (6.2.5) and (6.4.6) into (6.4.2) gives

$$G\tau_p - 1 = \frac{2q}{hc}\frac{1}{1-R}\lambda\frac{dP_{out}}{dJ}\ln\left[\frac{1-[2U-U^2]^{\frac{1}{2}}}{1-U}\right] \tag{6.4.7}$$

for the net modal gain normalized to the photon lifetime. The peak intensity I(0) can be found by fitting a parabola to the data points in the neighborhood of the peak. The advantage of this technique over taking the ratio of single-point maxima and minima is that more of the data is used, which should reduce the error due to noise.

Spectra are acquired using the setup shown in Figure 6.3.1, with horizontal windowing. The window was placed between the emitters 2 and 3 of 1D4, to capture only the light from the dominant lateral mode, to avoid multiple peaks in a longitudinal mode spacing. The normalized net modal gain for the dominant lateral mode is plotted against the injection current in Figure 6.4.1. The three data points at each current setting correspond to modes "S", "C" and "L" of Figure 6.3.2, in no particular order. Since the modes have slightly different gains (C>S>L), separate linear fits for each mode will give vertically displaced lines with nearly the same slope. Since displacements do not affect the slope $d(G\tau_p-1)/dJ$, the data of all three modes is combined and fit to a line. Note that extrapolating the linear fit gives $J_{th}\approx 112$

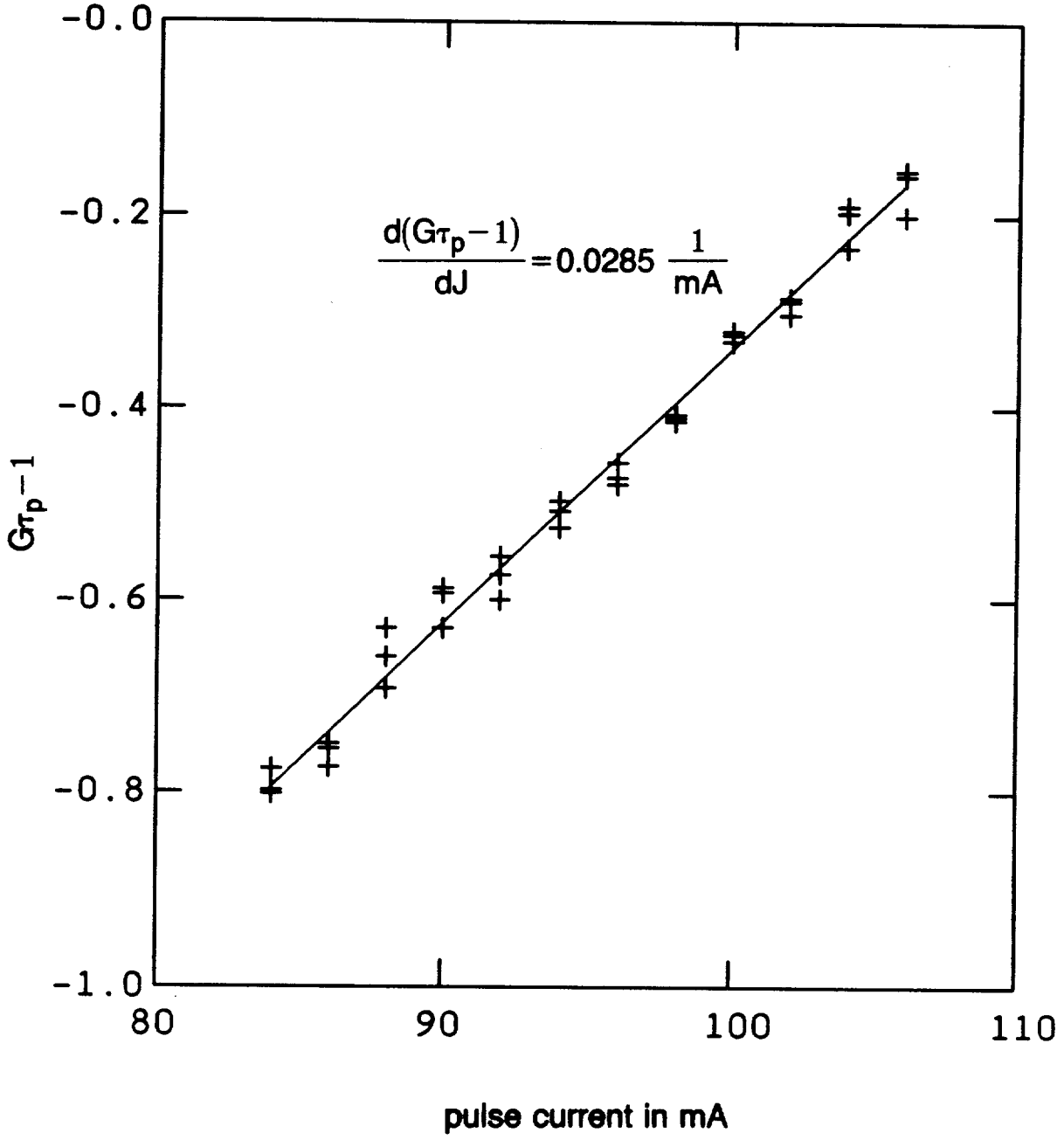

Figure 6.4.1 Differential Gain Measurement

Crosses represent measurements for modes "S", "C" and "L" of 1D4 in no particular order, at each current setting. The best linear fit is shown as a solid line.

mA, which seems to be at odds with the value J_{th}=86 mA reported in Section 6.2. This is because the pulse currents were measured at the peak, which is larger than the average current during the pulse for the non-rectangular PG-502 pulse. Since only derivatives with respect to current are of interest, it is assumed that this offset can be overlooked.

The measured quantity $d(G\tau_p-1)/dJ$=.0285 1/mA can be related to $[\partial G/\partial N]_{th}$ by

$$\left[\frac{\partial G}{\partial N}\right]_{th} = \frac{q}{\tau_s \tau_p}\frac{d(G\tau_p-1)}{dJ} \tag{6.4.8}$$

Evaluation requires τ_s, but for the purpose of verifying the in-phase stability boundary knowledge of $d(G\tau_p-1)/dJ$ is sufficient.

6.5 Linewidth-Enhancement Factor Measurement

The linewidth-enhancement factor was defined by (2.4.3.7). Because a functional relationship exists between N and J below threshold, (2.4.3.7) can be rewritten as

$$\alpha = \frac{\dfrac{d<Re[\chi]>}{dJ}}{\dfrac{d<Im[\chi]>}{dJ}} \tag{6.5.1}$$

To proceed, note that the effective index μ_e is related to its cold-cavity value and the spatially-averaged real part of the carrier-induced susceptibility by

$$\mu_e^2 = \mu_e^2(N=0) + <Re[\chi]> \tag{6.5.2}$$

so that

$$\frac{d<Re[\chi]>}{dJ} = 2\mu_e \frac{d\mu_e}{dJ} \tag{6.5.3}$$

The effective index is related to the wavelength of a particular longitudinal mode by

$$2\mu_e L = m\lambda \tag{6.5.4}$$

where m is the integer number of wavelengths in a cavity round trip. Differentiating (6.5.4) for constant m gives

$$\frac{d\mu_e}{dJ} = \frac{\mu_e}{\lambda}\frac{d\lambda}{dJ} \tag{6.5.5}$$

The spatially-averaged imaginary part of the carrier-induced susceptibility is related to the modal gain by (2.2.4.11). Therefore

$$\frac{d<Im[\chi]>}{dJ} = -\frac{\mu_e \mu_{g,e}}{2\pi c}\frac{\lambda}{\tau_p}\frac{d(G\tau_p - 1)}{dJ} \tag{6.5.6}$$

where $d\lambda/\lambda << dG/G$ was used to neglect the $d\lambda/dJ$ contribution. Substituting (6.5.3), (6.5.5), (6.5.6), (6.2.5) and (2.6.4) gives

$$\alpha = -8\pi \frac{q}{hc}\frac{\mu_e}{1-R}\frac{L}{\lambda}\frac{dP_{out}}{dJ}\frac{\frac{d\lambda}{dJ}}{\frac{d(G\tau_p - 1)}{dJ}} \tag{6.5.7}$$

The only parameter remaining to be measured is $d\lambda/dJ$, the modal wavelength shift. The FORTRAN program "fabry.perot.f", used in Section 6.4 to calculate $d(G\tau_p - 1)/dJ$, also finds the wavelength of the longitudinal modes from a parabolic fit to the peaks of the spectrum. The wavelengths of modes "S", "C" and "L" of 1D4 (see Figure 6.3.2) are plotted against injection current in Figure 6.5.1, over a wide

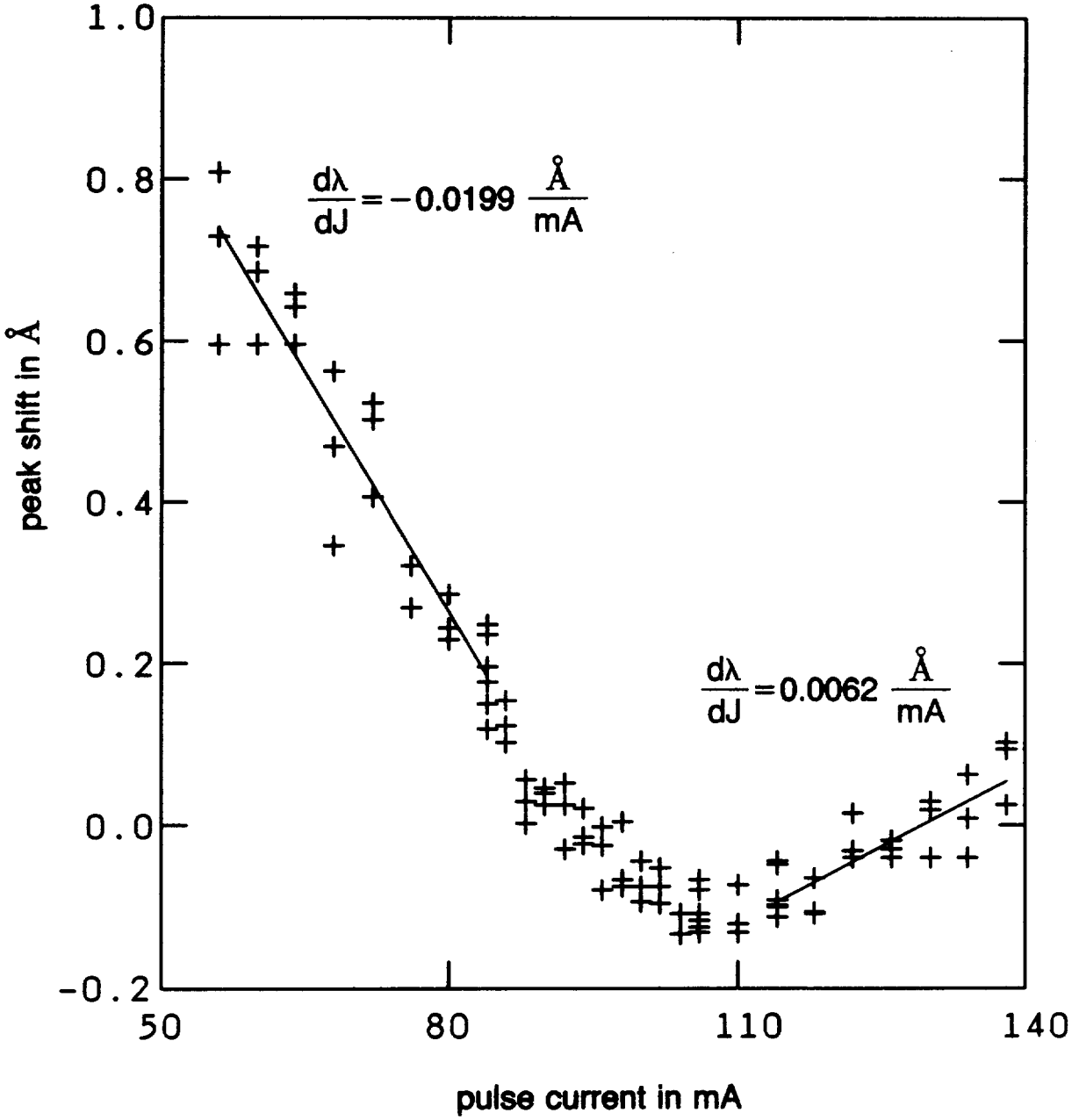

Figure 6.5.1 Linewidth-Enhancement Factor Measurement

Crosses represent the relative wavelengths of modes "S", "C" and "L" as they shift with injection current. At 84 mA, 106 mA and 114 mA, data sets overlap and six data points are displayed. Best linear fits to the 56−84 mA (far below threshold) and the 114−138 mA (above threshold) data sets are shown as solid lines.

range below and above $J_{th} \approx 112$ mA. Because of the great variation in light level over the range, four data sets (J=56-84, 84-106, 106-114 and 114-138 mA) were taken using different neutral density filters and entrance slit widths to attenuate the light, and joined together at their common injection currents. This data was taken using the same setup as used in Section 6.4. The scatter in the 56-84 mA data is due to low light levels.

As the injection current increases, two competing effects act to shift the wavelength of the longitudinal mode. Increasing carrier density decreases the effective index, and thus the wavelength according to (6.5.5), while rising temperature increases the effective index and wavelength. Far below threshold, both effects are apparently linear in the injection current, with the wavelength decrease associated with the carriers dominant. As threshold is approached, the carrier number becomes a sublinear function of injection current, due to a superlinear spontaneous recombination rate. Stimulated recombination "clamps" the carrier number above threshold. The junction temperature continues to increase, however, causing the wavelength shift to reverse. Since temperature changes are too slow to enter into the dynamics that we wish to study, the quantity of interest is the wavelength shift due to the carriers:

$$\left[\frac{d\lambda}{dJ}\right]_{\text{carriers}} = \left[\frac{d\lambda}{dJ}\right]_{\text{measured}} (J<J_{th}) - \left[\frac{d\lambda}{dJ}\right]_{\text{heating}} (J<J_{th}) \qquad (6.5.8)$$

Unfortunately, it is

$$\left[\frac{d\lambda}{dJ}\right]_{\text{heating}} (J>J_{th}) = \left[\frac{d\lambda}{dJ}\right]_{\text{measured}} (J>J_{th}) \qquad (6.5.9)$$

which is readily measured. To proceed, we must know the relationship between

$[d\lambda/dJ]_{heating}$ below and above lasing threshold.

It is commonly assumed (see Section 4.4.1 of Reference [20]) that these are equal. The following considerations call this assumption into question. The wavelength shift due to heating is proportional to the change in the effective index, which is in turn proportional to ΔT, the average temperature increase over the optical mode. Therefore,

$$\left[\frac{d\lambda}{dJ}\right]_{heating}(J<J_{th}) = \frac{\frac{d\Delta T}{dJ}(J<J_{th})}{\frac{d\Delta T}{dJ}(J>J_{th})}\left[\frac{d\lambda}{dJ}\right]_{heating}(J>J_{th}) \qquad (6.5.10)$$

We assume that

$$\Delta T \propto P_{dis} = V_{cav}J - 2P_{out} \qquad (6.5.11)$$

where P_{dis} is the power dissipated in the cavity (p-type cladding, active and n-type cladding layers), V_{cav} is the voltage dropped across the cavity, and $2P_{out}$ is the optical output power, which does not contribute to heating. As defined in (2.6.1), P_{out} is the output of one facet, and so is doubled in (6.5.11), assuming identical facets. Note that the equality in (6.5.11) simply expresses conservation of power. There are three contributions to P_{dis}: ohmic heating in the cladding layers, spontaneous recombination in the active layer and photon absorption by the waveguide.

We further assume that the voltage drop V_{SUB} across the high-conductivity substrate is negligible, so that

$$V_{cav} = V_{tot} - V_{SUB} \approx V_{tot} \qquad (6.5.12)$$

where V_{tot} is the measured voltage drop across the device. This can be linearized about its value V_{th} at lasing threshold

$$V_{tot} = V_0 + [V_{th}-V_0]\frac{J}{J_{th}} \qquad (6.5.13)$$

where V_0 is given by the intersection of the tangent to the J(V) characteristic at J_{th}, and the V-axis. This phenomenological treatment takes both ohmic and junction heating into account.

Substituting (6.5.12) and (6.5.13) into (6.5.11), differentiating with respect to J and evaluating at J_{th}, and substituting into (6.5.10) gives

$$\left[\frac{d\lambda}{dJ}\right]_{heating}(J<J_{th}) = \left[1-\frac{2\cdot dP_{out}/dJ}{2V_{th}-V_0}\right]^{-1}\left[\frac{d\lambda}{dJ}\right]_{heating}(J>J_{th}) \qquad (6.5.14)$$

The CW J(V) characteristic of 1D4 was used to obtain V_{th}=2.5 volts and V_0=2.0 volts. Using dP_{out}/dJ=.326 W/A (Section 6.2) gives 1.28 as the correction factor.

Linear fits to the 56-84 mA and 114-138 mA data in Figure 6.5.1 can be used in conjunction with (6.5.14) and (6.5.8) to obtain $[d\lambda/dJ]_{carriers}(J<J_{th})$=−.0275Å/mA. The device length of 1D4 was found to be 211 μm. Inserting these into (6.5.7) gives α=0.8. This value is quite low, but falls within the range given in Reference [101], α=0.5 to α=8 for various devices. A possible explanation is that 1D4 lased at a somewhat shorter wavelength than other devices from wafer PGE4600B (λ_{1D4}=8150 Å, λ_{36D2}=8180 Å and λ_{36D3}=8200 Å), which has been shown to reduce α (see Figure 6 of Reference [101]) by moving the gain peak toward the spontaneous emission peak.

6.6 Coupling Parameter Measurement

The setup used for this measurement has been described in Section 6.3. A hor-

izontal window containing the inner emitters is used to capture light from both of the three-emitter sub-array lateral modes, and exclude the others. The real part of the coupling parameter is related to the beat frequency of the lateral modes +++ and +−+ by (F.20). For 1D4, the beat frequency was found to be virtually independent of the injection current, and was $\Delta\nu$=34.3, 35.6 and 35.0 GHz for the longitudinal modes "S", "C" and "L" of Figure 6.3.2, respectively. Therefore, η_R=.126, .129, and .128 for modes S, C and L.

Note that the beat frequencies of the +++ and +−+ lateral modes of the longitudinal modes S, C and L of device 1D4 are approximately $2^{½}$ larger than the beat frequency measured for the two-stripe device PGE4600B#36D3, whose spectrally-resolved near-field is shown in Figure 7.2.1. This is expected from three-emitter theory (Appendix F), assuming that 1D4 and 36D3 have the same coupling parameter.

The imaginary part of the coupling parameter is more difficult to measure. It is related to the degree of suppression of one lateral mode by the other. In steady state, and neglecting gain compression and the stochastic contribution of spontaneous emission, either (4.4.14) or (4.4.15) give

$$[Z^{(0)} \pm \eta_I] X^{(0)2} + B = 0 \tag{6.6.1}$$

where + (−) is used for the out-of-phase (in-phase) mode. This relationship gives the optical power from either emitter with the array running purely in one mode or the other, and now we assume that the ratio of the average intensities of the concurrently-running modes is the same as the ratio of the intensities of the pure modes in steady-state, so that

$$U \equiv \frac{I(0)+I(\pi)}{I(0)-I(\pi)} = \frac{1}{\eta_I} Z \tag{6.6.2}$$

where I(0) and I(π) are the intensities of the in-phase and out-of-phase lateral modes, in arbitrary units. This quantity is different than that defined by (6.4.4). The definition of Z is given by (4.4.10), and can be used to obtain

$$U = U_0 + \frac{1}{2}\frac{d(G\tau_p - 1)}{dJ}\frac{1}{\eta_I}J \tag{6.6.3}$$

where U_0 is an unknown constant. A fit of (6.6.3) to experiment is shown in Figure 6.6.1. As shown in Appendix F, η_I obtained from (6.6.3) should be divided by $2^{\frac{1}{2}}$ for a three-emitter, which yields η_I=−.128, −.115 and −.104 for modes S, C and L.

6.7 Temporally-Resolved Near-Fields

Temporally-resolved near-fields are plots of intensity as a function of the lateral coordinate and time, in contrast with spectrally-resolved near-fields, in which the lateral coordinate and wavelength are the independent variables. These characterizations give supplemental information. For instance, a pair of lateral modes of comparable intensity may be observed in the emission spectrum, but whether the modes run simultaneously or one at a time in a bistable manner cannot be determined from the spectrum alone. Furthermore, if the modes run concurrently, are they locked or free-running? The temporally-resolved near-field may reveal rapid switching between modes with quiescent interludes, indicating bistability, or simultaneously running modes. A deterministic relationship may be inferred from the time series, indicating some degree of mode-locking, and a lack thereof may be interpreted as evidence of independence.

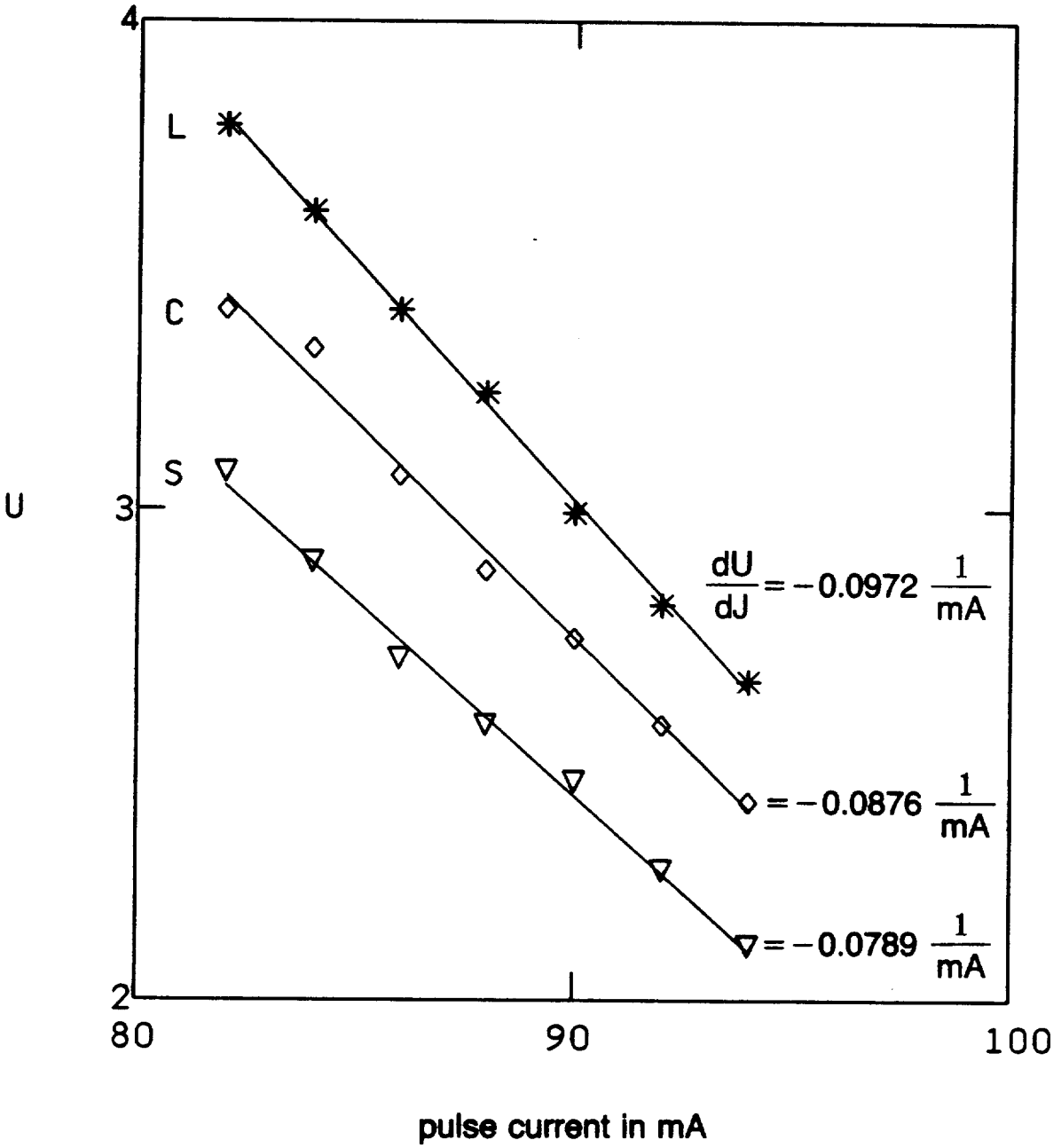

Figure 6.6.1 Measurement of η_I

The U parameter is plotted as a function of current for modes L (asterisk), C (diamond) and S (triangle) of 1D4. Best linear fits are shown as solid lines and yield estimates of η_I.

The setup used to record temporally-resolved near-fields is shown in Figure 6.7.1. The AVO-5-B pulser was used to provide a 60 ns current pulse. Only about 1 ns of the optical output was observed, taken about 30 ns after the beginning of the current pulse to allow the transient response to die. This simulates the CW dynamics addressed by the theory, while retaining the low duty cycle found to be necessary to achieve lasing with these devices. Both the pulser and the high-speed streak unit were triggered by the start of a video frame, with the appropriate relative delay provided by the timing block. Video frames were grabbed by the temporal analyzer, and the background was subtracted. The frame was then re-grabbed using the PEP-301 computer, and vertical windows were defined to allow the time series of individual emitters to be digitized. Time series data files were then transferred to the MicroVax computer for analysis.

Figure 6.7.2 shows a time series of emitter 3 at J=200 mA, or about $2.3 \cdot J_{th}$. No consistent structure is apparent, which suggests that quiescent behavior with some dynamical and measurement noise is being observed.

Figures 6.7.3 and 6.7.4 show the power spectra of 1D4 at J=200 mA and J=150 mA ($J=1.7 \cdot J_{th}$), respectively. Noise was reduced by averaging the absolute values of the discrete Fourier transforms of 20 time series, taken under identical conditions, using the FORTRAN program "exp.pwr.sp.f", listed in Appendix H. The frequency components are normalized by the program to give their mean-square power relative to the square of the average signal. Thus, 100 % sinusoidal modulation of a DC level would have DC and AC spectral components of 1.0 and 0.5, respectively. The small non-zero-frequency components seen in Figures 6.7.3 and 6.7.4 are indicative of quiescent behavior, in particular, note that no peaks appear near 35 GHz, which if present would indicate lateral mode beating. Note that because of the normalization of the

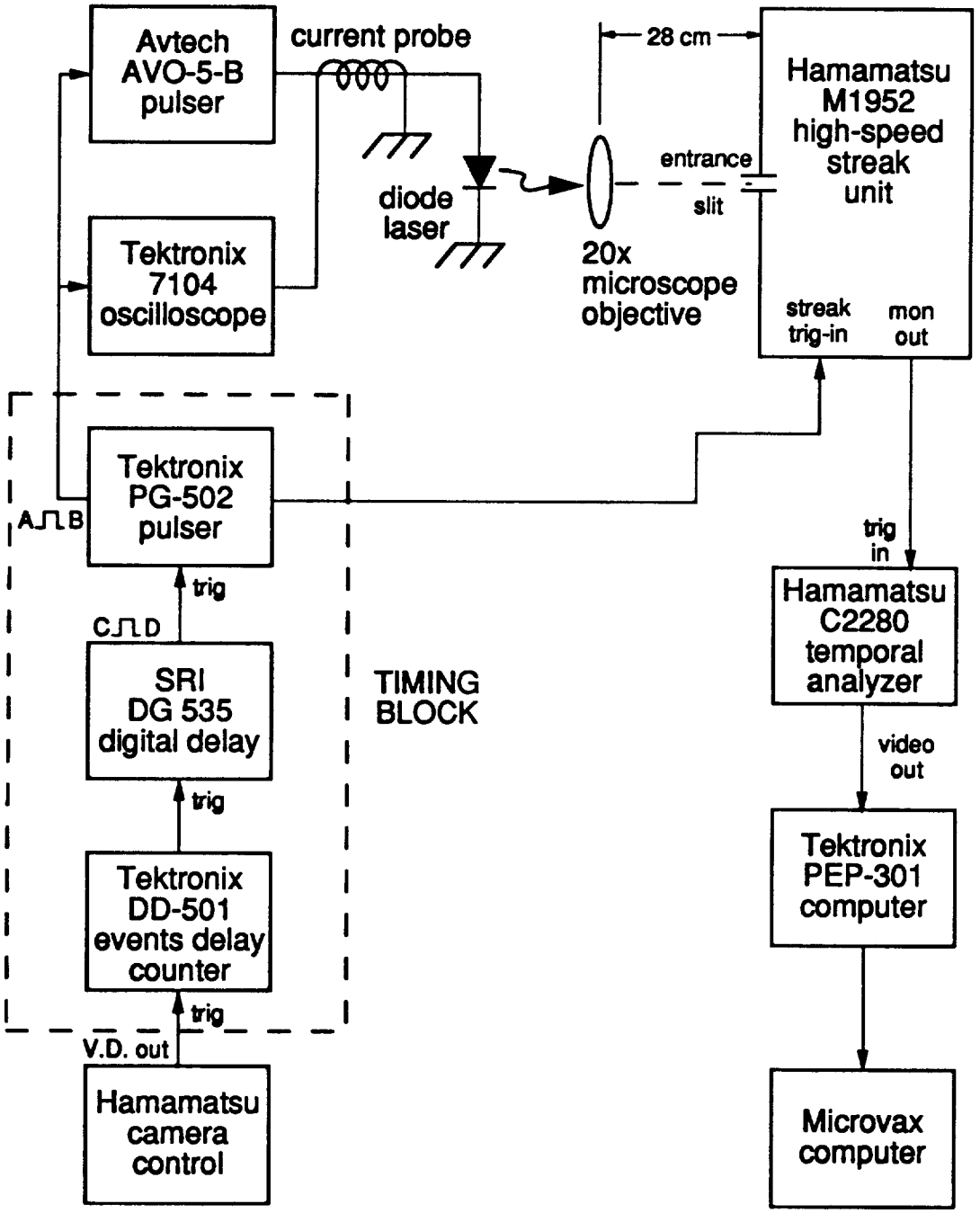

Figure 6.7.1 Temporally-Resolved Near-Field Measurement Setup

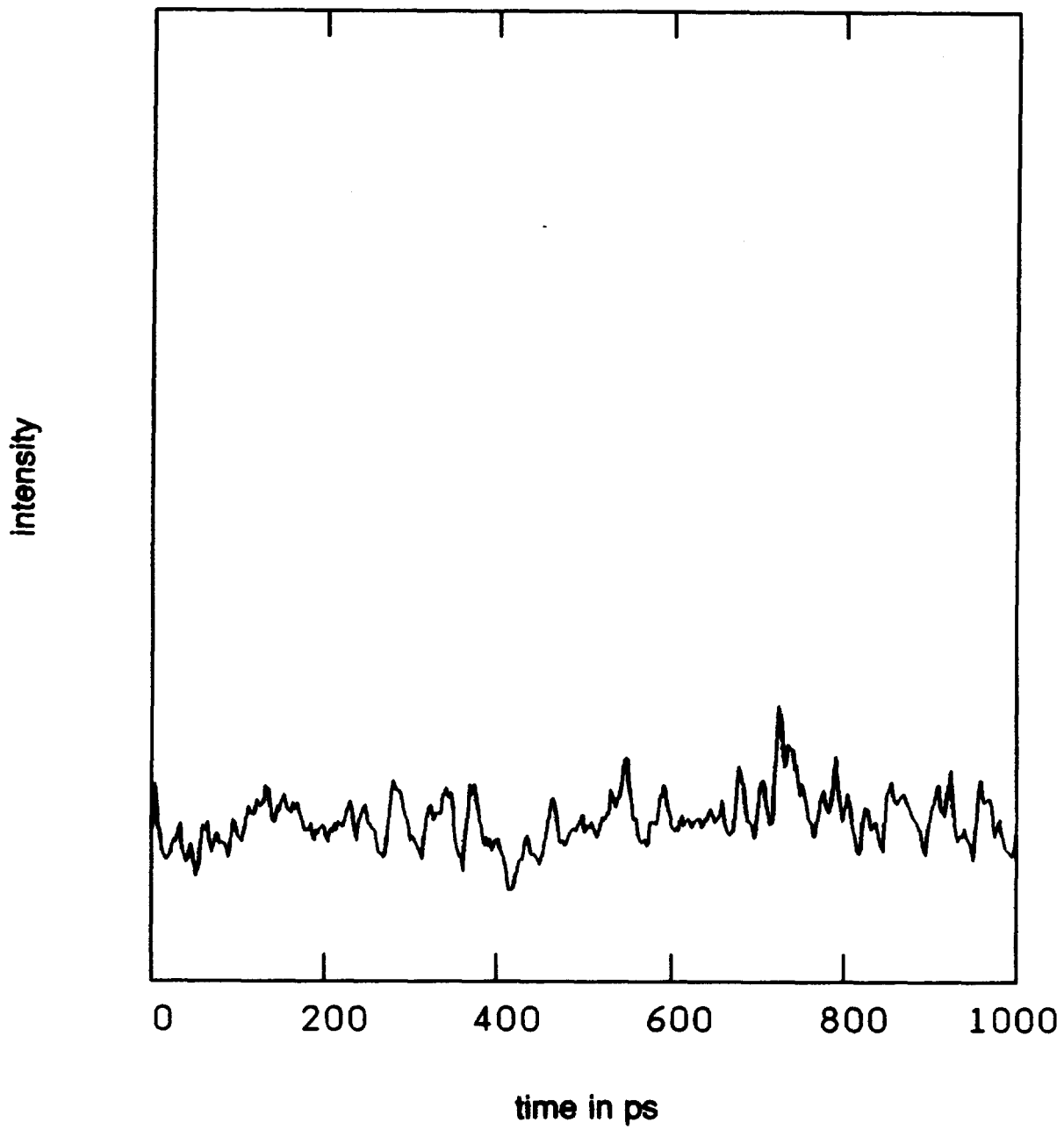

Figure 6.7.2 Intensity Time Series at $J=2.3 \cdot J_{th}$

The intensity range shown corresponds to the range of the streak camera vidicon.

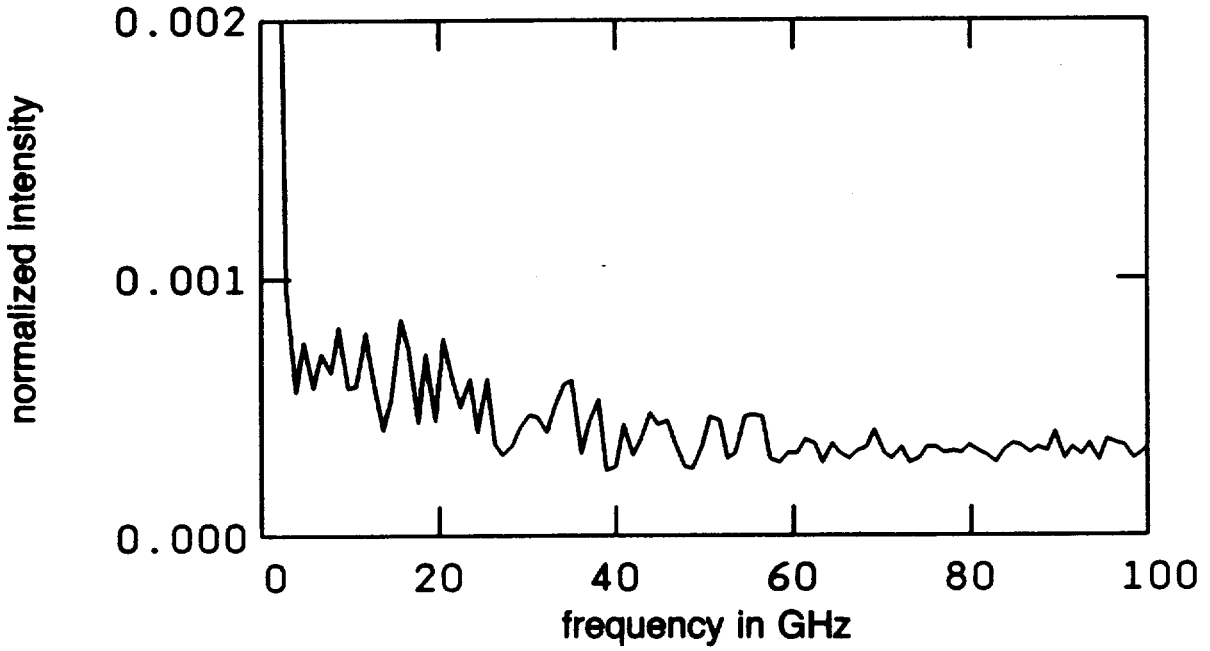

Figure 6.7.3 Average Power Spectrum at $J=2.3 \cdot J_{th}$

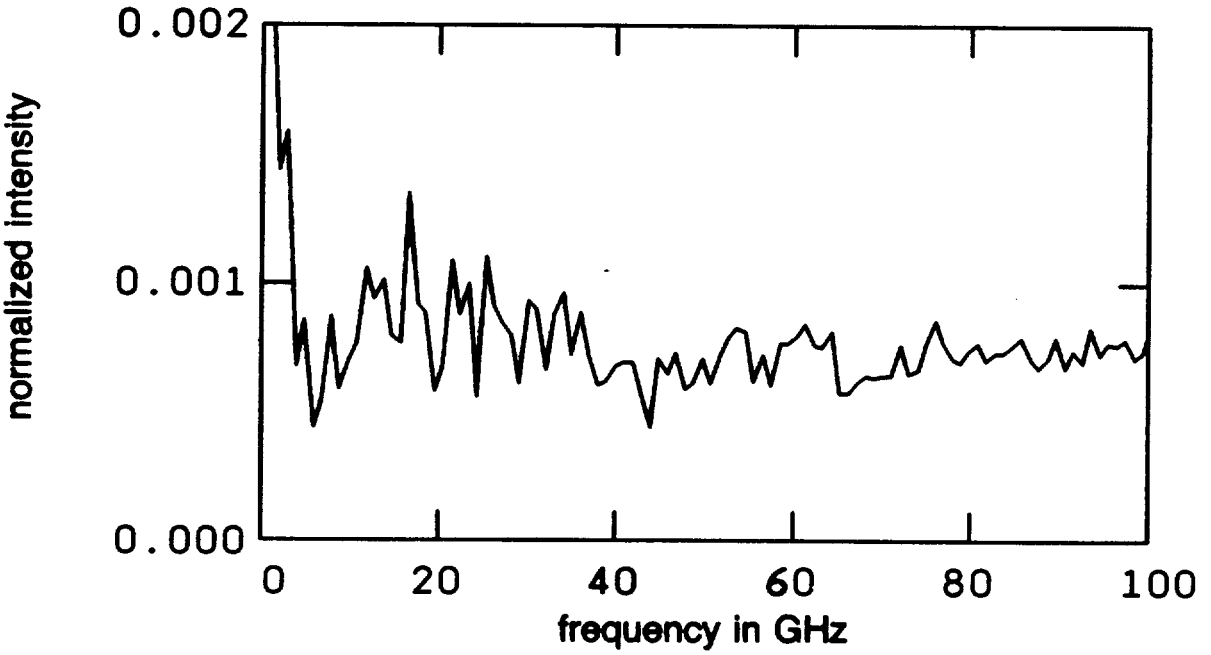

Figure 6.7.4 Average Power Spectrum at $J=1.7 \cdot J_{th}$

average signal to unity, the non-zero-frequency components are apparently larger for $J=1.7 \cdot J_{th}$ than for $J=2.3 \cdot J_{th}$, when in fact they are about the same magnitude.

The observed quiescent behavior of 1D4 is consistent with the prediction of stable in-phase operation of 1D4, discussed in Section 7.2. This agreement is the strongest evidence in support of twin-emitter theory presented in this thesis.

7. EXPERIMENTAL SUPPORT OF TWIN-EMITTER THEORY

7.1 Chapter Overview

Experimental support for the foregoing theory is presented in this chapter. Only the simplest verification was attempted, that of matching the predicted and observed stability properties. At the time of this writing, evidence for the twin-emitter theory is quite weak, due to the lack of devices to which the theory applies.

All of the devices tested (except M929Z223#3, discussed in Section 7.2) were cleaved from the wafer PGE4600B, obtained from Dr. Gary Evans of David Sarnoff Research Center. This wafer consisted of gain sections alternated with surface-emitting gratings, which were cleaved away to yield edge-emitters. The gain sections were 200 μm long and consisted of either two or four ridge waveguides. A scanning-electron micrograph of the facet of a four-stripe device is shown in Figure 7.1.1. A ridge width of 2.5 μm, center-to-center spacing of 4 μm, ridge height of 1 μm and active layer depth of 1.5 μm were measured. Bars with five devices were cleaved and mounted substrate-down with conductive epoxy onto small copper heat sinks, which served as the common electrical contact. The epilayer contacts were wire-bonded to gold-coated macor blocks built into the heat sink.

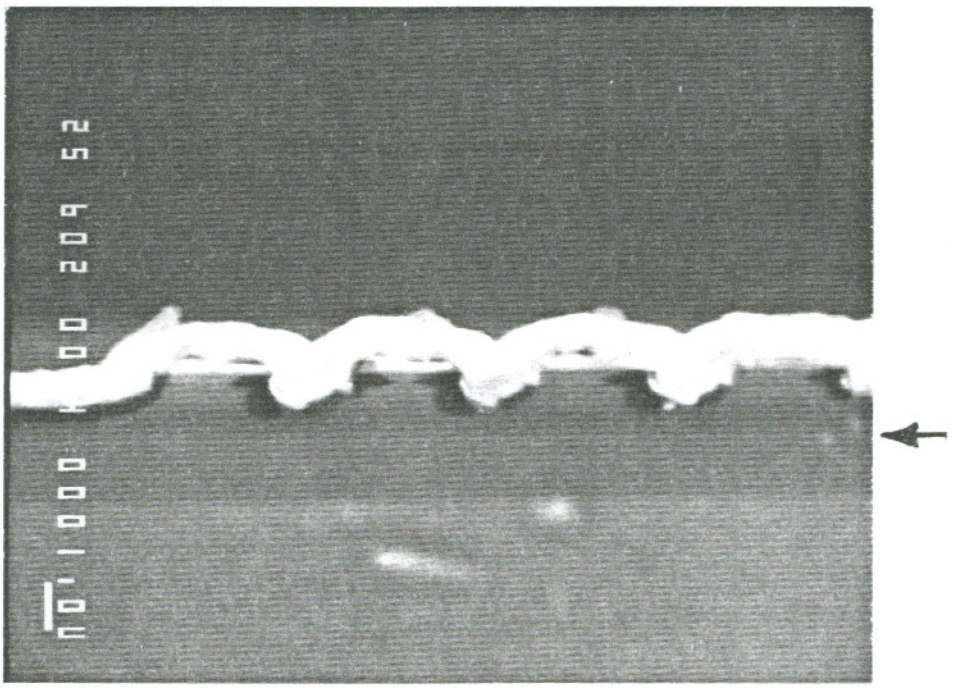

Figure 7.1.1 Four-Stripe Device Facet

A scanning-electron micrograph of the cleaved facet of a piece of wafer PGE4600B reveals the active layer (arrow) at a depth of about 1.5 μm from the tops of the ridges. Ridge depth, width and center-to-center spacing are about 0.5, 2.5 and 4 μm, respectively.

Section 7.2 discusses the characterization of pristine, or unmodified, two- and four-stripe arrays. The drawback of a fixed coupling parameter is discussed, and the predicted and observed stability properties of 1D4 are compared. Two types of modified four-stripe devices are described in Section 7.3, and results of preliminary fabrication attempts are given.

7.2 Pristine Devices

The most natural approach to experimental verification of twin-emitter theory is to study two-stripe devices. This is a three-step process. First, the spectrally-resolved near-field is examined to see if the device has the quality and amenability to twin-emitter theory to merit further attention. Next, the temporally-resolved near field is analyzed to determine the stability properties of the device. Finally, the process of measuring the parameters is undertaken, resulting in a diagram containing the stability boundaries and a point corresponding to the measured value of the coupling parameter. The predicted and observed stability are then compared, to support or refute the theory.

The problem is that each two-stripe device has a fixed coupling, so that at least two, and preferably many, with coupling parameters placing them in different stability regions, must be examined to convincingly affirm the theory. Aside from the enormous amount of characterization involved, some way of obtaining devices with a variety of coupling coefficients is needed. Assuming that random variation among devices will provide adequate diversity is questionable, and at best commits the experimenter to screening a large number of devices. Fabricating a family of devices

by varying one or more parameters, such as the emitter spacing, is more likely to succeed, but was beyond the resources available for this project.

A solution is to have a single device whose coupling can be continuously varied across one or more stability boundaries. The observation of predicted behavior upon both sides of a boundary, such as that seen in the numerical simulations of Chapter 5, would be compelling confirmation of the theory. Attempts to fabricate such a device are described in Section 7.3.

Despite their fixed coupling, several two-stripe devices were studied. Each of these was strongly-coupled, and thus twin-emitter theory was inapplicable. Figure 7.2.1 shows the spectrally-resolved near-field of device PGE4600B#36D3, taken below threshold where the modes have comparable intensities. The in-phase mode dominates above threshold. The out-of-phase mode resembles a linear combination of emitter modes, although with a rather large outward displacement of the lobes from stripe center. The single-lobed in-phase mode, however, cannot even approximately be expressed as a linear combination of emitter modes. Apparently, index guiding due to the ridge waveguides is overpowered by effects related to the carrier or temperature distributions in the lateral direction. Therefore, this should be considered a broad-area device, and either the continuum or coupled-lateral-mode model (Section 4.2) should be used. The lateral asymmetries of the modes also call the assumption of "twin" emitters into question. Device 36D2 was also strongly-coupled, but with more symmetric modes.

To contrast with the 4 μm on-center index-guided arrays discussed above, device M929Z223#3, a two-stripe gain-guided array with 4 μm stripes spaced 12 μm on-center, was examined. Despite the large center-to-center spacing, a relatively narrow

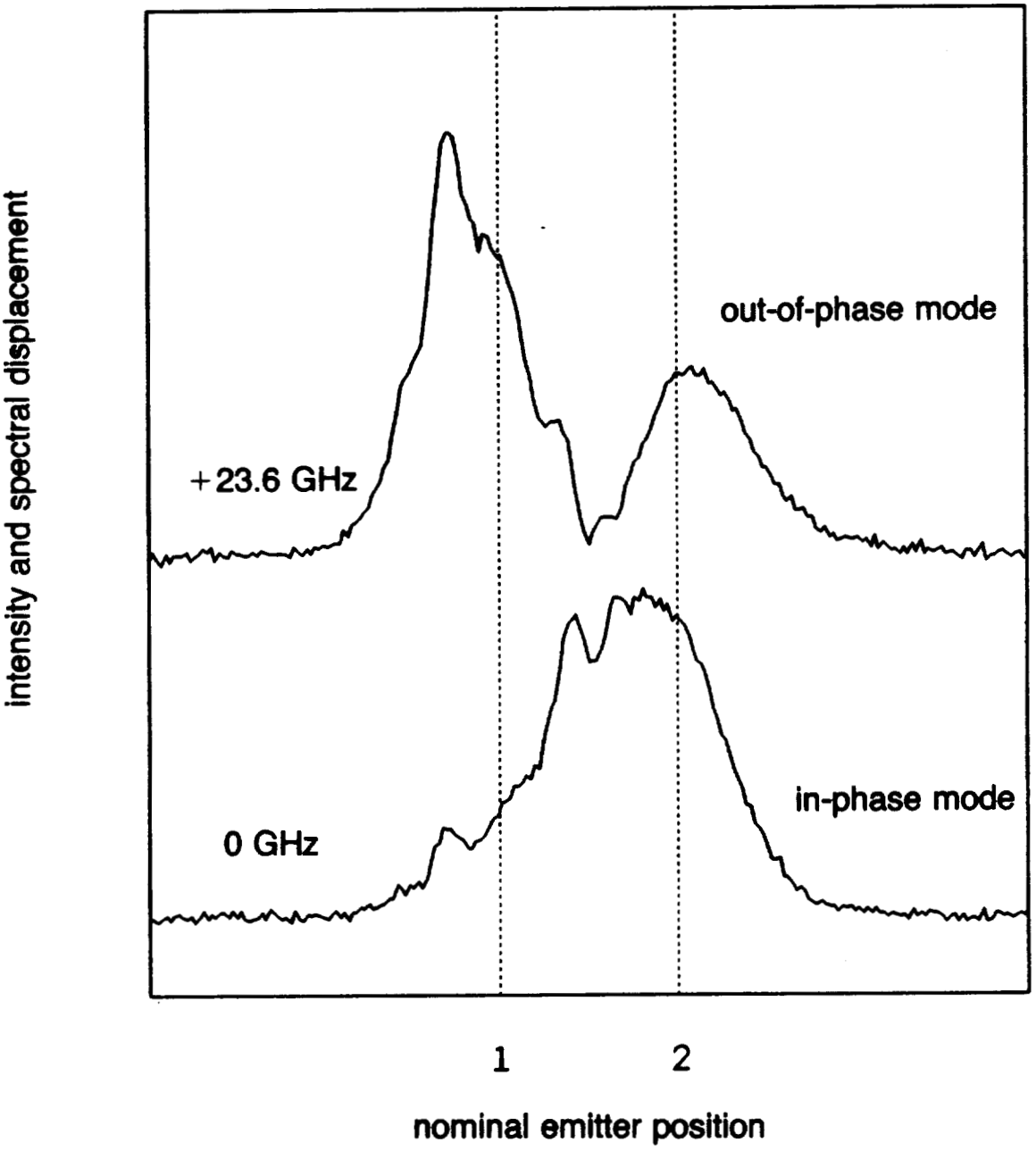

Figure 7.2.1 Spectrally-Resolved Near-Field of 36D3

The single-lobe in-phase mode indicates strong emitter coupling, which invalidates the twin-emitter model. Also, considerable lateral asymmetry is present.

(3 μm full-width half-maximum) single-lobe in-phase mode was found to dominate, indicating a great deal of current spreading in the p-type cladding and active layers.

Finally, among the PGE4600B four-stripe devices, 1D4 failed to exhibit locking of all four stripes, but consisted of a locked sub-array of emitters 2, 3 and 4 and the free-running emitter 1. It has been shown that the +++ lateral mode of the subarray is dominant (Section 6.3) and stable (Section 6.7) above threshold. In Appendix F it is shown that the three-emitter rate equations can be reduced to a form similar to those of the twin-emitter, and it is conjectured that the stability properties of the devices are similar. The twin-emitter in-phase stability boundary, given by (4.4.33), is plotted in Figure 7.2.2 using the parameters measured for 1D4 in Chapter 6. The effective coupling parameter η', given by (F.28), is also plotted. It can be seen that η' lies well within the in-phase stable region for both $J=2.3 \cdot J_{th}$ and $J=1.7 \cdot J_{th}$, which agrees with observed stability properties.

7.3 Modified Devices

To increase the variety of the coupling parameter, two schemes were devised for turning four-stripe devices into twin-emitters with altered or variable coupling. Both ideas involve device modification using focused ion-beam micromachining[102].

Q-spoiled devices are ones in which the inner emitters are prevented from lasing by micromachining a scattering center in their optical paths, as shown in Figure 7.3.1. The shape of the scattering center is not important, as long as it does not extend into the optical fields of the outer emitters, hampering their operation. It was

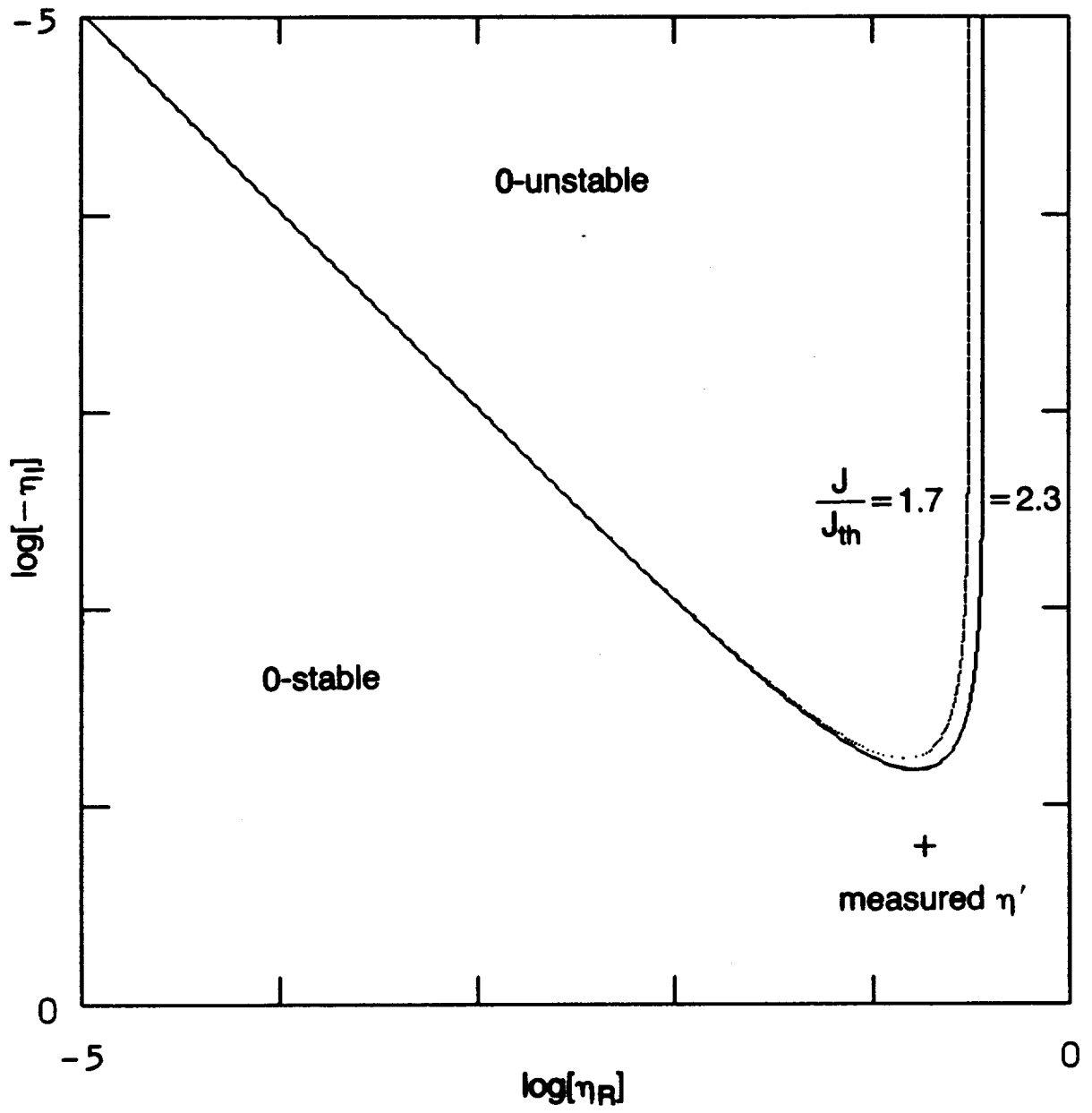

Figure 7.2.2 Predicted Stability of 1D4

The measured coupling parameter is found to be well within the in-phase mode stability region, which agrees with the quiescent behavior observed in Section 6.7.

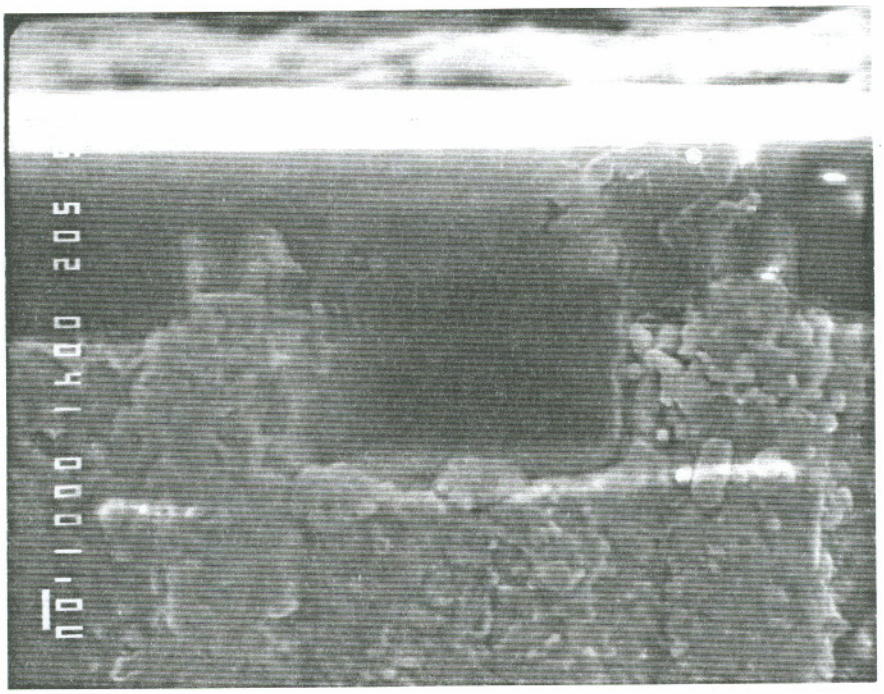

Figure 7.3.1 Micromachined Q-Spoiled Device

A scanning-electron micrograph top view of a pit micromachined between the outer emitters of the four-stripe device 36B3, to prevent lasing of the inner emitters. In this instance, only the left outer emitter lased after micromachining.

felt that after such a modification, the outer stripes could be considered a twin-emitter, and that the out-of-phase mode would be favored since its field is smaller in the low-Q central region. Such a device would thus have $\eta_I > 0$, in contrast with the in-phase $\eta_I < 0$ behavior observed for the unmodified two-stripe arrays. No working Q-spoiled devices were made. Extinction of the inner stripes, and unfortunately the right outer stripe, was achieved for device PGE4600B#36B3, shown in Figure 7.3.1.

The other idea was to create a variable-coupling device by electrically isolating the inner stripes from the outer stripes, and running the outer stripes as lasers but holding the inner stripes below threshold, so that their carrier density could be controlled via the injection current. It was felt that at low inner-stripe currents, the low-gain central region would favor the out-of-phase mode, while at currents approaching threshold, the in-phase mode would become dominant.

Ideally, this design could be implemented by micromachining electrical isolation grooves the length of the device, one between emitters 1 and 2 and the other between emitters 3 and 4. The grooves must be thin and shallow to minimize optical loss. Penetrating the metallization and cap layer are probably sufficient. The problem is making electrical contact to the central region, which is only 8 μm wide in this case. For this reason, the S-curve isolation groove design shown in Figure 7.3.2 was adopted. The ends of the four ridge waveguides can be seen near the rear facet (top edge of photo) for reference. The inner stripes (right outer stripe) lie mostly in the left (right) half of the S-curve, with the left outer stripe lying entirely to the left. Therefore, the left (right) contact pumps the outer (inner) stripes. There are penalties that come with simplifying electrical contact to the device. Note that the isolation groove is required to cross three of the stripes, which causes a trade-off between depth for good electrical isolation and shallowness to minimize damage to the

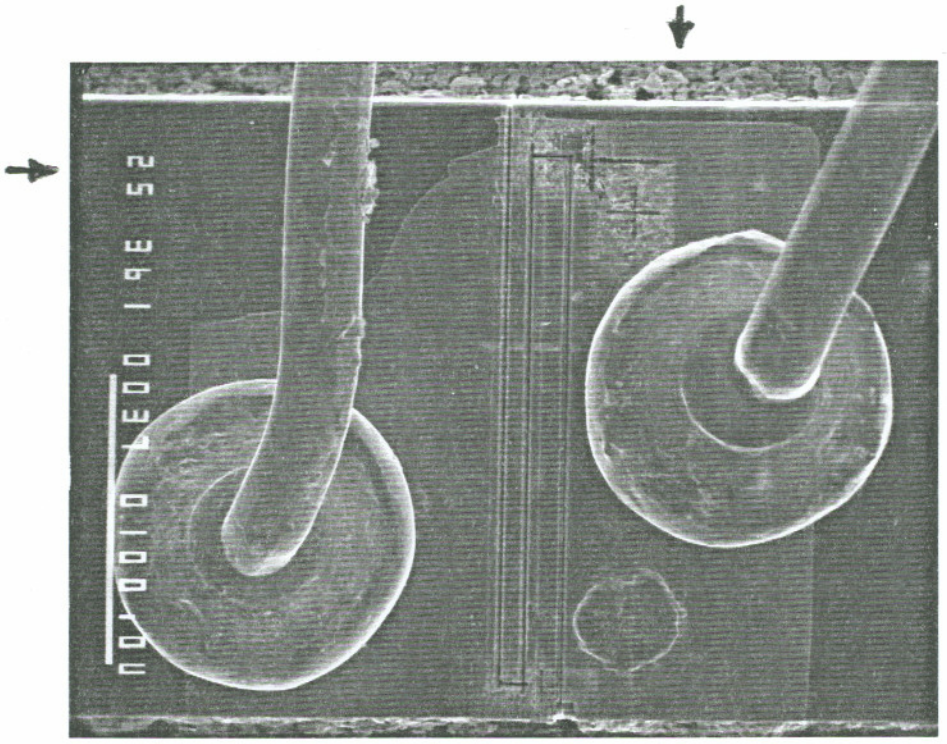

Figure 7.3.2 Micromachined Variable-Coupling Device

A scanning-electron micrograph top view of the four-stripe device 36B4 after micromachining electrical isolation grooves. The crack running along the rear facet (between arrows) may have prevented lasing.

waveguide. Even if both requirements could be simultaneously fulfilled, the crossed stripes lie partially in each electrically-isolated region, somewhat spoiling the original simplicity of the concept. Note that micromachining wide, shallow grooves in the lateral direction and narrow, deeper grooves in the longitudinal direction may give better results, should this technique be attempted in the future.

As it turned out, the device PGE4600B#36B4, shown in Figure 7.3.2, did not lase but had good electrical isolation (310 Ω) between sections. Both observations are consistent with excessive depth of the grooves. Another possible cause for device failure is the crack along the left side of the rear facet, which runs through all four stripes. Repeated attempts to place a third wire-bond in the left-rear corner of the device resulted in the torn metallization and the crack. Difficulty in wire-bonding due to poor metallization was a driving force in minimizing the number of contacts needed in modified-device designs. The author felt that the prospects for fabricating a working Q-spoiled or variable-coupling device with the present techniques and materials were not good enough to justify continued efforts.

8. MODULATION OF COHERENT ARRAYS

8.1 Chapter Overview

This chapter proposes a novel technique for high-frequency modulation of coherent semiconductor laser arrays[69-71]. Semiconductor lasers are important as transmitters in high-speed optical communications, largely because their optical output can be modulated directly by varying the injection current. InGaAsP lasers that emit in the fiber optic transmission window at 1.55 μm are an indispensable part of long-haul fiber optics communications technology[103]. Because they are rugged, compact and require no high-voltage power supplies, AlGaAs lasers are promising as transmitters for free-space satellite communications[104]. Their small size makes them good candidates for optical interconnects between integrated circuits, a technique that might increase the speed of supercomputers[105]. Finally, because they can be grown with other components on the same wafer, they are the natural light sources for integrated optoelectronic circuits[106].

The optical output of a single-mode semiconductor laser cannot be effectively modulated beyond its relaxation oscillation frequency, usually less than 10 GHz. On the other hand, a multi-longitudinal-mode device can be modulated near the frequency associated with the mode spacing[107]. This is usually greater than 100 GHz.

Because of high-frequency parasitics, principally stray capacitance, this frequency is beyond the range of present semiconductor laser driver technology. Furthermore, the bandwidth useful for communications is actually much smaller than this, as discussed in Section 8.2. A semiconductor laser that could be modulated at frequencies intermediate to the relaxation oscillation and longitudinal mode spacing frequencies would be highly desirable.

The beat frequencies of coherent array lateral modes are typically intermediate to the relaxation oscillation frequency and the longitudinal mode spacing. This suggests the possibility of actively mode-locking the lateral modes of the array by injection current modulation, analogous with active longitudinal mode-locking, but at more moderate frequencies.

A semiconductor laser acting as a transmitter in an optical communication system must be both responsive and stable. Responsivity is especially important at high frequencies, where modulation electronics may be able to supply only small signals. The transfer function (Section 3.3) should be flat over the bandwidth of the communication system. The transmitter must also lock to the modulating signal, so that the signal is faithfully reproduced. The rapidity of locking is related to the degree of stability of the response to small perturbations.

The electrical parasitics that plague high-frequency single-emitters are expected to be a problem with coherent arrays, with the added complications of separate contacts and phase-shifted signals. These design issues are beyond the scope of this chapter.

The twin-emitter semiconductor laser has been studied extensively[108]. In particular, it has been suggested that multi-gigahertz instabilities associated with cycling

among a continuum of non-stable near-field distributions might be effectively exploited in twin-emitter arrays[109], although no modulation scheme was proposed[110].

In Section 8.2, the twin-emitter rate equations of Section 4.4 are driven by small-signal sinusoidal injection current modulation, and the transfer functions for both in-phase and out-of-phase modulation are derived. Out-of-phase modulation of the emitters is shown to be essential for effective modulation beyond the relaxation oscillation frequency. It is found that both η_R and η_I, defined in Section 4.4, are important design parameters. η_R sets the frequency of peak response to out-of-phase modulation, while η_I must be chosen carefully to fulfill the requirements of responsivity and stability.

8.2 Small-Signal Sinusoidal Modulation

The goal of this section is to model the response of a twin-emitter array to small-signal sinusoidal injection current modulation as a function of the frequency and the relative phase of modulation of the emitters. Before deriving the small-signal transfer function, the stability of periodic solutions to the modulated rate equations should be addressed. Periodic solutions predicted by the model are of little interest if they are unstable and thus never observed. For infinitesimal modulation, it is easy to show that the periodic solutions should possess the same stability property as the equilibrium point of the autonomous system that they orbit. Therefore, the linear stability analysis of Section 4.4 can be directly applied in this section.

To obtain the transfer function, we use the twin-emitter rate equations (4.4.14)-

(4.4.18), neglecting spontaneous emission and gain compression for simplicity. Use of the rate equations becomes invalid as the modulation frequency approaches the polarization relaxation rate[111]. Since the latter is typically about $10^{13}\ s^{-1}$, rate equations are appropriate in the 10-100 GHz frequency range.

Sinusoidal modulation is introduced by setting

$$p_1(t) = p^{(0)} + \mathrm{Re}[p^{(1)}e^{i\Omega t}] \tag{8.2.1}$$

and

$$p_2(t) = p^{(0)} \pm \mathrm{Re}[p^{(1)}e^{i\Omega t}] \tag{8.2.2}$$

where the + (−) sign is to be used for in-phase (out-of-phase) modulation. For infinitesimal modulation, the rate equations can be linearized about an equilibrium point, and it suffices to discuss only the extremes of in-phase and out-of-phase modulation, since any intermediate case is a linear combination thereof.

To obtain the response of the array to small-signal current modulation, let $p^{(1)}$ be infinitesimal, so that the time-dependent perturbations of the dynamical variables are infinitesimal sinusoids. (4.4.14)-(4.4.18) can then be linearized by replacing their right-hand sides by the left-hand side of (4.4.23) with $\lambda \to i\Omega$, plus the column vector of driving terms. The common $e^{i\Omega t}$ time dependence is then dropped, and the matrix equation is solved for the dynamical variable perturbations.

For in-phase modulation, this procedure gives

$$\frac{X_1^{(1)}}{p^{(1)}} = \frac{X_2^{(1)}}{p^{(1)}} = \frac{X^{(0)}}{-T\Omega^2+i(1+2X^{(0)2})\Omega+2X^{(0)2}(1+2Z^{(0)})} \tag{8.2.3}$$

$$\frac{\theta^{(1)}}{p^{(1)}} = 0 \tag{8.2.4}$$

$$\frac{Z_1^{(1)}}{p^{(1)}} = \frac{Z_2^{(1)}}{p^{(1)}} = \frac{i\Omega}{-T\Omega^2+i(1+2X^{(0)2})\Omega+2X^{(0)2}(1+2Z^{(0)})} \tag{8.2.5}$$

while for out-of-phase modulation

$$\frac{X_1^{(1)}}{p^{(1)}} = -\frac{X_2^{(1)}}{p^{(1)}} = \frac{X^{(0)}\left[1+\frac{2i\alpha\eta_R\cos\theta^{(0)}}{\Omega'}\right]}{-T\Omega'^2+iA\Omega'+B-i\frac{C}{\Omega'}} \tag{8.2.6}$$

$$\frac{\theta^{(1)}}{p^{(1)}} = \frac{2\left[\alpha-\frac{2i\eta_R\cos\theta^{(0)}}{\Omega'}\right]}{-T\Omega'^2+iA\Omega'+B-i\frac{C}{\Omega'}} \tag{8.2.7}$$

$$\frac{Z_1^{(1)}}{p^{(1)}} = -\frac{Z_2^{(1)}}{p^{(1)}} = \frac{i\left[\Omega'-\frac{4\eta_R^2}{\Omega'}\right]}{-T\Omega'^2+iA\Omega'+B-i\frac{C}{\Omega'}} \tag{8.2.8}$$

where

$$\Omega' \equiv \Omega+2iZ^{(0)} \tag{8.2.9}$$

$$A \equiv 2TZ^{(0)}+1+2X^{(0)2} \tag{8.2.10}$$

$$B \equiv 4T\eta_R^2+2X^{(0)2}(1+2Z^{(0)}) \tag{8.2.11}$$

$$C \equiv 4\eta_R^2(2TZ^{(0)}+1+2X^{(0)2})-4\alpha\eta_R X^{(0)2}(1+2Z^{(0)})\cos\theta^{(0)} \tag{8.2.12}$$

The transfer function can be defined as in (3.3.4)

$$H(\Omega) \equiv \frac{q}{\tau_s}\frac{S^{(1)}}{J^{(1)}} = 2X^{(0)}\frac{X^{(1)}}{p^{(1)}} \tag{8.2.13}$$

using (4.4.9) and (4.4.11).

Figure 8.2.1 shows |H| as a function of the modulation frequency, for both in-phase and out-of-phase modulation, for a twin-emitter array characterized by η_R=0.1, η_I=0 and the parameters given in Table 2.6.1. These parameters were measured for a gain-guided twin-emitter[20] biased at $J=1.7 \cdot J_{thr}$, corresponding to $p^{(0)}$=0.66. For η_I=0, the response of a twin-emitter to in-phase modulation is identical to that of a single-emitter, with the peak response occurring at the relaxation oscillation frequency, 3.0 GHz in this example. This can be understood by noting that η_R has dropped out of (8.2.3). Since η_R is proportional to the rate at which photons are exchanged between the emitters, its failure to appear indicates that in-phase modulation is unable to drive the periodic energy transfer needed for a strong high-frequency response. This is reasonable on physical grounds because identical modulation to the emitters does nothing to drive energy transfer preferentially in either direction. Alternately, the goal can be considered to be the locking of the in-phase and out-of-phase lateral modes to produce a periodic response at the modulation frequency. It has been observed that spatially-homogeneous modulation is in general not effective for mode-locking[67,83]. The peak of |H| for in-phase modulation is much larger than actually observed because gain compression was neglected for simplicity. Nevertheless, semiconductor lasers tend to spike at the relaxation oscillation frequency when deeply modulated at a lower frequency[112], if the resonance response is sufficiently large. Such behavior would clearly be detrimental for communications applications.

The response to out-of-phase modulation is quite different. The peak response occurs at the beat frequency between modes, 21 GHz in this example. For η_I=0, the peak reaches 0 dB, as it does in the case of longitudinal mode locking[68]. The 3 dB band half-width about the modal beat frequency is the effective bandwidth for

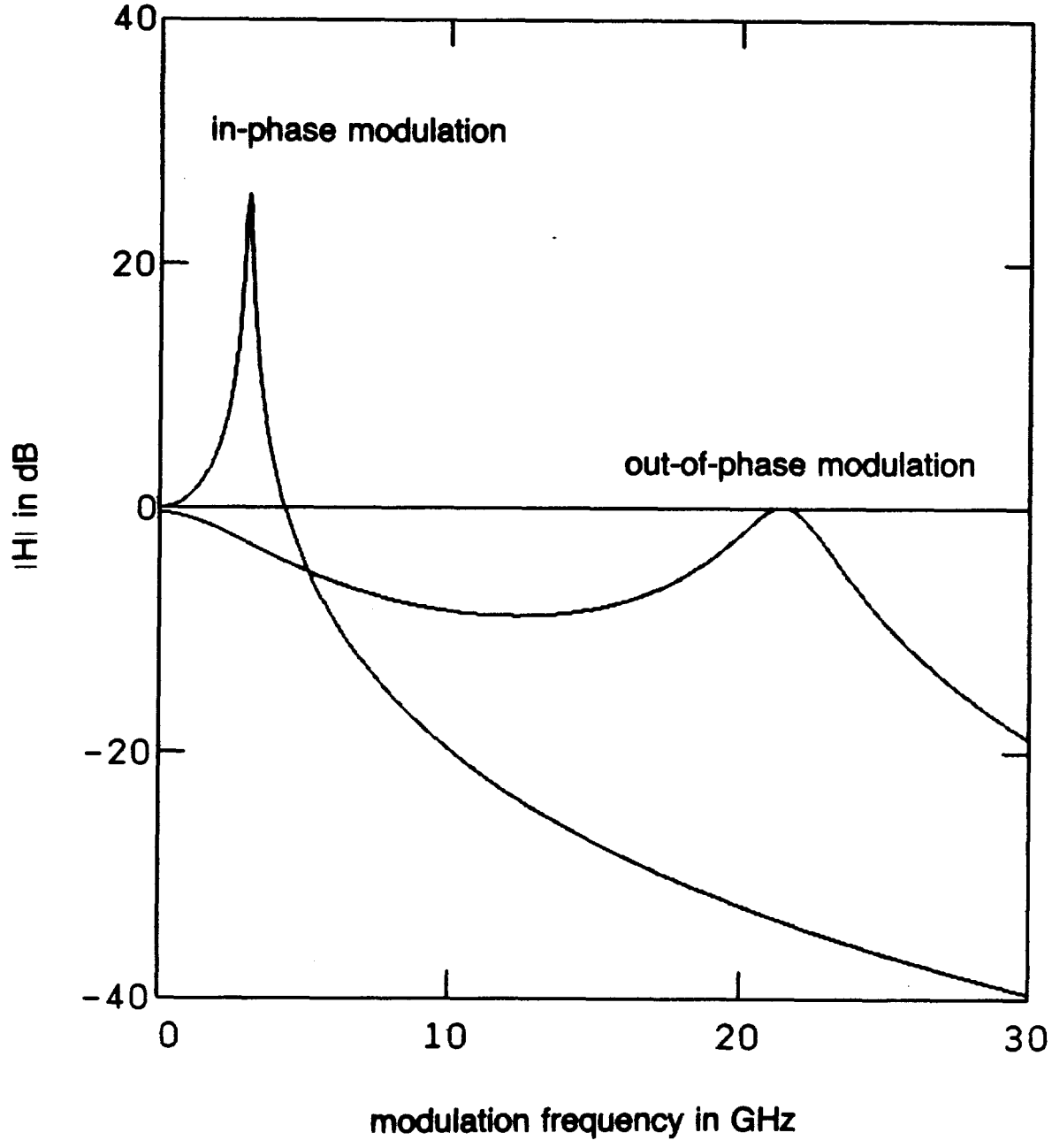

Figure 8.2.1 Twin-Emitter Modulation Transfer Functions for $\eta_l = 0$

Note the drastically different responses of the twin-emitter to in-phase and out-of-phase modulation. The in-phase modulation response peaks at the relaxation oscillation frequency (3 GHz). The out-of-phase resonant response at the lateral mode beat frequency (21 GHz) has a relatively wide 3 dB half-bandwidth of 1.6 GHz.

communications applications. It is interesting to compare them for longitudinal and lateral mode-locking. For longitudinal mode -locking[68],

$$\Delta\nu_{-3dB} = \frac{1}{4\pi}\frac{1}{\tau_p}\left[\frac{\Delta\lambda}{\Delta\lambda_{RO}}\right]^2 = 190 \text{ MHz} \tag{8.2.14}$$

where $\Delta\lambda$=3 Å is the inter-modal spacing and $\Delta\lambda_{RO}$=50 Å is the gain curve half-width, while for lateral mode-locking

$$\Delta\nu_{-3dB} = \frac{1}{4\pi}\frac{\alpha p^{(0)}}{\eta_R \tau_s} = 1.6 \text{ GHz} \tag{8.2.15}$$

For out-of-phase modulation, the lack of a peak at the relaxation oscillation frequency can be understood by noting that by (8.2.8), the average gain of the emitters is identically zero. Since both lateral modes respond to the average emitter gain, their amplitudes are constant and any modulation must be due to interference, which is driven efficiently only near the beat frequency. It should be emphasized that energy is transported back and forth between the emitters, not the lateral modes.

As found in Section 4.4, most of the η_R axis is in the region where both lateral modes are unstable, so the response of the hypothetical device with η_I=0 is of limited interest. Figure 8.2.2 shows |H| for out-of-phase modulation as a function of ν_{mod} and η_I for η_R=0.1, with η_I plotted in the same way as in Figures 4.4.3 and 4.4.4. The bold lines indicate the sections plotted in Figures 8.2.1 and 8.2.3. The most striking feature is the peak that occurs at

$$\nu_{res} = \frac{\eta_R}{\pi\tau_p} + \frac{p^{(0)}}{4\pi\tau_s\eta_R} \tag{8.2.16}$$

$$\eta_{I,res} = \frac{\alpha p^{(0)}\tau_p}{4\eta_R\tau_s} \tag{8.2.17}$$

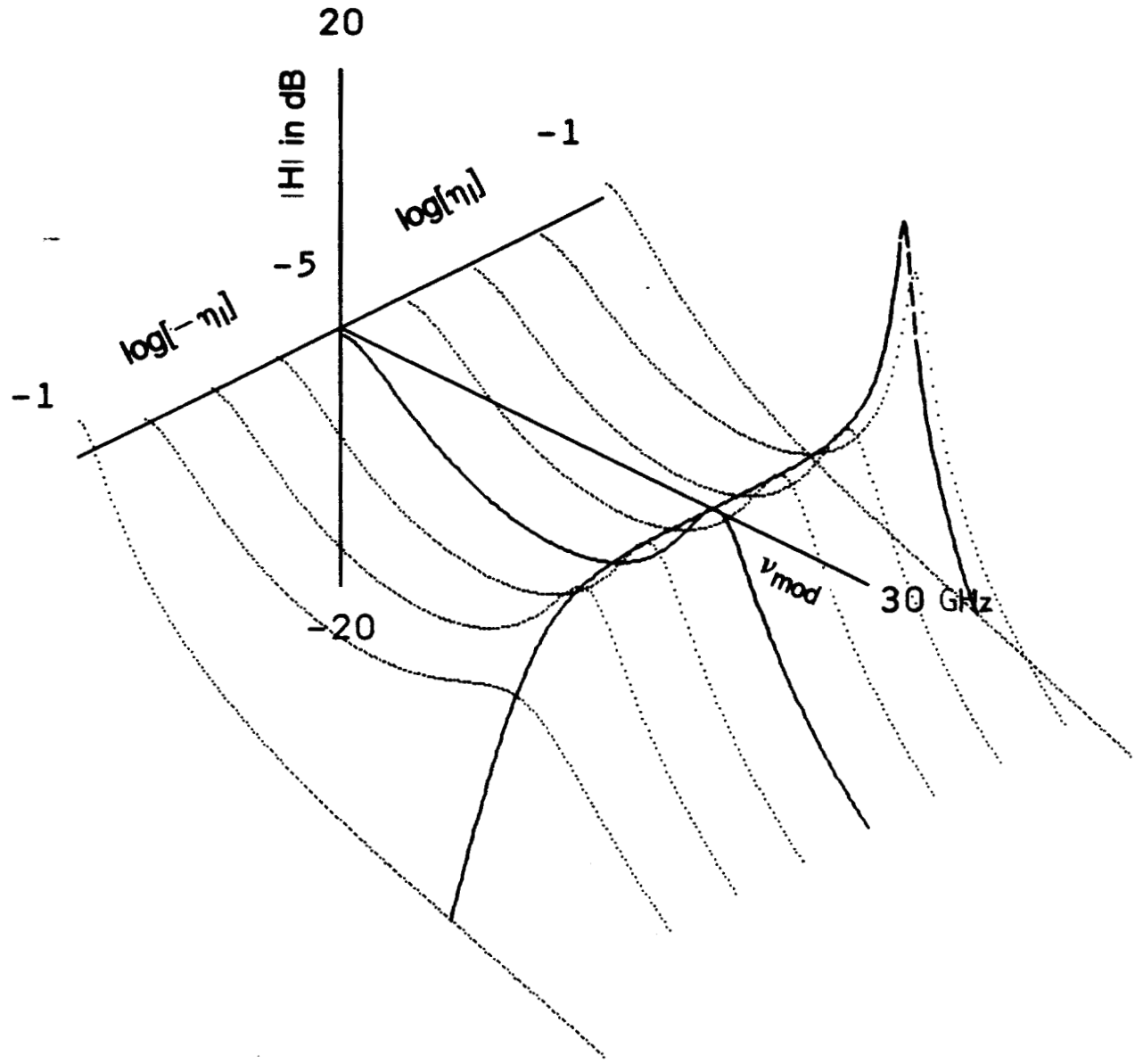

Figure 8.2.2 Out-of-Phase Modulation Transfer Function

The bold line along the modulation frequency axis represents the planar section plotted in Figure 8.2.1, while the other bold line is plotted in Figure 8.2.3.

to first order in $\tau_p/\tau_s<<1$. This is an exact resonance, in that $|H|\to\infty$, corresponding to the physically-meaningful root of the denominator of (8.2.6). For a device obeying (8.2.17), self-sustained oscillations are predicted by the theory. In reality, of course, physical mechanisms will dampen the resonant response. In contrast, the dependence of $|H|$ on η_I is very weak for in-phase modulation.

In the present case, the beat frequency of the modes is large compared to the relaxation oscillation frequency, and the boundary between the π-stable and unstable regions of the η-plane is given by

$$\eta_{I,bnd} = \frac{\alpha p^{(0)}\tau_p}{4\eta_R\tau_s} \tag{8.2.18}$$

as can be verified by expanding (4.4.34) to first order in $\tau_p/\tau_s<<1$. Comparison with (8.2.17) shows that the resonance lies on the out-of-phase stability boundary.

Figure 8.2.3 shows $|H|$ for out-of-phase modulation at the resonance frequency $\nu_{mod}=\eta_R/\pi\tau_p$ of a twin-emitter with $\eta_R=0.1$, as a function of η_I. Because of the stability properties of the equilibrium points, oscillation about the in-phase equilibrium point for $\eta_I<0$, and the out-of-phase equilibrium point for $\eta_I>0$ was assumed. Note that a large but stable response may be had by choosing $\eta_{I,bnd}<\eta_I<2\eta_{I,bnd}$. These values are quite small, so that the lateral modes have nearly equal gains and amplitudes. This is necessary for appreciable depth-of-modulation, and explains why $|H|$ falls off rapidly as $|\eta_I|$ increases. Modulation about the out-of-phase equilibrium point is preferred to modulation about the in-phase equilibrium point, because the small positive value of η_I needed to stabilize the former yields a response superior to that given by the large negative value of η_I needed to stabilize the latter.

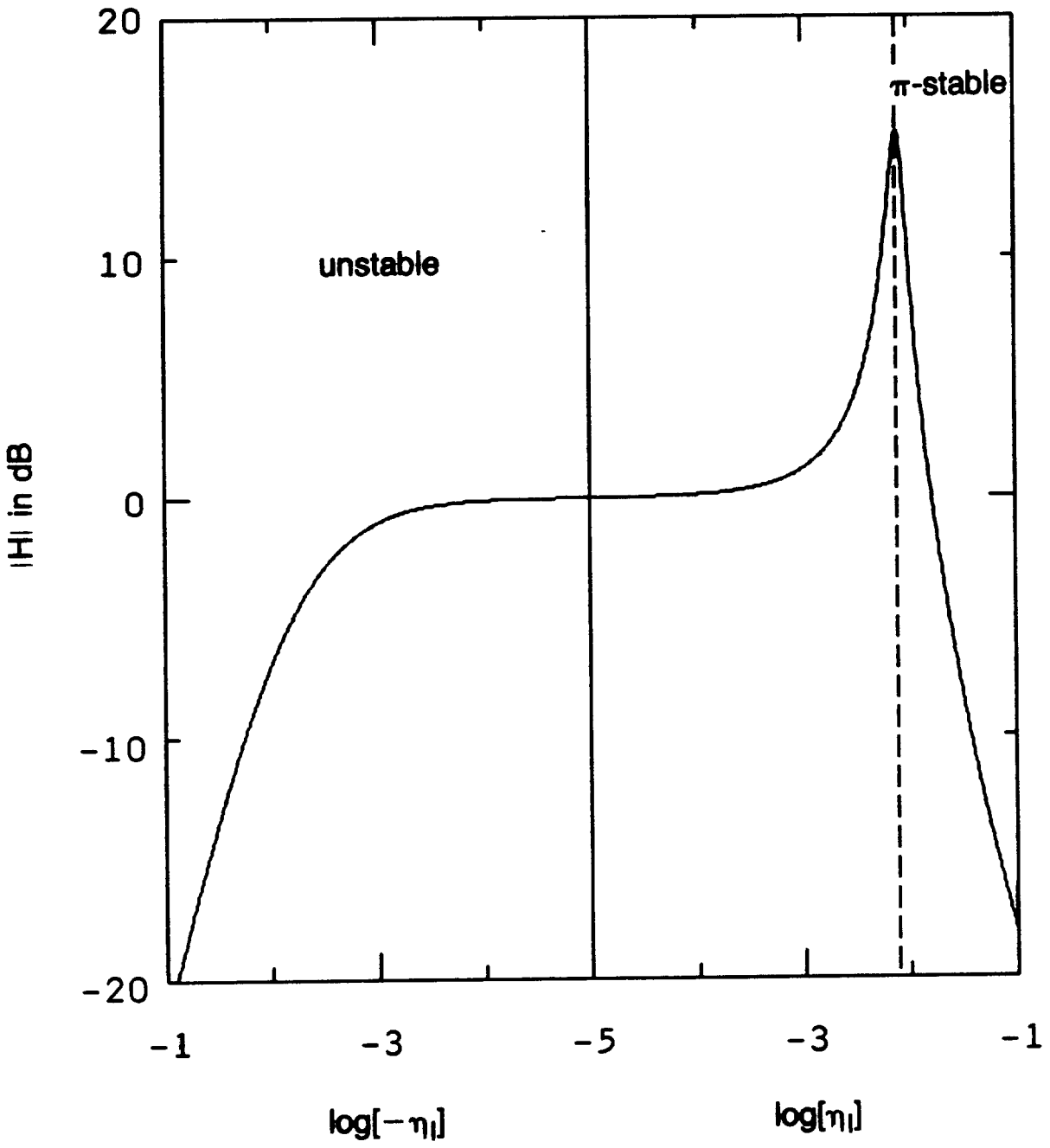

Figure 8.2.3 Out-of-Phase Transfer Function for Resonant Modulation

Stability and responsivity are simultaneously achieved if η_I is chosen somewhat inside the π-stable region.

Figure 8.2.4 contains the out-of-phase mode stability boundary shown in Figure 4.4.4. The "optimum design region" is bounded on the left (η_R=0.03, ν_{res}=6 GHz) by a desire for the mode-beating frequency to comfortably exceed the relaxation oscillation frequency, bounded on the right (η_R=0.3, ν_{res}=60 GHz) by the limits of physical realizability of design and model validity, as well as the present state of semiconductor laser driver technology, and bounded from below and above by $\eta_{I,bnd}$ and $2\eta_{I,bnd}$, respectively. Finally, η from Figure 4.5.4 is plotted with the emitter center-to-center spacing as the parameter, showing that the optimum design region is accessible by choosing the correct spacing.

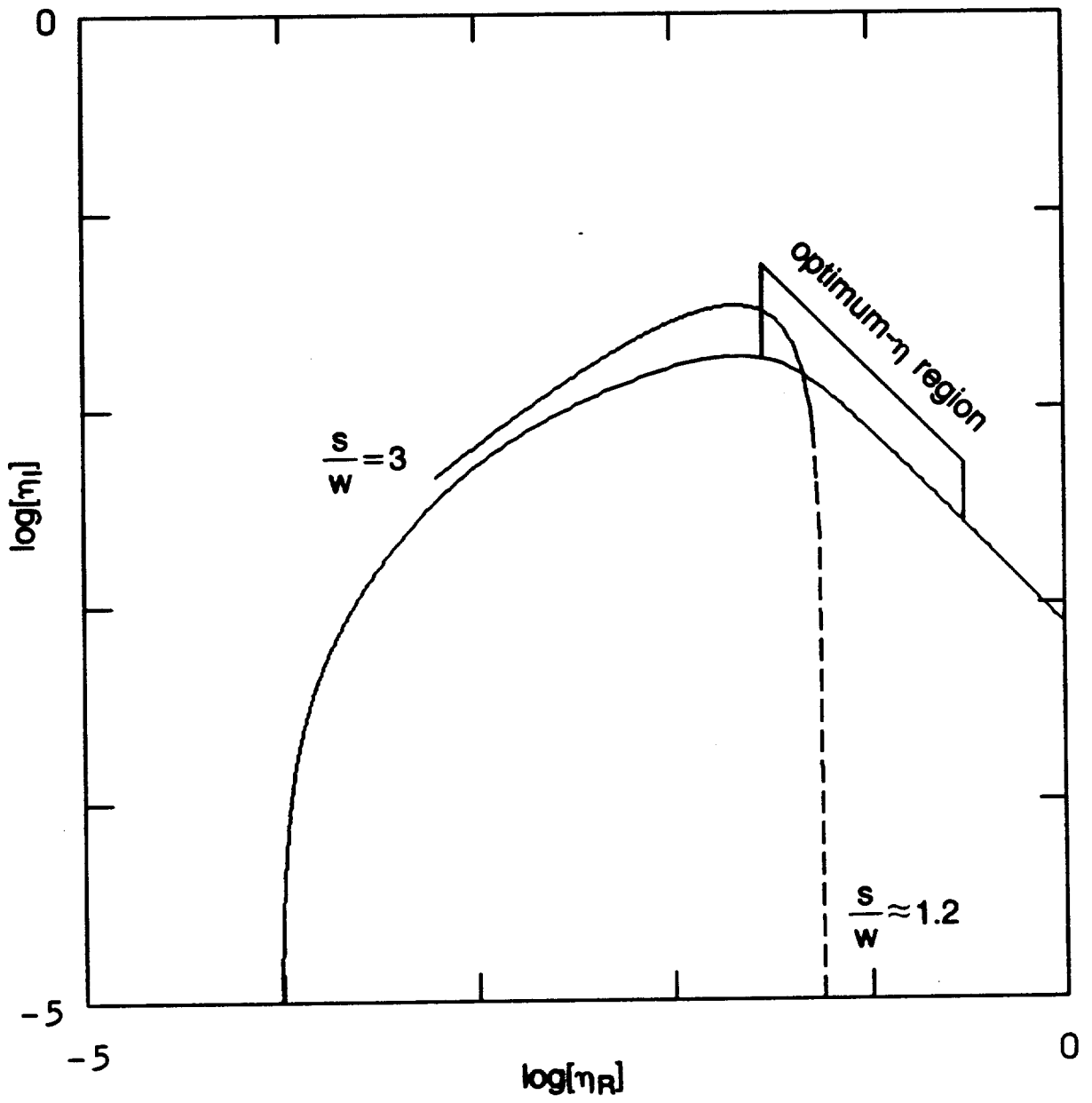

Figure 8.2.4 Twin-Emitter Optimum-η Region

Stability, responsivity and a 6−60 GHz resonant modulation frequency can be had within the optimum-η region. The η curve obtained from the five-layer model of Section 4.5 passes through the optimum-η region, raising hopes that twin-emitters with good modulation properties can be realized.

9. SUMMARY AND SUGGESTIONS FOR FUTURE WORK

A theoretical and experimental study of the picosecond dynamics of coherent semiconductor laser arrays has been presented. Single-emitter devices were discussed in Chapters 2 and 3. No dynamical effects with characteristic frequencies beyond the relaxation oscillation frequency are expected for single-emitters operating under ordinary experimental conditions. Since such frequencies have been observed in the intensity time series of arrays, they must be due to interactions among the emitters.

Coherent array rate equations were derived in Chapter 4, and the simplest case of a twin-emitter array was explored in detail. The stability of the lateral modes of the twin-emitter was determined as a function of the emitter coupling parameter, and the qualitative dependence of the coupling parameter on the spacing between the emitters was found.

The twin-emitter rate equations were numerically integrated in Chapter 5, to verify the foregoing analytical results and to more fully investigate the modeled dynamics.

Experimental results were presented in Chapters 6 and 7. No conclusive support for the twin-emitter model was obtained, largely because the available two-stripe devices had strongly-coupled emitters, undermining the validity of the model. Several results were consistent with predictions from coupled-emitter mode theory, however:

the $2^{1/2}$ ratio between the difference frequencies of the lateral modes of the three-emitter and the twin-emitter, the expected relationship between mode suppression and injection current, given by (6.6.3), and the matching of the predicted and observed asymptotic in-phase quiescence of device PGE4600B#1D4.

Injection current modulation of twin-emitters was discussed in Chapter 8. It was found that out-of-phase modulation of the emitters is essential to effective modulation beyond the relaxation oscillation frequency, and that both responsivity and stability can be achieved if the coupling parameter is chosen correctly.

The next step is a more thorough experimental evaluation of the twin-emitter model, using suitable devices. This may involve the fabrication of variable-coupling devices, as discussed in Chapter 7. If the model proves to be valid, research may proceed along two fronts: the study of the dynamics of free-running arrays, and the design of coherent arrays for high-frequency injection current modulation.

Future dynamical studies will require improved characterization techniques. The utility of the intensity power spectrum in distinguishing between various dynamical behaviors was mentioned in Chapter 5. The use of a fast photodiode and a spectrum analyzer to obtain real-time intensity power spectra would be vastly superior to Fourier-transforming intensity time series obtained from a streak camera. Auto- and cross-correlations of the fields or intensities from regions of the spatially-resolved near field may also be a useful experimental technique.

If dynamical chaos is to be identified and studied, more sophisticated characterizations[113] become necessary, such as the correlation dimension and the Lyapunov exponents of the intensity time series in reconstruction space. These characterizations typically require many more data points than available in a single streak cam-

era sweep ($\approx$500 data points). This can be surmounted in the case of the correlation dimension, in which the predecessor-successor relationship among data points neither enters its definition nor is used in algorithms for its calculation (see Chapter 7 of Reference [113]), by combining points from different video frames, as long as operating conditions are stable over the data-collection period. The predecessor-successor relationship is crucial in obtaining the Lyapunov exponents, however. Another problem is dynamical and measurement noise. Smoothing techniques[114] may be helpful in reducing noise and reconstructing local dynamics.

High-frequency optical communications systems are perhaps of greater technological interest. Engineering such a system around a coherent array will be a cross-disciplinary endevour; beside designing the array to fulfill the requirements of responsivity and stability, it must have good electrical characteristics, which may be difficult considering the frequencies and dimensions to be dealt with. To implement out-of-phase modulation, the upper electrical contact must consist of interleaved microwave strip lines, requiring a multi-step metallization process. Since the total optical output remains constant during out-of-phase modulation, the light-collection optics must spatially discriminate to effectively transfer the signal. Appropriate modulation (e.g., AM, FM) and transmission (e.g., line-of-sight, short-haul optical fiber) schemes must be identified. Finally, note that high-frequency modulation of 2-D VCSEL arrays may have applications in image processing, and that out-of-phase modulation of adjacent emitters can be effected by horizontally interleaving the upper-surface contacts, rather than the vertical-interleaving necessary for edge-emitting arrays. This may decrease parasitic capacitance, improving high-frequency electrical characteristics.

References

1. R. N. Hall, G. E. Fenner, J. D. Kingsley, T. J. Soltys, and R. O. Carlson, "Coherent light emission from GaAs p-n junctions," *Phys. Rev. Lett.*, vol. 9, pp. 366-368, 1 November 1962.
2. M. I. Nathan, W. P. Dumke, G. Burns, F. H. Dill, and G. J. Lasher, "Stimulated emission of radiation from GaAs p-n junctions," *Appl. Phys. Lett.*, vol. 1, pp. 62-64, November 1962.
3. I. Hayashi, M. B. Panish, P. W. Foy, and S. Sumski, "Junction lasers which operate continuously at room temperature," *Appl. Phys. Lett.*, vol. 17, pp. 209-211, 1 August 1970.
4. G. H. B. Thompson, "A theory for filamentation in semiconductor lasers including the dependence of dielectric constant on injected carrier density," *Optoelectronics*, vol. 4, p. 257, 1972.
5. H. C. Casey, Jr. and M. B. Panish, *Heterostructure Lasers*, Academic Press, New York, 1978.
6. J. E. Ripper, J. C. Dyment, L. A. D'Asaro, and T. L. Poole, "Stripe-geometry double heterostructure junction lasers: mode structure and CW operation above room temperature," *Appl. Phys. Lett.*, vol. 18, pp. 155-157, 15 February 1971.
7. T. P. Lee, C. A. Burrus, B. I. Miller, and R. A. Logan, "$Al_xGa_{1-x}As$ double heterostructure rib-waveguide injection laser," *IEEE J. Quantum Electron.*, vol. QE-11, pp. 432-435, July 1975.
8. T. Tsukada, "GaAs-$Ga_{1-x}Al_xAs$ buried-heterostructure injection lasers," *J. Appl. Phys.*, vol. 45, pp. 4899-4906, November 1974.
9. Z. L. Liau and J. N. Walpole, "Surface-emitting GaInAsP/InP laser with low threshold current and high efficiency," *Appl. Phys. Lett.*, vol. 46, pp. 115-117, 15 January 1985.
10. J. Puretz, R. K. DeFreez, R. A. Elliott, J. Orloff, and T. L. Paoli, "300 mW operation of a surface-emitting phase-locked array of diode lasers," *Electron. Lett.*, vol. 23, pp. 130-131, 29 January 1987.
11. G. A. Evans, N. W. Carlson, J. M. Hammer, M. Lurie, J. K. Butler, S. L. Palfrey, R. Amantea, L. A. Carr, F. Z. Hawrylo, E. A. James, C. J. Kaiser, J. B. Kirk, W. F. Reichert, S. R. Chinn, J. R. Shealy, and P. S. Zory, "Coherent, monolithic two-dimensional (10×10) laser arrays using grating surface emission," *Appl. Phys. Lett.*, vol. 53, pp. 2123-2125, 28 November 1988.
12. K. Iga, S. Kinoshita, and F. Koyama, "Microcavity GaAlAs/GaAs surface-emitting laser with $I_{th} = 6$ mA," *Electron. Lett.*, vol. 23, pp. 134-136, 29 January 1987.
13. M. Orenstein, E. Kapon, N. G. Stoffel, L. T. Florez, and J. P. Harbison, "Effects of Array Geometry on the Supermodes of 2-Dimensional Vertical Cavity Semiconductor Laser Arrays," *Technical Digest of the 1990 IEEE Lasers and Electro-Optics Society Annual Meeting (LEOS '90)*, Boston, Massachusetts, 4-9 November 1990. Paper SDL1.7/MKK7
14. E. Kapon, J. Katz, and A. Yariv, "Supermode analysis of phase-locked arrays of semiconductor lasers," *Opt. Lett.*, vol. 10, pp. 125-127, April 1984.

15. J. K. Butler, D. E. Ackley, and M. Ettenberg, "Coupled-Mode Analysis of Gain and Wavelength Oscillation Characteristics of Diode Lase Phased Arrays," *IEEE J. Quantum Electron.*, vol. 21, pp. 458-464, May 1985.

16. E. Kapon, Z. Rav-Noy, S. Margalit, and A. Yariv, "Phase-Locked Arrays of Buried-Ridge InP/InGaAsP Diode Lasers," *J. Lightw. Technol.*, vol. LT-4, pp. 919-925, July 1986.

17. D. F. Welch, P. Cross, D. Scifres, W. Streifer, and R. D. Burnham, "In-phase emission from index-guided laser array up to 400 mW," *Electron. Lett.*, vol. 22, pp. 293-294, 13 March 1986.

18. D. Botez, L. Mawst, P. Hayashida, G. Peterson, and T. J. Roth, "High-power, diffraction-limited beam operation from phase-locked diode-laser arrays of closely spaced "leaky" waveguides (antiguides)," *Appl. Phys. Lett.*, vol. 53, pp. 464-466, 8 August 1988.

19. R. A. Elliott, R. K. DeFreez, T. P. Paoli, R. D. Burnham, and W. Streifer, "Dynamic Characteristics of Phase-Locked Multiple Quantum Well Injection Lasers," *IEEE J. of Quantum Electron.*, vol. QE-21, pp. 598-602, June 1985.

20. N. Yu, *Dynamic Characterization of Coherent Semiconductor Laser Arrays, Ph.D. Thesis,* Oregon Graduate Institute of Science and Technology, Beaverton, Oregon, 1990.

21. R. K. DeFreez, N. Yu, D. J. Bossert, M. Felisky, G. A. Wilson, R. A. Elliott, H. G. Winful, G. A. Evans, N. W. Carlson, and R. Amantea, "Experimental Characterization of the Picosecond Spatio-Temporal Properties of Coherent Semiconductor Laser Arrays," *Proceedings of the OSA Topical Meeting on Nonlinear Dynamics in Optical Systems,* Afton, Oklahoma, June 4-8, 1990. Paper ThA1

22. R. K. DeFreez, R. A. Elliott, K. Hartnett, and D. F. Welch, "Quasi-Instantaneous ($<$20 ps) Phase Locking in Single-Lobe Y-Coupled Laser Diode Arrays," *Electron. Lett.*, vol. 23, pp. 589-590, 21 May 1987.

23. N. Yu, R. K. DeFreez, D. J. Bossert, R. A. Elliott, H. G. Winful, and D. F. Welch, "Observation of Sustained Self-Pulsation in CW Operated Flared Y-Coupled Laser Arrays," *Electron. Lett.*, vol. 24, pp. 1203-1024, 15 September 1988.

24. R. K. DeFreez, D. J. Bossert, N. Yu, K. Hartnett, R. A. Elliott, and H. G. Winful, "Spectral and picosecond temporal properties of flared guide Y-coupled phase-locked laser arrays," *Appl. Phys. Lett.*, vol. 53, pp. 2380-2382, 12 December 1988.

25. N. Yu, R. K. DeFreez, D. J. Bossert, G. A. Wilson, R. A. Elliott, S. S. Wang, and H. G. Winful, "Spatio-Spectral and Picosecond Spatio-Temporal Properties of a Broad Area Operating Channeled-Substrate-Planar Laser Array," *Appl. Opt.*, vol. 30, pp. 2503-2513, 20 June 1991.

26. R. K. DeFreez, D. J. Bossert, N. Yu, J. M. Hunt, H. Ximen, R. A. Elliott, N. W. Carlson, M. Lurie, G. A. Evans, J. M. Hammer, D. P. Bour, S. L. Palfrey, R. Amantea, H. G. Winful, and S. S. Wang, "Picosecond Optical Properties of a Grating Surface Emitting Two-Dimensional Coherent Laser Array," *IEEE Photonics Tech. Lett.*, vol. 1, pp. 209-211, August 1989.

27. R. K. DeFreez, M. Felisky, D. J. Bossert, G. A. Wilson, G. A. Evans, N. W. Carlson, R. Amantea, and H. G. Winful, "Spatio-temporal Properties of Grating

Surface Emitting Ring Lasers," *unpublished.*

28. M. Felisky, R. K. DeFreez, G. A. Wilson, G. A. Evans, N. W. Carlson, S. K. Liew, R. Amantea, J. H. Abeles, C. A. Wang, H. K. Choi, J. N. Walpole, and H. G. Winful, "Dynamics of CW Grating-Surface-Emitting Laser Arrays," *Technical Digest of the 1991 Conference on Lasers and Electro-Optics (CLEO '91)*, Baltimore, Maryland, May 12-17, 1991. Paper CWE6
29. M. Felisky, R. K. DeFreez, G. A. Wilson, G. A. Evans, N. W. Carlson, S. K. Liew, C. A. Wang, H. K. Choi, J. N. Walpole, and H. G. Winful, "Dynamics of CW Grating-Surface-Emitting Laser Arrays," *unpublished.*
30. F. T. Arecchi and R. G. Harrison, eds., *Instabilities and Chaos in Quantum Optics,* Springer-Verlag, Berlin, 1987.
31. L. M. Narducci, J. R. Tredicce, L. A. Lugiato, N. B. Abraham, and D. K. Bandy, "Mode-mode competition and unstable behavior in a homogeneously broadened ring laser," *Phys. Rev. A*, vol. 33, pp. 1842-1854, March 1986.
32. S. S. Wang and H. G. Winful, "Dynamics of phased-locked semiconductor laser arrays," *Appl. Phys. Lett.*, vol. 52, pp. 1774-1776, 23 May 1988.
33. H. G. Winful and S. S. Wang, "Stability of phase locking in coupled semiconductor laser arrays," *Appl. Phys. Lett.*, vol. 53, pp. 1894-1896, 14 November 1988.
34. S. S. Wang and H. G. Winful, "Dynamics of lateral modes in semiconductor laser arrays," *Proceedings of the Optical Society of America Topical Meeting on Nonlinear Dynamics in Optical Systems*, Afton, Oklahoma, 4-8 June 1990. Paper PdP3
35. E. Garmire, P. Menendez-Caldes, M. Ohtaka, and M. Ramadas, "Transverse-mode competition in gain-guided semiconductor laser arrays modelled as a single strongly-coupled multimode laser," *Proceedings of the Optical Society of America Topical Meeting on Nonlinear Dynamics in Optical Systems*, Afton, Oklahoma, 4-8 June 1990. Paper THA2
36. J. D. Jackson, *Classical Electromagnetism, 2nd Edition,* John Wiley & Sons, Inc., 1975.
37. G. P. Agrawal and N. K. Dutta, *Long-Wavelength Semiconductor Lasers,* Van Nostrand Reinhold, New York, 1986.
38. W. B. Joyce, "Carrier transport in double-heterostructure active layers," *J. Appl. Phys.*, vol. 53, pp. 7235-7239, November 1982.
39. J. A. Copeland, "Single-Mode Stabilization by Traps in Semiconductor Lasers," *IEEE J. Quantum Electron.*, vol. 16, pp. 721-727, July 1980.
40. G. R. Hadley, J. P. Hohimer, and A. Owyoung, "Comprehensive Modeling of Diode Arrays and Broad-Area Devices With Applications to Lateral Index Tailoring," *IEEE J. Quantum Electron.*, vol. 24, pp. 2138-2152, November 1988.
41. R. Olshansky, C. B. Su, J. Manning, and W. Powazinik, "Measurement of Radiative and Nonradiative Recombination Rates in InGaAsP and AlGaAs Light Sources," *IEEE J. Quantum Electron.*, vol. QE-20, pp. 838-854, August 1984.
42. G. Lasher and F. Stern, "Spontaneous and Stimulated Recombination Radiation in Semiconductors," *Phys. Rev.*, vol. 133, pp. A553-A563, 20 January 1964.

43. M. Yamada, "Analysis of gain suppression in undoped injection lasers," *J. Appl. Phys.*, vol. 52, pp. 2653-2664, April 1981.

44. R. A. Smith, *Semiconductor, 2nd Edition,* Cambridge University Press, Cambridge, 1978.

45. G. P. Agrawal, "Spectral hole-burning and gain saturation in semiconductor lasers: Strong-signal theory," *J. Appl. Phys.*, vol. 63, pp. 1232-1235, 15 February 1988.

46. G. P. Agrawal, "Gain Nonlinearities in Semiconductor Lasers: Theory and Application to Distributed Feedback Lasers," *IEEE J. Quantum Electron.*, vol. QE-23, pp. 860-868, June 1987.

47. R. F. Kazarinov, C. H. Henry, and R. A. Logan, "Longitudinal mode self-stabilization in semiconductor lasers," *J. Appl. Phys.*, vol. 53, pp. 4631-4644, July 1982.

48. K. A. Shore and T. E. Rozzi, "Transverse Switching Due to Hopf Bifurcation in Semiconductor Lasers," *IEEE J. Quantum Electron.*, vol. 20, pp. 246-255, March 1984.

49. B. C. Johnson and A. Mooradian, "Observation of gain compression in a GaAlAs diode laser through a picosecond transmission measurement," *Appl. Phys. Lett.*, vol. 49, pp. 1135-1137, 3 November 1986.

50. G. P. Agrawal, "Effect of Gain and Index Nonlinearities on Single-Mode Dynamics in Semiconductor Lasers," *IEEE J. Quantum Electron.*, vol. 26, pp. 1901-1909, November 1990.

51. G. H. B. Thompson, *Physics of Semiconductor Laser Devices,* John Wiley and Sons, 1980.

52. B. N. Gomatam and A. P. DeFonzo, "Theory of Hot Carrier Effects on Nonlinear Gain in GaAs-GaAlAs Lasers and Amplifiers," *IEEE J. Quantum Electron.*, vol. 26, pp. 1689-1704, October 1990.

53. K. Petermann, *Laser Diode Modulation and Noise,* Kluwer Academic Publishers, Dordrecht, 1988.

54. S. Wiggins, *Introduction to Applied Nonlinear Dynamical Systems and Chaos,* Springer-Verlag, New York, 1990.

55. M. W. Hirsch and S. Smale, *Differential Equations, Dynamical Systems, and Linear Algebra,* Academic Press, 1974.

56. N. Minorsky, *Nonlinear Oscillations,* Robert E. Krieger Publishing Company, Malabar, Florida, 1962.

57. G. P. Agrawal, "Effect of Gain Nonlinearities on the Dynamic Response of Single-Mode Semiconductor Lasers," *IEEE Photonics Tech. Lett.*, vol. 1, pp. 419-421, December 1989.

58. R. S. Tucker, "High-Speed Modulation of Semiconductor Lasers," *Jour. Lightw. Tech.*, vol. LT-3, pp. 1180-1192, December 1985.

59. K. Y. Lau, N. Bar-Chaim, I. Ury, Ch. Harder, and A. Yariv, "Direct amplitude modulation of short-cavity GaAs lasers up to X-band frequencies," *Appl. Phys. Lett.*, vol. 43, pp. 1-3, 1 July 1983.

60. K. Y. Lau and A. Yariv, "Ultra-High Speed Semiconductor Lasers," *IEEE J. Quantum Electron.*, vol. 21, pp. 121-138, February 1985.

61. S. Takahashi, T. Kobayashi, H. Saito, and Y. Furukawa, "GaAs/AlGaAs DH Lasers with buried facets," *Japan. J. Appl. Phys.*, vol. 17, pp. 865-870, 1978.

62. I. Suemune, L. A. Coldren, M. Yamanishi, and Y. Kan, "Extremely wide modulation bandwidth in a low threshold current strained quantum well laser," *Appl. Phys. Lett.*, vol. 53, pp. 1378-1380, 10 October 1988.

63. E. Meland, R. Holmstrom, J. Schlafer, R. B. Lauer, and W. Powazinik, "Extremely High-Frequency (24 GHz) InGaAsP Diode Lasers with Excellent Modulation Efficiency," *Electron. Lett.*, vol. 26, pp. 1827-1829, 11 October 1990.

64. R. S. Tucker and D. J. Pope, "Microwave Circuit Models of Semiconductor Injection Lasers," *IEEE Trans. Microwave Theory Tech.*, vol. 31, pp. 289-294, March 1983.

65. J. E. Bowers, B. R. Hemenway, A. H. Gnauck, and D. P. Wilt, "High-Speed InGaAsP Constricted-Mesa Lasers," *IEEE J. Quantum Electron.*, vol. 22, pp. 833-844, June 1986.

66. M. A. Newkirk and K. J. Vahala, "Measurement of the fundamental modulation response of a semiconductor laser to millimeter wave frequencies by active-layer photomixing," *Appl. Phys. Lett.*, vol. 55, pp. 939-941, 4 September 1989.

67. K. Y. Lau, I. Ury, and A. Yariv, "Passive and active mode locking of a semiconductor laser without an external cavity," *Appl. Phys. Lett.*, vol. 46, pp. 1117-1119, 15 June 1985.

68. K. Y. Lau, "Narrow-Band Modulation of Semiconductor Lasers at Millimeter Wave Frequencies ($>$ 100 GHz) by Mode Locking," *IEEE J. of Quantum Electron.*, vol. 26, pp. 250-261, February 1990.

69. G. A. Wilson, R. K. DeFreez, and H. G. Winful, "Modulation of Twin-Emitter Semiconductor Lasers Beyond the Frequency of Relaxation Oscillations," *Optics Comm.*, vol. 82, pp. 293-298, 15 April 1991.

70. G. A. Wilson, R. K. DeFreez, and H. G. Winful, "Modulation of Phased-Array Semiconductor Lasers Beyond the Frequency of Relaxation Oscillations," *Technical Digest of the 1991 Conference on Lasers and Electro-Optics (CLEO '91)*, Baltimore, Maryland, May 12-17, 1991. Paper CWE3

71. G. A. Wilson, R. K. DeFreez, and H. G. Winful, "Modulation of Phased-Array Semiconductor Lasers at K-Band Frequencies," *IEEE J. Quantum Electron.*, vol. 27, pp. 1696-1704, June 1991.

72. W. H. Loh, A. T. Schremer, and C. L. Tang, "Polarization Self-Modulation at Multigigahertz Frequencies in an External-Cavity Semiconductor Laser," *IEEE Photonics Tech. Lett.*, vol. 2, pp. 467-469, July 1990.

73. M. Nakamura, K. Aiki, N. Chinone, R. Ito, and J. Umeda, "Longitudinal-mode behaviors of mode-stabilized $Al_xGa_{1-x}As$ injection lasers," *J. Appl. Phys.*, vol. 49, pp. 4644-4648, September 1978.

74. J. Manning, R. Olshansky, D. M. Fye, and W. Powazinik, "Strong Influence of Nonlinear Gain on Spectral and Dynamic Characteristics of InGaAsP Lasers," *Electron. Lett.*, vol. 21, pp. 496-497, 23 May 1985.

75. W. Streifer, R. D. Burnham, and D. R. Scifres, "Dependence of Longitudinal Mode Structure on Injected Carrier Diffusion in Diode Lasers," *IEEE J. Quantum Electron.*, vol. 13, pp. 403-404, June 1977.

76. M. Ohtsu and Y. Otsuka, "Precise measurements and computer simulations of mode-hopping phenomena in semiconductor lasers," *Appl. Phys. Lett.*, vol. 46, pp. 108-110, 15 January 1985.

77. G. Gray and R. Roy, "Bistability and Mode-Hopping in a Semiconductor Laser," *J. Opt. Soc. Am. B*, vol. 8, pp. 632-638, March 1991.

78. M. Yamada, "Theory of Mode Competition Noise in Semiconductor Injection Lasers," *IEEE J. Quantum Electron.*, vol. 22, pp. 1052-1059, July 1986.

79. R. W. Tkach and A. R. Chraplyvy, "Regimes of Feedback Effects in 1.5-μm Distributed Feedback Lasers," *J. Lightwave Tech.*, vol. 4, pp. 1655-1661, November 1986.

80. D. Lenstra, B. H. Verbeek, and A. J. Den Boef, "Coherence Collapse in Single-Mode Semiconductor Lasers Due to Optical Feedback," *IEEE J. Quantum Electron.*, vol. 21, pp. 674-679, June 1985.

81. H. Olesen, J. H. Osmundsen, and B. Tromborg, "Nonlinear Dynamics and Spectral Behavior for an External Cavity Laser," *IEEE J. Quantum Electron.*, vol. 22, pp. 762-773, June 1986.

82. D. Kato, "Microscale degradation in (GaAl)As double-heterostructure diode lasers," *Appl. Phys. Lett.*, vol. 31, pp. 588-590, 1 November 1977.

83. A. E. Siegman, *Lasers,* University Science Books, 1986.

84. H. A. Haus, "Theory of Mode-Locking with a Slow Saturable Absorber," *IEEE J. Quantum Electron.*, vol. 11, pp. 736-746, 1975.

85. R. Lang, "Intensity Pulsation Enhancement by Self-Focusing in Semiconductor Injection Lasers," *Japan. J. Appl. Phys.*, vol. 19, pp. L93-L96, February 1980.

86. J. Buus, "Models of the Static and Dynamic Behavior of Stripe Geometry Lasers," *IEEE J. Quantum Electron.*, vol. 19, pp. 953-960, June 1983.

87. F. R. Nash, "Mode guidance parallel to the junction plane of double-heterostructure GaAs lasers," *J. Appl. Phys.*, vol. 44, pp. 4696-4707, October 1973.

88. R. Lang, "Lateral Transverse Mode Instability and Its Stabilization in Stripe Geometry Injection Lasers," *IEEE J. Quantum Electron.*, vol. 15, pp. 718-726, August 1979.

89. J. P. Van Der Ziel, "Self-Focusing Effects in Pulsating $Al_xGa_{1-x}As$ Double-Heterostructure Lasers," *IEEE J. Quantum Electron.*, vol. 17, pp. 60-68, January 1981.

90. P. A. Kirkby, A. R. Goodwin, G. H. B. Thompson, and P. R. Selway, "Observations of Self-Focusing in Stripe Geometry Semiconductor Lasers and the Development of a Comprehensive Model of Their Operation," *IEEE J. Quantum Electron.*, vol. 13, pp. 705-719, August 1977.

91. D. C. van Eck, "Wavefront measurements on semiconductor lasers," *IEEE J. Quantum Electron.*, vol. QE-19, pp. 966-968, June 1983.

92. A. Yariv, *Optical Electronics, 3rd Edition,* Holt, Rinehart and Winston, 1985.

93. D. R. Scifres, W. Streifer, and R. D. Burnham, "Beam scanning with twin-stripe injection lasers," *Appl. Phys. Lett.*, vol. 33, pp. 702-704, 15 October 1978.

94. K. A. Shore, "Semiconductor laser bistable operation with an adjustable trigger," *Opt. Quantum Electron.*, vol. 14, pp. 321-326, 1982.

95. I. H. White, J. E. Carroll, and R. G. Plumb, "Closely coupled twin-stripe lasers," *IEE Proc.*, vol. 129-I, pp. 291-296, December 1982.

96. K. A. Shore and P. J. Hartnett, "Diffusion and waveguiding effects in twin-stripe injection lasers," *Opt. Quantum Electron.*, vol. 14, pp. 169-176, 1982.

97. T. Kumar, R. F. Ormondroyd, and T. E. Rozzi, "A Self-Consistent Model of the Lateral Behavior of a Twin-Stripe Injection Laser," *IEEE J. Quantum Electron.*, vol. 22, pp. 1975-1985, October 1986.

98. J. K. Butler, D. E. Ackley, and D. Botez, "Coupled-mode analysis of phase-locked injection laser arrays," *Appl. Phys. Lett.*, vol. 44, pp. 293-295, 1 February 1984.

99. H. G. Unger, *Planar Optical Waveguides and Fibres,* Clarendon Press, Oxford, 1977.

100. B. W. Hakki and T. L. Paoli, "Gain Spectra in GaAs double-heterostructure injection lasers," *J. Appl. Phys.*, vol. 46, pp. 1299-1306, March 1975.

101. S. S. Lee, L. Figueroa, and R. Ramaswamy, "Variations of linewidth enhancement factor and linewidth as a function of laser geometry in (AlGa)As lasers," *IEEE J. Quantum Electron.*, vol. QE-25, pp. 862-870, May 1989.

102. R. K. DeFreez, "Focused-Ion Beam Micromachining: A Fabrication Tool for Prototypal Semiconductor Lasers," *Proceedings of the Second International Meeting on Advanced Processing and Characterization Technologies*, vol. AIP Conference Proceedings No. 227, Clearwater Beach, Florida, USA, May 8-10, 1991.

103. J. E. Bowers and M. A. Pollack, *Optical Fiber Telecommunications II,* Academic Press, Inc., 1988.

104. R. A. Peters, ed., "A Special Issue on Inter-satellite Links," *Satellite Communications*, vol. 6, 1988.

105. H. Matsueda, "AlGaAs OEIC Transmitters," *Jour. Lightw. Tech.*, vol. LT-5, pp. 1382-1390, October 1987.

106. N. Bar-Chaim, I. Ury, and A. Yariv, "Integrated Optoelectronics," *IEEE Spectrum*, pp. 38-45, May 1982.

107. K. Y. Lau, "Efficient narrow-band direct modulation of semiconductor injection lasers at millimeter wave frequencies of 100 GHz and beyond," *Appl. Phys. Lett.*, vol. 52, pp. 2214-2216, 27 June 1988.

108. K. A. Shore and T. E. Rozzi, *Optical Nonlinearities and Instabilities in Semiconductors, Chapter 17,* Academic Press, Inc., 1988.

109. K. A. Shore and T. E. Rozzi, "Switching frequency for transverse modes in stripe-geometry injection lasers," *Opt. Quantum Electron.*, vol. 15, pp. 497-506, 1983.

110. K. A. Shore, *Private Communication.*

111. G. P. Agrawal, "Effect of Intraband Gain Saturation on Semiconductor Laser Dynamics," *Proceedings of the OSA Topical Meeting on Nonlinear Dynamics in Optical Systems, Paper MA2,* Afton, Oklahoma, June 4-8, 1990.

112. E. Hemery, L. Chusseau, and J.-M. Lourtioz, "Dynamical Behaviors of Semiconductor Lasers Under Strong Sinusoidal Current Modulation: Modeling and Experiments at 1.3 μm," *IEEE J. Quantum Electron.*, vol. 26, pp. 633-641, April 1990.

113. T. S. Parker and L. O. Chua, *Practical numerical algorithms for chaotic systems,* Springer-Verlag, Berlin, 1989.

114. E. J. Kostelich and J. A. Yorke, "Noise reduction in dynamical systems," *Phys. Rev. A,* vol. 38, pp. 1649-1652, 1 August 1988.

115. R. K. Willardson and A. C. Beer, *Semiconductors and Semimetals, Vol. 2,* Academic Press, 1966.

116. I. S. Gradshteyn and I. M. Ryzhik, *Table of Integrals, Series, and Products,* Academic Press, New York, 1980.

A. DYNAMICAL EFFECTS OF HEATING

Local heat generation during operation causes a temperature distribution in the transverse plane. An increase in temperature has various effects: in the active region, the band gap shrinks, shifting the gain peak to a longer wavelength, and the Fermi distribution of carrier state occupancy is broadened, reducing the peak gain. Also, the effective index of the waveguide increases, shifting the modes to longer wavelengths.

The time-dependent heat diffusion equation for the temperature T(x,y,t) can be written as

$$C\frac{\partial}{\partial t}T - \kappa\nabla_t^2 T = r_q(x,y,t) \tag{A.1}$$

where C is the heat capacity per unit volume, r_q is the rate of generation of heat energy per unit volume and κ is the thermal conductivity. This equation holds for devices with abrupt boundaries between regions, so that both C and κ are piecewise-constant. The appropriate boundary condition is the conservation of the normal component of heat flow per unit area, $-\kappa\nabla_t T\cdot\hat{n}$. As is the case with the carrier distribution, it is not our goal to solve for the static temperature distribution, but rather to determine whether temperature fluctuations can enter into the 500 MHz-50 GHz dynamical regime of interest. We turn now to this question.

It has been argued that the dominant source of heat generation is the non-radiative decay of carriers[40]. Accepting this argument yields

$$r_q = \frac{n(y,t)}{\tau_{nr}} \hbar\omega_0 d\delta(x-x_{act}) \tag{A.2}$$

where $\hbar\omega_0$ is the energy released by decay, τ_{nr} is the time constant for non-radiative decay of carriers and δ is the Dirac δ-function, representing a thin active layer at $x=x_{act}$. For simplicity we neglect lateral dependence and reduce the problem to one-dimensional heat diffusion in the vertical direction, and assume that C and κ are piecewise-constant and independent of T. Lasers mounted epilayer-up have more severe heating problems than those mounted epilayer-down, so we will model the worst case by assuming that a heat sink of constant temperature T_{hs} is at $x\leq 0$ and that $\kappa=0$ for $x>x_{act}$, so that heat is forced to flow toward the heat sink. This converts (A.1) into homogeneous form subject to the boundary condition

$$\lim_{x\to x_{act}} \left[\frac{\partial T}{\partial x}\right](t) = \frac{n(t)\hbar\omega_0 d}{\tau_{nr}\kappa} \tag{A.3}$$

Assume that the carrier density is given by

$$n(t) = n^{(0)} + n^{(1)}\cos[\Omega t] \tag{A.4}$$

to obtain the temperature response at the frequency Ω. The temperature distribution when $n^{(1)}=0$ is

$$T^{(0)} = T_{hs} + \frac{n^{(0)}\hbar\omega_0 d}{\tau_{nr}\kappa} x \tag{A.5}$$

The temperature distribution due to $n^{(1)}\neq 0$ is

$$T^{(1)} = \frac{n^{(1)}\hbar\omega_0 d}{\tau_{nr}} \left[\frac{1}{\kappa C\Omega}\right]^{1/2} \exp\left[\frac{x-x_{act}}{L_T}\right] \cos\left[\frac{x-x_{act}}{L_T} + \Omega t - \frac{\pi}{4}\right] \tag{A.6}$$

where the characteristic length

$$L_T \equiv \left[\frac{2\kappa}{C\Omega}\right]^{\frac{1}{2}} \tag{A.7}$$

has been used.

The dynamic temperature distribution $T^{(1)}$ induces a periodic fluctuation in the gain and index of refraction near the active layer. Temperature waves should be unable to affect the optical mode if their characteristic length is much shorter than the vertical spot size. Setting $L_T=w_x$ to get the high-frequency cutoff, we note that $w_x \ll x_{act} \approx 100$ μm for an epilayer-up device. This justifies neglecting the other damped-traveling-wave solution in matching the $T^{(1)}(x=0)=0$ boundary condition in (A.6). The high-frequency cutoff for temperature waves is therefore

$$\nu_{max} = \frac{\kappa}{\pi C L_T^2} \tag{A.8}$$

For GaAs, pages 17 and 52 of Reference [115] give $\kappa=0.45$ W/cm/kelvin and $C=1.7$ J/cm^3/kelvin, respectively. If we set $L_T=0.5$ μm, a typical vertical spot size, then $\nu_{max}=34$ MHz. This is much lower than the 500 MHz-50 GHz range of concern in this thesis, and strongly indicates that temperature is negligible as a dynamical effect.

To further justify the neglect of temperature fluctuations, we can calculate the maximum temperature fluctuation corresponding to this frequency, given by

$$T_{max}^{(1)} = \frac{n^{(1)}\hbar\omega_0 d}{\tau_{nr}}\left[\frac{1}{2\pi\kappa C\nu_{max}}\right]^{\frac{1}{2}} \tag{A.9}$$

Assuming that $n^{(1)}=n_{th}$ and $\tau_{nr}=\tau_s$, and using values from Table 4.2 of Reference [20] $n_{th}=3\times10^{18}$ cm^{-3}, $\hbar\omega_0=1.52$ eV, $\tau_s=2.4$ ns and $d=0.14$ μm, then $T_{max}^{(1)}=0.35$

kelvin for ν_{max}=34 MHz, which is negligible.

B. POPULATION PULSATIONS AND FOUR-WAVE MIXING

The goal of this appendix is to justify the neglect of population pulsations and four-wave mixing in the dynamical regime of interest. The major difference between these effects is that four wave mixing involves three modes which need to be fairly evenly-spaced in frequency for phase-matching, while population pulsation involves two modes and is thus automatically phase-matched. Population pulsations contribute to the suppression of side modes. Because of the automatic phase-matching, this contribution is static, so that the population pulsation mechanism can be left out of the dynamics.

Four wave mixing, however, can have a non-zero beat frequency that can drive dynamics. The contribution to the susceptibility of the mth mode involves interactions of the mth, kth and (2k−m)th modes[46], where k is summed over all the modes such that $k \neq m$. The beat frequency of the four wave mixing interaction and the mth mode is

$$\Delta\nu_{m,k} = 2\nu_k - \nu_m - \nu_{2k-m} \tag{B.1}$$

In a Fabry-Perot cavity, the longitudinal modes are nearly evenly-spaced, and $\Delta\nu_{m,k}$ is small but non-zero. If we interpret the mode index j as the number of wavelengths of light in a cavity round trip, then

$$\nu_j = \frac{c}{2L\mu_{e,j}}j \tag{B.2}$$

where j can be considered continuous and Fabry-Perot modes exist at integer values of j. Expanding ν_k in a Taylor Series about ν_m

$$\nu_k = \nu_m + \left[\frac{\partial \nu}{\partial j}\right]_m (k-m) + \frac{1}{2}\left[\frac{\partial^2 \nu}{\partial j^2}\right]_m (k-m)^2 \tag{B.3}$$

Substituting (B.3) into (B.1) gives

$$\Delta\nu_{m,k} = -\left[\frac{\partial^2 \nu}{\partial j^2}\right]_m (k-m)^2 \tag{B.4}$$

A simple model for the effective phase index frequency dependence is

$$\mu_{e,j} = \frac{\mu_{e,m}}{1-\left[\frac{\mu_{g,e,m}}{\mu_{e,m}}-1\right]\left[\frac{\nu_j}{\nu_m}-1\right]} \tag{B.5}$$

which by construction satisfies (2.2.2:11). Substituting (B.5) into (B.2) and rearranging gives

$$\nu_j = \nu_m \frac{j}{\frac{\mu_{e,m}}{\mu_{g,e,m}} m + \left[1-\frac{\mu_{e,m}}{\mu_{g,e,m}}\right] j} \tag{B.6}$$

Differentiating twice and evaluating at j=m, using (B.2) evaluated at j=m to eliminate m and using

$$\hbar\omega = \frac{hc}{\lambda} \tag{B.7}$$

transforms (B.4) into

$$\Delta\nu_{m,k} = \frac{c\lambda_m}{2\mu_{e,m}\mu_{g,e,m}L^2}\left[1-\frac{\mu_{e,m}}{\mu_{g,e,m}}\right](k-m)^2 \tag{B.8}$$

Using $c=3\times10^{10}$ cm/s, λ_m=818 nm, L=240 μm, $\mu_{e,m}$=3.3 and $\mu_{g,e,m}$=4.1 gives

$$\Delta\nu_{m,k} = 31\ \text{MHz}\cdot(k-m)^2 \qquad \text{(B.9)}$$

which requires $|k-m|>4$ to push $\Delta\nu$ into the 500 MHz-50 GHz realm of interest. Since the ratio of the four-wave mixing to the spectral hole-burning contributions to the susceptibility of the main mode is third-order in the ratio of side-mode to main-mode amplitudes (see Equations (17) and (19) of Reference [46]), the four-wave mixing contribution is either too weak (for distant sidemodes) or too low in frequency (for neighboring sidemodes) to be significant.

C. LINEAR STABILITY THEORY

Assume we have a set of N autonomous, ordinary nonlinear differential equations

$$\dot{y}_k = f_k(y_1,\ldots,y_N) \tag{C.1}$$

that has at least one equilibrium solution

$$f_k(y_1^{(0)},\ldots,y_N^{(0)}) = 0 \tag{C.2}$$

for each k. To study the evolution of small perturbations about the equilibrium point, let

$$y_k = y_k^{(0)} + y_k^{(1)}(t) \tag{C.3}$$

Using the chain rule on (C.1) and substituting (C.2) and (C.3) gives

$$\dot{y}_k^{(1)} = \sum_{m=1}^{N} \left[\frac{\partial f_k}{\partial y_m}\right]^{(0)} y_m^{(1)} \tag{C.4}$$

or in matrix notation,

$$\dot{\mathbf{y}}^{(1)} = \mathbf{J}^{(0)}\, \mathbf{y}^{(1)} \tag{C.5}$$

where $\mathbf{J}^{(0)}$ is the N×N Jacobian matrix evaluated at the equilibrium point.

The system has been linearized for a small neighborhood about the equilibrium point. It is well-known that linear ordinary differential equations with constant

coefficients have solutions of the form

$$y_k^{(1)} = y_k^{(1)}(t=0)\, e^{\lambda t} \tag{C.6}$$

where λ is a complex constant, often called a Lyapunov exponent in this context. Substituting (C.6) into (C.5) gives

$$[\lambda \mathbf{I} - \mathbf{J}^{(0)}]\, \mathbf{y}^{(1)}(t=0) = 0 \tag{C.7}$$

where $\mathbf{I}$ is the N×N identity matrix. Since $\mathbf{y}^{(1)}(t=0)$ can be arbitrarily chosen, it is required that

$$\det\, [\lambda \mathbf{I} - \mathbf{J}^{(0)}] = 0 \tag{C.8}$$

This gives an Nth degree polynomial equation in λ, with in general N complex roots. The condition for stability of the equilibrium point to small perturbations is

$$\mathrm{Re}\, [\lambda_k] < 0 \tag{C.9}$$

for all k.

The Hurwitz criterion (see Chapter 5 of Reference [56]) gives the necessary and sufficient conditions that the roots of a real polynomial all have negative real parts. The specific cases N=2 and N=3 are applicable to the twin-emitter model of Section 4.4.

For N=2, the characteristic equation is

$$\lambda^2 + A_1 \lambda + A_2 = 0 \tag{C.10}$$

and the Hurwitz criterion is

$$A_1 > 0 \;\cap\; A_2 > 0 \tag{C.11}$$

For N=3, the characteristic equation is

$$\lambda^3 + A_1\lambda^2 + A_2\lambda + A_3 = 0 \tag{C.12}$$

and the Hurwitz criterion is

$$A_1 > 0 \ \cap \ A_1A_2 - A_3 > 0 \ \cap \ A_3 > 0 \tag{C.13}$$

Stability boundaries are found by changing one of the inequalities of (C.11) or (C.13) to an equality to obtain a relationship among the parameters making up the coefficients of the characteristic equation. That boundary can then be associated with the condition being violated. Note that $A_1=0$ cannot be imposed on (C.13) without simultaneously violating one of the other conditions, so that no new stability boundaries are found by doing that.

The imaginary part of a root crossing into the $\mathrm{Re}[\lambda]>0$ half-plane gives the angular frequency of the incipient instability at the stability boundary. If we set $A_2=0$ in (C.11) or $A_3=0$ in (C.13), the critical root passes through the origin so that this frequency is zero, and the trajectories in the neighborhood of the equilibrium point are radial. If we set $A_1=0$ in (C.11), then

$$\lambda = \pm i \cdot A_2^{1/2} \tag{C.14}$$

Finally, if we set $A_1A_2-A_3=0$ in (C.13), (C.12) factors into

$$(\lambda^2+A_2)(\lambda+A_1) = 0 \tag{C.15}$$

It is clear that the first factor contributes the roots of interest, which are given by (C.14).

D. OPTICAL FEEDBACK ESTIMATION

An important parameter in calculating the optical feedback to a semiconductor laser in an external cavity is

$$C \equiv \left[\frac{R_{ext}}{R}\right]^{\frac{1}{2}} (1-R) \cdot \frac{\tau_{ext}}{\tau_L} \cdot [1+\alpha^2]^{\frac{1}{2}} \qquad (D.1)$$

given in Chapter 9 of Reference [53]. Here, R and R_{ext} are the power reflectivities of the facet and the external cavity, respectively, and τ_{ext} and τ_L are the round-trip times of the external cavity and the laser, respectively. In the experiments described in this thesis, R_{ext} represents undesired reflections from optical components in a setup for characterizing coherent semiconductor laser arrays, rather than an actual external cavity. The goal of this appendix is to estimate R_{ext}.

A typical optical setup is shown in Figure D.1. The semiconductor laser is imaged onto the entrance slit of either a streak camera or a spectrometer using a microscope objective. Typically, a large image-to-object conjugate ratio is used. Optical feedback comes from two sources: direct reflections from the surfaces of the microscope objective, and the imaging of the partially-reflecting slit blades back onto the semiconductor laser facet. We assume that the optical output of the semiconductor laser is an elliptical gaussian beam, a convenient approximation that is adequate for the purpose at hand.

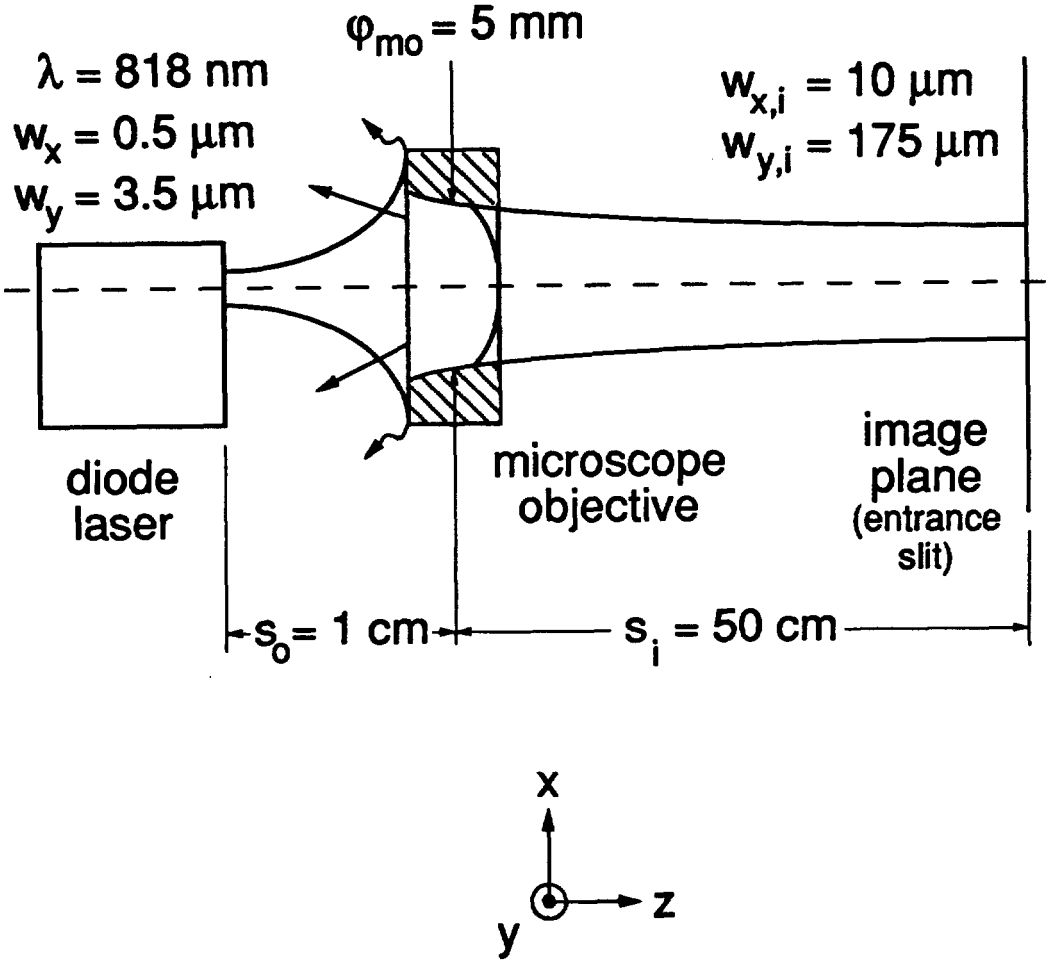

Figure D.1 Characterization Experiment Input Optics

The large conjugate-ratio imaging optics typical of a characterization experiment subject the semiconductor laser to optical feedback from two sources: specular reflection from the front surface of the microscope objective and re-imaged partial reflection from the physical object in the image plane.

To estimate the first contribution, we note that the object distance is typically much greater than either of the confocal parameters of the beam, so that the beam is in the far-field regime by the time it reflects from the microscope objective and returns to the facet. The intensity of an elliptical gaussian beam in the far-field, normalized to unit power crossing the any transverse plane, is

$$I(x,y) = \frac{2\pi w_x w_y}{\lambda^2 z^2} \exp\left[-2\frac{\pi^2 w_x^2}{\lambda^2 z^2}x^2\right] \exp\left[-2\frac{\pi^2 w_y^2}{\lambda^2 z^2}y^2\right] \tag{D.2}$$

Multiplying the axial value at $z=2s_o$ by the area of the guided mode

$$\text{area} = \pi w_x w_y \tag{D.3}$$

and multiplying by the power reflectivity of the microscope objective front surface R_{mo} gives the overlap of the returning beam with the guided mode, approximately equal to R_{ext}

$$R_{ext} \approx 2R_{mo}\left[\frac{\pi w_x w_y}{2s_o\lambda}\right]^2 \tag{D.4}$$

which gives $R_{ext} = 3\times10^{-9}$, using $R_{mo} = .04$ and the values given in Figure D.1. This is far too small to be of any practical importance.

The problem of light returning from the slit is much more serious. We envision this process as follows: some fraction η of the beam from the semiconductor laser passes through the aperture of the microscope objective and is imaged onto the partial reflector. Usually the spot size in the lateral direction at the microscope objective is small compared to the ϕ_{mo}, the diameter of the microscope objective, but the vertical spot size is somewhat greater than ϕ_{mo}. Therefore

$$\eta \approx [2\pi]^{1/2}\frac{w_x\phi_{mo}}{\lambda s_o} \tag{D.5}$$

The partial reflector is for our purposes is characterized by

$$H = \frac{\text{axial reflected power per steradian}}{\text{incident power}} \tag{D.6}$$

Therefore

$$R_{ext} = \eta H \frac{\pi \phi_{mo}^2}{4 s_i^2} \tag{D.7}$$

The parameter H was measured using the setup shown in Figure D.2. A lens internal to the microscope objective formed a real image of the filament in the object plane. This was imaged through the neutral density filter by the 50 mm lens onto the image plane, at which either a power meter or a partial reflector could be placed. In the latter case, the reflected light was imaged by the 50 mm lens onto the re-image plane, using the neutral density filter as a beam-splitter. It was observed that the reflected light was uniform over the area subtended by the 50 mm lens. By measuring the ratio of the power at the re-image plane to the power at the image plane, corrected for loss at the neutral density filter, and knowing the solid angle subtended by the 50 mm lens as seen from the image plane, H could be calculated. H=3.5/steradian was measured for a shiny end-milled aluminum block similar in roughness to the stainless-steel entrance slit blades of the SPEX 1.26 meter grating spectrometer. H=.12/steradian was measured for a black-anodized aluminum block. The uncertainty of these values was estimated to be about 5 %.

Using η=.3, H=3.5/steradian and the values given in Figure D.1, (D.7) gives $R_{ext} = 2 \times 10^{-5}$, which may be large enough to destabilize the semiconductor laser. Actually, there is another effect that will reduce this somewhat, that of phase disruption of the reflected beam by roughness of the surface of the slit. This effect was not

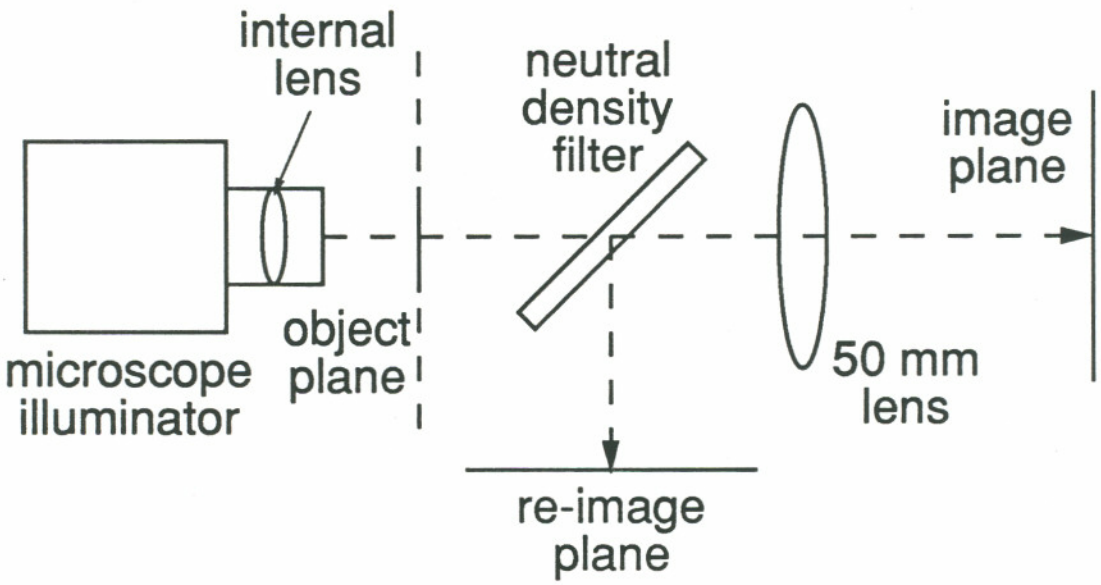

Figure D.2 Backscattering of Light Measurements

accounted for by the experiment illustrated in Figure D.2 because an incoherent source was used. This effect can be estimated by calculating the overlap of the ideal and actual reflected modes at the image plane, given by

$$\Theta \equiv \int_{-\infty}^{\infty} dx \int_{-\infty}^{\infty} dy \; G^2(x,y) e^{i\phi(x,y)} \tag{D.8}$$

where G is the field of the fundamental elliptical gaussian mode at the image plane

$$G(x,y) = \left[\frac{2}{\pi w_{x,i} w_{y,i}}\right]^{1/2} \exp\left[-\frac{x^2}{w_{x,i}^2}\right] \exp\left[-\frac{y^2}{w_{y,i}^2}\right] \tag{D.9}$$

where

$$w_{x(y),i} \equiv \frac{s_i}{s_o} w_{x(y)} \tag{D.10}$$

and ϕ is a random variable such that

$$\langle e^{i\phi(x,y)} \rangle = 0 \tag{D.11}$$

and

$$\langle e^{-i\phi(x',y')} e^{i\phi(x,y)} \rangle = d^2 \delta(x'-x, y'-y) \tag{D.12}$$

(D.11) embodies the assumption that the surface roughness is much larger than a wavelength of light, effectively randomizing the phase of the reflected light at any point. (D.12) holds if d, the characteristic length of the surface features, is small compared to $w_{x,i}$ and $w_{y,i}$. The expectation value for the reduction due to phase disruption is

$$\langle |\Theta|^2 \rangle^{1/2} = \frac{d}{[\pi w_{x,i} w_{y,i}]^{1/2}} \tag{D.13}$$

The end-milled aluminum block was found to have a characteristic roughness length

of d=3 μm, giving $<|\Theta|^2>^{1/2}=.025$. This must be regarded as a very crude estimate. Using $<|\Theta|^2>^{1/2}R_{ext}$ and R_{ext} as estimates of the range of the external reflectivity gives $R_{ext}=5\times10^{-7}$ to $R_{ext}=2\times10^{-5}$.

E. SUPERMODES AND EMITTER COUPLING

This appendix demonstrates the application of the dynamical theory of emitter coupling developed in Section 4.3, assuming that the array lateral modes are given by the well-known supermodes that result from a coupled-mode description of coherent semiconductor laser arrays.

In supermode theory[14,98], the array modes are assumed to be linear combinations of the P single-emitter modes

$$f_m(y) = \sum_{p=1}^{P} f_0(y-y_p)\cdot S_{p,m} \tag{E.1}$$

where there are P supermodes, since no more can be linearly independent. Multiplying (E.1) by $f_0^*(y-y_q)$ and integrating over the lateral coordinate gives the matrix equation

$$\mathbf{B} = \mathbf{A}\cdot\mathbf{S} \tag{E.2}$$

where **A** and **B** are defined by (4.3.7) and (4.3.8), respectively, and **S** is the P×P matrix whose elements are $S_{p,m}$. This allows the simplification of (4.3.16) to

$$\boldsymbol{\eta} = \mathbf{S}\cdot\boldsymbol{\Lambda}\cdot\mathbf{S}^{-1} \tag{E.3}$$

where Λ is defined by (4.3.13). One particular case that has been discussed in the literature[14] is

$$S_{p,m} = \sin\left[\pi \frac{pm}{P+1}\right] \tag{E.4}$$

$$\Lambda_{m,m} = \frac{\Delta}{2}\cos\left[\pi \frac{m}{P+1}\right] \tag{E.5}$$

where Δ is the angular frequency difference between the lowest- and highest-order supermodes in the $P\to\infty$ limit, normalized to τ_p.

The inverse of $\mathbf{S}$ is given by

$$\mathbf{S}^{-1} = \frac{2}{P+1}\mathbf{S} \tag{E.6}$$

which we digress to prove before proceeding:

$$[\mathbf{S}^{-1}\cdot\mathbf{S}]_{p,r} = [\mathbf{S}\cdot\mathbf{S}^{-1}]_{p,r} = \frac{2}{P+1}\sum_{q=1}^{P}\sin\left[\pi \frac{pq}{P+1}\right]\sin\left[\pi \frac{qr}{P+1}\right] \tag{E.7}$$

Using a trigonometric identity this becomes

$$[\mathbf{S}\cdot\mathbf{S}^{-1}]_{p,r} = \frac{1}{P+1}\sum_{q=1}^{P}\cos\left[\pi \frac{(p-r)q}{P+1}\right] - \cos\left[\pi \frac{(p+r)q}{P+1}\right] \tag{E.8}$$

which can be evaluated using

$$\sum_{q=1}^{P}\cos\left[\pi \frac{nq}{P+1}\right] = \begin{bmatrix} P \\ -1 \\ 0 \end{bmatrix} \quad \text{for n} \quad \begin{bmatrix} 0 \\ \neq 0 \text{ and even} \\ \neq 0 \text{ and odd} \end{bmatrix} \tag{E.9}$$

to obtain

$$[\mathbf{S}\cdot\mathbf{S}^{-1}]_{p,r} = \delta_{p,r} \tag{E.10}$$

where $\delta_{p,r}$ is the Kronecker symbol, verifying (E.6).

Substituting (E.4) and (E.6) into (E.3) gives

$$\eta_{p,r} = \frac{\Delta}{P+1} \sum_{q=1}^{P} \sin\left[\pi \frac{pq}{P+1}\right] \cos\left[\pi \frac{q}{P+1}\right] \sin\left[\pi \frac{qr}{P+1}\right] \tag{E.11}$$

Using trigonometric identities this becomes

$$\eta_{p,r} = \frac{\Delta}{4(P+1)} \sum_{q=1}^{P} \cos\left[\pi \frac{(p-r-1)q}{P+1}\right] + \cos\left[\pi \frac{(p-r+1)q}{P+1}\right]$$

$$-\cos\left[\pi \frac{(p+r-1)q}{P+1}\right] - \cos\left[\pi \frac{(p+r+1)q}{P+1}\right] \tag{E.12}$$

which can be simplified using (E.9) to get

$$\eta_{p,r} = \frac{\Delta}{4}[\delta_{p,r+1} + \delta_{p,r-1}] \tag{E.13}$$

In other words, the coupling matrix is bi-diagonal so that each emitter is coupled only to its nearest neighbors. Moreover, the coupling is the same for any pair of adjacent emitters. We have just worked backward from the conclusions to the assumptions of Reference [14], which demonstrates the relationship of the dynamical theory developed in Section 4.3 to an accepted static theory.

F. THREE-EMITTER THEORY

The three-emitter analogs of the twin-emitter rate equations (4.4.14)-(4.4.18), without spontaneous emission and gain compression, are

$$\tau_p \frac{d}{dt} X_1 = Z_1 X_1 - \eta_R X_2 \sin\theta_1 - \eta_I X_2 \cos\theta_1 \tag{F.1}$$

$$\tau_p \frac{d}{dt} X_2 = Z_2 X_2 + \eta_R X_1 \sin\theta_1 - \eta_I X_1 \cos\theta_1$$

$$- \eta_R X_3 \sin\theta_2 - \eta_I X_3 \cos\theta_2 \tag{F.2}$$

$$\tau_p \frac{d}{dt} X_3 = Z_3 X_3 + \eta_R X_2 \sin\theta_2 - \eta_I X_2 \cos\theta_2 \tag{F.3}$$

$$\tau_p \frac{d}{dt} \theta_1 = -\alpha[Z_2 - Z_1] + \eta_R \left[\frac{X_1}{X_2} - \frac{X_2}{X_1}\right] \cos\theta_1 + \eta_I \left[\frac{X_1}{X_2} + \frac{X_2}{X_1}\right] \sin\theta_1$$

$$+ \eta_R \frac{X_3}{X_2} \cos\theta_2 - \eta_I \frac{X_3}{X_2} \sin\theta_2 \tag{F.4}$$

$$\tau_p \frac{d}{dt} \theta_2 = -\alpha[Z_3 - Z_2] + \eta_R \left[\frac{X_2}{X_3} - \frac{X_3}{X_2}\right] \cos\theta_2 + \eta_I \left[\frac{X_2}{X_3} + \frac{X_3}{X_2}\right] \sin\theta_2$$

$$- \eta_R \frac{X_1}{X_2} \cos\theta_1 - \eta_I \frac{X_1}{X_2} \sin\theta_1 \tag{F.5}$$

$$\tau_s \frac{d}{dt} Z_1 = p_1(t) - Z_1 - [1+2Z_1]X_1^2 \tag{F.6}$$

$$\tau_s \frac{d}{dt} Z_2 = p_2(t) - Z_2 - [1+2Z_2]X_2^2 \tag{F.7}$$

$$\tau_s \frac{d}{dt} Z_3 = p_3(t) - Z_3 - [1+2Z_3]X_3^2 \tag{F.8}$$

Assuming constant pumping p_i for i=1 to 3, and setting d/dt=0 gives the autonomous equilibrium conditions.

For simplicity, we impose the symmetry conditions

$$p_1 = p_3 \tag{F.9}$$

$$X_1 = X_3 \tag{F.10}$$

$$Z_1 = Z_3 \tag{F.11}$$

$$\theta_1 = -\theta_2 \tag{F.12}$$

and define

$$u \equiv \frac{X_2}{X_1} \tag{F.13}$$

Using (F.9)-(F.13), (F.1) and (F.3) become identical and yield

$$Z_1 = u[\eta_R \sin\theta_1 + \eta_I \cos\theta_1] \tag{F.14}$$

and (F.2) yields

$$Z_2 = \frac{2}{u}[-\eta_R \sin\theta_1 + \eta_I \cos\theta_1] \tag{F.15}$$

Either (F.4) or (F.5) can be used with (F.14) and (F.15) to get

$$\tan\theta_1 = \frac{\eta_R+\alpha\eta_I}{\alpha\eta_R-\eta_I}\frac{2-u^2}{2+u^2} \tag{F.16}$$

For simplicity, assume that since the emitters have a common p-contact, the injection current distributes itself so that the carrier number and thus the gain in each emitter is the same. This is equivalent to neglecting the resistance of the cladding layers, so that the (constant) voltage drop across the device terminals equals the potential difference between the quasi-Fermi-levels of the electrons and holes in the active layer. Obviously this is a questionable approximation, but is implicit in supermode theory. A different approximation is to assume that the differential resistance of the p-n junction is zero, so that it is an ideal voltage sink. This fixes the voltage dropped by the cladding layers, and thus the injection current, assuming a constant terminal voltage. Thus the emitter currents, but not necessarily their gains, would be equal. This leads to a more complicated situation that will not be further discussed.

Using $Z_1=Z_2$ to equate (F.14) and (F.15), and using (F.16) gives

$$u^4 = 2 \quad \rightarrow \quad u = 2^{1/4} \tag{F.17}$$

as the only real, non-negative root. Substituting (F.17) into (F.16) gives

$$\theta_1 = 0 \text{ or } \pi \tag{F.18}$$

corresponding to an in-phase mode +++ and an out-of-phase mode +−+, respectively.

Note that a third mode +0−, predicted from supermode theory, requires that $X_2=0$. This renders Z_2 undeterminable from the steady-state version of (F.2), and requires $Z_1=Z_3=0$, by (F.1) and (F.3), and thus $Z_2=0$ by the equal-gain assumption.

What this means is that the +0− mode can exist only in passive coupled waveguides, where the net gains are identically zero. A physical interpretation is that the +0− mode is energetically unfavorable since it wastes the gain in the center emitter.

The shift in oscillation frequency of the lateral modes from the isolated emitter mode is given by[14]

$$\Delta\omega_N = -\frac{2\eta_R}{\tau_p}\cos\left[\pi\frac{N+1}{P+1}\right] \tag{F.19}$$

where P=3 is the number of emitters and N=0 (2) is the number of nodes of the +++ (+−+) mode. Thus

$$\eta_R = \frac{\tau_p}{8^{1/2}}(\omega_{+-+}-\omega_{+++}) \tag{F.20}$$

The relationship between the imaginary part of the coupling parameter and the equilibrium gain is found by substituting (F.17) and (F.18) into either (F.14) or (F.15) to get

$$Z = \pm 2^{1/2}\eta_I \tag{F.21}$$

where + (−) is used for the +++ (+−+) mode. Therefore, for the three-emitter, η is a factor of $2^{1/2}$ smaller than the value calculated using the twin-emitter theory, as accounted for in Section 6.6.

Since the allowed modes are both symmetrical with respect to reflection in the y=0 plane, given (F.9), lateral asymmetry is forbidden and (F.10)-(F.12) hold at all times, not only at equilibrium. This allows (F.3), (F.5) and (F.8) to be dropped as redundant, and the remaining equations to be rewritten as

$$\tau_p\frac{d}{dt}X_1 = Z_1X_1 - \eta'_RX'\sin\theta_1 - \eta'_IX'\cos\theta_1 \tag{F.22}$$

$$\tau_p \frac{d}{dt} X' = Z_2 X' + \eta'_R X_1 \sin\theta_1 - \eta'_I X_1 \cos\theta_1 \tag{F.23}$$

$$\tau_p \frac{d}{dt} \theta_1 = -\alpha[Z_2 - Z_1]$$

$$+ \eta'_R \left[\frac{X_1}{X'} - \frac{X'}{X_1} \right] \cos\theta_1 + \eta'_I \left[\frac{X_1}{X'} + \frac{X'}{X_1} \right] \sin\theta_1 \tag{F.24}$$

$$\tau_s \frac{d}{dt} Z_1 = p_1(t) - Z_1 - [1+2Z_1]X_1^2 \tag{F.25}$$

$$\tau_s \frac{d}{dt} Z_2 = p_2(t) - Z_2 - [1+2Z_2]2X'^2 \tag{F.26}$$

where

$$X' \equiv 2^{-\frac{1}{2}} X_2 \tag{F.27}$$

and

$$\eta' = 2^{\frac{1}{2}} \eta \tag{F.28}$$

Note that (F.22)-(F.26) are identical in form to the twin-emitter equations (4.4.14)-(4.4.18), but for the factor of 2 in the last term of (F.26). Thus, it is reasonable to suppose that the stability properties are similar. Note that η' would be the value measured if twin-emitter theory were applied directly to the three-emitter 1D4 in Section 6.6.

G. PROPOSED DIFFRACTION-COUPLED TWIN-EMITTER

Since both techniques discussed in Section 7.3 failed to produce working devices with altered or variable coupling, a different approach was sought for future work. In the interest of simplicity, a monolithic solution is preferred. In this appendix, the idea of including a diffractive coupling section by cleaving one of the facets beyond the end of the waveguides is explored.

A schematic of the proposed device is shown in Figure G.1. Each of the twin emitters consists of a guided-wave gain section and an unpumped diffractive section. The complex round-trip propagation factor Y is defined as the ratio of the electric field to its value on the previous round-trip for an isolated emitter, and encompasses the following processes: round-trip propagation through both the amplifying and lossy regions, reflection from both facets, and mode-mismatch loss when the returning diffracted wave re-enters the waveguide. Partial reflection of the wave as it emerges from the guide into the diffractive section is neglected, and the unpumped diffractive section is considered unsaturable for simplicity. For an isolated stripe, Y=1 is the familiar steady-state condition.

For a twin-emitter, temporarily neglecting evanescent coupling, diffractive coupling can be incorporated by writing

$$E_1 = Y[E_1+\epsilon E_2] \qquad (G.1)$$

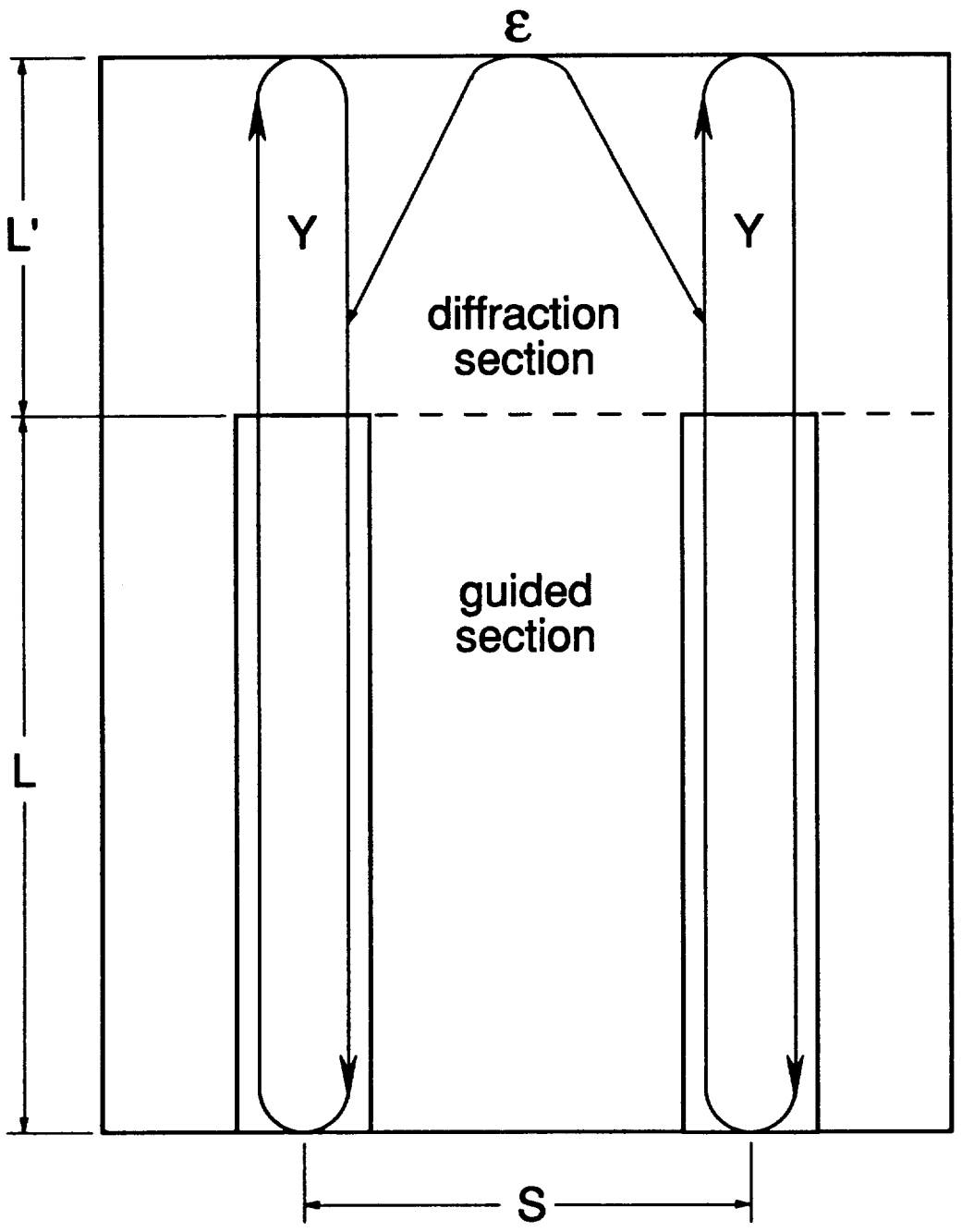

Figure G.1 Proposed Diffraction-Coupled Twin-Emitter

where E_1 and E_2 are the steady-state electric fields upon emergence from the guide into the diffractive section for emitters 1 and 2, and ϵ is the ratio of the overlap integral of the diffracted wave from emitter 1 and the guided mode of emitter 2, to the overlap integral of the diffracted wave from emitter 1 and the guided mode of emitter 1. A relationship similar to (G.1) can be found by interchanging the subscripts, and combined with (G.1) to give

$$Y = 1 - \pm\epsilon \tag{G.2}$$

to first order in the small quantity ϵ, where the + (−) sign is to be chosen for the in-phase (out-of-phase) mode. $|Y|$ and $\arg(Y)$, and thus $\mathrm{Re}(\epsilon)$ and $\mathrm{Im}(\epsilon)$, are related to the threshold gain and oscillation frequency, respectively, of the mode. For the in-phase mode, $\mathrm{Re}(\epsilon)>0$ decreases the threshold by reducing $|Y|$, and $\mathrm{Im}(\epsilon)>0$ decreases the oscillation frequency by reducing $\arg(Y)$, which is positive because of the phase-sign convention established by (2.2.2.2). The opposite statements hold for the out-of-phase mode.

The foregoing result suggests that diffractive coupling can be viewed as a linear perturbation in the same way as evanescent coupling, and that the two contributions are additive. The next step is to relate ϵ to η_{diff}, the diffractive contribution. The magnitude of the round-trip field gain is given by (6.4.2), where the round-trip transit time is given by (6.4.6) with L→L+L′. By using these with (2.4.3.5) (neglecting gain roll-off and compression), (4.4.10) and (6.2.5), we get

$$\ln|Y| = \frac{hc}{q}\frac{1-R}{\lambda}\frac{1}{\dfrac{dP_{out}}{dJ}}Z \tag{G.3}$$

Substituting (G.2), expanding the logarithm to first order in $\mathrm{Re}(\epsilon)$ and using (4.4.21)

gives

$$\mathrm{Im}(\eta_{\mathrm{diff}}) = -\frac{q}{hc}\frac{\lambda}{1-R}\frac{dP_{out}}{dJ}\mathrm{Re}(\epsilon) \tag{G.4}$$

Assuming the other quadrature bears the same relationship gives

$$\eta_{\mathrm{diff}} = -i\frac{q}{hc}\frac{\lambda}{1-R}\frac{dP_{out}}{dJ}\epsilon \tag{G.5}$$

Finally, ϵ must be related to the device parameters, particularly the diffractive section length L′. This can be done by assuming that the guided mode is gaussian with a plane phase-front, that begins to spread is the lateral direction upon entering the diffractive region, occupying $0<z<L'$. The electric field can be written

$$\mathbf{E}(y,z) = \hat{y}U(y,z)\exp(ikz) \tag{G.6}$$

where

$$U \equiv \left(\frac{2}{\pi}\right)^{1/4}\left[\frac{1}{w_y(z)}\right]^{1/2}\exp\left[\frac{i}{2}\tan^{-1}\left(\frac{z}{b}\right)\right]$$

$$\cdot\exp\left[-\left(1-i\frac{z}{b}\right)\left(\frac{y}{w_y(z)}\right)^2\right] \tag{G.7}$$

$$w_y(z) = w_y\left[1+\frac{z^2}{b^2}\right]^{1/2} \tag{G.8}$$

$$b = \frac{\pi\mu_e w_y^2}{\lambda} \tag{G.9}$$

and k is the longitudinal propagation factor in the diffractive section, w_y is the beam waist size (e^{-1} half-width of the field) and b is the confocal parameter.

Propagation of the wave from z=0 to z=L′, reflection from the facet and return to z=0, and uni-directional propagation from z=0 to z=2L′ are equivalent for calculating the overlap integrals of the guided modes of the two emitters and the diffracting wave. This allows ϵ to be written

$$\epsilon = \frac{\zeta(S)}{\zeta(0)} \tag{G.10}$$

where

$$\zeta(S) \equiv \int_{-\infty}^{\infty} dy \, \exp\left[-\left(\frac{y-S}{w_y}\right)^2 - \left(1-i\frac{2L'}{b}\right)\left(\frac{y}{w_y(z)}\right)^2\right] \tag{G.11}$$

after the common z-dependent complex amplitude is cancelled. An analytic solution to $\zeta(S)$ is given by Equation 3.923 of Reference [116]. After some algebra, (G.10) gives

$$\epsilon = \exp\left[\frac{1}{1+L'^2/b^2}\frac{S^2}{2w_y^2}\left(-1+i\frac{L'}{b}\right)\right] \tag{G.12}$$

The dependence of ϵ on L′ is of interest. $|\epsilon|$ monotonically increases with L′

$$0 \rightarrow L' \rightarrow \infty \quad \Rightarrow \quad |\epsilon|_{min} \rightarrow |\epsilon| \rightarrow 1 \tag{G.13}$$

so that for an infinitely long diffractive section, each emitter injects as much light into its neighbor as it injects into itself. Of course, L′ is limited in a real device by diffraction and absorption. Device PGE4600B#31A2 with L′>50 μm failed to lase, while PGE4600B#2E5 with L′<20 μm had a threshold comparable to similar devices without a diffractive section. arg(ϵ) monotonically increases with L′ to exactly one maximum

$$0 \to L' \to b \quad \Rightarrow \quad 0 \to \arg(\epsilon) \to \frac{S^2}{4w_y^2} \tag{G.14}$$

and then monotonically decreases

$$b \to L' \to \infty \quad \Rightarrow \quad \frac{S^2}{4w_y^2} \to \arg(\epsilon) \to 0 \tag{G.15}$$

If the lateral spot size w_y and the thus confocal parameter b are fixed by waveguide design considerations, then only L′ and S are available for optimization. Assuming η_{diff} is given we can use the identity

$$\ln(z) = \ln|z| + i\cdot\arg(z) + 2\pi m \tag{G.16}$$

where z is complex and m is an integer, to rewrite (G.5) as

$$\ln(\epsilon) = \ln\left[\frac{hc}{q}\frac{1-R}{\lambda}\frac{|\eta_{diff}|}{dP_{out}/dJ}\right] + i[\arg(\eta_{diff})+\pi/2+2\pi m] \tag{G.17}$$

Equating (G.17) to the logarithm of (G.12) and taking the real part gives

$$\frac{1}{1+\left(\frac{L'}{b}\right)^2}\frac{S^2}{2w_y^2} = \ln\left[\frac{q}{hc}\frac{\lambda}{1-R}\frac{dP_{out}}{dJ}\frac{1}{|\eta_{diff}|}\right] \tag{G.18}$$

Since the left-hand side must be positive, the coupling parameter is constrained such that

$$|\eta_{diff}| < \frac{q}{hc}\frac{\lambda}{1-R}\frac{dP_{out}}{dJ} \tag{G.19}$$

Using λ=815 nm, R=0.32 and dP_{out}/dJ=.326 W/A (Section 6.2) gives $|\eta_{diff}| < 0.32$, which is not a serious limitation.

The ratio of the imaginary parts to real parts of (G.17) equated to the logarithm

of (G.12) gives

$$\frac{L'}{b} = \frac{\arg(\eta_{diff})+\pi/2+2\pi m}{\ln\left[\frac{q}{hc}\frac{\lambda}{1-R}\frac{dP_{out}}{dJ}\frac{1}{|\eta_{diff}|}\right]} \qquad \text{(G.20)}$$

Suppose that we are designing a twin-emitter for high-frequency injection current modulation (Chapter 8), and have chosen $\eta_{diff}=0.1+0.01\cdot i$, near the center of the "optimum-η region" of Figure 8.2.4. The smallest value (m=0) given by (G.20) is $L'/b=1.46$, and then (G.18) gives $S/w_y=2.68$. Using $w_y=2$ μm and $\mu_e=3.3$ gives $b=50$ μm, so that $L'=73$ μm and $S=5.4$ μm. Due to its great length, the diffractive section would probably have to be pumped for the device to lase, or at least to avoid saturable-absorption instability. Also, the emitter spacing is probably small enough so that the evanescent coupling contribution should be added to the diffractive coupling, and the total coupling calculated self-consistently.

H. FORTRAN PROGRAM SOURCE CODES

STABILITY finds the stability boundaries of the in-phase and out-of-phase equilibrium points of the twin-emitter array, and the characteristic frequency of the onset of instability along the out-of-phase stability boundary. It was used to generate Figures 4.4.3-4.4.5, 5.3.1 and 8.2.4.

FIVE.GUIDE calculates the real and imaginary parts of the coupling parameter as a function of emitter spacing using the five-layer dielectric-slab waveguide model described in Section 4.5. It also calculates the error in fitting the emitter modes to the array modes. It was used to generate Figures 4.5.2-4.5.4.

TWOSTRIP integrates the twin-emitter rate equations as described in Section 5.2. The parameter file TWOSTRIP.PRM is listed as well. TWOSTRIP was used to generate Figures 5.3.2-5.3.9.

POWERSP, CRL and BIFPEP calculate the power spectrum, autocorrelation and bifurcation set of a model-generated intensity time series, respectively.

FABRY.PEROT calculates the depth of modulation of the emission spectrum and the wavelengths of the Fabry-Perot peaks to aid in determining the differential gain and linewidth-enhancement factor, as described in Sections 6.4 and 6.5, respectively. It was used to generate Figures 6.4.1 and 6.5.1.

EXP.PWR.SP calculates the average power spectrum of a user-specified number of experimentally-obtained intensity time series. It was used to generate Figures 6.7.3 and 6.7.4.

STABILITY, FIVE.GUIDE and FABRY.PEROT were written by G. A. Wilson. POWERSP, CRL and BIFPEP were written by R. K. DeFreez. EXP.PWR.SP was adapted by Wilson from POWERSP. TWOSTRIP was written by R. K. DeFreez, G. A. Wilson and P. D. Carleson. Some programs use routines from the NAG library.

Appendix H: STABILITY source code

```
C STABILITY by Geoffrey Wilson, 11 March 1991
C (Modified version of geoffw/chaos/src/new.stability)
C
C This program finds the stability boundaries of the equilibrium
C solutions to Winful's generalized (includes complex coupling)
C two-stripe equations.
C
C The two-stripe laser is described by the parameters f
C (linewidth enhancement factor), t (carrier lifetime/
C photon lifetime).
C
C The operating point is specified by p (normalized pumping)
C and the complex coupling coefficient eta is represented
C by r (real part) and i (imaginary part). For a fixed p,
C the stability boundaries are plotted in the r-i plane.
C
C Parameters for device PGE4600B#1D4
C
      integer ii
      double precision f,t,p,t2,p2,p3,p4,i
      double precision c,b,a,rp,rn,hi,b
      logical pflg,nflg
C Laser parameters.
      f=.96
      t=6.6d2
C I=2.3xIth.
      p=.912d0
C Set limit for |s*i|.
      hi=.25d0*(dsqrt(1.d0+(2.d0+4.d0*p)/t)-1.d0)
      if (hi.gt.p) then
        hi=p
      end if
C Constants.
      t2=t*t
      p2=p*p
      p3=p*p2
      p4=p*p3
C Open output files.
      open(1,file='o2p')
      open(2,file='o2n')
      open(3,file='e3p')
      open(4,file='e3n')
      open(7,file='f2p')
      open(8,file='f2n')
C Start loop over range of i (imaginary part of eta).
      do 900 ii=-469,469
      if (ii.le.0) then
        i=-(10.d0**(dfloat(-500-ii)/100.d0))
      else
        i=10.d0**(dfloat(-500+ii)/100.d0)
      end if
      if (i.lt.-hi) go to 200
C 3 X 3 matrix second-order Hurwitz criterion.
      si2=-2.d0*i
      x2=(p+i)/(1.d0+si2)
C   Calculate the coefficient of r**0.
      c=-((4.d0*si2-4.d0)*x2*x2+((2.d0*si2-6.d0*si2*si2)*t+6.d0*
     &si2-2.d0)*x2+2.d0*si2*si2*si2*t*t-4.d0*si2*si2*t+2.d0*si2)/t/t
C   Calculate the coefficient of r**1.
      b=(2.d0*f*si2+2.d0*f)*x2/t
C   Calculate the coefficient of r**2.
      a=-2.d0*si2
C   Solve the quadratic equation for r, record roots.
      call quad(a,b,c,rp,pflg,rn,nflg)
      if (pflg) then
        if (rp.lt.0.d0) then
```

Appendix H: STABILITY source code

```
            write(1,*)5.+log10(sngl(-.5d0*rp)),float(ii)/100.
C     Instability angular frequency normalized to photon lifetime.
            b=dsqrt(rp*rp+si2*si2-2.d0*si2/t-(2.d0*si2-2.d0)*x2/t)
            write(7,*)5.+log10(sngl(-.5d0*rp)),log10(sngl(b))
            end if
          end if
        if (nflg) then
          if (rn.lt.0.d0) then
            write(2,*)5.+log10(sngl(-.5d0*rn)),float(ii)/100.
C     Instability angular frequency normalized to photon lifetime.
            b=dsqrt(rn*rn+si2*si2-2.d0*si2/t-(2.d0*si2-2.d0)*x2/t)
            write(8,*)5.+log10(sngl(-.5d0*rn)),log10(sngl(b))
            end if
          end if
200     if (i.gt.hi) go to 900
C 3 X 3 matrix third-order Hurwitz criterion.
        si2=2.d0*i
        x2=(p-i)/(1.d0+si2)
C     Calculate the coefficient of r**0.
        c=-(2.d0*si2*x2-si2*si2)/t
C     Calculate the coefficient of r**1.
        b=-(2.d0*f*si2+2.d0*f)*x2/t
C     Calculate the coefficient of r**2.
        a=(2.d0*x2+1.d0)/t
C     Solve the quadratic equation for r, record roots.
        call quad(a,b,c,rp,pflg,rn,nflg)
        if (pflg) then
          if (rp.gt.0.d0) then
            write(3,*)5.+log10(sngl(.5d0*rp)),float(ii)/100.
            end if
          end if
        if (nflg) then
          if (rn.gt.0.d0) then
            write(4,*)5.+log10(sngl(.5d0*rn)),float(ii)/100.
            end if
          end if
C Finished with loop.
900     continue
        close(1)
        close(2)
        close(3)
        close(4)
        close(7)
        close(8)
        stop
        end
C ***************** Functions & Subroutines ****************
C Subroutine for solving quadratic equations a*x*x+b*x+c=0.
        subroutine quad(a,b,c,xp,pflg,xn,nflg)
        double precision a,b,c,xp,xn,dis
        logical pflg,nflg
C Special case: a=0.
        if (a.eq.0.) then
C     Special subcase: b=0.
          if (b.eq.0.) then
            pflg=.false.
            nflg=.false.
            return
            end if
C     Special subcase: b<>0.
          xp=-c/b
          pflg=.true.
          nflg=.false.
          return
          end if
C General case.
```

Appendix H: STABILITY source code

```
      dis=b*b-4.*a*c
C Test for complex roots.
      if (dis.lt.0.) then
        pflg=.false.
        nflg=.false.
        return
        end if
C Real roots.
      xp=.5*(-b+dsqrt(dis))/a
      pflg=.true.
      xn=.5*(-b-dsqrt(dis))/a
      nflg=.true.
      return
      end
```

Appendix H: FIVE.GUIDE source code

```
C 'five.guide.f' by Geoffrey Wilson 30 March 1990
C
C Used to test the validity of the stripe-field representation
C of a two-stripe index-guided device as a function of center-
C to-center spacing.
C
C Modified by Geoffrey Wilson 21 June 1990 to include gain in the
C guiding regions and loss in the cladding regions to calculate
C the imaginary part of the eta matrix.
C
      integer iplim,ip,i,i1,i2,ifail
      double precision pi,hpi,rt2,rt3,ex,plim,pstp,p,lo,hi,tnh,lhs,rhs
      double precision gam0,kap0,const,bnd,bnd2,c0,s0,ex2,snh,csh,g2,k2
      double precision dk,dk2,gamp,kapp,gamn,kapn,tnh,sum,dif,den,z(5)
      double precision fp,cp,sp,thp,ap,bp,gp,fn,cn,sn,thn,an,bn,gn
      double precision amat(2,2),cmat(2,2),lambda(2,2),imat(2,2)
      double precision ainv(2,2),bmat(2,2),binv(2,2),aa(2,2),bb(2,2)
      double precision temp(2,2),eta(2,2)
      double precision pp,nn,errp(1000),errn(1000),slf(1000),crs(1000)
      double precision lambdai(2,2),etai(2,2),slfi(1000),crsi(1000)
      double precision conf0,confp,confn
C Begin executables.
      ifail=0
      imat(1,1)=1.d0
      imat(1,2)=0.d0
      imat(2,1)=0.d0
      imat(2,2)=1.d0
      pi=3.141592654
      hpi=pi/2.
      rt2=dsqrt(2.d0)
      rt3=dsqrt(3.d0)
      i1=20
      i2=20
C Get stripe spacing range "p" from the terminal.
      print*,"Supply the stripe spacing limit in units of stripe width"
      read*,plim
C Get stripe spacing mesh size "pstp" from the terminal.
      print*,"Supply the stripe spacing mesh in units of stripe width"
      read*,pstp
      iplim=idint((plim-1.)/pstp)
C Constant of proportionality for converting transverse wavevectors
C to angular frequency splittings normalized to the photon lifetime.
      const=.195
C Get "kap0" upper bound from the terminal.
      print*,"Supply kap0 upper bound in units of pi/2 (0 to 1)"
      read*,bnd
      bnd=hpi*bnd
      bnd2=bnd*bnd
C Find "kap0" and "gam0".
      lo=0.
      hi=bnd
      kap0=.5*bnd
      gam0=.5*rt3*bnd
      do 50 i=1,i2
      lhs=dtan(kap0)
      rhs=gam0/kap0
      if (lhs.gt.rhs) then
        hi=kap0
      else
        lo=kap0
      end if
      kap0=.5*(lo+hi)
      gam0=dsqrt(bnd2-kap0*kap0)
50    continue
C Useful constants.
      c0=dcos(kap0)
```

Appendix H: FIVE.GUIDE source code

```
      s0=dsin(kap0)
      ex=dexp(gam0)
      ex2=ex*ex
      snh=dsinh(gam0)
      csh=dcosh(gam0)
C Diagonal elements of matrix "A".
      amat(1,1)=kap0*kap0/gam0+bnd*s0+bnd2
      amat(2,2)=amat(1,1)
C Confinement factor for the isolated stripe mode.
      conf0=(bnd*s0+bnd2)/amat(1,1)
C Start loop thru values for half-center-to-center spacing "p".
      do 1000 ip=1,iplim
      p=1.+dfloat(ip)*pstp
      dk=dexp(-gam0*p)
      dk2=dk*dk
C Off-diagonal elements of matrix "A".
      amat(1,2)=kap0*kap0*dk2*(1./gam0+2.*(2.*gam0/bnd2+p-1.)*ex2)
      amat(2,1)=amat(1,2)
C Solve eigenvalue equation for "kapp".
      lo=0.
      hi=kap0
      kapp=.5*(lo+hi)
      gamp=dsqrt(bnd2-kapp*kapp)
      do 200 i=1,i2
      tnh=dtanh(gamp*(p-1.))
      k2=kapp*kapp
      g2=gamp*gamp
      lhs=dtan(kapp)
      rhs=bnd*dsqrt(k2+tnh*tnh*g2)-k2+tnh*g2
      rhs=rhs/gamp/kapp/(1.+tnh)
      if (lhs.gt.rhs) then
        hi=kapp
      else
        lo=kapp
      end if
      kapp=.5*(lo+hi)
      gamp=dsqrt(bnd2-kapp*kapp)
200   continue
C Done finding even array mode eigenvalue "kapp".
C Solve eigenvalue equation for "kapn".
      lo=kap0
      hi=bnd
      kapn=.5*(lo+hi)
      gamn=dsqrt(bnd2-kapn*kapn)
      do 400 i=1,i2
      tnh=dtanh(gamn*(p-1.))
      k2=kapn*kapn
      g2=gamn*gamn
      lhs=dtan(kapn)
      rhs=bnd*dsqrt(tnh*tnh*k2+g2)-tnh*k2+g2
      rhs=rhs/gamn/kapn/(1.+tnh)
      if (lhs.gt.rhs) then
        hi=kapn
      else
        lo=kapn
      end if
      kapn=.5*(lo+hi)
      gamn=dsqrt(bnd2-kapn*kapn)
400   continue
C Done finding odd array mode eigenvalue "kapn".
C Calculate "lambda" matrix.
      lambda(1,1)=const*(kap0*kap0-kapp*kapp)
      lambda(1,2)=0.
      lambda(2,1)=0.
      lambda(2,2)=const*(kap0*kap0-kapn*kapn)
C Calculate matrix "C".
```

Appendix H: FIVE.GUIDE source code

```
C   Constants for even array mode.
      fp=kapp/dcosh(gamp*(p-1.))
      cp=dcos(kapp)
      sp=dsin(kapp)
      thp=dtanh(gamp*(p-1.))
      ap=kapp*cp+gamp*thp*sp
      bp=-kapp*sp+gamp*thp*cp
      gp=ap*cp+bp*sp
C Calculate even array mode inner product.
      z(1)=gp*gp/gamp
      z(2)=2.*ap*ap*(cp*sp/kapp+1.)
      z(3)=2.*bp*bp*(1.-cp*sp/kapp)
      z(4)=fp*fp*(.5*dsinh(2.*gamp*(p-1.))/gamp+(p-1.))
      pp=z(1)+z(2)+z(3)+z(4)
C Confinement factor for the even array mode.
      confp=(z(2)+z(3))/pp
C   Constants for odd array mode.
      fn=kapn/dcosh(gamn*(p-1.))
      cn=dcos(kapn)
      sn=dsin(kapn)
      thn=dtanh(gamn*(p-1.))
      an=gamn*sn+kapn*thn*cn
      bn=gamn*cn-kapn*thn*sn
      gn=an*cn+bn*sn
C Calculate odd array mode inner product.
      z(1)=gn*gn/gamn
      z(2)=2.*an*an*(cn*sn/kapn+1.)
      z(3)=2.*bn*bn*(1.-cn*sn/kapn)
      z(4)=fn*fn*(.5*dsinh(2.*gamn*(p-1.))/gamn-(p-1.))
      nn=z(1)+z(2)+z(3)+z(4)
C Confinement factor for the odd array mode.
      confn=(z(2)+z(3))/nn
C Calculate "lambdai" matrix.
      lambdai(1,1)=1.d0-confp/conf0
      lambdai(1,2)=0.d0
      lambdai(2,1)=0.d0
      lambdai(2,2)=1.d0-confn/conf0
C   Even array mode matrix elements.
      sum=gam0+gamp
      dif=gam0-gamp
      z(1)=gp*kap0*(1.+dk2)/sum
      den=kapp*kapp+gam0*gam0
      z(2)=2.*ap*kap0*dk2*ex/den*(gam0*snh*cp+kapp*csh*sp)
      z(3)=2.*bp*kap0*dk2*ex/den*(-kapp*snh*cp+gam0*csh*sp)
      z(4)=fp*kap0*dk*ex*(dsinh(sum*(p-1.))/sum+dsinh(dif*(p-1.))/dif)
      z(5)=ap*bnd*(dsin(kapp-kap0)/(kapp-kap0)
     &+dsin(kapp+kap0)/(kapp+kap0))
      cmat(1,1)=z(1)+z(2)+z(3)+z(4)+z(5)
      cmat(2,1)=cmat(1,1)
C   Odd array mode matrix elements.
      sum=gam0+gamn
      dif=gam0-gamn
      z(1)=gn*kap0*(1.-dk2)/sum
      den=kapn*kapn+gam0*gam0
      z(2)=-2.*an*kap0*dk2*ex/den*(gam0*snh*cn+kapn*csh*sn)
      z(3)=-2.*bn*kap0*dk2*ex/den*(-kapn*snh*cn+gam0*csh*sn)
      z(4)=fn*kap0*dk*ex*(dsinh(sum*(p-1.))/sum-dsinh(dif*(p-1.))/dif)
      z(5)=an*bnd*(dsin(kapn-kap0)/(kapn-kap0)
     &+dsin(kapn+kap0)/(kapn+kap0))
      cmat(1,2)=z(1)+z(2)+z(3)+z(4)+z(5)
      cmat(2,2)=-cmat(1,2)
      print*,ip,sngl(confp),sngl(conf0),sngl(confn)
C Calculate the inverse of "A".
      call f04aef(amat,2,imat,2,2,2,ainv,2,z,aa,2,bb,2,ifail)
C Calculate the product Ainv x C.
      call f01ckf(bmat,ainv,cmat,2,2,2,z,5,1,ifail)
```

Appendix H: FIVE.GUIDE source code

```
C Calculate the inverse of "B".
      call f04aef(bmat,2,imat,2,2,2,binv,2,z,aa,2,bb,2,ifail)
C Calculate the product B x lambda x Binv.
      call f01ckf(temp,bmat,lambda,2,2,2,z,5,1,ifail)
      call f01ckf(eta,temp,binv,2,2,2,z,5,1,ifail)
      slf(ip)=eta(1,1)
      crs(ip)=eta(1,2)
C Calculate the product B x lambdai x Binv.
      call f01ckf(temp,bmat,lambdai,2,2,2,z,5,1,ifail)
      call f01ckf(etai,temp,binv,2,2,2,z,5,1,ifail)
      slfi(ip)=etai(1,1)
      crsi(ip)=etai(1,2)
C Calculate normalized residuals "errp" and "errn".
      errp(ip)=1.-2.*cmat(1,1)*cmat(1,1)/pp/(amat(1,1)+amat(1,2))
      errn(ip)=1.-2.*cmat(1,2)*cmat(1,2)/nn/(amat(1,1)-amat(1,2))
1000  continue
C Write output files.
      open(1,file='self')
      open(2,file='cross')
      open(3,file='errorp')
      open(4,file='errorn')
      open(7,file='logp')
      open(8,file='logn')
      open(9,file='selfi')
      open(10,file='crossi')
      do 2000 ip=1,iplim
      p=1.+dfloat(ip)*pstp
      write(1,*)sngl(p),sngl(slf(ip))
      write(2,*)sngl(p),sngl(crs(ip))
      write(3,*)sngl(p),sngl(errp(ip))
      write(4,*)sngl(p),sngl(errn(ip))
      write(7,*)sngl(dlog10(crs(ip))),sngl(dlog10(errp(ip)))
      write(8,*)sngl(dlog10(crs(ip))),sngl(dlog10(errn(ip)))
      write(9,*)sngl(p),sngl(slfi(ip))
      write(10,*)sngl(p),sngl(crsi(ip))
2000  continue
      close(1)
      close(2)
      close(3)
      close(4)
      close(7)
      close(8)
      close(9)
      close(10)
      stop
      end
```

Appendix H: TWOSTRIP source code

```
c       Program twostrip.for
C
C This program integrates Winful's rate equations (including complex
C coupling, spontaneous emission and injection current modulation)
C for a two-stripe array to obtain the time series of the stripe
C electric field amplitudes (X1 and X2), the inter-stripe phase
C difference (theta) and the stripe net gains (Z1 and Z2).
C
C A parameter file 'twostrip.prm' is read to get the necessary
C information. Since generally the device is to be modulated,
C the first part of the program looks for a limit cycle in the
C response at a sub-multiple of the modulation cycle frequency.
C The convergence to the limit cycle is recorded in the output
C file 'converge', which contains the RMS difference between the
C beginning and end of each reponse cycle. The output file 'X.plane'
C contains data pairs (X1,X2) for the beginning of each response cycle.
C
C After attempting to obtain a limit cycle, the program writes the
C time series of the dynamical variables to output files X1.*, X2.*,
C theta.*, Z1.* and Z2.*, where * is a text string determined by the
C complex coupling constant 'eta'.
C
C ***********************************************************************
C Revisions:
C       24 Jul 90 PDC Ported to Microsoft PC Fortran, Carleson
C                       Appends .DAT to data files at synth.
C        8 Aug 90 Modified to include automatic calculation of
C                modulation frequency based on value of etar, DeFreez
C        8 Auf 90 Modified to write data output files on d:, DeFreez
C       26 Sep 90 Modified to establish a modulation frequency
C                  commensurate with the record length; Wilson
C ***********************************************************************
C
C Quantities to be read from the parameter file 'twostripe.prm'.
      integer sigfigr, tenpwrr, sigfigi, tenpwri
      integer phase, eql, j, period, settle
      double precision alpha, taus, taup, beta, z0, p0, freq, depth
      double precision offset, outtol, mesh, record
      character*80 txt1
      character*8 txt2
C Other quantities
      integer nout, n, iw, ir, mped, icyc, i2, i, ifail
      double precision pi, pp, radfreq, rhop, etar, etai, h, tol
      double precision aa, bb, cc, w(5,23), y(5), yold(5)
      double precision x, xend, sum, term
      character*16 fn1, fn2, fn3, fn4, fn5
      character*23 fnn1, fnn2, fnn3, fnn4, fnn5
        character*7 destdir
      logical flag
C Quantities added 26 Sep 90 by Wilson.
      integer lookup(9)
C NAG routine d02ebf is used
      external fcn, out, pederv
C Common blocks
      common /params/ etar, etai, alpha, p0, pp, taus, taup, rhop, z0,
     &phase, radfreq
      common /outblk/ xend, h, i, flag
C Lookup table values assure modulation frequency a multiple of 250 MHz,
C and a divisor of 1 THz. This requires a record length of 8 ns and a
C step size of 1 ps.
```

Appendix H: TWOSTRIP source code

```
      data lookup /16,20,25,32,40,50,80,100,125/
C Evaluate pi
      pi=3.1415926535898
C Integration routine constants
      nout = 6
      n = 5
      iw = 23
      ir = 0
      mped = 1
C Read parameter files
      open(1,file='d:\mod.dat\twostrip.prm')
        open(2,file='d:\mod.dat\etatable.prm')
      read(1,1)txt1
      read(1,1)txt1
C Linewidth enhancement factor
      read(1,*)txt2,alpha
      read(1,1)txt1
C Carrier lifetime in picoseconds
      read(1,*)txt2,taus
      read(1,1)txt1
C Photon lifetime in picoseconds
      read(1,*)txt2,taup
      read(1,1)txt1
C Spontaneous emission factor
      read(1,*)txt2,beta
      read(1,1)txt1
C Cold-cavity normalized loss
      read(1,*)txt2,z0
C Significant figure of the real part of the coupling coefficient
      read(2,*)sigfigr
C (Neg.) power of ten of the real part of the coupling coefficient
      read(2,*)tenpwrr
C Significant figure of the imaginary part of the coupling coefficient
      read(2,*)sigfigi
C (Neg.) power of ten of the imaginary part of the coupling coefficient
      read(2,*)tenpwri
      read(1,1)txt1
      read(1,1)txt1
C Average normalized above-threshold injection current
      read(1,*)txt2,p0
      read(1,1)txt1
C Modulation frequency in GHz
      read(1,*)txt2,freq
      read(1,1)txt1
C Depth of modulation (average-to-peak/ average above-threshold)
      read(1,*)txt2,depth
      read(1,1)txt1
C Modulation phase (1=stripes modulated in-phase, -1=out-of-phase)
      read(1,*)txt2,phase
      read(1,1)txt1
      read(1,1)txt1
C Equilibrium solution to start near (0=in-phase, 1=out-of-phase)
      read(1,*)txt2,eql
      read(1,1)txt1
C Starting distance from equilibrium solution in units of pi radians
      read(1,*)txt2,offset
      read(1,1)txt1
      read(1,1)txt1
C (Negative) power of ten of the tolerance for the integration routine
      read(1,*)txt2,j
```

Appendix H: TWOSTRIP source code

```
      read(1,1)txt1
C Modulation cycles per response cycle
      read(1,*)txt2,period
      read(1,1)txt1
C Maximum number of response cycles before recording output files
      read(1,*)txt2,settle
      read(1,1)txt1
C Tolerance for convergence to limit cycle
      read(1,*)txt2,outtol
      read(1,1)txt1
C Number of response cycles to record in output files
      read(1,*)txt2,record
      read(1,1)txt1
C Step size between data points in output files in picoseconds
      read(1,*)txt2,mesh
      close(1)
        close(2)
1     format(a)
C Done reading parameter files
C Evaluate auxilliary quantities
      pp=depth*p0
      radfreq=2.*pi*freq
      rhop=.5d0*beta
C Synthesize output file names out of key parameters
        destdir='c:\tmp\'
        if((sigfigr.ge.0).and.(sigfigi.ge.0)) then
       fn1='X1'//char(sigfigr+48)//char(tenpwrr+48)
      $   //char(sigfigi+48)//char(tenpwri+48)//'.dat'
       fn2='X2'//char(sigfigr+48)//char(tenpwrr+48)
      $   //char(sigfigi+48)//char(tenpwri+48)//'.dat'
       fn3='th'//char(sigfigr+48)//char(tenpwrr+48)
      $   //char(sigfigi+48)//char(tenpwri+48)//'.dat'
       fn4='Z1'//char(sigfigr+48)//char(tenpwrr+48)
      $   //char(sigfigi+48)//char(tenpwri+48)//'.dat'
       fn5='Z2'//char(sigfigr+48)//char(tenpwrr+48)
      $   //char(sigfigi+48)//char(tenpwri+48)//'.dat'
c
        elseif ((sigfigr.ge.0).and.(sigfigi.lt.0)) then
        sigfigi=iabs(sigfigi)
       fn1='X1'//char(sigfigr+48)//char(tenpwrr+48)
      $   //"-"//char(sigfigi+48)//char(tenpwri+48)//'.dat'
       fn2='X2'//char(sigfigr+48)//char(tenpwrr+48)
      $   //"-"//char(sigfigi+48)//char(tenpwri+48)//'.dat'
       fn3='th'//char(sigfigr+48)//char(tenpwrr+48)
      $   //"-"//char(sigfigi+48)//char(tenpwri+48)//'.dat'
       fn4='Z1'//char(sigfigr+48)//char(tenpwrr+48)
      $   //"-"//char(sigfigi+48)//char(tenpwri+48)//'.dat'
       fn5='Z2'//char(sigfigr+48)//char(tenpwrr+48)
      $   //"-"//char(sigfigi+48)//char(tenpwri+48)//'.dat'
        sigfigi=-1*sigfigi
c
        elseif ((sigfigr.lt.0).and.(sigfigi.ge.0)) then
        sigfigr=iabs(sigfigr)
       fn1='X1'//"-"//char(sigfigr+48)//char(tenpwrr+48)
      $   //char(sigfigi+48)//char(tenpwri+48)//'.dat'
       fn2='X2'//"-"//char(sigfigr+48)//char(tenpwrr+48)
      $   //char(sigfigi+48)//char(tenpwri+48)//'.dat'
       fn3='th'//"-"//char(sigfigr+48)//char(tenpwrr+48)
      $   //char(sigfigi+48)//char(tenpwri+48)//'.dat'
       fn4='Z1'//"-"//char(sigfigr+48)//char(tenpwrr+48)
```

Appendix H: TWOSTRIP source code

```
     $   //char(sigfigi+48)//char(tenpwri+48)//'.dat'
      fn5='Z2'//"-"//char(sigfigr+48)//char(tenpwrr+48)
     $   //char(sigfigi+48)//char(tenpwri+48)//'.dat'
         sigfigr=-1*sigfigr
c
         else
         sigfigr=iabs(sigfigr)
         sigfigi=iabs(sigfigi)
      fn1='X1'//"-"//char(sigfigr+48)//char(tenpwrr+48)
     $   //"-"//char(sigfigi+48)//char(tenpwri+48)//'.dat'
      fn2='X2'//"-"//char(sigfigr+48)//char(tenpwrr+48)
     $   //"-"//char(sigfigi+48)//char(tenpwri+48)//'.dat'
      fn3='th'//"-"//char(sigfigr+48)//char(tenpwrr+48)
     $   //"-"//char(sigfigi+48)//char(tenpwri+48)//'.dat'
      fn4='Z1'//"-"//char(sigfigr+48)//char(tenpwrr+48)
     $   //"-"//char(sigfigi+48)//char(tenpwri+48)//'.dat'
      fn5='Z2'//"-"//char(sigfigr+48)//char(tenpwrr+48)
     $   //"-"//char(sigfigi+48)//char(tenpwri+48)//'.dat'
         sigfigr=-1*sigfigr
         sigfigi=-1*sigfigi
         endif
         fnn1=destdir//fn1
         fnn2=destdir//fn2
         fnn3=destdir//fn3
         fnn4=destdir//fn4
         fnn5=destdir//fn5
C Program segment before 26 Sep 90.
C       etar=dfloat(sigfigr)*10.d0**(-dfloat(tenpwrr))
C       etai=dfloat(sigfigi)*10.d0**(-dfloat(tenpwri))
C ********************
C        freq=etar*1000./pi/taup
C       radfreq=2.*pi*freq
C        record=40.*freq
C ********************
C New program segment.
       freq=25.d0*10.d0**(-dfloat(tenpwrr))*dfloat(lookup(sigfigr))
       radfreq=2.*pi*freq
       mesh=1.d0
         record=40.*freq
       etar=pi*taup*freq/1000.d0
       etai=pi*taup/40.d0*10.d0**(-dfloat(tenpwri))
      &*dfloat(lookup(sigfigi))
       print*,'etar = ',sngl(etar)
       print*,'etai = ',sngl(etai)
C End of new segment.
C Done synthesizing output file names
C
C Attempt to find limit cycle by integrating over complete cycles
C Open file to record attempt at convergence
       open(1,file='d:\mod.dat\converge')
C Open file to record successive start-cycle points in the X1-X2 plane
c      open(2,file='d:\mod.dat\X.plane')
C Set flag for limit cycle search mode
       flag=.false.
C Set the data report interval h (ps) equal to the response period
       h=1.d3*dfloat(period)/freq
C Set initial integration error tolerance
 33      tol = 10.d0**(-j)
          write (nout,99999) tol
          write (nout,99998)
```

Appendix H: TWOSTRIP source code

```
C Initial conditions near equilibrium point
        aa=1.d0-2.d0*rhop
        bb=p0+dfloat(eql)*etai+(1.d0+2.d0*z0)*rhop
        cc=p0*dfloat(eql)*etai-z0*rhop
        y(4) = (bb-dsqrt(bb*bb-4.d0*aa*cc))/2.d0/aa
        y(5) = y(4)
        y(1) = dsqrt((p0-y(4)+2.d0*(z0+y(4))*rhop)/
     &  (1.d0+2.d0*dfloat(eql)*etai))
        y(2) = y(1)
        y(3) = pi*(dfloat(eql)+1.d-6)
C Start loop to find limit cycle
        do 40 icyc=1,settle
C Record previous cycle finish-point as present cycle start-point
        do 38 i2=1,5
38      yold(i2)=y(i2)
C Set x and xend to report no intermediate points
        x = 0.d0
        xend = h
        i = 0
        ifail = 1
C Integrate over response cycle
        call d02ebf(x,xend,n,y,tol,ir,fcn,mped,pederv,out,w,
     *    iw, ifail)
C        write (nout,99997) ifail
C If ... then reset integration tolerance
        if (ifail.eq.3) then
                j=j-1
                goto 33
        endif
        if (tol.lt.0.d0) write (nout,99995)
C Write the finish-point (X1,X2) to the file 'X.plane'
C       write(2,*)sngl(y(1)),sngl(y(2))  ***
C Calculate RMS difference between start-point and finish-point
        sum=0.d0
        do 39 i2=1,5
C Skip troublesome 'theta' difference
        if (i2.eq.3) go to 39
        term=y(i2)-yold(i2)
        sum=sum+term*term
39      continue
        sum=dsqrt(sum/4.d0)
C Write the RMS difference to the file 'converge'
        write(1,*)icyc,sngl(sum)
C If ... then limit cycle tolerance has been reached, exit loop
        if (sum.lt.outtol) go to 50
40      continue
        print*,'Failed to converge.'
C Limit cycle found. Record in plottable output files
50      close(1)
c       close(2)
C Reset flag that toggles output subroutine mode
        flag=.true.
        open(11,file=fnn1)
        open(12,file=fnn2)
        open(13,file=fnn3)
        open(14,file=fnn4)
        open(15,file=fnn5)
C Set time series limits
        x = 0.d0
        xend = dfloat(record)*h
```

Appendix H: TWOSTRIP source code

```
C Set the data report interval h (ps)
      h=mesh
 53     tol = 10.d0**(-j)
C One less than the number of points in the time series
         i = idint(xend/h)-1
         ifail = 1
         call d02ebf(x,xend,n,y,tol,ir,fcn,mped,pederv,out,w,
     *    iw, ifail)
         write (nout,99997) ifail
        if (ifail.eq.3) then
               j=j-1
               goto 53
        endif
         if (tol.lt.0.d0) write (nout,99995)
        close(11)
        close(12)
        close(13)
        close(14)
        close(15)
99999 format (22h0calculation with tol=, d9.2)
99998 format (40h x and solution at equally spaced points)
99997 format (8h  ifail=, i1)
99995 format (24h range too short for tol)
      end
      subroutine fcn(t, y, f)
      integer phase
      double precision radfreq, z0
      double precision t
      double precision f(5), y(5),temp3,tempr3,tempi3
      double precision etar,etai,alpha,taus,taup,rhop,p0,pp,p1,p2
      double precision tempr1,tempi1,tempr2,tempi2
        double precision cs, sn
      common /params/ etar, etai, alpha, p0, pp, taus, taup, rhop, z0,
     &phase, radfreq
        common /trigs/ cs, sn
        cs = dcos(y(3))
        sn = dsin(y(3))
      tempr1 = y(4)*y(1)-etar*y(2)*sn
      tempi1 = rhop*(y(4)+z0)/y(1)-etai*y(2)*cs
      f(1) = (tempr1+tempi1)/taup
      tempr2 = y(5)*y(2)+etar*y(1)*sn
      tempi2 = rhop*(y(5)+z0)/y(2)-etai*y(1)*cs
      f(2) = (tempr2+tempi2)/taup
      temp3 = -alpha*(y(5)-y(4))
      tempr3 = temp3+etar*(y(1)/y(2)-y(2)/y(1))*cs
      tempi3 = etai*(y(1)/y(2)+y(2)/y(1))*sn
      f(3) = (tempr3+tempi3)/taup
      p1 = p0 + pp*dsin(1.d-3*radfreq*t)
      p2 = p0 + phase*pp*dsin(1.d-3*radfreq*t)
      f(4)= (p1-y(4)-(1.d0+2.d0*y(4))*y(1)*y(1))/taus
      f(5)= (p2-y(5)-(1.d0+2.d0*y(5))*y(2)*y(2))/taus
      return
      end
      subroutine pederv(x, y, pw)
      integer phase
      double precision radfreq, z0
      double precision x
      double precision pw(5,5), y(5)
      double precision etar,etai,alpha,taus,taup,rhop,p0,pp
      double precision temp311, temp312, temp321, temp322
```

Appendix H: TWOSTRIP source code

```
      double precision temp331, temp332
        double precision cs, sn
      common /params/ etar, etai, alpha, p0, pp, taus, taup, rhop, z0,
     &phase, radfreq
        common /trigs/ cs, sn
      pw(1,1) = (y(4)-rhop*(y(4)+z0)/y(1)/y(1))/taup
      pw(1,2) = (-etar*sn-etai*cs)/taup
      pw(1,3) = (-etar*y(2)*cs+etai*y(2)*sn)/taup
      pw(1,4) = (y(1)+rhop/y(1))/taup
      pw(1,5) = 0.d0
      pw(2,1) = (etar*sn-etai*cs)/taup
      pw(2,2) = (y(5)-rhop*(y(5)+z0)/y(2)/y(2))/taup
      pw(2,3) = (etar*y(1)*cs+etai*y(1)*sn)/taup
      pw(2,4) = 0.d0
      pw(2,5) = (y(2)+rhop/y(2))/taup
      temp331 = y(1)/y(2)-y(2)/y(1)
      temp332 = y(1)/y(2)+y(2)/y(1)
      temp311 = temp332/y(1)
      temp312 = temp331/y(1)
      temp321 = -temp332/y(2)
      temp322 = -temp331/y(2)
      pw(3,1) = (etar*cs*temp311+etai*sn*temp312)/taup
      pw(3,2) = (etar*temp321*cs+etai*temp322*sn)/taup
      pw(3,3) = (-etar*temp331*sn+etai*temp332*cs)/taup
      pw(3,4) = alpha/taup
      pw(3,5) = -alpha/taup
      pw(4,1) = -2.d0*(1.d0+2.d0*y(4))*y(1)/taus
      pw(4,2) = 0.d0
      pw(4,3) = 0.d0
      pw(4,4) = -(1.d0+2.d0*y(1)*y(1))/taus
      pw(4,5) = 0.d0
      pw(5,1) = 0.d0
      pw(5,2) = -2.d0*(1.d0+2.d0*y(5))*y(2)/taus
      pw(5,3) = 0.d0
      pw(5,4) = 0.d0
      pw(5,5) = -(1.d0+2.d0*y(2)*y(2))/taus
      return
      end
      subroutine out(x, y)
      integer i
      double precision x, y(5), xend, h, pi
      logical flag
      common /outblk/ xend, h, i, flag
        pi=3.1415926535898
C If ... then report time series data points
      if (flag) then
      write (11,99999) sngl(y(1)*y(1))
      write (12,99999) sngl(y(2)*y(2))
      write (13,99999) sngl(y(3)/pi)
       write (14,99999) sngl(y(4))
       write (15,99999) sngl(y(5))
      end if
C Decrement time and data point index
      x = xend - dfloat(i)*h
      i = i - 1
      return
99999 format (e13.6)
      end
```

Appendix H: parameter file TWOSTRIP.PRM

```
'STRIPE PARAMETERS'
'  linewidth enhancement factor'
'    alpha===' 7.5d0
'  carrier lifetime in picoseconds'
'    taus====' 2400.d0
'  photon lifetime in picoseconds'
'    taup====' 1.5d0
'  spontaneous emission factor'
'    beta====' 1.6d-4
'  cold-cavity normalized loss'
'    z0======' .939d0
'  gain compression factor'
'    capc====' .7d0
'OPERATING PARAMETERS'
'  average normalized above-threshold injection current'
'    p0======' .66d0
'  modulation frequency in gigahertz'
'    freq====' 1.0d0
'  depth of modulation (average-to-peak/ average above-threshold)'
'    depth===' 3.d-1
'  modulation phase (1=stripes modulated in-phase, -1=out-of-phase)'
'    phase===' -1
'INITIAL CONDITIONS'
'  equilibrium solution to start near (0=in-phase, 1=out-of-phase)'
'    eql=====' 0
'  starting distance from equilibrium solution in units of pi radians'
'    offset==' 1.d-6
'PROGRAM PARAMETERS'
'  (negative) power of ten of the tolerance for the integration routine'
'    j=======' 12
'  modulation cycles per response cycle'
'    period==' 1
'  maximum number of response cycles before recording output files'
'    settle==' 0
'  tolerance for convergence to limit cycle'
'    outtol==' 1.d-6
'  number of response cycles to record in output files'
'    record==' 80.d0
'  step size between data points in output files in picoseconds'
'    mesh====' 1.0d0
```

Appendix H: POWERSP source code

```
C**********************************************************************
C
C Program powersp.for
C
C       This program calculates the discrete fourier transform of
C optical intensity from a single emitter.  This corresponds to a
C DFT in the time domain.  The data is read a column at a time into
C a real 1D array required by the NAG routine c06eaf.  The original
C sequence is a real sequence and consequently the DFT is a particular
C type of complex sequence, a Hermitian sequence with the following
C properties:
C       a(N-k)=a(k)
C       b(N-k)=-b(k) , b(0)=0 , b(N/2)=0 for N even
C where DFT{z(k)} = a(k) + ib(k)  when z(k)=x(k) (z real).
C A Hermitian sequence of N complex values can then be uniquely
C specified by N independent real values.  The NAG routine c06eaf writes
C the real parts a(k) for 0<k<N/2 in the first (N/2 + 1) components of
C array x. The non-zero imaginary components b(k) are written in reverse
C order to the remaining (N/2 - 1) components of array x.  The results
C are normalized to one and read back into an array file.
C
C**********************************************************************
C
      integer ifail,j,jm1,n2,nj,n,nnn
        integer sigfigr,tenpwrr,sigfigi,tenpwri
      double precision cjm1,cmax,deltat
      double precision y(8000),xnull
      double precision r(4000),im(4000),c(4000)
        character*7 destdir1
        character*11 destdir2
        character*16 fn1,fn2
        character*23 fnn1
        character*27 fnn2
C  read the data points of time series
c       print *,'input data point number of time series...'
c       read *,n
        n=8000
C  read the unit length of the time series
c       print *,'input unit (ps/channel) of the time series...'
c       read *,deltat
        deltat=1.0d0
      deltat=deltat*1.0d-03
        destdir1='c:\tmp\'
        destdir2='d:\mod.dat\'
        open(unit=2,file='d:\mod.dat\etatable.prm')
        read(2,*)sigfigr
        read(2,*)tenpwrr
        read(2,*)sigfigi
        read(2,*)tenpwri
C Synthesize file names out of key parameters
        if((sigfigr.ge.0).and.(sigfigi.ge.0)) then
     fn1='X1'//char(sigfigr+48)//char(tenpwrr+48)
     $   //char(sigfigi+48)//char(tenpwri+48)//'.dat'
     fn2='dft'//char(sigfigr+48)//char(tenpwrr+48)
     $   //char(sigfigi+48)//char(tenpwri+48)//'.dat'
c
        elseif ((sigfigr.ge.0).and.(sigfigi.lt.0)) then
        sigfigi=iabs(sigfigi)
     fn1='X1'//char(sigfigr+48)//char(tenpwrr+48)
     $   //"-"//char(sigfigi+48)//char(tenpwri+48)//'.dat'
```

Appendix H: POWERSP source code

```
      fn2='dft'//char(sigfigr+48)//char(tenpwrr+48)
     $   //"-"//char(sigfigi+48)//char(tenpwri+48)//'.dat'
         sigfigi=-1*sigfigi
c
         elseif ((sigfigr.lt.0).and.(sigfigi.ge.0)) then
         sigfigr=iabs(sigfigr)
      fn1='X1'//"-"//char(sigfigr+48)//char(tenpwrr+48)
     $   //char(sigfigi+48)//char(tenpwri+48)//'.dat'
      fn2='dft'//"-"//char(sigfigr+48)//char(tenpwrr+48)
     $   //char(sigfigi+48)//char(tenpwri+48)//'.dat'
         sigfigr=-1*sigfigr
c
         else
         sigfigr=iabs(sigfigr)
         sigfigi=iabs(sigfigi)
      fn1='X1'//"-"//char(sigfigr+48)//char(tenpwrr+48)
     $   //"-"//char(sigfigi+48)//char(tenpwri+48)//'.dat'
      fn2='dft'//"-"//char(sigfigr+48)//char(tenpwrr+48)
     $   //"-"//char(sigfigi+48)//char(tenpwri+48)//'.dat'
         sigfigr=-1*sigfigr
         sigfigi=-1*sigfigi
         endif
         close(2)
         fnn1=destdir1//fn1
         fnn2=destdir2//fn2
       open (unit=1,file=fnn1)
         nnn=40000-n
         do 437 i=1,nnn
         read(1,*)xnull
 437     continue
C  read time series data into y
       do 40 j = 1, n
            read (1,*) y(j)
40     continue
       close(1)
       ifail = 0
C  call the NAG routine that calculates the DFT of a real array y of
C  length n
       call c06eaf(y,n,ifail)
C  real and imaginary components are returned to y(j) see the above
C  program description for the specific locations of the components
C  r(j), im(j) the first components are given by
       r(1) = y(1)
       im(1) = 0.0d0
       c(1)=r(1)*r(1)
C  now determine the remaining DFT components
       n2 = (n+1)/2
       do 60 j=2,n2
            nj = n -j + 2
            r(j) = y(j)
            im(j) = y(nj)
C  find the power spectrum of the complex value of the DFT
            c(j) = r(j)*r(j) + im(j)*im(j)
         if (j.ge.4) then
            if (c(j).gt.cmax) then
                 cmax=c(j)
            end if
         end if
60     continue
C  determine the last value if n is even
```

Appendix H: POWERSP source code

```
      if (mod(n,2) .ne. 0) go to 80
      r(n2 + 1) = y(n2 + 1)
      im(n2 + 1) = 0.0d0
      c(n2 + 1) = r(n2 + 1)*r(n2 + 1) +im(n2 + 1)*im(n2 + 1)
      if (c(j).gt.cmax) then
            cmax=c(n2+1)
      end if
80    open (unit=2, file = fnn2)
      do 700 j=4,n2
            jm1 = j - 1
            cjm1=jm1/(dfloat(n)*deltat)
C  normalize the DFT results
            c(j)=c(j)/cmax
            write(2,900) cjm1, c(j)
700   continue
      close (2)
900   format (f7.3,f9.5)
      end
```

Appendix H: CRL source code

```
C**********************************************************************
C
C Program crl.for
C
C       This program determines the auto-correlation of optical
C intensity from a single emitter.  Before this is calculated, the
C mean of the each of the columns is determined and is subtracted
C from each of the values.  A copy of the original column vector
C is needed since the NAG routine c06ekf writes the result array
C back into the first column vector.
C
C**********************************************************************
C

      integer ifail,j,jj,jm1,n,index
        integer sigfigr,tenpwrr,sigfigi,tenpwri
      double precision crl(4000)
      double precision xa(4000),xxa(4000)
      double precision ya(4000),yya(4000)
      double precision cjm1,deltat,cmax
      double precision sum,avg
        character*11 destdir2
        character*16 fn1,fn2
        character*27 fnn1,fnn2
C  read the data points of the time series
c       print *,'input data point number of the time series...'
c       read *,n
        n=4000
C  read the unit length of the time series...'
c      print *,'input unit (ps/channel) of the time series...'
c       read *, deltat
        deltat=1.0d0
      deltat=deltat*1.0d-03
        destdir1='c:\tmp\'
        destdir2='d:\mod.dat\'
        open(unit=2,file='d:\mod.dat\etatable.prm')
        read(2,*)sigfigr
        read(2,*)tenpwrr
        read(2,*)sigfigi
        read(2,*)tenpwri
C Synthesize file names out of key parameters
        if((sigfigr.ge.0).and.(sigfigi.ge.0)) then
       fn1='X1'//char(sigfigr+48)//char(tenpwrr+48)
     $    //char(sigfigi+48)//char(tenpwri+48)//'.dat'
       fn2='crl'//char(sigfigr+48)//char(tenpwrr+48)
     $    //char(sigfigi+48)//char(tenpwri+48)//'.dat'
c
        elseif ((sigfigr.ge.0).and.(sigfigi.lt.0)) then
        sigfigi=iabs(sigfigi)
       fn1='X1'//char(sigfigr+48)//char(tenpwrr+48)
     $    //"-"//char(sigfigi+48)//char(tenpwri+48)//'.dat'
       fn2='crl'//char(sigfigr+48)//char(tenpwrr+48)
     $    //"-"//char(sigfigi+48)//char(tenpwri+48)//'.dat'
        sigfigi=-1*sigfigi
c
        elseif ((sigfigr.lt.0).and.(sigfigi.ge.0)) then
        sigfigr=iabs(sigfigr)
       fn1='X1'//"-"//char(sigfigr+48)//char(tenpwrr+48)
     $    //char(sigfigi+48)//char(tenpwri+48)//'.dat'
       fn2='crl'//"-"//char(sigfigr+48)//char(tenpwrr+48)
```

Appendix H: CRL source code

```
     $   //char(sigfigi+48)//char(tenpwri+48)//'.dat'
         sigfigr=-1*sigfigr
c
         else
         sigfigr=iabs(sigfigr)
         sigfigi=iabs(sigfigi)
        fn1='X1'//"-"//char(sigfigr+48)//char(tenpwrr+48)
     $   //"-"//char(sigfigi+48)//char(tenpwri+48)//'.dat'
        fn2='cr1'//"-"//char(sigfigr+48)//char(tenpwrr+48)
     $   //"-"//char(sigfigi+48)//char(tenpwri+48)//'.dat'
         sigfigr=-1*sigfigr
         sigfigi=-1*sigfigi
         endif
         close(2)
         fnn1=destdir2//fn1
         fnn2=destdir2//fn2
        open (unit=1,file=fnn1)
C  read the time series data into xa
        do 40 j=1,n
              read (1,*) xa(j)
 40     continue
        close(1)
C  copy this array, xa, into xxa since c06ekf writes
C  the correlation results back into xa
        do 200 j=1,n
              ya(j)=xa(j)
              xxa(j) = xa(j)
              yya(j) = xa(j)
200     continue
c         Find Average value of array xxa
          sum=0.d0
          do 201 j=1,n
          sum=sum+xxa(j)
 201      continue
          avg=sum/dfloat(n)
c         Make array xxa have zero mean
          do 202 j=1,n
          xxa(j)=xxa(j)-avg
          yya(j)=yya(j)-avg
          xa(j)=xa(j)-avg
 202      continue
        ifail = 0
C  call the NAG program that does correlations by
C  giving the first argument of the call as 2 and
C  then giving the two vectors to be compared and their length
C  (the argument '2' directs the NAG routine c06ekf to do a
C   correlation of the two vectors--a first argument of '1'
C   would result in a fourier transform of the correlation)
        call c06ekf(2,xa,ya,n,ifail)
        cmax=0.0d0
        do 375 j=1,n
              crl(j) = xa(j)
              if (dabs(crl(j)).gt.cmax) then
                    cmax=dabs(crl(j))
              endif
375     continue
C  normalize the results to one
        do 400 j=1,n
              crl(j)=crl(j)/cmax
400     continue
```

Appendix H: CRL source code

```
      open (unit=2,file=fnn2)
      do 700 j=(n/2 + 2),n
            jm1 = j-1
            jj =(jm1 - n/2)
            index = jj - 1
            cjm1=index*deltat
            write(2,900) cjm1, crl(jj)
700   continue
      close (2)
900   format (f7.3,f9.5)
      end
```

Appendix H: BIFPEP source code

```
C**********************************************************************
C
C Program bifpep.for
C with new and improved format 7/31/90, Carleson
C**********************************************************************
        real x(4000),y(4000),xa(4000),loogetar,loogetai
        integer n,k,kk,sigfigr,tenpwrr,sigfigi,tenpwri
        character*16 fn1, fn2
        character*11 destdir2
        character*23 fnn1
        character*27 fnn2
        destdir2='d:\mod.dat\'
        n=4000
        open(unit=2,file='d:\mod.dat\etatable.prm')
        read(2,*)sigfigr
        read(2,*)tenpwrr
        read(2,*)sigfigi
        read(2,*)tenpwri
C Synthesize file names out of key parameters
        if((sigfigr.ge.0).and.(sigfigi.ge.0)) then
      fn1='X1'//char(sigfigr+48)//char(tenpwrr+48)
     $   //char(sigfigi+48)//char(tenpwri+48)//'.dat'
      fn2='bo'//char(sigfigr+48)//char(tenpwrr+48)
     $   //char(sigfigi+48)//char(tenpwri+48)//'.dat'
c
        elseif ((sigfigr.ge.0).and.(sigfigi.lt.0)) then
        sigfigi=iabs(sigfigi)
      fn1='X1'//char(sigfigr+48)//char(tenpwrr+48)
     $   //"-"//char(sigfigi+48)//char(tenpwri+48)//'.dat'
      fn2='bo'//char(sigfigr+48)//char(tenpwrr+48)
     $   //"-"//char(sigfigi+48)//char(tenpwri+48)//'.dat'
        sigfigi=-1*sigfigi
c
        elseif ((sigfigr.lt.0).and.(sigfigi.ge.0)) then
        sigfigr=iabs(sigfigr)
      fn1='X1'//"-"//char(sigfigr+48)//char(tenpwrr+48)
     $   //char(sigfigi+48)//char(tenpwri+48)//'.dat'
      fn2='bo'//"-"//char(sigfigr+48)//char(tenpwrr+48)
     $   //char(sigfigi+48)//char(tenpwri+48)//'.dat'
        sigfigr=-1*sigfigr
c
        else
        sigfigr=iabs(sigfigr)
        sigfigi=iabs(sigfigi)
      fn1='X1'//"-"//char(sigfigr+48)//char(tenpwrr+48)
     $   //"-"//char(sigfigi+48)//char(tenpwri+48)//'.dat'
      fn2='bo'//"-"//char(sigfigr+48)//char(tenpwrr+48)
     $   //"-"//char(sigfigi+48)//char(tenpwri+48)//'.dat'
        sigfigr=-1*sigfigr
        sigfigi=-1*sigfigi
        endif
        loogetar=-tenpwrr+(float(sigfigr-1))/10.0
        if (sigfigi.lt.0) then
                loogetai=-tenpwri+(float(sigfigi+1))/10.0
        else
                loogetai= tenpwri+(float(sigfigi-1))/10.0
        endif
        close(2)
        fnn1=destdir2//fn1
        fnn2=destdir2//fn2
```

Appendix H: BIFPEP source code

```
      open (unit=1,file=fnn1)
C  read the time series data into x
      do 40 j=1,n
               read (1,*) x(j)
 40   continue
        close(1)
c Throw out all sequentially equal pts.
        kk=1
        do 45 j=1,n-1
        if(x(j).eq.x(j+1)) then
        goto 45
        else
        xa(kk)=x(j)
        kk=kk+1
        endif
 45     continue
        if(kk.eq.1) then
               k=2
               y(1)=x(1)
               goto 51
        endif
c  Find local maxima of the array x
        k=1
        do 50 j=2,kk-2
               if(xa(j).gt.xa(j-1).and.xa(j).gt.xa(j+1)) then
               y(k)=xa(j)
               k=k+1
               endif
 50     continue
c       write local maxima to bif.out file
 51     open(unit=15,file=fnn2)
        do 60 j=1,k-1
               write(15,999)loogetar,y(j)
 60     continue
c   Write a " " at end of file so gr.new will know end of set
c       write(15,*)'" "'
        close(15)
 999    format(F5.2,1X,e13.6)
      end
```

Appendix H: FABRY.PEROT source code

```
C "fabry.perot.f", by Geoffrey Wilson 17 June 1991
C
C This program reads data files containing emission spectra and
C generates the pixel position of the peaks, and the normalized
C net modal gain.
C
C Parameters currently set for device PGE4600B#1D4
C
      integer pixel0,pixel, pixel1,pixel2,npeaks,peak,i,j
      integer count,pkpix,window
      double precision pi,coeff,delpix,satlevel,p,p0,pmax,y,ybar,margin
      double precision x0,x2,x4,x,y0,y1,y2,a,b,c,xcen,ycen,ratio,xbar
      double precision dp(0:639)
      logical satflag
      character*2 prefix
      character*3 suffix
      character*6 fn1,fn2
      character*8 fn3,fn4
C Begin main body.
      pi=3.1415926565898d0
C Speed of light * photon lifetime / group index / device length.
C Also: electronic charge / Planck's constant / speed of light *
C wavelength * two-facet differential efficiency / facet transmission.
      coeff=0.630d0
C Number of peaks.
      npeaks=3
C First pixel in the usable range.
      pixel0=55
C Mean longitudinal mode spacing in pixels.
      delpix=177.d0
C Flag to warn of saturation possibility.
      satflag=.false.
C Saturation level.
      satlevel=0.99d0
C Minimum signal to include a data point in the window about the peak.
      margin=0.9d0
C Query user for file prefix.
      print*,'Supply the two-character file prefix:'
      read(5,1)prefix
1     format(a2)
C Query user for file suffix (drive current in mA).
      print*,'Supply the three-digit file suffix:'
      read(5,3)suffix
3     format(a3)
C Create data file name.
      fn1=prefix//'.'//suffix
C Create background file name.
      fn2=prefix//'.000'
C Create peak position output file name.
      fn3=fn1//'.p'
C Create normalized net modal gain output file name.
      fn4=fn1//'.g'
C Open data and background files.
      open(1,file=fn1)
      open(2,file=fn2)
C Read the data and backgound files.
      do 200 pixel=0,639
      read(1,*)j,p
C Test for saturation possibility.
      if (satflag) go to 100
      if (p.gt.satlevel) then
        satflag=.true.
        print*,'WARNING: possibility of saturation.'
        end if
100   read(2,*)j,p0
C Subtract background.
```

Appendix H: FABRY.PEROT source code

```
      dp(pixel)=p-p0
200   continue
C Close data and background files.
      close(1)
      close(2)
C Open output files.
      open(3,file=fn3)
      open(4,file=fn4)
C Begin loop, one pass for each peak.
      do 1000 peak=1,npeaks
C Set integration limits for this peak.
      pixel1=pixel0+idint(dfloat(peak-1)*delpix)
      pixel2=pixel0-1+idint(dfloat(peak)*delpix)
C Read the data for this peak, find the maximum of the net signal and
C and the average of the net signal reciprocal.
      count=0
      pmax=0.d0
      ybar=0.d0
      do 300 pixel=pixel1,pixel2
C Do not use the point if the signal is not positive.
      if (dp(pixel).le.0.d0) go to 300
C Use point, increment counter.
      count=count+1
C Test point against running maximum.
      if (dp(pixel).gt.pmax) then
        pmax=dp(pixel)
        pkpix=pixel
      end if
C Calculate the reciprocal signal.
      y=1.d0/dp(pixel)
C Accumulate the sum of the reciprocal signal.
      ybar=ybar+y
C Done searching peak range.
300   continue
C If count equals zero, no acceptable points were found.
      if (count.eq.0) then
        print*,'ERROR: count is equal to zero.'
        stop
        end if
C Normalize the reciprocal sum to get the average.
      ybar=ybar/dfloat(count)
C Get the range of contiguous points about the peak.
      window=0
400   if (dp(pkpix-window-1).lt.margin*pmax) go to 500
      if (dp(pkpix+window+1).lt.margin*pmax) go to 500
      window=window+1
      go to 400
500   continue
C Fit a parabola to the contiguous set of points about the peak.
C Calculate some necessary constants.
      x0=0.d0
      x2=0.d0
      x4=0.d0
      do 600 i=-window,window
      x=dfloat(i)
      x0=x0+1.d0
      x2=x2+x*x
      x4=x4+x*x*x*x
600   continue
C Calculate the weighted intensities.
      y0=0.d0
      y1=0.d0
      y2=0.d0
      do 700 i=-window,window
      x=dfloat(i)
      y=1.d0/dp(pkpix-i)
```

Appendix H: FABRY.PEROT source code

```
      y0=y0+y
      y1=y1+x*y
      y2=y2+x*x*y
700   continue
C Calculate the best fit to a quadratic function.
C If window is zero, warn the user and do not curve fit.
      if (window.eq.0) then
        print*,'WARNING: window is equal to zero.'
        xcen=0.d0
        ycen=y0
      else
        a=(x4*y0-x2*y2)/(x0*x4-x2*x2)
        b=y1/x2
        c=(x0*y2-x2*y0)/(x0*x4-x2*x2)
C Find the center of the parabola.
        xcen=-.5d0*b/c
C Calculate the minimum in the reciprocal net signal.
        ycen=a-.25d0*b*b/c
      end if
C Record the peak position.
      write(3,*)peak,sngl(dfloat(pkpix)+xcen)
C Calculate the ratio of the minimum-to-average net signal.
      ratio=ycen/ybar
C Stop if ratio is not between zero and one, exclusive.
      if (ratio.le.0.d0) then
        print*,'ERROR: ratio is less than or equal to zero.'
        stop
        end if
      if (ratio.ge.1.d0) then
        print*,'ERROR: ratio is greater than or equal to one.'
        stop
        end if
C Calculate the gain at the peak.
      xbar=(1.d0-dsqrt(2.d0*ratio-ratio*ratio))/(1.d0-ratio)
C Record the normalized net modal gain.
      write(4,*)peak,sngl(coeff*dlog(xbar))
C Done with this peak.
1000  continue
C Close the output files.
      close(3)
      close(4)
      stop
      end
```

Appendix H: EXP.PWR.SP source code

```
C*********************************************************************
C
C Program exp.pwr.sp.f, by Geoffrey Wilson, 13 June 1991
C
C Reads a data file containing k experimentally-obtained time series,
C each 480 data points long (number of rows in the PEP 301 video
C frame) and calculates the average power spectrum. Based on
C "powersp.for", discussed below.
C
C*********************************************************************
C
C Program powersp.for
C
C       This program calculates the discrete fourier transform of
C optical intensity from a single emitter.  This corresponds to a
C DFT in the time domain.  The data is read a column at a time into
C a real 1D array required by the NAG routine c06eaf.  The original
C sequence is a real sequence and consequently the DFT is a particular
C type of complex sequence, a Hermitian sequence with the following
C properties:
C       a(N-k)=a(k)
C       b(N-k)=-b(k) , b(0)=0 , b(N/2)=0 for N even
C where DFT{z(k)} = a(k) + ib(k)  when z(k)=x(k) (z real).
C A Hermitian sequence of N complex values can then be uniquely
C specified by N independent real values.  The NAG routine c06eaf writes
C the real parts a(k) for 0<k<N/2 in the first (N/2 + 1) components of
C array x. The non-zero imaginary components b(k) are written in reverse
C order to the remaining (N/2 - 1) components of array x.  The results
C are normalized to one and read back into an array file.
C
C*********************************************************************
C
      integer ifail,i,j,jm1,n2,nj,n,k,ik
      double precision cjm1,cmax,deltat
      double precision y(480)
      double precision r(240),im(240),c(240),cc(240)
        character*8 fn1
        character*12 fn2
C  read the data points of time series
c       print *,'input data point number of time series...'
c       read *,n
        n=480
C  read the unit length of the time series
c       print *,'input unit (ps/channel) of the time series...'
c       read *,deltat
C For "10 ns" setting of Hamamatsu streak camera.
C       deltat=12.09d0
C For "5 ns" setting of Hamamatsu streak camera.
C       deltat=5.78d0
C For "2 ns" setting of Hamamatsu streak camera.
      deltat=2.14d0
C For "1 ns" setting of Hamamatsu streak camera.
C       deltat=1.20d0
C For "0.3 ns" setting of Hamamatsu streak camera.
C       deltat=.34d0
C Convert from picoseconds to nanseconds to yield frequency in GHz.
      deltat=deltat*1.0d-03
C Acquire the number of time series in the data file.
      print*,'How many time series are in the data file?'
      read*,k
C Acquire the data file name from the user.
      print*,'Supply the data file name (8 characters):'
      read(5,1)fn1
1     format(a8)
C Create output file name.
      fn2=fn1//'.eps'
```

VITA

Geoffrey A. Wilson was born in Riverside, California on January 14, 1959. He received the B.S. degree (Cum Laude, Distinction) from Sonoma State University, Rohnert Park, California in June, 1984.

In April 1987, he began his studies at Oregon Graduate Institute of Science and Technology. In November 1989, he completed requirements for the M.S. degree in Applied Physics, including a thesis titled "Diode Laser Pumped 1645-nm Er:YAG Lasers as Sources for Differential Absorption LIDAR Methanometry".

In January 1992, he successfully defended this Ph.D. thesis, and joined the Physics Department of the University of Oregon in Eugene, Oregon, as a postdoctoral research associate.